Light manipulation of ultra-cold matter waves on board a vehicle : from fundamental physics to inertial navigation

Baptiste Battelier

UNIVERSITÉ DE BORDEAUX

École Doctorale des Sciences Physiques et de l'Ingénieur

Laboratoire Photonique, Numérique et Nanosciences

HABILITATION A DIRIGER DES RECHERCHES

presented by
Baptiste BATTELIER

Light manipulation of ultra-cold matter waves on board a vehicle : from fundamental physics to inertial navigation

Defended on February 19th 2021 at Institut d'Optique d'Aquitaine

in front of the following jury :

President :	Christophe Salomon	LKB - Paris
Reviewer :	Wolf Von Klitzing	FORTH- Heraklion
	Ernst Rasel	LUH - Hannover
	Barry Garraway	University of Sussex- Brighton
Examinator :	Guglielmo Tino	LENS - Firenze
	Philippe Bouyer	LP2N - Talence
Invited member :	Arnaud Landragin	SYRTE - Paris

Remerciements

Je souhaite tout d'abord remercier chaleureusement le jury de mon « habilitation à diriger des recherches » : Wolf Von Klitzing, Ernst Rasel, Barry Garraway, Guglielmo Tino, Christophe Salomon. Ce fut l'occasion de lancer des discussions enthousiasmantes et fructueuses, ce qui était l'un de mes objectifs lors de cette soutenance.

Ensuite, je souhaiterais remercier Philippe Bouyer de m'avoir accueilli dans son groupe, pour une aventure passionnante qui a débuté il y a maintenant 13 ans. A l'époque, la miniaturisation des interféromètres atomiques était un domaine vierge, que j'ai pris beaucoup de plaisir à défricher. Cette activité a connu un beau succès, et s'est donc poursuivi dans le temps et dans l'espace, puisque nous avons déménagé à Bordeaux à la création du LP2N.

En parallèle de ces activités de recherche partenariale, je me suis fait les dents sur l'expérience embarquée à bord de l'avion 0g. Je tiens à ce sujet remercier Arnaud Landragin (observatoire de Paris), le second papa de cette manip, et avec qui j'ai également beaucoup collaboré sur les activités industrielles. J'ai survécu à des changements de génération sur ce projet au long cours, avec une expérience qui a été renouvelé à 100% plusieurs fois. Je tiens donc à remercier la « first generation » : Rémi, Vincent (Ménoret), Guillaume, Patrick, ainsi que mes collègues de l'ONERA qui ont participé au succès de ce premier interféromètre atomique embarqué : Nassim Zahzham, Alexandre Bresson, Yannick Bidel. Je tiens ensuite à exprimer ma gratitude envers la « second generation » : Pierre-Alain, Laure, Laura et bien sur Brynle avec qui on a poursuivi notre collaboration jusqu'à récemment avec le laboratoire commun iXAtom. Ensuite, je remercie et souhaite bon courage aux plus jeunes de la « third generation » : Martin, Gabriel, Romain, Celia et Vincent (Jarlaud).

Je remercie les agences spatiales pour les campagnes de vols paraboliques, les financements de thèses et des projets clés pour les futures applications spatiales. Je tiens notamment à remercier Linda Mondin et Thomas Lévêque du CNES qui nous apporte un énorme soutien depuis de nombreuses années, ainsi qu'Olivier Carraz de l'ESA pour son regard pertinent sur nos travaux.

L'arrivée à Bordeaux a été associée à la création de muQuanS. Je remercie Bruno Desruelle pour m'avoir permis de contribuer au début de développement des produits phares de l'entreprise, avec des échanges très dynamisant sur les lasers, le gravimètre, et l'horloge atomique.

Je tiens à remercier chaleureusement Henri Porte et Fabien Napolitano qui ont décidé de relever avec moi le défi de la navigation inertielle avec les atomes froids. Le soutien d'iXblue est très important et donne une grande dynamique au laboratoire commun iXAtom. Je remercie Lauriane, Baptiste (Gouraud), Simon (Templier), Pierrick, et Brynle pour leur contribution qui a permis de développer cette activité durant ces 5 premières années.

On part aujourd'hui sur une seconde phase avec une nouvelle équipe, et je souhaite bonne chance à Theo, Simon et Quentin (qui a le plus long nom de tous mes étudiants) pour aller vers la première campagne sur un bateau et la miniaturisation de l'accéléromètre atomique.

Dans le cadre de mes nombreux projets de développements de composants, je souhaite remercier Margaux qui a pu apprivoiser les nouvelles fibres polarisantes.

J'ai bien sur une pensée particulière pour mes collègues du groupe Atomes froids à Bordeaux : Benjamin, Andrea, Simon. Les échanges avec eux m'ont notamment transmis les idées de refroidissement par états noirs pour le chargement du piège dipolaire et de doubled-dressed states pour les bulles quantiques. Merci également aux plus jeunes qui participe ou ont participé au dynamisme de notre groupe.

Je remercie de manière générale les chercheurs et ingénieurs de recherche du LP2N et en particulier Giorgio Santarelli, avec qui j'ai eu des échanges particuliers sur les lasers, et en particulier au cours d'une belle collaboration pour développer une source laser fibrée pour le Césium.

Il n'est bien sûr pas possible de mener ces activités à forte composante expérimentale sans un soutien des compétences techniques présentes au LP2N. Je souhaite remercier Philippe Teulat (service mécanique), Jean-Hugues Codarbox et Arnaud Tizon (service électronique). De plus, je tiens à remercier Stéphanie Shultze, Fabien Lehoux, et Laurent Porcel qui composent les services administratifs du LP2N, et forme notamment une interface efficace avec nos tutelles.

Enfin je finirai par une tendre pensée envers mon épouse Mélanie, ma fille ainée Léocadie, ainsi qu'à la toute, toute, petite dernière qui est sur le point de naitre, et avec qui j'ai créé un véritable petit cocon dans cette belle région.

Table des matières

Chapitre 1

Introduction

Wave/particle duality is one of the most remarkable phenomena described by quantum mechanics. The wave behavior of matter, a concept introduced by Louis de Broglie in 1924, has been demonstrated by many experiments, which are often based on slowing the particles down, since the size of the associated wave is inversely proportional to the square root of the temperature. Manipulation of matter waves is based on laser cooling which were developed in the 80's and gave a Nobel Prize to Claude Cohen-Tannoudji, Bill Phillips and Steven Chu in 1997. The radiation pressure force brought into play here allows to cool and trap an atom cloud at the center of six laser beams.

Naturally it is possible to make these matter waves interfere. As well as classic optics, the idea is to split and recombine coherently the wave packets to create multiple paths which interfere. Consequently, the phase shift of the fringes depend on the different paths followed by the wave packets. Considering the non zero mass of the atoms, it is understood that *matter waves interferometers* are extremely sensitive to inertial effects. The high accuracy of the atom interferferometers is based on the fact that the atoms are by principle perfect proof masses following an ideal free fall trajectory (see chapter 2).

Light Manipulation of matter is at heart of atom interferometers and the evolution in this field is strongly related to the technology development of lasers. For instance ultracold atom sources for the new generation of atom sensors can be produced using an optical tweezer, an invention which offered to Arthur Ashkin a Nobel prize in 2018. What was not possible experimentally 30 years ago can now be achievable using laser sources providing high power light and which can be controlled with a high tunability. Lasers at new wavelengths enlarge the catalogue of atom species used for condensed matter experiments and metrology. Technological development in light engineering also implies advances in atomic physics, not only in laboratory (optical lattices, Digital Mirror Devices, Spatial Light Modulation, microscopy...) but also brings a significant increase of the Technology Readiness Level for onboard applications.

The first objective of my research activities is to improve as far as possible the performances of cold atoms inertial sensors. Potentially the extreme accuracy of these instruments will allow to shed light on some essential questions of fundamental physics, especially about the nature of gravitation, using experiments bringing into play microscopic phenomena described by quantum mechanics. Space is the playground of ambitious experiments to explore fundamental concepts such as Lisa for the detection of gravitational waves, Microscope to test the Universality of free fall or ACES to measure the gravitational red shift or to search for a shift of the fine-structure constant among other goals. In this context, we aim to develop the ultimate cold atom interferometer for Space. To reach this goal, it is necessary to put the experiment in **microgravity** to increase the interrogation time and tackle the challenges

expected with an instrument on board a satellite. In this context, we developed a compact system which can be tested on several microgravity platforms such as the zero-g plane and the zero-g simulator installed in our laboratory (see Chapter 3).

Through the development of this instrument, we also faced the issues of **embarquability** and integration/miniaturization (see Chapter 4). If we are able to build **compact** and transportable systems sensitive to inertial effects, these quantum sensors can constitute a technology breakthrough in the field of gravimetry and inertial navigation. This second part of my work aims to improve the technology of cold atoms sensors. In relation with several companies, I led specific technical developments of fibred laser systems, a compact cold atom gravimeter and a multi-axis atom accelerometer. These developments led to a technology transfer and a start-up (μQuans). Today many challenges need to be overcome, especially in the frame of inertial navigation : compactness of the apparatus, atomic gyroscope of improved sensitivity, and robustness in an environment with a high level of vibrations and strong rotation rates. For the future, we will aim at **miniaturizing** these quantum atom sensors using new technological key components such as atom chips.

Finally, light matter-interaction also allow to "paint" new types of atom traps. We are particularly interested in optical methods to produce **ultra-cold** atom sources. The list of techniques includes not only dipole traps, but also velocity selective coherent trapping, Raman cooling ... (see chapter 2). This aspect is essential for experiments in free fall for which the temperature can limit the interrogation time. Thanks to the optical techniques we developed and the access to microgravity platforms, we envision for the future the production of traps of ultra-cold gases with new geometries bringing out topological phase transitions especially rich to study (see Chapter 5).

Chapitre 2

Light Manipulation of ultra-cold matter waves

First we want to emphasize the strong analogy of matter waves optics with its photonic counterpart but also a few differences, in the general context of atom interferometry. Then we focus more specifically on inertial sensing using cold atom sensors. Large momentum transfer and multi-axis atom optics are currently studied to extend the performances and the robustness of the future quantum sensors. Then we present several examples of laser techniques involved to produce a perfect atom source (trapping and cooling, state preparation) to improve the performances of the atom interferometers.

2.1 Propagation of matter waves

The wave/particle duality was formalized by Louis de Broglie who extended to any particle the concept of coexistence of waves and particles discovered by Albert Einstein in 1905 in the case of light and photons. He introduced the de Broglie wavelength, matter analog of the photonic wavelength :

$$\lambda_{dB} = \frac{h}{m v_{at}} \tag{2.1}$$

where h is the Planck constant and m the mass of the particle and v_{at} the velocity. Wave properties (diffraction, interferences) is more prominent with large wavelength, which is the case for small mass and/or low momentum.

Remark : this general definition is usually "adapted" to define the coherence of an atom source related to the temperature T. The "thermal" DeBroglie wavelength is :

$$\lambda_{th} = \frac{h}{\sqrt{2\pi m k_B T}} \tag{2.2}$$

where k_B is the Boltzmann constant. For this definition, the velocity has been replaced by the width of the velocity distribution σ_v.

The propagation of matter waves is described by the following equation :

$$-\frac{\hbar^2}{2m}\Delta\psi(\mathbf{r},t) + V(\mathbf{r})\psi(\mathbf{r},t) = i\hbar\frac{\partial}{\partial t}\psi(\mathbf{r},t) \tag{2.3}$$

From this formula, we can get the dispersion law for matter waves in vacuum $V(\mathbf{r}) = 0$.

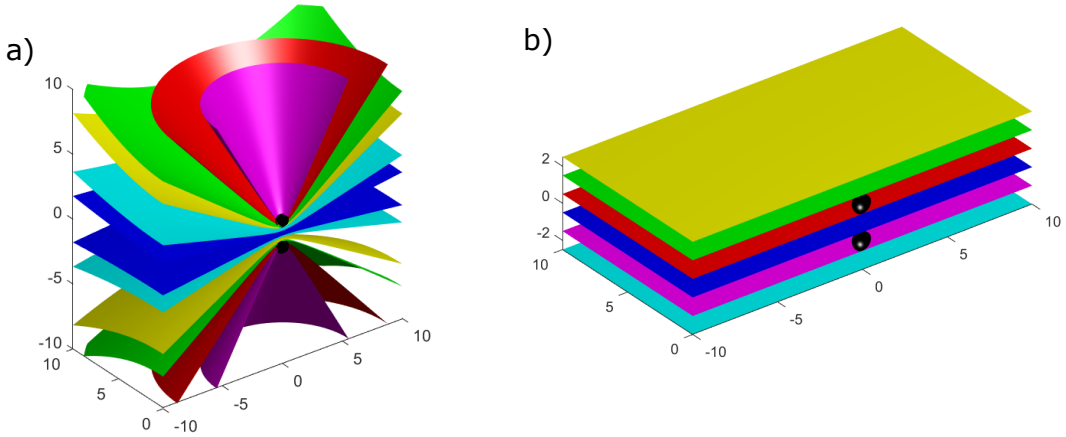

FIGURE 2.1 – 3D fringes produced by two point sources separated along the vertical axis (black) in optics (a) and with matter waves (b). In optics, the equiphases are hyperboloids. With matter waves, the equiphases are planes.

Considering a monochromatic wave-packet $\psi \propto e^{-i\omega t}$, equation 2.3 becomes :

$$\Delta\psi + \frac{2m\omega}{\hbar}\psi = 0 \tag{2.4}$$

Considering now a propagating wave in the x direction $\psi \propto e^{i(kx-\omega t)}$, we get the relation :

$$\omega = \frac{\hbar k^2}{2m} \tag{2.5}$$

The group velocity $v_g = d\omega/dk$ and the phase velocity $v_\phi = \omega/k$ are different which means the wave packets naturally spread. Matter is a dispersive source even in vacuum and in absence of interaction ! Note that we can see it right away with the definition of the DeBroglie wavelength which is inversely proportional to the velocity.

Matter wave diffraction for monokinetic atomic source propagated after a time T can be expressed in the plane $X - Y$ orthogonal to the propagation direction :

$$\psi(x, y) = \psi_0 \exp[i\frac{E_c T}{\hbar}] = \psi_0 \exp[i\frac{m}{2\hbar T}(x^2 + y^2)] \tag{2.6}$$

where E_c is the kinetic energy. We get a spherical wave.

Let's take an example to emphasize the consequences of the dispersion by comparison with light. The goal is to define the 3D spatial fringes coming from two point sources.

In optics, the phase difference between the two paths coming from each point source can be written as :

$$\Delta\phi = \frac{2\pi}{\lambda}(d_1 - d_2) \tag{2.7}$$

where d_1 and d_2 are the distances between the point source 1 (respectively 2) and the point where we evaluate the phase difference. $\Delta\phi$ =Cste is the equation of an elliptic hyperboloid (two sheets), where the two point sources are the focal points of the hyperboloid. Equiphase profiles are plotted on Fig. 2.1 (a) for two point sources separated along the vertical axis. We find the expected rings in the cross section of an horizontal plane and the fringes profile. The fringes from the Young's points can be seen in the cross-section with a vertical plane as well.

In atom optics, the phase difference between the two paths coming from each point source

has the following equation :

$$\Delta\phi_A = \frac{\hbar}{mT}\left(x^2 + y^2 + z^2 - (x^2 + y^2 + (z-a)^2)\right) \tag{2.8}$$

where T is the time of propagation, a is the distance between the two point sources, and x, y, z the coordinates of the point where we evaluate the phase difference. $\Delta\phi_A$ =Cste leads to the equation z =Cste and corresponds to a plane normal to the axis defined by the two point sources.

2.2 Matter wave interferometer to measure inertial effects

2.2.1 Mach-Zehnder interferometer

The coherent splitting and the recombination of matter waves are done using interaction between a light pulse and an atom. The most common method is the Raman transition, which is a two photon process coupling two states of the atom.

Here the atom can be considered as a two level system for which Rabi oscillations between the two states $|1\rangle$ and $|2\rangle$ are achieved. Let's consider the case where the atom is in state $|1\rangle$. If we apply a pulse called $\pi/2$, we achieve a quarter of Rabi oscillation, and the atom will be in a coherent superposition of states $|1\rangle + |2\rangle$. From a quantum point of view, this pulse is analogous to a beam splitter and the atom analogous to a photon. if we a apply a π pulse, which is twice longer, we achieve half an oscillation and the atom is thus transferred from the state $|1\rangle$ to the state $|2\rangle$, which is equivalent to a mirror. We should notice the Raman transition plays not only on the internal state of the atom but also on the external state, given a momentum $\hbar(\mathbf{k_1} + \mathbf{k_2}) = \hbar\mathbf{k_{eff}}$ to the wave packet if this one is diffracted in the state $|2\rangle$, $\mathbf{k_1}$ and $\mathbf{k_2}$ being the wave vectors of the two Raman photons. More particularly this effect is significant if the two beams are counter-propagating. The superposition of states is both internal and external and it implies a spatial separation of the paths traveled by the wave packets.

With a sequence of 3 pulses $\pi/2$-π-$\pi/2$ we achieve a Mach-Zehnder interferometer for which we switch the role of light and matter (see Fig. 2.2).

2.2.2 Phase shift of an atom interferometer

When we calculate the phase shift of this interferometer, we get the sum of three terms :

$$\Phi = \Phi_{laser} + \Phi_{prop} + \Phi_{sep} \tag{2.9}$$

The term Φ_{prop} corresponds to the phase shift due to the propagation of the wave packets in the interferometer, Φ_{sep} is the phase shift due to a spatial separation between the two wave packets at the interferometer input or output, and Φ_{laser} is the phase shift due to the atom-laser interaction.

Calculation of Φ_{prop}

The probability amplitude for a particle to travel from $A(\mathbf{r}_a, t_a)$ to $B(\mathbf{r}_b, t_b)$ is the Feynman propagator :

$$K(\mathbf{r}_b, t_b; \mathbf{r}_a, t_a) = \sum_{\Gamma} e^{iS_\Gamma/\hbar} \tag{2.10}$$

where S_Γ is the action along the path Γ. The sum is over all the paths from A to B. The

wave function at B is given by the sum of all the probabilities :

$$\psi(\mathbf{r}_b, t_b) = \int K(\mathbf{r}_b, t_b; \mathbf{r}_a, t_a)\psi(\mathbf{r}_a, t_a)d\mathbf{r}_a \tag{2.11}$$

The action S_Γ is deduced from the Lagrangian $\mathcal{L} = E_c - V$:

$$S_\Gamma = \int_{t_a}^{t_b} \mathcal{L}(\mathbf{r}(t), \dot{\mathbf{r}}(t), t)dt \tag{2.12}$$

In the summation over all paths $\sum_\Gamma e^{iS_\Gamma/\hbar}$ only the stationary phases contribute significantly, which means we keep the path Γ minimizing the action, i.e. classical trajectories. For a Lagrangian at most quadratic in $\mathbf{r}$ and $\dot{\mathbf{r}}$, K is deduced from the classical action :

$$K \propto e^{iS_{cl}/\hbar} \tag{2.13}$$

This is similar to the principle of least action or Fermat's principle in optics.

$$\psi(\mathbf{r}_b, t_b) = e^{-\frac{i}{\hbar}S_\Gamma}\psi(\mathbf{r}_a, t_a) \tag{2.14}$$

We can deduce the expression of Φ_{prop} :

$$\Phi_{prop} = (S_{cl,B} - S_{cl,A})/\hbar \tag{2.15}$$

Applying the approach of Feynman path integrals to a Lagrangian at most quadratic in position and momentum in the case of a constant acceleration, it is shown that $\Phi_{prop} = 0$ [1]. We can cite several examples of Lagrangian satisfying these conditions. First the free particle follows :

$$\mathcal{L} = m\dot{\mathbf{r}}^2/2 \tag{2.16}$$

A particle in gravitational field can be used in the case of a gravimeter :

$$\mathcal{L} = m\dot{\mathbf{r}}^2/2 - mgz \tag{2.17}$$

A particle in an harmonic trap corresponds to guided ultra-cold atoms solutions which are proposed to combine compactness of the apparatus (for instance on an atom chip) and long interrogation times :

$$\mathcal{L} = m\dot{\mathbf{r}}^2/2 - m\omega_0^2 r^2/2 \tag{2.18}$$

A particle in a rotating frame can be is an interesting case to consider especially for all on board applications. For inertial navigation, we want to measure the rotation of the mobile using a gyroscope and a rotating reference frame can be relevant to be considered. This is also essential on a satellite. Even on ground Earth rotation need to be taken into account for long interrogation times :

$$\mathcal{L} = m\dot{\mathbf{r}}^2/2 + m\dot{\mathbf{r}} \cdot (\Omega \times \mathbf{r}) + m(\Omega \times \mathbf{r})^2/2 \tag{2.19}$$

Calculation of Φ_{sep}

A separation between the wavepackets creates a phase shift :

$$\Phi_{sep} = \mathbf{p}\boldsymbol{\Delta}\mathbf{r}/\hbar \tag{2.20}$$

If the Mach Zhender interferometer is perfectly symmetrical (same time T between the first

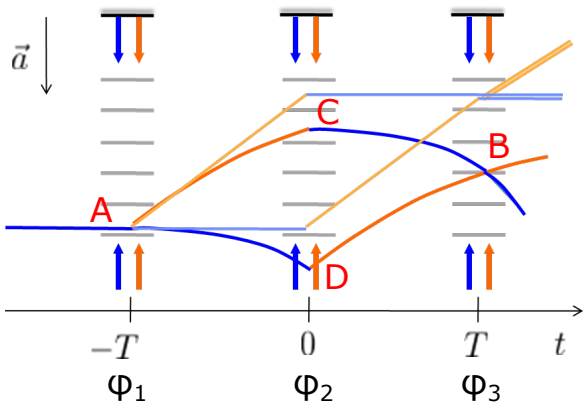

FIGURE 2.2 – Matter wave Mach Zehnder interferometer, similar to the optical one, except that we switched the role of light and matter. In presence of a constant acceleration, the atom trajectory is curved and the wake packets will cross the phase ruler defined by the laser beams at different positions and thus acquire a different phase at the output of the interferometer.

and second pulse as the time between the second and third pulse), the wavepackets are overlapped and $\Phi_{sep} = 0$.

We can show the interference fringes depends only of the laser phase where the atoms are located at the time of the pulses. The mid-point theorem [2] says the phase depends on the center of mass position of the atomic wave packet :

$$\Phi_{laser} = k(z_C - z_B + z_D - z_A) + \phi_1 - 2\phi_2 + \phi_3 \tag{2.21}$$

2.2.3 Inertial measurements with an atom interferometer

In practice, the Raman transition is created using a beam including two optical frequencies and retro-reflected by a mirror. Consequently the laser phase is defined by the position of this reference mirror. A simple picture to understand the sensitivity of an atom interferometer is to consider that each pulse encodes in the matter wave an information about the position of the center of mass of the wave packet. A sequence of three pulses amounts to measure the position of the atom at three different times using an optical ruler with a reference defined by the position of the mirror. Thus we can retrieve the relative acceleration of the matter wave compared to the mirror. In the case of a constant acceleration $\mathbf{a}$ the phase is :

$$\Phi = \mathbf{k_{eff}} \cdot \mathbf{a}T^2 \tag{2.22}$$

where T is the duration between two pulses.

The high sensitivity of the atom interferometers can be understood using the model of the phase ruler. We measure the displacement of the atoms with a step at the scale of the wavelength (780 nm for Rubidium for instance). If the Signal to Noise Ratio (SNR) is 1000, then we can resolve the step with a precision of 1 : 1000, and measure the fall of the atoms over 1 s with a precision of 10^{-10} m.s^{-2}.

An atom interferometer measures the relative acceleration of the atoms compared to the mirror $\mathbf{a} = \mathbf{a_{mirror}} - \mathbf{g}$. For a gravimeter [3], the mirror is fixed on the ground ($\mathbf{a_{mirror}} = \mathbf{0}$) and we measure the acceleration of the atoms in free fall ($\mathbf{a} = \mathbf{g}$). We remark vibrations on the ground constitutes a limitation of the measurement of g since $\mathbf{a_{mirror}}$ fluctuates around zero. That's why the most sensitive measurements are done on anti-vibration platforms.

To improve the sensitivity of the measurement, the game is to increase the interrogation time T (equation 2.22) since the phase increases as the square of this time. This duration is naturally limited by the fall duration inside the experiment. Some research groups built 10 meter high atomic fountains [4, 5]. Our group chose an alternative approach which consists in making the experiment fall with the atoms and put it in microgravity on board the zero-g plane in order to prepare future Space missions on board a satellite (see chapter 3).

In principle it is possible to measure accelerations and rotations with atom interferometers and build a complete quantum inertial navigation system (INS) [6]. In this case, we switch the role between the atoms and the reference mirror compared to a gravimeter. We measure the trajectory of the mirror compared to the atoms in free fall which follow a perfect reference parabola (see chapter 4). Similar to any classical accelerometer, it is necessary to know the value of $\mathbf{g}$ to retrieve the acceleration we want to measure $\mathbf{a_{mirror}}$. If we want to measure the rotations $\mathbf{\Omega}$, the atoms are launched with an initial velocity $\mathbf{v}$, which implies a Coriolis acceleration [7] :

$$\mathbf{a_{Cor}} = 2\mathbf{v} \wedge \mathbf{\Omega} \tag{2.23}$$

By replacing $\mathbf{a}$ by $\mathbf{a_{Cor}}$ in equation 2.22, we can write the expected phase shift which follows the Sagnac law :

$$\Phi = \frac{4\pi}{\lambda_{dB} v} \mathbf{\Omega} \cdot \mathbf{A} \tag{2.24}$$

where v is the velocity of the atoms and λ_{dB} the DeBroglie wavelength. We notice the rotation sensitivity of the atoms, for the same interferometer area $\mathbf{A}$ is $\frac{mc^2}{\hbar\omega} \sim 10^{11}$ higher than their optical counterparts (fiber or laser).

We can find back the sensitivity to the area of the interferometer using the perturbative approach described in [1] :

$$\mathcal{L} = \mathcal{L}_0 + \epsilon \mathcal{L}_1 \tag{2.25}$$

where $\mathcal{L}_0$ is the unperturbed Lagrangian and $\epsilon \ll 1$.

Of the first order in ϵ, the phase shift $\delta\phi$ is determined by the integral of the perturbation along the classical path :

$$\delta\phi = \frac{\epsilon}{\hbar} \oint_{\Gamma_{cl}^{(0)}} \mathcal{L}_1 dt \tag{2.26}$$

Let's take the case of gravity $\epsilon\mathcal{L}_1 = mgz(t)$.

$$\delta\phi^{prop} = -\frac{mg}{\hbar} \oint_{ABCDA} dt z(t) = -\frac{mg}{\hbar}\mathcal{A} \tag{2.27}$$

where $\mathcal{A} = -\hbar k/mT^2$ is the spacetime area of the atom interferometer. In this case the phase shift is not included in the laser phase term anymore but on the propagation term.

Similarly in the case of a rotation $\epsilon = \Omega\Delta t$, the phase shift between A and B is :

$$\delta\phi^{prop} = \frac{m\Omega}{\hbar} \int_{t_A}^{t_B} r(t) \times dr(t) = 2\frac{m\Omega}{\hbar}\mathcal{A}_{\mathcal{AB}} \tag{2.28}$$

The total phase shift of the atom interferometer is then :

$$\delta\phi^{prop} = \frac{m\Omega}{\hbar} \oint_{ABCDA} r(t) \times dr(t) = 2\frac{m\Omega}{\hbar}\mathcal{A} \tag{2.29}$$

where $\mathcal{A}$ is the spatial area of the atom interferometer.

2.2.4 Sensitivity and transfer functions

Initially developed for atomic clocks, the sensitivity function is an efficient tool to characterize the influence of different kinds of noise on the phase. Let's assume a phase jump $\delta\phi$ occurs on the laser phase at time t during the interferometer sequence. It implies a change in the transition probability $\delta P(\delta\phi, t)$. The sensitivity function is then defined :

$$g(t) = 2 \lim_{\delta\phi \to 0} \frac{\delta P(\delta\phi, t)}{\delta\phi} \tag{2.30}$$

For a Mazh Zehnder interferometer, the sensitivity function [8] is an odd function, whose expression is given here for $t > 0$ if the condition $\Omega_R \tau = \pi/2$ (Fig. 2.3 (a)) :

$$g(t) = \begin{cases} \sin(\Omega_R t) & 0 < t < \tau_R \\ 1 & \tau_R < t < T + \tau_R \\ -\sin(\Omega_R (T - t)) & T + \tau_R < t < T + 2\tau_R \end{cases} \tag{2.31}$$

We can retrieve the interferometric sensitivity :

$$\delta\Phi = \int_{-\infty}^{\infty} g_s(t) d\phi(t) = \int_{-\infty}^{\infty} g_s(t) \frac{d\phi(t)}{dt} dt \tag{2.32}$$

Let's consider the case of constant acceleration g. The oddity of the function implies the phase is not sensitive to the initial velocity. If we fix the phase of the laser ϕ_{las} =Cste, The laser phase varies as a function of time :

$$\phi(t) = k \frac{g t^2}{2} \tag{2.33}$$

We get the following phase shift :

$$\delta\Phi = \int_{-\infty}^{+\infty} g_s(t) k g t dt = k g (T + 2\tau_R) \left[T + \frac{2}{\Omega_R} \tan\left(\frac{\Omega_R \tau_R}{2} \right) \right] \tag{2.34}$$

Note that this formula includes the exact scale factor including the effects of the pulses.

To evaluate the sensitivity of the Mach-Zhender interferometer to laser phase noise, we calculate the Fourier transform of the sensitivity function :

$$G(\omega) = \int_{-\infty}^{+\infty} e^{-i\omega t} g_s(t) dt \tag{2.35}$$

The transfer function is then :

$$H(\omega) = |\omega G(\omega)| = -\frac{4 i \omega \Omega_R}{\Omega^2 - \Omega_R^2} \sin\left(\frac{\omega(T + 2\tau)}{2} \right) \left(\cos\left(\frac{\omega(T + 2\tau)}{2} \right) + \frac{\Omega_R}{\omega} \sin\left(\frac{\omega T}{2} \right) \right) \tag{2.36}$$

The interferometer acts as a filter (Fig. 2.3 (c)). The first term in $H(\omega)$ is a low pass filter with a cutting frequency $\Omega_R/(2\pi)$. With the second term, we show the transfer function cancelled for specific frequencies $2\pi/(T + 2\tau)$.

this transfer function is used to calculate the influence of a phase noise of power spectral density $S_\phi(\omega)$. For one single measurement of the atom interferometer we get :

$$\sigma_\phi^2 = \int_0^{+\infty} |\omega G(\omega)|^2 S_\phi(\omega) \frac{d\omega}{2\pi} \tag{2.37}$$

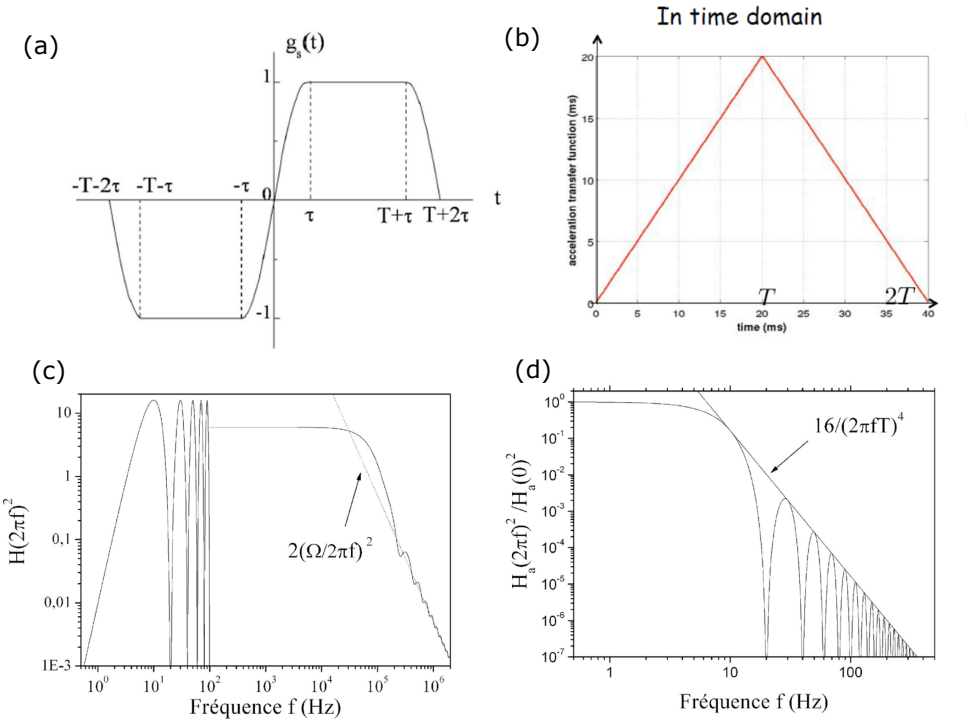

FIGURE 2.3 – (a) Sensitivity function of the Mach-Zehnder interferometer to a phase jump $\delta\phi$. (b) Response function to a varying accelerometer $a(t)$. (c) Transfer function in terms of phase noise. (d) Transfer function in terms of acceleration noise.

Experimentally we repeat the measurement with a cycling time T_c and we have an aliasing effect for frequencies above $2/T_c$ such as for atomic clocks. The integrated phase noise over a time τ is a sum of the harmonics of $1/T_c$:

$$\sigma_\phi^2(\tau) = \frac{1}{\tau}\sum_{n=1}^{\infty} |H(2\pi n f_c)|^2 S_\phi(2\pi n f_c) \tag{2.38}$$

Similarly we can use this method for all sources of noise which act or appears as a phase noise : magnetic field, light shifts... One important effect for on board applications is the acceleration. The laser phase can be written as the sum of two terms $\varphi = \phi + kz$. The position z is related to the acceleration :

$$a_z = \frac{\delta^2 z}{\delta t^2} \tag{2.39}$$

The response function in terms of acceleration is a primitive of the sensitivity function (Fig. 2.3 (b)) :

$$f(t) = \int_{-\infty}^{t} g_s(t')dt' \tag{2.40}$$

We then get the phase due to a fluctuating acceleration $a(t)$

$$\phi_a = k\int_{-\infty}^{\infty} f(t)a(t)dt \tag{2.41}$$

We can also define a transfer function for acceleration noise (Fig. 2.3 (d)) :

$$|H_a(\omega)|^2 = \frac{k_{eff}^2}{\omega^4}|H(\omega)|^2 \tag{2.42}$$

and the integrated phase noise for an acceleration noise of power spectral density $S_a(\omega)$:

$$\sigma_\phi^2(\tau_m) = \frac{k_{eff}^2}{\tau_m}\sum_{n=1}^{\infty}\frac{|H(2\pi n f_c)|^2}{(2\pi n f_c)^4}S_a(2\pi n f_c) \tag{2.43}$$

2.2.5 Multiaxis atom optics and interferometer

We have studied theoretically how to measure simultaneously the acceleration along several axes. We have proposed new techniques allowing to create multidimensional atom beamsplitters and mirrors. Our method relies on a recently developed formalism for multi-dimensional atom optics and interferometer geometries that creates coherent superpositions of matter waves along three spatial directions and enables the simultaneous measurement of accelerations and rotations in 3D [9]. This new arsenal of atom optical tools is based on two or three mutually orthogonal excitation beams that exchange momentum with atoms along more than one spatial direction at a time (see Fig. 2.5). The leading-order phase shift of this interferometer is

$$\Phi_{3D} = [\mathbf{\Delta K}\cdot\mathbf{a} + 2\frac{\hbar}{m}(\mathbf{\Delta K}\times\mathbf{K})\cdot\mathbf{\Omega}]T^2 \tag{2.44}$$

where $\mathbf{\Delta K}$ is the difference between two orthogonal wavevectors, $\hbar\mathbf{K}$ is the center-of-mass momentum transferred to the atom, $\mathbf{a}$ and $\mathbf{\Omega}$ are the total acceleration and rotation vectors, respectively, $\hbar/m$ is the ratio of Planck's constant to the atomic mass, and T is the free-fall time between pulses. With the correct combination of 2D and 3D atomic beam splitters and mirrors, leading to the generation of several simultaneous interferometers, one can reconstruct the three components of $\mathbf{a}$ and $\mathbf{\Omega}$ in a single shot from a linear combination of the different phases [9].

In the 2D case, the state of an atom can be written :

$$|\Psi(p_x,p_y,t)\rangle = c_1(t)|1,p_x,p_y\rangle + c_2(t)|2,p_x+\hbar k_x,p_y\rangle + c_3(t)|2,p_x,p_y+\hbar_y\rangle \tag{2.45}$$

where the states are labeled by their internal energy and the photon momentum transfer along each direction. This system exhibits Rabi oscillations (see Fig. 2.4) in the population between states, where the vector of state amplitudes $\mathbf{C}^T = (c_1, c_2, c_3)$ evolves according to :

$$C(t) = exp\left[-i\begin{pmatrix}0 & \chi_x^* & \chi_y^*\\ \chi_x & -\delta_x & 0\\ \chi_y & 0 & -\delta_y\end{pmatrix}t\right]C(0) \tag{2.46}$$

where χ_x and χ_y are the Rabi frequencies and δ_x and δ_y are the detuning frequencies.

If $\delta_x = \delta_y$, the effective Rabi frequency is :

$$\Omega_R = \frac{1}{2}\sqrt{\delta^2 + |\chi_x|^2 + |\chi_y|^2} \tag{2.47}$$

2D Rabi oscillations are similar to the double diffraction case [10] (see Fig. 2.4). The latter case corresponds to a particular situation where the two wavevectors k_x and k_y are colinear and counter-propagating.

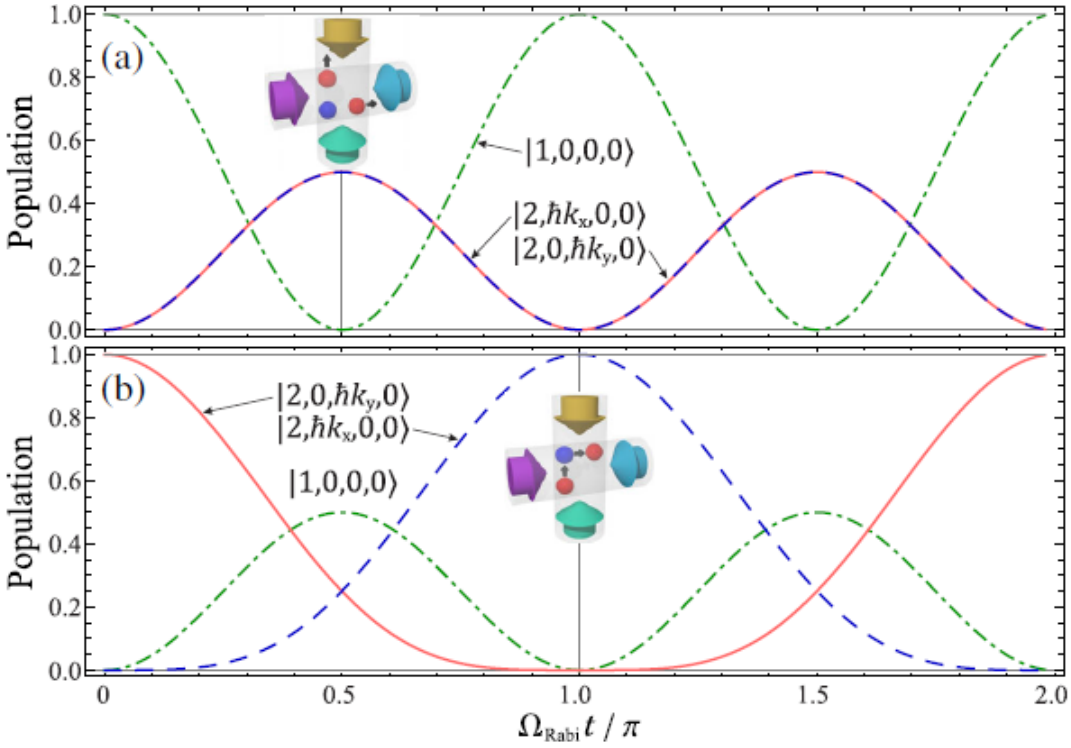

FIGURE 2.4 – Rabi oscillations for a 2D beam splitter (a) and a 2D mirror (b) realized using pulse areas of $\Omega_R t = \pi/2$ and π, respectively. The insets show the corresponding physical picture.

Figure 2.5 (a) shows an architecture of a 2D atom accelerometer. In this case, the interferometer phase shift is :

$$\Phi_{2D} = (\mathbf{k_x} - \mathbf{k_y}) \cdot \left[\mathbf{a} + \mathbf{g} + \frac{\hbar}{m}(\mathbf{k_x} + \mathbf{k_y}) \times \mathbf{\Omega}\right] T^2 \tag{2.48}$$

where k_x (resp. k_y) is the wave vector along the x (resp. y) direction.

Moreover 2D double-diffraction atom optics allows to generate four simultaneous 2D Mach-Zehnder interferometers from a single atomic source, as shown in Fig. 2.5 (b) and (c). Linear combinations of the four phases obtained from a single shot give access to two components of acceleration and one rotation (e.g. a_x, a_y, and Ω_z).

Hence, for upper and lower pathways with different initial kick directions Using linear

$\mathbf{k_x}$	$\mathbf{k_y}$	$\Delta\Phi_{2D}$	
$+k_x\hat{\mathbf{x}}$	$+k_y\hat{\mathbf{y}}$	$\Delta\Phi_{xy}$	$= (+k_x a_x - k_y a_y)T^2 + \frac{2\hbar}{m} k_x k_y \Omega_z T^2$
$+k_x\hat{\mathbf{x}}$	$-k_y\hat{\mathbf{y}}$	$\Delta\Phi_{x(-y)}$	$= (+k_x a_x + k_y a_y)T^2 - \frac{2\hbar}{m} k_x k_y \Omega_z T^2$
$-k_x\hat{\mathbf{x}}$	$+k_y\hat{\mathbf{y}}$	$\Delta\Phi_{(-x)y}$	$= (-k_x a_x - k_y a_y)T^2 - \frac{2\hbar}{m} k_x k_y \Omega_z T^2$
$-k_x\hat{\mathbf{x}}$	$-k_y\hat{\mathbf{y}}$	$\Delta\Phi_{(-x)(-y)}$	$= (-k_x a_x + k_y a_y)T^2 + \frac{2\hbar}{m} k_x k_y \Omega_z T^2$

TABLE 2.1 – Table of the different phase shifts in the a 2D double diffraction atom interferometer

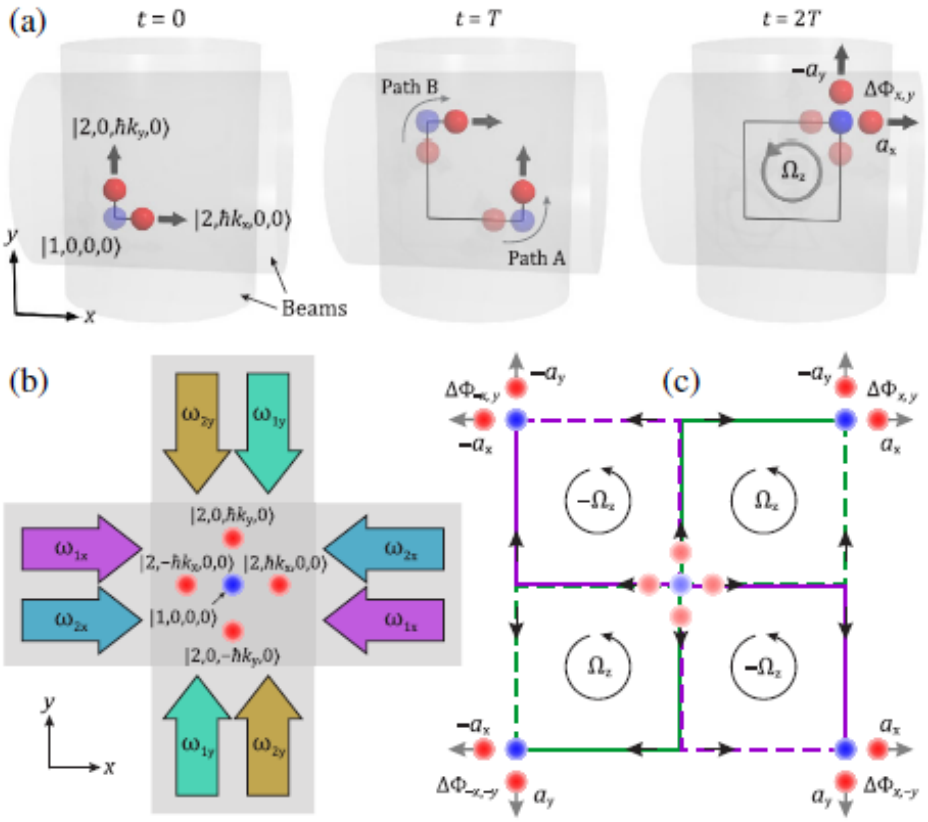

FIGURE 2.5 – (a) A sequence of atom-optical pulses constituting a 2D Mach-Zehnder interferometer. (b) A retroreflected beam geometry enabling 2D double-diffraction atom optics, which symmetrically transfer $\hbar k_\mu$ of momentum along each axis $\mu = x, y$. (c) Four simultaneous 2D Mach-Zehnder AIs derived from the same atomic source. Linear combinations of the four phase shifts allow one to isolate the three inertial components a_x,a_y, and Ω_z with increased sensitivity.

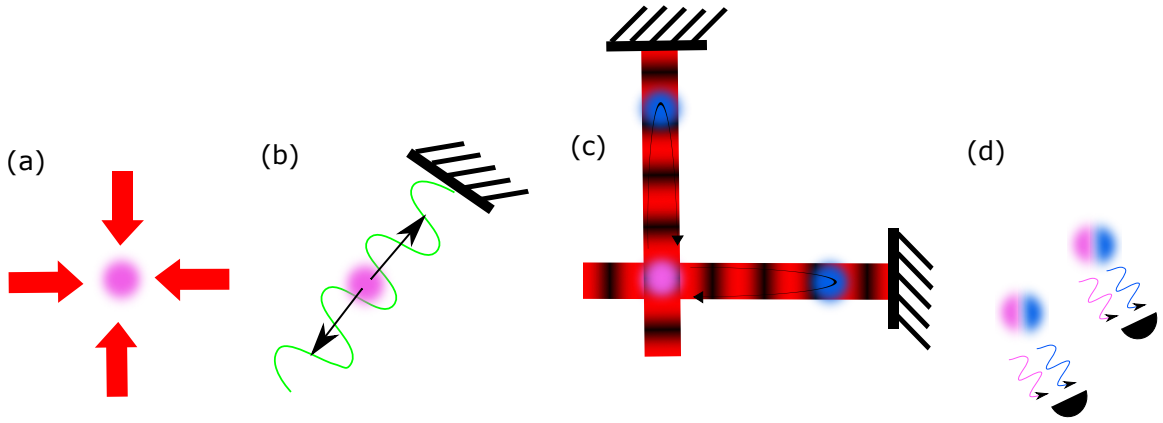

FIGURE 2.6 – Simultaneous measurement of the acceleration in 2 dimensions using ultracold atoms. After cooling in a dipole trap (a), Bloch oscillations (green lattice) allow to split in momentum two atomic sub-assembles along the diagonal direction between the two axes of measurement (b). Thanks to Doppler effect, we can interrogate independently each cloud for a dedicated axis using the Raman frequency condition (c). For detection, we wait for the spatial splitting of the two clouds and we detect by fluorescence the state $|1\rangle$ and $|2\rangle$ for each cloud (d).

components of there phases one can isolate each component :

$$\frac{1}{2}(\Delta\Phi_{xy} + \Delta\Phi_{x(-y)}) = k_x a_x T^2 \tag{2.49}$$

$$\frac{1}{2}(\Delta\Phi_{xy} + \Delta\Phi_{(-x)y}) = -k_y a_y T^2 \tag{2.50}$$

$$\frac{1}{2}(\Delta\Phi_{x(-y)} + \Delta\Phi_{(-x)y}) = -\frac{2\hbar}{m} k_x k_y \Omega_z T^2 \tag{2.51}$$

We should emphasize the rotation term in the third equation has a scale factor which can be very accurate and doesn't depend on the velocity or gravity. This method thus allows to achieve atom gyroscopes with the advantages to control precisely the scale factor unlike the usual techniques where the atoms are launched by moving molasses or an atomic beam.

In case of a 3D interferometer, the detection of these fringes combines 2 CCD cameras and two imaging beams for fluorescences, imaging two orthogonal planes to reconstruct the 3D interference pattern[11]. This method allows us to discriminate spatially the different inertial phases along the axes x, y et z.

Alternative methods to extract the signal can be implemented. The idea is to modulate independently each axes and extract the relevant modulated signal. This modulation can be applied on the laser phase for instance.

Using ultracold atoms can offer alternative strategies to achieve multiaxis measurements. Fig. 2.6 describes a sequence based on a combination of Bloch oscillations and Raman transitions to achieve simultaneously two orthogonal interferometers located at the same place. A combination of spatial imaging and state dependent fluorescence detection allows to extract the outputs of both interferometers.

Finally, multidimensional atom optics pave the way to a large panel of new geometries in the field of atom interferometry [12]. Among them, one architecture is particularly interesting. A full loop cold atom gyroscope can be achieved using a sequence of 5 pulses.

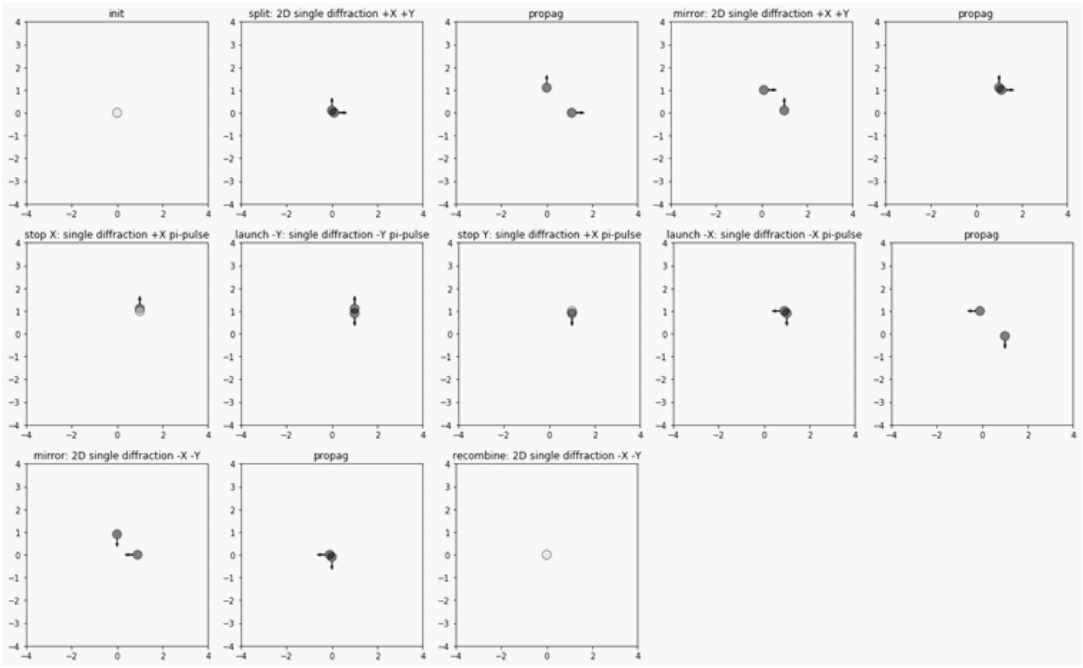

FIGURE 2.7 – Principle of a 2D full loop atom gyroscope. The displacement of the wavepackets is simulated using the Hamiltonians describing the atom-light interaction in the configuration of two orthogonal counter-propagating Raman beam pairs. Each picture describes the position (circle) and the momentum of the wavepackets at one instant during the atom interferometer.

The phase shift of the full loop atom interferometer is the following :

$$\delta\phi_{loop} = -\frac{k^2 T^2 \hbar}{m}\Omega_z \tag{2.52}$$

where $k = k_x = k_y$. Here again the phase shift is not dependent on the initial velocity of the atom.

Another strong advantage of this configuration is the absence of contrast loss because the wavepackets are necessarly overlapped at the end of the interferometer. Indeed the separation of the wave packets is null at the first order. If we look at the first terms (in T^3 and Ω^2), the separation in momentum is null $\delta\mathbf{p} = 0$ and the separation in position is :

$$\delta\mathbf{q} = \begin{pmatrix} \Omega_z^2 \\ -\Omega_z^2 \\ 0 \end{pmatrix} \frac{3kT^3\hbar}{4m} \tag{2.53}$$

2.2.6 Prospect : creating artificial gauge fields using multiaxis Raman transitions

The process of 2D Raman transitions and closed loop geometries can play a role for other applications such as topological phases in lattices. Rotating a neutral particle system is equivalent to giving these particles a unit charge and placing them in a magnetic field proportional to the rotation vector. Other possibilities have been suggested for applying an artificial gauge field on a neutral gas. The common idea in these proposals is to exploit the Berry's phase [13] that arises when the atomic ground level is split (e.g., by an electromagnetic field) into several space-dependent sublevels, and the atoms follow one of them adiabatically. The idea is to induce a nonvanishing phase of particles moving along a closed path on the

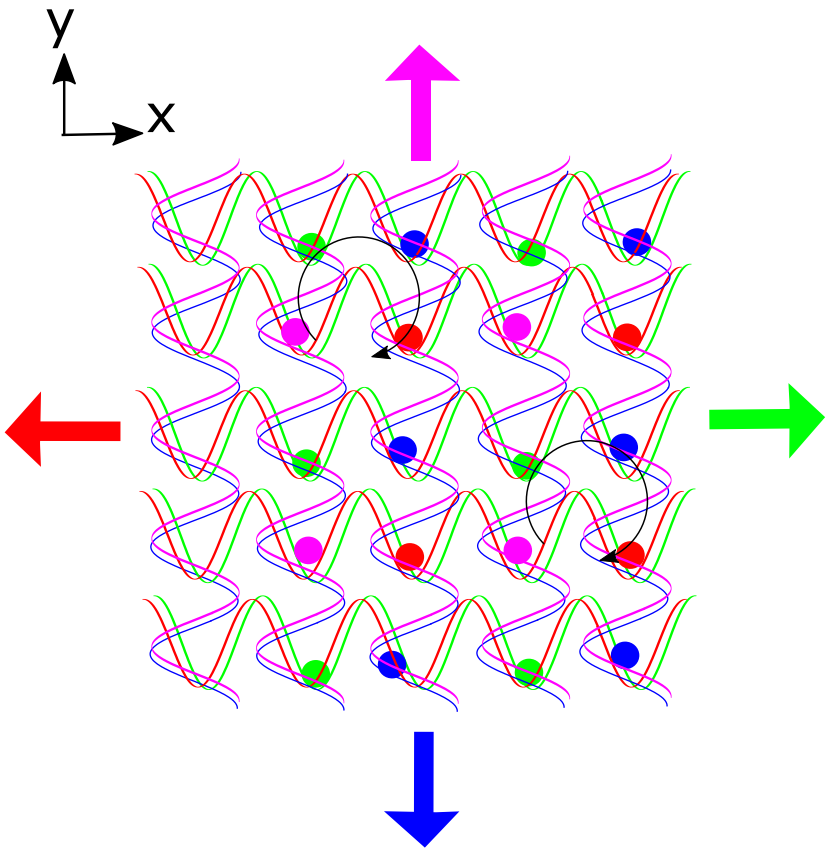

FIGURE 2.8 – The system is composed of 4 moving lattices going towards respectively $+X$ (green), $-X$ (red), $+Y$ (magenta), $-Y$ (blue). The atom in the state $|0, +k_y\rangle$ (magenta full circle) is transported by the magenta lattice, then a 2D Raman pulse transfer it in the $|-k_x, 0\rangle$ (red full circle) to be transported by the red lattice. The next step consists in a second 2D Raman pulse to transfer the atom in the $|0, -k_y\rangle$. Repeating the same process, each atom will follow a loop.

lattice. Such proposals have been done and Jaksch and Zoller [14] showed that one can reach a "high-magnetic-field" regime that is not experimentally accessible for electrons in metals, characterized by a fractal band structure (the Hofstadter butterfly).

Using our technique of 2D atom optics, we propose an alternative scheme to achieve high artificial magnetic fields in lattices. Most of the other proposals are based on playing with different internal states of the atoms. On the contrary, we propose to play with the external states of the atom corresponding to their momentum in the 2D $x - y$ plane k_x and k_y. The other particularity of our proposal is the fact that the 2D system is composed of two counter propagating moving lattices on each axis x and y with a constant velocity corresponding to the recoil $\hbar k/m$ where m is the mass of the atoms.

Fig. 2.8 illustrates the principles of our strategy. Let's start with the atoms in the state $|+k_x, 0\rangle$ (the atom is in the same internal state during the full loop). The atoms are adiabatically carried by the lattice moving in the $+X$ direction but don't "see" the three other lattices if the parameters are chosen to avoid adiabatic transfer and Bloch oscillations. By applying a 2D pulse, the atoms is transferred in the state $|0, +k_y\rangle$. The atoms are then transported in the moving lattice $+Y$. The 2D Raman transition allows a good coupling between the Wannier functions of two orthogonal propagating lattices. This way it is possible to close the loop and print a phase corresponding to an artificial magnetic field.

2.3 All optical methods for atom cooling and trapping

After a short discussion about the requirement to reduce the velocity dispersion of the atom cloud for atom interferometry, we present several optical methods to produce ultracold atom sources.

2.3.1 An ultracold atom source for atom interferometry

The major challenge for the next generation of atom interferometers is to increase the interrogation time. In this context it is essential to reduce the temperature of the atoms. The first reason is to increase the coherence length of the source defined by the DeBroglie wavelength λ_{th}. Secondly the contrast can be improved because the efficiency of the counter-propagating Raman transitions (beam splitters and mirror of the Mach-Zehnder interferometer) depends strongly of the velocity dispersion. Finally the control of the initial position and the velocity as well as the mitigated spatial expansion of the cloud provide strong advantages in terms of systematic errors. For instance, the spatial size of the atom cloud makes the interferometer sensitive to the imperfection of the intensity and phase profile of the laser beam. Even if it is not a fundamental limit the creation of an homogeneous large beam is very demanding.

If our definition of the temperature is related to the velocity dispersion σ_v, cooling is often defined as an increase of the Phase Space Density (PSD) :

$$PSD = n\lambda_{th}^3 \tag{2.54}$$

where n is the atom density. The PSD is the essential criteria for Bose Einstein Condensation (BEC). BEC occurs when the wavepackets size (λ_{th}) is larger than the distance between them ($1/n^{1/3}$) and overlapped, or in other words when PSD is about 1 (actually 2.612 in a 3D harmonic trap). This is equivalent to an atom laser for which where all the atoms are described by the same wave function.

At first glance the achievement of a BEC is not necessary for atom interferometry. Nevertheless the requirements of a high atom number (to reduce the atom shot noise), a small size and a reduced velocity dispersion all together lead to approach the BEC regime even if the phase space density is not exactly the relevant parameter.

Different techniques can be implemented to reduce the velocity dispersion σ_v :

— Filtering a velocity class by a Raman selective pulse or a physical slit. Of course the drawback of this method is the atom loss.

— An adiabatic decompression of the atom trap or the delta kick collimation allow to mitigate σ_v. In both cases the phase space density is constant.

— Evaporative cooling is the most common technique to increase the PSD, with a certain cost in terms of atom loss

— Laser cooling in optical traps can also increase the PSD. Raman cooling to produce a Rb BEC in a dipole trap has been demonstrated [15]. This technique can be very interesting because the process is fast and the atom loss is weak.

2.3.2 Grey molasses

Grey molasses [16, 17, 18, 19, 20, 21, 22] have been recently considered for atom species for which standard molasses are not efficient enough (Potassium, Lithium) but has never been used for atom interferometry until our results with Potassium. The principle of the

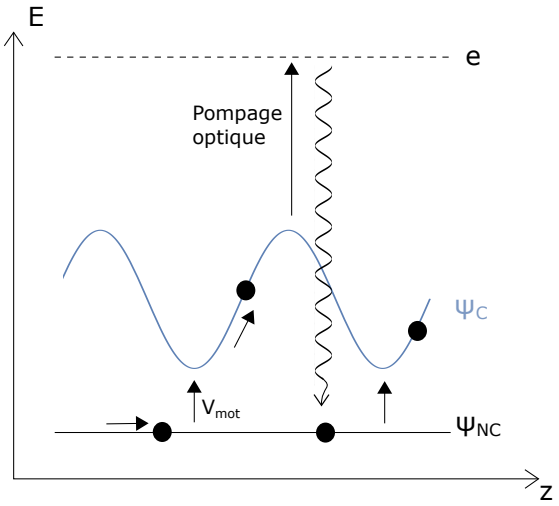

FIGURE 2.9 – Sisyphus cooling in grey molasses. The atom in a Zeeman Dark State (Ψ_{NC} on the figure) is transferred in a bright state Ψ_C by motional coupling. When the laser is blue detuned, this atom climbs a potential slope until the probability to be optically pumped back in Ψ_{NC} is significant which is the case at the top of the hill.

grey molasses combines Sisyphus effect and Velocity-Selective Coherent Population Trapping (VSCPT) applied to a configuration involving states which are non coupled to light.

Grey molasses commonly rely on Zeeman dark states (ZDSs), i.e., linear combinations of Zeeman sublevels not coupled to lasers blue-detuned with respect to the cooling transition [23] (see Fig. 2.10 (a)). Generally, ZDSs are not eigenstates of the kinetic-energy operator, and free evolution turns them into bright, absorbing states. Moreover, the presence of a repumper laser spoils these ZDSs, limiting the cooling efficacy [24, 25].

Grey-molasses cooling results from a spatially-varying light shift that allows moving atoms to undergo a Sisyphus-like cooling process until being optically pumped to a dark state $|\mathrm{ZDS}\rangle$. Atoms stay in $|\mathrm{ZDS}\rangle$ until velocity-induced motional coupling brings them back to a bright state where cooling begins again (see Fig 2.9). The lifetime of $|\mathrm{ZDS}\rangle$, where atoms do not scatter light, sets the minimum achievable temperature. For the $|F = 2\rangle \rightarrow |F' = 2\rangle$ transition, only the ground states $|m_F = 0, p = 0\rangle$ and $|m_F = \pm 2, p = \pm 2\hbar k\rangle$ are coupled, where m_F is a magnetic quantum number, p is the momentum, and k is the wavevector of the cooling light. Hence, the dark state can be written as the superposition of three momentum states

$$|\mathrm{ZDS}\rangle = \frac{1}{\sqrt{3}}(|-2, -2\hbar k\rangle - |0, 0\rangle + |2, 2\hbar k\rangle). \tag{2.55}$$

As a result of this superposition, $|\mathrm{ZDS}\rangle$ is very short lived which limits the minimum temperature.

2.3.3 Λ enhanced grey Molasses

We add now a condition on the second laser (repumping beam) to create long-lived dark states. With a configuration where the repumper and cooler frequencies are equally detuned from the excited state,i.e., a Raman configuration (see Fig. 2.10 (b)), hyperfine dark states (HDSs) can be created. These HDSs have been rigorously studied in the context of coherent population trapping and electromagnetically induced transparency [26, 27, 28], but not yet for grey molasses cooling.

In the Λ-enhanced scheme, the second laser is blue detuned from $|F = 1\rangle \rightarrow |F' = 1\rangle$,

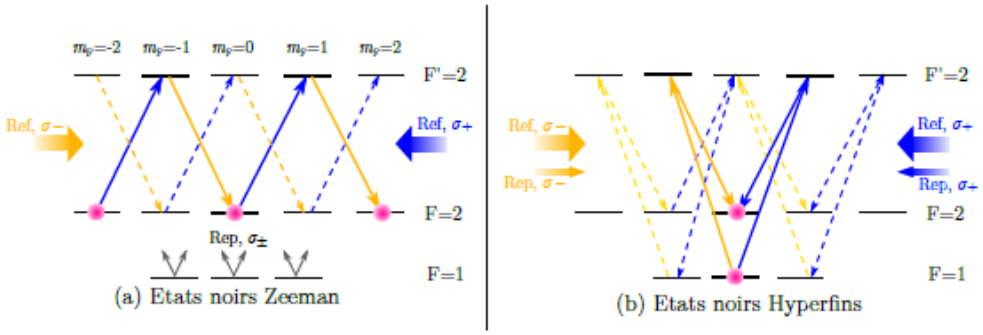

FIGURE 2.10 – VSCPT on the D2 line of ^{87}Rb or on the D1 line of ^{39}K. (a) Inverted-W atom level configuration : no criteria on the repumping beam which has no phase relation with the cooling beam. Existence of a transient dark state constituting of the different Zeeman states of the level $|F = 2\rangle$. (b) Double Λ configuration : the repumping beam is in phase with the cooling beam. Existence of long-lived dark states made of a superposition of different magnetic sub-levels of the two hyperfine states $|F = 1\rangle$ and $|F = 2\rangle$.

and is phase locked to the first via the EOM. Consequently, $|\mathrm{NC}\rangle$ will mix with states in the $F = 1$ manifold, forming a more complex but longer-lived non-coupled state :

$$|\mathrm{NC}\rangle = (\Omega_H|G\rangle - \Omega_G|H\rangle)/\sqrt{\Omega_G^2 + \Omega_H^2} \tag{2.56}$$

where cold atoms are stored for larger durations—enhancing the cooling effect. Here, $|G\rangle$ and $|H\rangle$ represent superpositions of different magnetic sub-levels within the $|F = 1\rangle$ and $|F = 2\rangle$ manifolds, and $\Omega_{G,H}$ are effective optical pumping rates between these levels. The specific combinations of levels depends on the relative intensities of the cooling and repumping beams, and their polarization gradient potentials [19].

The existence of these HDSs depends on the number of degenerate ground (N_g) and excited (N_e) Zeeman states [26, 23] : (i) for $N_g > N_e$, a DS always exists provided the laser frequencies match the Raman condition ; (ii) for $N_g \leq N_e$, additional conditions on the complex Rabi frequencies must be satisfied. For instance, DSs where the connectivity between ground and excited states forms a loop exist if the summed phase of each complex Rabi frequency is 0 (mod 2π) [26, 29]. These states are particularly relevant for grey molasses cooling because they can be eigenstates of the momentum, thus stable both under free evolution and in the presence of a slowly varying external potential. The DSs for case (ii) can exist in the usual $\sigma + /\sigma-$ cooling configuration, provided that the lasers tuned to the cooling $|F = 2\rangle \rightarrow |F' = 2\rangle$ and repumping $|F = 1\rangle \rightarrow |F' = 2\rangle$ transitions are both phased locked to fulfill the phase requirements on the Rabi frequencies. In addition, the excited Zeeman states $|F' = 2, m'_F\rangle$ must be degenerate (see Fig. 2.10(b)), e.g., at zero magnetic field.

Efficient laser cooling for Potassium

Standard cooling techniques using a laser detuned on the red of the atomic transition are limited in the case of Potassium because of the atom level structure. Indeed the excited states on the D2 transition are very tightened (see Fig. 2.11 (a)).

Using the grey molasses technique on the D1 transition (see Fig. 2.11 (b)) we produced a potassium source with $6 \cdot 10^7$ atoms at 5.7μK. It is the lowest temperature obtained with Potassium and using dissipative laser cooling [31]. Interrogating the D1 transition requires to generate an additional wavelength (770 nm). Our technology based on telecom components

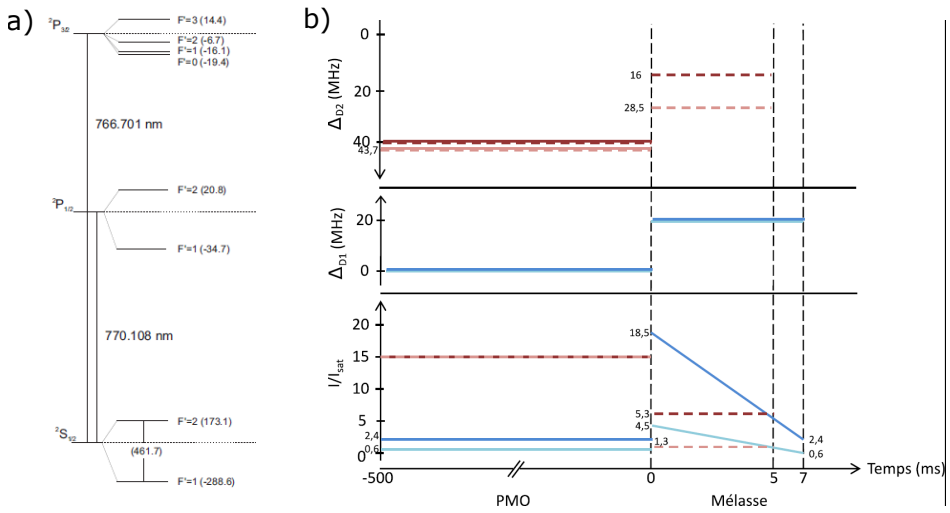

FIGURE 2.11 – (a) Optical transitions of the $D1$ and $D2$-lines of ^{39}K (from Tiecke [30]). (b) Cooling sequences. Dotted line : MOT+red molasses. Solid line : MOT+grey molasses. Blue : D1 laser. Red : D2 laser. Light colors : repumping beam. Dark colors : cooling beam.

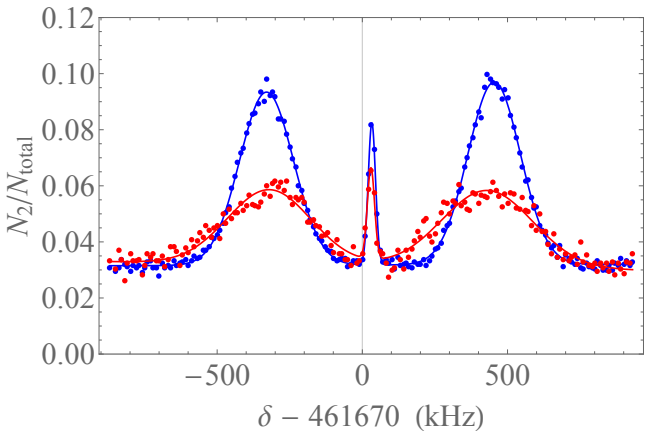

FIGURE 2.12 – Raman spectrum of the Potassium atom cloud in counter-propagating configuration after red detuned molasses (red) and after grey molasses (blue). Pulse duration of the Raman transition : $\tau_\pi = 30\ \mu$s.

and frequency doubling (see chap. 4) is compliant with this wavelength and doesn't increase the complexity of our laser system.

We compared the grey molasses cooling of ^{39}K and the standard red detuned molasses on the D2 transition [32, 33]. The parameters used for each sequence are summarized on Fig. 2.11 (b). Using counter-propagating Raman transition of the Zeeman state $m_F = 0$ (figure 2.12) the spectroscopy allows to probe the velocity distribution of the atom cloud and measure the temperature. The two curves were acquired with the same experimental parameters. Indeed, the width of the co-propagating Raman resonance is identical for both cases and the absence of light shifts between the two spectrum guarantees a similar Raman power. Moreover, the superposition of the counter-propagating Raman peaks shows the duration between the end of the molasses and the Raman pulse is the same for both cases. The width of the counter-propagating Raman peaks are larger for red detuned molasses and the amplitude is thus lower.

Table 2.2 summarize the gain obtained with grey molasses. We show that for the same atom number, the temperature is three times lower.

	Red detuned molasses	Grey Molasses
Laser transition for the MOT phase	D2	D2+D1
Laser transition pour the molasses phase	D2	D1
Atom number	$(5.0 \pm 1.2) \cdot 10^7$	$(6.0 \pm 1.4) \cdot 10^7$
Temperature	16 ± 1.0 μK	5.7 ± 0.1 μK

TABLE 2.2 – Capture and cooling efficiency for the two sequences "Red detuned molasses" and "Grey molasses".

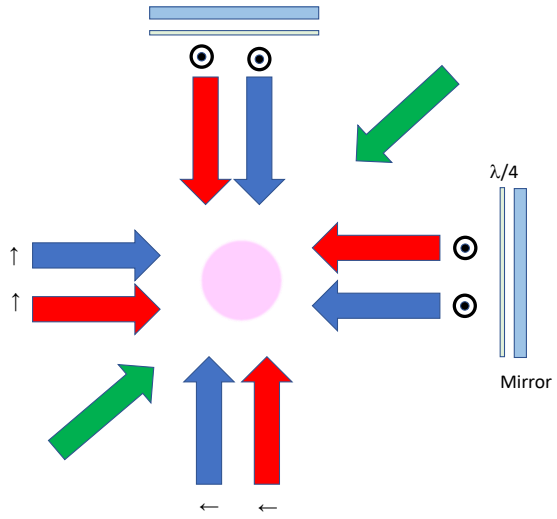

FIGURE 2.13 – Raman cooling scheme in 2D. Two orthogonal retroreflected Raman beam including the two frequencies (respectively blue and red) in lin⊥lin configuration. A waveplate in front of each reference mirror is present ($\lambda/4$) for laser cooling (Sisyphus) and Raman transitions. An alternance between two counter-propagating repumping beams (green) oriented in a diagonal direction is required.

2.3.4 Raman cooling

Raman cooling in free space has been demonstrated experimentally in 1D, 2D and 3D [34, 35]. It consists in shaping the velocity distribution using a sequence of counter-propagating Raman pulses of different widths and central frequencies. After each Raman pulse, a repumping beam colinear to the Raman transition is required so it implies the Raman beams are not retro-reflected for these experiments. Moreover, in a sequential strategy, the switching time between the axes is critical. Switching between the Raman beams can be achieved using AOMs or Pockels cells (microsecond), but mechanical solutions are too slow (millisecond).

It can be interesting to study a retro-reflecting architecture, especially for our 3 axis accelerometer (iXAtom, see chapter 4). Indeed, we have already three Raman beams on the experiment. Moreover, our laser source is strongly agile and can produce the required optical frequencies for both Raman and repumping beams. Fig. 2.13 shows a possible scheme in the 2D case.

2D Raman cooling have been demonstrated in [34]. In this experiment the cooling is achieved in the 4 directions simultaneously. A different detuning is applied for the orthogonal axes to avoid parasitic lattices. The repumping beam is orthogonal to the cooling plane and is reversed after each cooling cycle of 6 pulses. A cycle of 150 μs is repeated during 2 ms. We can adapt this scheme by using a repumping beam in a diagonal direction. Pulse shaping

(triangular or Blackman pulses In 3D) can help to increase the efficiency [35].

2.3.5 Time averaged dipole trap at telecom wavelength

Standard laser cooling techniques such as red molasses or grey molasses [36] presented in the previous paragraph are limited by the recoil due to the spontaneous emission of photons brought into play in the cooling process. For these temperature ($T \sim 1\mu$K), the spatial expansion of the atom cloud limits the interrogation time T of atom interferometer (typically 200 ms). For $T \sim$ 1s, it is necessary to reduce further the velocity distribution of the atom source. To reach this goal, our choice is to confine the atoms in a dipole trap, which consists in trapping atoms at the focus point of a laser far detuned compared to the atomic transition, like an optical tweezer. Evaporative cooling is the most spread technique, but we will also consider alternative laser cooling approach which will limit the atom loss inherent to evaporative cooling and increase the cooling speed. Both aspects are primordial for atom interferometry and especially in Space.

We consider a two-level atom. If the rotating wave approximation is valid (the detuning frequency is small compared to the laser frequency $\delta \ll \omega_L$) and if the laser power doesn't saturate the atomic transition (the saturation parameter satisfying $s \ll 1$), the potential created by the laser is :

$$U(\mathbf{r}) = \frac{\hbar\Omega(\mathbf{r})^2}{4\delta} = \frac{\hbar\Gamma^2}{8\delta}\frac{I(\mathbf{r})}{I_S} \tag{2.57}$$

where Ω is the Rabi pulsation, Γ the natural linewidth of the excited state and the saturation intensity I_S. The potential energy seen by the atoms is then proportional to the laser intensity. If the emitted laser wavelength is red detuned compared to the atomic transition ($\delta < 0$), the atoms are trapped at the potential minimum corresponding to the intensity maximum. Our dipole trap setup have three particularities. We demonstrated the all-optical production of Bose-Einstein condensates using a combination of grey molasses cooling, light-shift engineering and optical trapping in a painted potential [37].

First, our 1550 nm optical dipole trap (ODT) creates a transparency volume due to a strong light shift of the $5^2P_{3/2}$ excited state that results from coupling with the $5^2D_{5/2}$ state [38]. In this way, it is possible to store the atoms in the dipole trap without emission and reabsorption of near-resonant photons [39].

Second, we create a time-averaged or *painted* potential by spatially modulating the ODT beam. This technique leads to both a high capture volume and fast evaporative cooling with a high collision rate [40]. The key advantage of the painted potential is to break the fixed power-law relationship between the trap depth U and the frequencies ω by modifying the shape of the trap (see subsection 2.6).

As atoms move toward the center of the ODT, the grey-molasses light becomes increasingly blue detuned from $|F = 1, 2\rangle \rightarrow |F' = 2\rangle$, which strongly reduces light scattering. The total power in the ODT beams during this loading phase is 10 W. Under these conditions, the light shift of $|F' = 2\rangle$ is -170 MHz at the trap center, as shown in Fig 2.14(a). This leaves the $|F = 1, 2\rangle \rightarrow |F' = 3\rangle$ transitions far off resonance—enabling low temperature atoms to become trapped in the transparency volume of the ODT [see inset of Fig 2.14(b)]. In principle, the ODT-induced light shifts hinder grey molasses cooling [38]. Nevertheless, in our painted potential, atoms still have a strong probability to be cooled and pumped into $|\mathrm{NC}\rangle$ because the pumping rate ($\sim$ 6 MHz) is much higher than the modulation frequency of 280 kHz. Consequently a large fraction (about half) of the atoms should still undergo grey molasses cooling while being in the ODT volume. The sharp features in Fig 2.14(b) comply

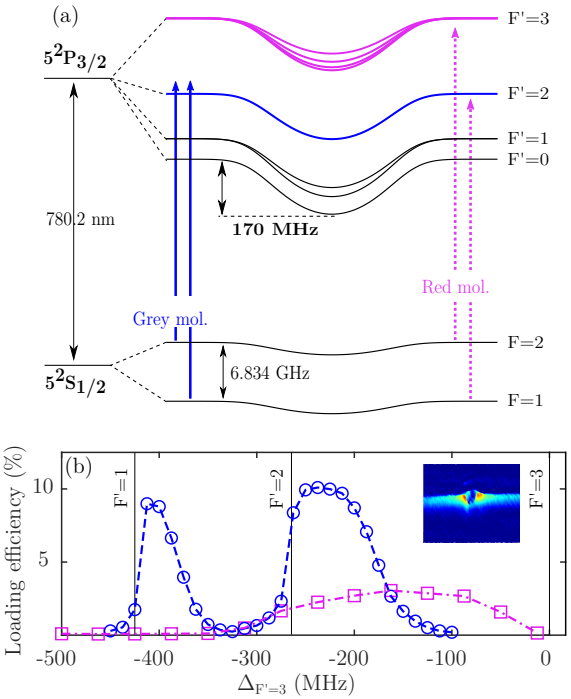

FIGURE 2.14 – (a) Level structure of the atoms including the light shift due to the painted ODT ($P \simeq 10$ W, $h = 100$ μm). The cooling and repumping frequencies are shown for the grey (solid blue lines) and red (dashed pink lines) molasses. The cooling and repumping light intensities are respectfully $I_{cool} \approx 6I_S$ and $I_{rep} \approx 0.6I_S$. The light shift of the excited (ground) state at the center of the ODT is $\sim$ 170 MHz (2.5 MHz). (b) ODT loading efficiency as a function of the detuning relative to $|F = 2\rangle \rightarrow |F' = 3\rangle$ for the red (pink squares) and grey (blue circles) molasses. The atom numbers are estimated from absorption imaging. For each point, 5 images have been taken, averaged and fitted with a 2D gaussian profile. The standard deviation of the fit residuals gives an uncertainty of 5% about the loading efficiency. Inset : absorption image of atoms in the ODT using near-resonant light. Atoms at the center of the trap are transparent to the cooling beams.

with this hypothesis. When the cooling beams are switched off, approximately 5×10^6 atoms remain in the painted potential with an in-trap temperature of 15 μK at a depth of 120 μK ($\eta = U/k_BT = 8$). This temperature is limited by the potential energy due to the dipole trap. We evaluate the gain of the grey molasses process by comparing it with a loading sequence using a standard red molasses. In this case, because of the light shifts, the optimal detuning varies strongly with the optical power of the ODT. In contrast, the grey molasses yields a 4-fold increase in atom number compared to the red molasses, as shown in fig 2.14(b). Moreover, the grey molasses scheme is relatively insensitive to the ODT power, and it occurs on faster timescales (< 1 ms) than red molasses (> 5 ms) [41], even though the final temperatures are comparable. This effect is consistent with our increased loading with the grey molasses : the longer times required for red molasses cooling lead to expansion of the atoms, which lowers the central density and therefore the loading efficiency.

An alternative method to load the atoms in a telecom dipole trap had been studied in an other experiment where the dipole trap is not spatially modulated [42]. The main difference is that the loading of the atoms is localized only on the edge of the dipole trap. Far from the trap the grey molasses cooling is not efficient because the atoms don't reach the dipole trap region. There is a strong resonance for one frequency corresponding to atoms on the edge of the dipole trap. The shark peak is due to the velocity dependence of the dark states

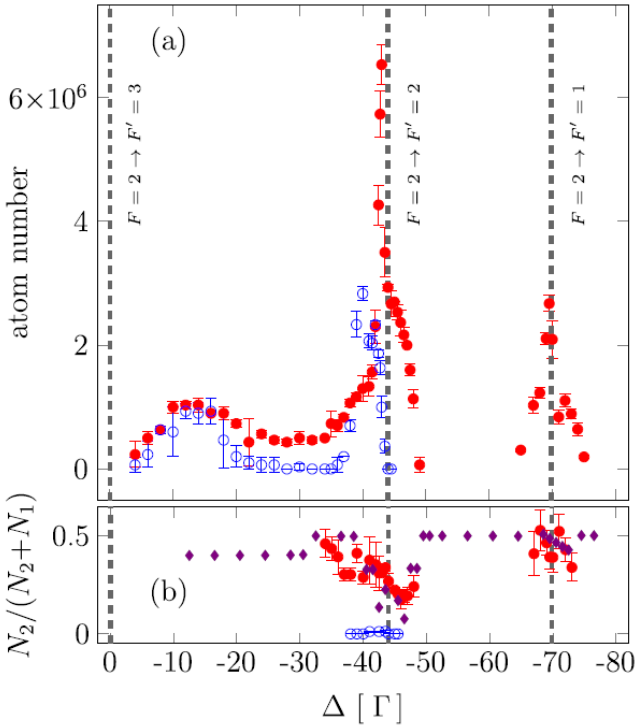

FIGURE 2.15 – (a) Atoms loaded into the FORT as a function of the cooling laser detuning from the $|F = 2\rangle \rightarrow |F' = 3\rangle$ resonance during the sub-Doppler cooling phase, for an independent repumper (empty blue circles), and for a repumper in Raman condition with the cooler (filled red circles). (b) Population fraction of atoms in $|F = 2\rangle$ with the repumper in the two configurations as above; $N_{1,2}$ indicate the atomic populations of the $|F = 1, 2\rangle$ manifolds. The violet points result from a numerical evaluation of the DSs forming at each detuning.

(see section 2.3.3). Since there is a velocity/position correlation on the edge of the trap, only the atoms specifically localized on these edges are efficiently cooled and trapped, and thus contribute to this resonance effect in the scan of the laser frequency. Moreover, HDSs relying on two (or more) magnetic sublevels with different $|m_F|$ are strongly modified and probably inhibited when atoms move in the inhomogeneous FORT intensity. Nevertheless, by playing with the detuning Δ, it is possible to address different velocity classes inside the trap : the loading efficiency is significant even when the laser is red detuned compared to the transition $|F = 2\rangle \rightarrow |F' = 3\rangle$ (see Fig. 2.15).

2.3.6 Evaporative cooling

Once trapped, evaporative cooling allows to decrease the temperature much below the one photon recoil limit. The principle is based on the escape of the most energetic atoms due to the finite dipole trap depth. By decreasing the power of the laser beam, the barrier is lowered down and thus the temperature of the trapped gas is decreased. This very efficient process allows to increase the phase space density (PSD) and reach Bose-Einstein condensation (BEC). Using this all optical process, we produce a BEC of 4×10^4 Rb atoms in 1.4 s with a critical temperature of $T_c = 140$ nK.

The usual limitation due to the decompression of the dipole trap which prevents from reaching the run away regime can be mitigated with the time averaged potential. In [40], they demonstrated a optimization of the evaporation dynamics to produce a BEC of Yb with

a high atom number.

2.3.7 Delta kick collimation

The technique of delta kick collimation doesn't increase the phase space density, but constitutes a useful tool for atom interferometry for which the reduction of the spatial expansion of the cloud is essential.

After a free expansion of the atom cloud during a time t_f, a strong correlation between the position and the velocity is obtained if the initial size r_0 is very small compared to the size after expansion $r_f = v_0 t_f$. For an harmonic trap, this condition is satisfied when :

$$t_f \gg \frac{r_0}{v_0} = \tau_0 \tag{2.58}$$

where τ_0 is the period of the oscillation in the trap.

The principle of the delta kick collimation (or atom lensing) is to apply a potential pulse to give the good $\ll$ momentum $\gg$ to each velocity class. The momentum given by an harmonic potential of frequency ω at point A applied during a time t_k is :

$$\Delta p_A = -m\omega^2 r_A t_k \tag{2.59}$$

Compensating the velocity at the point A $\Delta p_A = -m v_A$ is satisfied by the condition :

$$t_f t_k = \frac{1}{\omega^2} \tag{2.60}$$

The temperature is then decreased by a factor :

$$1/\alpha = \left(\frac{r_0}{r_f}\right)^2 = \left(\frac{\tau_0}{t_f}\right)^2 \tag{2.61}$$

The same "cooling" effect can be done by decompressing the trap adiabatically ($t_0 \ll t_d$). But the advantage of the atom lensing is that it is faster, it happens in a time $\sqrt{\alpha}\tau_0$ versus $\alpha\tau_0$.

These formulas are estasblished for a thermal cloud, but the principle stands by taking into account the expansion of an interacting gas in the Thomas-Fermi regime [43]. The elliptical trap is a well known case with a simple analytic solution at the first order. The transverse expansion follows the law :

$$\lambda_\perp = \sqrt{1+\tau^2} \tag{2.62}$$

where $\tau = \omega_\perp t$.

This expansion is similar to a thermal cloud, except that this is the trap frequency and not the temperature which gives the expansion rate.

The longitudinal direction expands much slowly :

$$\lambda_z = 1 + \epsilon^2[\tau \arctan(\tau) - \ln\sqrt{1+\tau^2}] + O(\epsilon^4) \tag{2.63}$$

where $\epsilon = \omega_z/\omega_\perp$. This gives the so called ellipticity inversion. The spatial mode matching of the atom lens need to take this effect into account for a 3D collimation. For us, one advantage with our time averaged potential is that we can easily adapt the shape of the dipole trap between the trapping and the delta kick which allow us to use the same laser for the whole sequence.

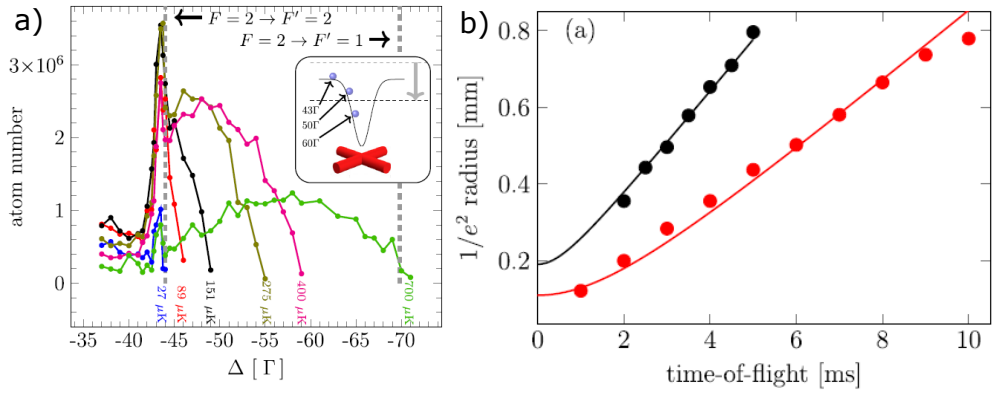

FIGURE 2.16 – (a) HDS cooling near the $|F = 2\rangle \rightarrow |F' = 2\rangle$ transition at different FORT depths indicated in colors. The sharp peak at -43.5Γ is given by atoms cooled just outside the FORT. The broader peak underneath corresponds to atoms residing within the FORT volume. Inset : The radially changing FORT power results in a position dependent excited-state light shift, represented for a FORT depth of 700 μK. The effect can be exploited to selectively cool the optically trapped atoms at specific radial positions, or to progressively cool the atoms in the FORT from its borders and towards its center, by sweeping Δ as indicated by the grey arrow.(b) Ballistic expansion of the atomic cloud released from the FORT : cloud size vs time of flight. The fits (solid lines) yield a temperature of 198 μK before the cooling sweep (black points) and 48 μK after it (red points).

Several experiments demonstrated the delta kick technique with magnetic fields. Optically, a temperature of 50 pK (in 2D) has been demonstrated using the atom lensing technique with a time of flight $t_f = 1.1s$, a refocusing time $t_{ref} = 1.8s$ and an initial temperature of 1 nK [44]. For our experiment, with an initial temperature of 50 nK, our goal is to decrease the temperature by a factor $\alpha = 10000$ to reach 5 pK. We consider the following parameters : t_f =457 ms, $t_k = 5\mu$s and $\omega = 2\pi\times100$Hz for the dipole potential during the kick.

2.3.8 Laser cooling in a Dipole trap

It is also possible to cool the atoms inside the dipole trap using grey molasses [42]. In an harmonic trap, there is a strong correlation between position and velocity. By adjusting the detuning of the grey molasses laser, it is possible to cool a dedicated velocity class (Fig. 2.16 (a)). By chirping the detuning, it is possible to cool the atom cloud (Fig. 2.16 (b)).

The method pave the way in the production of ultracold atomic samples including many key features : high speed, minimal scattering, no atom loss, and no need for cycling transitions. Remarkably, cooling and loading happen simultaneously, which solves the mode matching issue for optical dipole traps preventing the need for an intermediate step often relying on magnetic trapping. Efficient cooling in the tight harmonic trap without atom loss we can expect a high critical temperature to reach BEC :

$$T_c = \frac{\hbar\omega}{k_B}\left(\frac{N}{1.202}\right)^{\frac{1}{3}} \tag{2.64}$$

With $\bar{\omega} = 2\pi \times 1$kHz and 10^7 atoms the critical temperature is expected to be 10μK.

Alternatively, Raman cooling in a dipole trap has been demonstrated in Vuletic's group for Rb [15] (Fig. 2.17 (a)). One difficulty is light assisted collision loss when the atom density is increased. Light-induced collisions are minimized by tuning the cooling light into a spectral gap between photo-association resonances (Fig. 2.17 (b)). Fig. 2.17 (c) presents the Raman

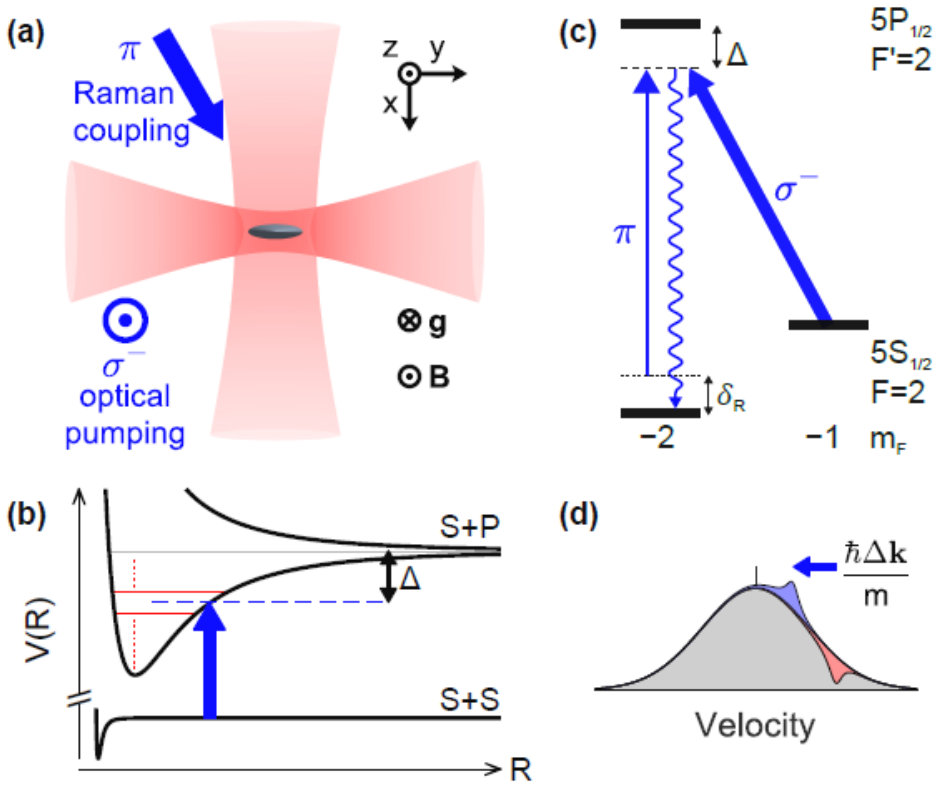

FIGURE 2.17 – From [15] (a) Geometry of the experimental setup with trapping, optical pumping, and Raman coupling beams. (b) Molecular potentials. Light-assisted collisions are suppressed if the detuning from atomic resonance Δ is chosen to avoid photo-association resonances (solid red horizontal lines). (c) Partial atomic level scheme. The Raman transition is resonant for atoms with a two-photon Doppler shift δ_R. (d) Velocity distribution of the atoms along the two-photon momentum $\hbar\Delta\mathbf{k}$. A Raman transition reduces the velocity of atoms in the velocity class $\delta_R/|\Delta\mathbf{k}|$ by $\hbar\Delta\mathbf{k}/m$.

transition scheme, which allows to produce a BEC with $2.5 \cdot 10^4$ atoms after 1.4 s of cooling.

2.4 Light Manipulation of the internal states

The preparation of the atoms in a pure internal state is essential to assure a good signal to noise ratio of the interference fringes. The standard solution to prepare Rubidium or Cesium atoms in the good internal state consists in applying a microwave signal tuned on the clock transition and to use a push beam to remove the atoms stayed in the bad hyperfine level. In the case of ^{39}K, the atomic level structure make this solution difficult to use, since the clock frequency is 461.67 MHz, corresponding to a half wavelength of $\Lambda_K/2 \approx 32$ cm which is larger than the diameter of our titanium vacuum chamber (25 cm). Considering this difficulty, we developed a new all optical technique for the state preparation compliant with all metal vacuum device with limited optical access. The key idea of this method is to use the D1 laser source to achieve optical pumping without heating the atoms.

We first apply a "depumping" pulse using the laser resonant with the D1 transition, including only the cooling frequency resonant with the $|F = 2\rangle \rightarrow |F' = 2\rangle$ transition. Consequently the atoms are distributed equally between the $|F = 1\rangle$ manifold. In order to split them using Zeeman effect, a magnetic field bias (0.175 Gauss) is added along the direction of

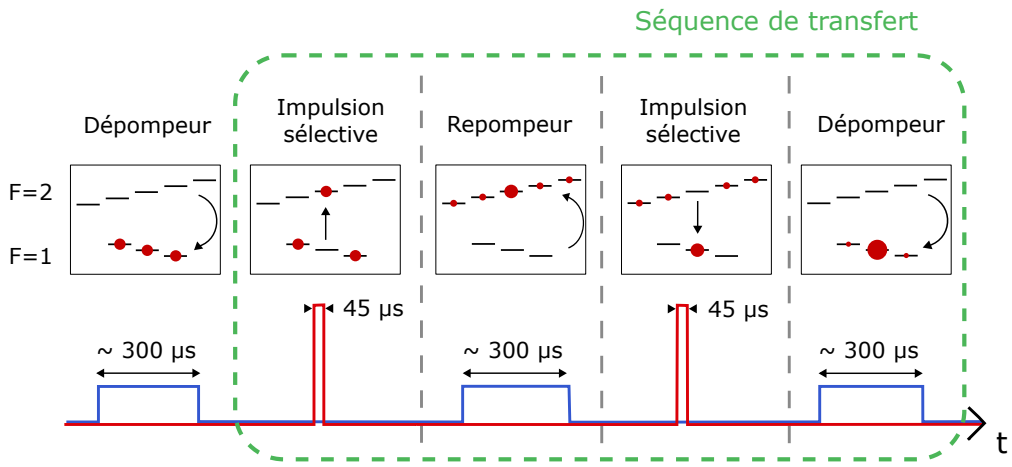

FIGURE 2.18 – The state preparation sequence tested to prepare the atoms of ^{39}K in the non sensitive magnetic state $|\mathrm{F}=1,\mathrm{m_F}=0\rangle$. The function of each optical pulse on the atomic states is shown in the first row. The second row represents the transfer between the level $|\mathrm{F}=1\rangle$ and $|\mathrm{F}=2\rangle$ at each step and the third row the intensities of the laser resonant with the D2 (red) and D1 (blue) transition. Note that the selection beam has two frequencies (labeled as ω_1 and ω_2) to make Raman transitions. The steps circled in the red loop indicate the transfer sequence, which is repeated to increase the fraction of atoms in the target state. At the end of this loop, a near-resonant push beam removes atoms remaining in $|\mathrm{F}=2\rangle$ to improve the purity of the target state.

the interferometer beam. Then we execute a transfer sequence represented on Fig 2.18. These sequence aim to put all the atoms in the non sensitive magnetic state $|F=1,m_F=0\rangle$ can be repeated several times if necessary to improve the efficiency of the transfer. The first step of the sequence is a optical pulse resonant with a single m_F, and playing the role of the microwave signal. This pulse achieves a co-propagating Raman transition with $\tau_\pi = 30$ μs, the frequency being red detuned of about 700 MHz compared to the level $|F'=3\rangle$ of the D2 transition, and allowing to transfer the atoms from $|F=1,m_F=0\rangle$ to $|F=2,m_F=0\rangle$. We then apply a repumping pulse using the D1 laser resonant with the transition $|F=1\rangle \rightarrow |F'=2\rangle$. This pulse of duration about 300 μs homogeneously distributes the atoms not transferred previously in the $|F=2\rangle$ manifold, and this increasing the atom number in $|F=2,m_F=0\rangle$. To conclude the cycle, the same process is reproduced from $|F=2\rangle$ to $|F=1\rangle$ with a similar selective pulse and a depumping pulse.

Unlike the standard sequence based on microwaves and a push beam, this method has the advantage to keep more atoms in the transfer mechanism. Moreover the transfer sequence is a fast process (2.3 ms). By adjusting the Raman frequency of the selective pulse, this sequence can be adapted to transfer atoms in a magnetic state sensitive to the magnetic field ($m_F \neq 0$)

We evaluate the increase of the contrast and SNR of the ^{39}K interferometer fringes for a short interrogation time $T = 0.1$ ms (see Fig. 2.19).

	Red Molasses	Grey Molasses	Grey Molasses+state preparation
Contrast	10%	17%	38%
Signal to Noise Ratio	20	30	45

TABLE 2.3 – Improvement of the Signal to Noise Ratio thanks to grey molasses and the all optical state preparation for ^{39}K (see Fig 2.19).

According to the table 2.3, the implementation of the grey molasses increased the contrast

and the SNR by a factor 2. Thanks to the state preparation in the $m_F = 0$ state, the fringe contrast is 38% and the SNR above 45. We demonstrated for the first time ^{39}K atom interferometer with an interrogation time above $T = 20$ms. These new techniques make the potassium available for metrology (see also K atomic clock in section 3.3.7).

2.5 Mapping of the telecom dipole trap

Tomography imaging of the atoms inside the trap is possible thanks to the correlation between the position of the atoms and the resonance frequency of the imaging beam in presence of the strong light shift of the excited state (Fig. 2.20 (b) Inset).

We use this method to measure experimentally the light shifts of the excited states of the atoms *in situ* in the trap. While keeping the dipole traps on (cf. Figure 2.20 (b)) [45], the shift of the imaging/probe laser detuning allows to address atoms situated at different equipotentials. When the probe beam is on resonance with the transition $|^5S_{1/2}, F = 2\rangle \rightarrow$

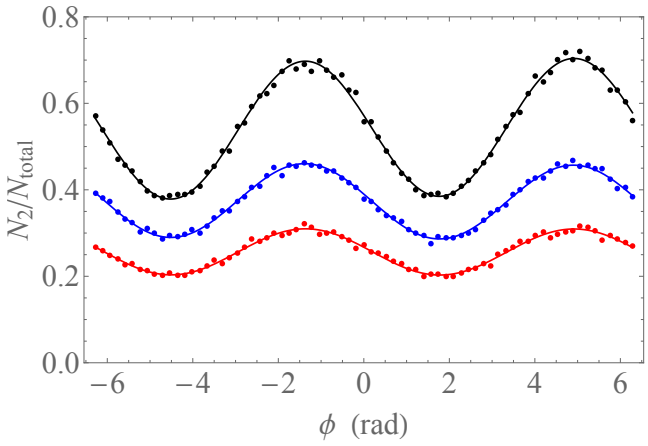

FIGURE 2.19 – Interference fringes for $T = 0.1$ ms. Red : red molasses, no state preparation (atoms in $F = 1$ manifold). Blue : grey molasses, no state preparation. Black : grey molasses, all optical state preparation

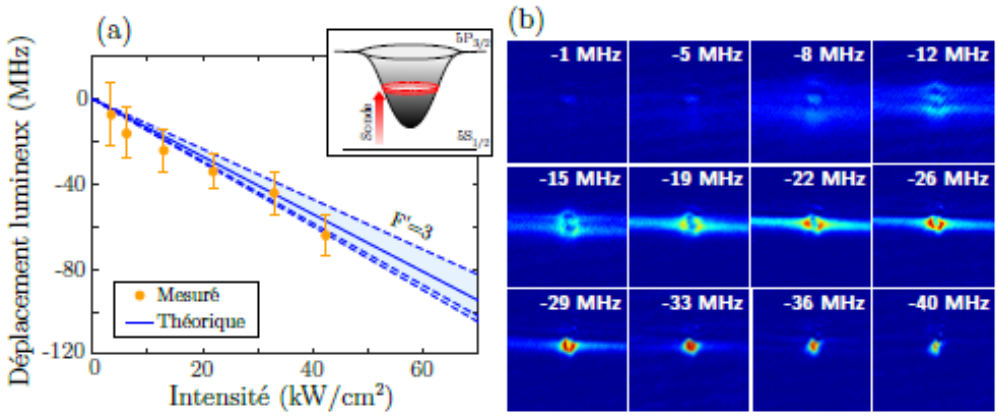

FIGURE 2.20 – Tomography of the atom cloud in the dipole trap. (a) Light shift of the level $^5P_{3/2}$ measured and calculated versus the intensity of the dipole trap laser. Inset : 2D profile of the potential energy and equipotential ring addressed by the probe beam for a fixed detuning frequency. (b) Image of the atoms inside the dipole trap for several detuning frequencies of the probe beam.

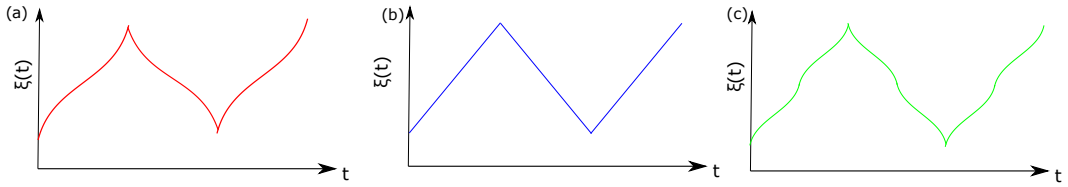

FIGURE 2.21 – Spatial modulation profile for (a) an harmonic potential, (b) a box shaped trap and (c) a double (quadruple in a 2D modulated crossed trap) well potential.

$|^5P_{3/2}, F_0 = 3\rangle$, no atom is imaged. Then, when the negative detuning is increased, atoms situated deeper and deeper inside the trap are imaged by the probe. The value of the detuning for which there is no detected atoms gives the light shift we want to measure.

It can be interesting to create an atom waveguide along the direction of a single dipole trap laser beam. Associated to the grey molasses technique, the atoms trapped in the matter-waveguide are transparent to the cooling beams while the atoms on the edge are continuously cooled by the cooling beams. this method paves the way towards a continuous atom source at high phase density such as it has been demonstrated for Strontium [46].

2.6 Shaping of the painted potential

Here we discuss about some examples of time averaged potentials we can produce with our setup. We consider the laser beam as a Dirac. The spatial modulation of the dipole trap is described by the position of the beam versus time $\xi(t)$ along the x axis. An harmonic trap is obtained with the following modulation function :

$$\frac{d\xi}{dt} = \frac{v_0}{1 - \left(\frac{x}{h_0}\right)^2} \tag{2.65}$$

where v_0 is a constant depending on the amplitude modulation h_0. From this equation we can calculate the profile of $\xi(t)$ (see Fig. 2.21 (a)).

The main advantage of the harmonic painted potential is to mitigate the decrompression of the trap while decreasing the optical power and the depth of the dipole trap during the evaporative cooling. In the case of a spatially modulated single-beam ODT, the trap frequencies can be expressed as $\omega_{mod}^2 = \frac{8\alpha P}{\pi m w_0^4} f_\omega(h/w_0)$ in the direction of the spatial modulation, $\omega_\perp^2 = \frac{8\alpha P}{\pi m w_0^4} f_U(h/w_0)$ in the transverse direction, $\omega_z^2 = \frac{4\alpha P}{\pi m w_0^2 z_R^2} f_\omega(h/w_0)$ along the propagation of the beam, and depths as $U = \frac{2\alpha P}{\pi w_0^4} f_U(h/w_0)$. α is the polarizability of the atomic ground state at λ_D, P is the optical power, m is the atomic mass, $z_R = \pi w_0^2/\lambda_D$ is the Rayleigh length, and h is the amplitude of the spatial modulation. The functions $f_\omega(h/w_0)$ and $f_U(h/w_0)$ are the fractional reduction factors due to the spatial modulation of the beam [40]. The capture volume is proportional to h^2 and can be increased with a good trade-off on the trap depth U due to the factor $f_U(h/w_0)$.

Not only this technique allows to produce a pure harmonic trap but also give us a tool to "paint" different trap geometries such as a box or double well potential. We can get a box with a spatial modulation satisfying $d\xi/dt$ =Cste, which corresponds to a triangle modulation (see Fig. 2.21 (b)). This trap geometry is interesting because the modified density of states have strong influence on the expected transition phases (see perspectives in chapter 5). A double well potential (1D modulation) is produced by copying the case of the harmonic trap and double the S-shape (see Fig. 2.21 (c)). The same modulation in the case of a 2D modulated

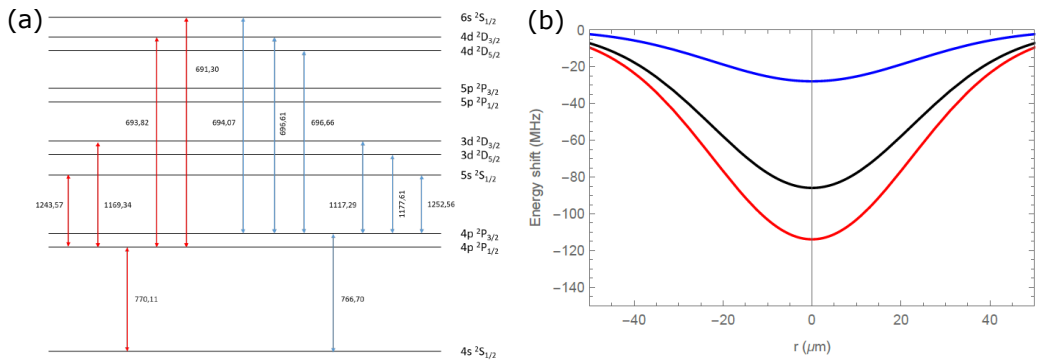

FIGURE 2.22 – (a) Level structure of Potassium ^{39}K .(b) Spatial light shift of the ground state level $^2S_{1/2}$ (blue) and the excited state $^2P_{1/2}$ (red) created by the dipole trap beam. The black curve represents the difference between the two levels.

crossed trap gives 4 wells.

2.7 Ultra-cold gas of Potassium

Several experiments of Bose-Einstein condensation of Potassium have been developed in the laboratories [47] without any constraints of duty cycle or compactness. Just as our work on Rubidium, we need to develop methods adapted to our compact experiment and allowing a fast production compliant with our experiments of atom interferometry which requires a cycling time of 1 s or less. The method presented here for Rubidium can be partially used and adapted for Potassium. Our loading strategy will combine the use of a spatially modulated laser beam and grey molasses cooling. Just as for Rubidium, we expect to achieve "free space" grey molasses cooling for atoms situated in the zone of the modulated dipole trap, which enhances the loading efficiency. Grey molasses on the D1 transition is already implemented for Potassium on our experiment. The main expected difference is the light shift of the excited states which will be weaker because Potassium has no transition close to the telecom wavelength (1550 nm) of the dipole trap laser.

Based on the spectrum data of Potassium [48], we estimate the light shifts of the excited states for a waist of 25 μm and an optical power of 23 W (see Fig. 2.22). The light shift of the excited state for Potassium is about 10 times weaker but can be partially compensated by an increase of the optical power.

Trapping and laser cooling inside the dipole trap (see section 2.3.8) can be achieved using grey molasses on the D1 transition which has the advantage to avoid the presence of the $|F' = 3\rangle$ level. Consequently the full laser power is available without the risk to be limited by the light shifted $|F' = 3\rangle$ level.

2.8 Publications

— D. S. Naik, H. Eneriz-Imaz, M. Carey, T. Freegarde, F. Minardi, B. Battelier, P. Bouyer, and A. Bertoldi, *Loading and cooling in an optical trap via hyperfine dark states*, Phys. Rev. Research **2**, 013212 (2020)

— G. Condon, M. Rabault, B. Barrett, L. Chichet, R. Arguel, H. Eneriz-Imaz, D. Naik, A. Bertoldi, B. Battelier, P. Bouyer, and A. Landragin, *All-Optical Bose-Einstein Condensates in Microgravity*, Phys. Rev. Lett. **123**, 240402 (2019)

— B. Barrett, P. Cheiney, B. Battelier, F. Napolitano, and P. Bouyer, Multidimensional Atom Optics and Interferometry, Phys. Rev. Lett. **122**, 043604 (2019)
— L. Antoni-Micollier, B. Barrett, L. Chichet, G. Condon, B. Battelier, A. Landragin, P. Bouyer, *Generation of high-purity, low-temperature samples of 39K for applications in metrology* Phys. Rev. A, **96**, 0223608 (2017)

Chapitre 3

A quantum test of the gravitation theory

Our long term motivation is to achieve a quantum test of the weak equivalence principle. The high sensitivity and accuracy of the atom interferometers associated to the potential to increase the performances using a large apparatus or benefiting from long and unperturbed measurement in Space give us hope to achieve a test below the level of 10^{-15}. Moreover the quantum properties of matter waves make this measurement fundamentally different from the classical tests and particularly relevant since Quantum Mechanics (QM) and General Relativity (GR) are difficult to reconcile.

3.1 Quantum test of the Weak Equivalence Principle

Einstein's theory of General Relativity (GR) is a cornerstone of our current description of the physical world at macroscopic scales and accounts for the gravitational laws of the universe. Gravitation interacts in the same way to any mass/energy, which allows a geometric description of gravitation as the effect of the curvature of space-time. The phenomenological manifestation of this universal coupling is known as the Einstein Equivalence Principle (EEP). Precise tests of this principle can advance the search for physics beyond the Standard Model and GR, and may shed new light on our understanding of the universe and its constituents, especially cold dark matter and dark energy [49, 50, 51, 52].

3.1.1 Einstein Equivalence Principle

The Einstein Equivalence Principle (EEP) [53] is generally divided into three sub-principles : the Weak Equivalence Principle (WEP) also known as the Universality of Free Fall (UFF), the Local Lorentz Invariance (LLI), and the Local Position Invariance (LPI). The EEP is satisfied if and only if all three sub-principles are satisfied. Below we describe these three sub-principles :

— WEP states that if any uncharged test body is placed at an initial event in space-time and given an initial velocity there, then its subsequent trajectory will be independent of its internal structure and composition. The most common test of WEP consists in measuring the relative acceleration of two test bodies of different internal structure and composition freely falling in the same gravitational field. If WEP is satisfied, their differential acceleration is zero.

— LLI states that the outcome of any local non-gravitational test experiment is independent of the velocity and orientation of the (freely falling) apparatus. Tests of LLI

usually involve a local experiment (e.g. the comparison of the frequency of two different types of clocks) whose velocity and/or orientation is varied in space-time. LLI is verified if the result of the experiment is unaltered by that variation.

— LPI states that the outcome of any local non-gravitational test experiment is independent of where and when in the Universe it is performed. Tests of LPI usually involve a local experiment (e.g. the measurement of a fundamental constant, or the comparison of two clocks based on different physical processes) at different locations and/or times. In particular, varying the local gravitational potential allows for searches of some anomalous coupling between gravity and the fields involved in the local experiment. A particular version of such tests, known as test of the gravitational red-shift, uses the same type of clock, but at two different locations (different local gravitational potentials) and compares them via an electromagnetic signal. Then it can be shown (see Sec. 2.4c in Ref. [53]]) that the measured relative frequency difference is equal to $\Delta U/c^2$ (where ΔU is the difference in gravitational potential) if and only if LPI is satisfied.

3.1.2 Strong Equivalence Principle

The Strong Equivalence Principle (SEP) is a generalization of EEP to include "test" bodies with non-negligible self-gravitation, together with experiments involving gravitational forces (e.g. Cavendish-type experiments) or the propagation of gravitational waves. Obviously, SEP includes EEP as a special case in which gravitational forces can be ignored. Typical tests of SEP involve moons, planets, stars or local gravitational experiments.

In the SEP case, the relevant test body differences are the fractional contributions to their masses (m_G is the gravitational mass and m_I the inertial mass) by gravitational self-energy. Although general relativity assumes that the SEP is exact, many modern theories of gravity typically violate the SEP by including new fields of matter, notably scalar fields. The ratio of the gravitational-to-inertial masses for a body can be parameterized as

$$\left[\frac{m_G}{m_I}\right] = 1 + \zeta\frac{U}{mc^2} \tag{3.1}$$

where m is the mass of a body, U is the body's gravitational self-energy ($U < 0$),mc^2 is its total mass-energy, and ζ is a dimensionless constant for SEP violation. Because of the extreme weakness of gravity, a test of the SEP requires bodies of astronomical sizes. This is related to the Eötvös parameter :

$$\eta = \frac{\Delta a}{a} = \left[\frac{m_G}{m_I}\right]_1 - \left[\frac{m_G}{m_I}\right]_2 \tag{3.2}$$

At present, the Earth–Moon–Sun system provides the best solar system arena for testing the SEP. The Lunar Laser Ranging (LLR) led to a measurement of $[m_G/m_I]_E - [m_G/m_I]_M = (-0.8 \pm 1.3) \times 10^{-13}$ [54] (E stands for Earth and M for Moon). Time series of the highly accurate measurements of the distance between the Earth and Moon provide unique information used to determine whether, in accordance with the EP, both of these celestial bodies are falling toward the Sun at the same rate, despite their different masses, compositions, and gravitational self-energies.

A SEP test with a pulsar in a triple stellar system is also reported [55]. This object has the

advantage to have a higher self-gravity. This test is measured using the following parameter :

$$\Delta = (m_G/m_I) - 1 \tag{3.3}$$

This parameter is measured at a level of $(+0.5 \pm 1.8) \times 10^{-6}$ and constitutes a better test than LLR because self gravity is more important. For this parameter LLR gives $(-0.2 \pm 1.1) \times 10^{-4}$. LLR is considered as a test of the lower limit of SEP at the frontier of the WEP.

3.1.3 Weak Equivalence Principle

The test of the Weak Equivalence Principle (WEP) is an experiment consisting in measuring the differential acceleration between bodies of different masses. To quantify the measurement, the Eötvös parameter η is defined :

$$\eta = 2 \times \frac{|a_1 - a_2|}{|a_1 + a_2|}, \tag{3.4}$$

where a_1 are a_2 are the respective accelerations of the two bodies.

Table 3.1 presents the current state of the art of the WEP tests. We can cite two of the best classical WEP tests :

— Rotating torsion balances have been used for a measurement of the Eötvös parameter $\eta = (0.3 \pm 1.8) \times 10^{-13}$ [56]. The torsion balance compares the horizontal accelerations of test bodies made from two different materials. Acceleration differences that depend only on the test-body material violate the equivalence principle. Torsion balances have the unique feature that they are sensitive to the angle between the forces on their test bodies. In particular, if the the forces on the test bodies are parallel there will be no torque on the balance, even if the forces have different magnitudes. This explains why torsion balances can be used to make measurements at the part in 10^{13} level even though no part of the balance is itself good to that precision.

— The MICROSCOPE (MICRO-Satellite à traînée Compensée pour l'Observation du Principe d'Equivalence) Space mission started in April 2016 and consisted in comparing the measurement of two electro-static accelerometers of different composition and mass on board a satellite in orbit around the Earth. They achieved the best current WEP test measuring $\eta = (-1 \pm 9) \times 10^{-15}$ [57] . A new approach to test the WEP is implemented by taking advantage of the very quiet space environment. Non-gravitational forces acting on the satellite are counteracted by cold gas thrusters making it possible to compare the accelerations of two test masses of different compositions "freely falling" in the same orbit around Earth for a long period of time. This is done by accurately measuring the force required to keep the two test masses in relative equilibrium.

3.1.4 Quantum test of the weak equivalence principle

Cold atom interferometers are exquisite candidates to test the WEP, because atoms are intrinsically quantum, and their composition and mass are well known. Moreover, the sensitivity of a cold atom interferometer (CAI) is already high and can be enhanced by increasing the interrogation time. This time extension is a major challenge for our community. The state of the art to test the WEP with CAI is presented table 3.1.

Class	Elements	η	Year [Ref]	Comments
Classical	Be-Ti	2×10^{-13}	2008 [56]	Torsion Balance
	Pt-Ti	1×10^{-14}	2017 [57]	MICROSCOPE first results
Hybrid	^{133}Cs-CC	7×10^{-9}	2001 [58]	AI and macroscopic corner cube (CC)
	^{87}Rb-CC	7×10^{-9}	2010 [59]	
Quantum	^{39}K - ^{87}Rb	5×10^{-7}	2014[60]	different elements
	^{87}Sr - ^{88}Sr	2×10^{-7}	2014 [61]	same element, fermion vs Boson
	^{85}Rb-^{87}Rb	3×10^{-8}	2015 [62]	same element, different isotope
	^{85}Rb-^{87}Rb	7×10^{-10}	2019[63]	Arxiv
	^{87}Rb	3×10^{-10}	2020[64]	Hyperfine state
	^{85}Rb-^{87}Rb	3.4×10^{-12}	2020 [65]	$\geq$ 10 m towers
	^{85}Rb-^{87}Rb	(10^{-13})	2020+ [66]	$\geq$ 10 m towers
	^{170}Yb-^{87}Rb	(10^{-13})	2020+ [5]	$\geq$ 10 m towers
Antimatter	$\bar{H} - H$	(10^{-2})	2020+[67]	under construction at CERN

TABLE 3.1 – State of the art of the current and future WEP tests.

Quantum Mechanics and General Relativity

Although there is no established theory that favors quantum tests of the EEP, there are nonetheless a number of difficulties in the frontier between QM and GR due to the absence of a quantum theory of gravitation, that call for experiments lying at that frontier, like quantum tests of the EEP.

Quantum tests of the Equivalence Principle differ from classical ones because classical and quantum descriptions of motion are fundamentally different. In particular, the WEP has a clear significance in the classical context where it means that space-time trajectories of test particles do not depend on the composition of these particles. How UFF/WEP is to be understood in quantum mechanics is a much more delicate point. More generally, considering quantum phenomena in the context of gravity poses many conceptual and fundamental difficulties. When comparing classical EEP tests to quantum ones, a number of implicit assumptions are made, like e.g. that quantum mechanics is valid in the freely falling frame associated with classical test bodies in the definition of WEP. Indeed, the usual definition of the EEP states that special relativity holds in the freely falling frame of WEP without reference to quantum mechanics. Of course, this extension of the notion of freely falling frame to quantum mechanics is always implicit and "obvious". It is used when one computes the phase shift of a matter wave interferometer in a gravity field, using the full machinery of quantum mechanics, for instance Feynman's path integral formalism [1].

However, in general the variety of quantum states is much larger than that of classical ones and it seems therefore plausible that quantum tests may ultimately be able to see deeper details of couplings between matter and gravity than classical ones (see [68] for a more detailed discussion). Let us consider the free fall in a gravitational field of a particle in Quantum Mechanics (QM) described by the wave function Ψ. We assume that the wave function is initially Gaussian. The Schrödinger's equation with the Hamilton operator

$$\hat{H} = \frac{\hat{p}_z^2}{2m} + mg\hat{z} \tag{3.5}$$

is satisfied, where the first term is the kinetic energy and the second term is the usual Newtonian gravitational potential. The time of flight is statistically distributed with the

mean value agreeing with the classical universal value,

$$T\sqrt{\frac{2z_0}{g}} \tag{3.6}$$

where $z_0 = \langle\hat{z}\rangle_{\Psi_0}$ is the initial position being determined by the expectation value of the position in the Gaussian initial state Ψ_0.

However, the standard deviation of the measured values of the time of flight around T depends on the mass of the particle

$$\sigma = \frac{\hbar}{\Delta_0 mg} \tag{3.7}$$

where Δ_0 is the width of the initial Gaussian wave packet. In this sense the quantum motion of the particle is non-universal, as it depends on the value of its mass [69, 70, 71].

Another example is the role of intrinsic spin of quantum probes, that has no classical equivalent. CAI can also be performed with other Zeeman sublevels (spin polarized states with $m_F \neq 0$) with a somewhat reduced precision due to the first-order coupling with magnetic fields. This possibility of performing spin-dependent tests is an obvious advantage of quantum tests over classical versions of EEP tests.

The WEP and the role of inertial and gravitational masses in quantum mechanics have been studied theoretically in numerous works. It was shown recently [72] that the validity of the equivalence principle for classical objects does not imply the validity of its quantum formulation, i.e., the equivalence between inertial and gravitational mass operators. Such considerations point towards new experimental approaches involving quantum test particles described by superposition states of internal degrees of freedom. Very recently, an atom interferometry test of such a quantum formulation of the equivalence principle has been performed by measuring the free-fall acceleration of an atom in a superposition of different internal energy states [73].

A new king of quantum WEP test with entangled states of different species A and B was proposed in [74]. The entanglement between the two atoms is created during the initial beam splitter of the interferometers through the detection of a single photon emitted by either of the atoms, together with the impossibility of distinguishing which atom emitted the photon. In this proposal, the main phase shift of the interferometer, $\Delta\Phi_{WEP} \equiv k_z(g^A - g^B)T^2$, represents a coherent measurement of the difference in the gravitational acceleration between the two atoms. More precisely, the interferometer measures the gravity acceleration of the two-entangled-atom state.The effect of entanglement on the free fall can thus be directly assessed by comparing the differential gravity obtained with the entangled atoms ($g^A - g^B$ in $\Delta\Phi_{WEP}$) to that obtained with the classically independent atoms (g^A and g^B measured independently).

Choice of the atom species

The choice of the atom species depends on both scientific and technical considerations.

On a scientific point of view, according to the dilation model [51], a violation may be caused by forces acting differently on neutron and proton. With the introduced effective charges $Q'^1_{A,B}$ and $Q'^2_{A,B}$ calculated from the composition of a test particle, a measurement of the Eötvös ratio set bounds to the parameters D_1 and D_2 according to the formula

$$\eta_{A,B} \cong D_1\left(\Delta Q'^1_{A,B}\right) + D_2\left(Q'^2_{A,B}\right) \tag{3.8}$$

A	B	Reference	$\Delta Q'^1_{A,B}$ $\cdot 10^4$	$\Delta Q'^2_{A,B}$ $\cdot 10^4$	Δf_{-n} $\cdot 10^2$	Δf_{+n} $\cdot 10^4$	$\Delta \bar{f}_{-n}$ $\cdot 10^5$	$\Delta \bar{f}_{+n}$ $\cdot 10^4$
^{9}Be	Ti	[56]	-15.46	-71.2	1.48	-4.16	-0.24	-16.24
Cu	^{238}U	[75]	-19.09	-28.62	-7.08	-8.31	-89.89	-2.38
^{6}Li	^{7}Li	[76]	0.79	-10.07	-7.26	7.79	-72.05	5.82
^{85}Rb	^{87}Rb	[77]	0.84	-0.79	-1.01	1.81	1.04	1.67
^{87}Sr	^{88}Rb	[61]	0.42	-0.39	-0.49	2.04	10.81	1.85
^{39}K	^{87}Rb	This work	-6.69	-23.69	-6.31	1.9	-62.3	0.64
^{87}Rb	^{170}Yb	[5]	-12.87	-13.92	-1.36	-8.64	86.00	-5.46

TABLE 3.2 – Comparison of choices for test masses A and B employed in existing and planned tests of the UFF parametrized for violation scenarios with respect to their effective charges $Q'^1_{A,B}$, $Q'^2_{A,B}$, and $f_{\beta^{e+p+n}_{A,B}}$,$f_{\beta^{e+p-n}_{A,B}}$, $f_{\beta^{\bar{e}+\bar{p}+\bar{n}}_{A,B}}$,$f_{\beta^{\bar{e}+\bar{p}-\bar{n}}_{A,B}}$, calculated according to [51] and [52].

A similar kind of parametrization can be given for the standard model extension [52]

$$\eta_{A,B} \cong \Delta f_{-n} + \Delta f_{+n} + \Delta \bar{f}_{-n} + \Delta \bar{f}_{+n} \tag{3.9}$$

with the defined violation parameters for matter and anti-matter linked to neutron excess and total baryon number

$$\Delta f_{-n} = f_{\beta^{e+p-n}_A}\beta^{e+p-n} - f_{\beta^{e+p-n}_B}\beta^{e+p-n} \tag{3.10}$$

$$\Delta f_{+n} = f_{\beta^{e+p+n}_A}\beta^{e+p+n} - f_{\beta^{e+p+n}_B}\beta^{e+p+n} \tag{3.11}$$

$$\Delta \bar{f}_{-n} = f_{\beta^{\bar{e}+\bar{p}-\bar{n}}_A}\beta^{\bar{e}+\bar{p}-\bar{n}} - f_{\beta^{\bar{e}+\bar{p}-\bar{n}}_B}\beta^{\bar{e}+\bar{p}-\bar{n}} \tag{3.12}$$

$$\Delta \bar{f}_{+n} = f_{\beta^{\bar{e}+\bar{p}+\bar{n}}_A}\beta^{\bar{e}+\bar{p}+\bar{n}} - f_{\beta^{\bar{e}+\bar{p}+\bar{n}}_B}\beta^{\bar{e}+\bar{p}+\bar{n}} \tag{3.13}$$

Table 3.2 shows the effective sensitivity to a potential WEP test of the pair of test masses. It is clearly very interesting to choose two different species such as Rubidium and Potassium.

Technically, Rubidium and Potassium have the advantage to be compliant with the technology of telecom laser and frequency doubling. The robustness of the laser system is indeed a key point for on board applications, especially in Space (see section 3.1.5). The two wavelengths are close enough to use the same optics, the same detectors (photodiode, CCD camera) but far enough to combine them with interferential filters, and allowing an independent control of each atom interferometer (767 nm light has no strong influence on Rubidium and reciprocally). Moreover, efficient laser cooling and fluorescence detection makes Rubidium suitable for interferometry. It is more complicated for Potassium but our team made strong effort to improve these experimental aspects (see chapter 2). Finally, double species Rb-K ultracold atom sources can be produced, but required Feshbach resonances.

The choice of other atom species is of course possible. The state of the art with cold atoms is achieved with the two isotopes of Rubidium which gives a WEP test accuracy of 3.4×10^{-12} [65]. The technology difficulties are mitigated especially compared to WEP test using two different species but the expected WEP violation is lower (table 3.2). Because it is heavy, Cesium is very interesting and commonly used for atom interferometry. Unfortunately it is very difficult to produce ultra-cold atoms and no telecom laser source is available. Yb, Sr own very interesting properties, such as the production of a continuous atom source at high phase space density [46] or the existence of an optical clock transition allowing one photon interferometry [78]. Nevertheless, at this stage, they requires complex and less mature laser technology and are thus not fully compliant for on board applications. Lithium is a light atom which can be interesting for the difference of the test masses but this is not very suitable for

atom interferometry.

The choice of the Rubidium isotope is justified considering the favorable collisions properties to reach Bose Einstein condensation of ^{87}Rb. On the contrary, ^{85}Rb condensation requires Feshbach resonances to change the scattering length. The choice of the Potassium isotope is an open question. At the stage of our project, it is easier to use the most abundant isotope ^{39}K. Most of the techniques we developed work for the the three isotopes (grey molasses, state preparation, fast photodiodes).

Targeted accuracy

To conclude, we could discuss about the target accuracy, even if obviously we need to improve the precision as long as no WEP violation is measured. On the contrary, we could wonder why the WEP test is not violated yet at the level of $10^{-13} - 10^{-14}$. Table 3.1 presents the target accuracy for several experiments on grounds, based on reasonable extrapolations of what we can expect by increasing the interrogation time. The next step is a WEP test in Space to gain at least two orders of magnitude and go below the "conventional" benchmark number of 10^{-15}.

Space mission versus large atomic fountains

The high accuracy of the atom interferometers relies on the fact the atoms are perfect proof masses in perfect free fall. Nevertheless, from an experimental point of view, parasitic effects must be tackled. Magnetic field gradient, phase and intensity fluctuations of the laser beam during the pulses can lead to systematic errors. The requirements are more and more demanding when our wanted accuracy is decreased with the increase of the interrogation time. To increase this interrogation time, one approach is to construct a large (10 meter high typically) atomic fountain where the atom cloud propagates along a large spatial zone. Controlling the magnetic field and laser profile on such an area is very demanding technically. On the contrary, the central idea of our experiment is to achieve the complete experimental sequence at the central point of the sensor head to facilitate the control of the magnetic and optical parameters. For instance the quality of the laser profile (phase, intensity) is easier to guarantee because of the shorter propagation length (50 cm versus 20 m typically).

Moreover the environment for the inertial measurement is very well controlled on the satellite, unlike ground based experiments. A very low noise level of residual acceleration has been demonstrated with Microscope [57] and Lisa pathfinder missions [79]. Finally, the absence of Newtonian noise in Space is also a strong advantage.

3.1.5 Test of the Weak Equivalence Principle in Space

Our long term scientific goal is to test the Weak Equivalence Principle (WEP) by measuring the differential acceleration of two atom species (^{87}Rb and ^{39}K) using atom interferometry. To increase the interrogation time and thus the sensitivity of the measurement, our strategy is to build an instrument for a Space mission (STE-QUEST) on board a satellite in a low noise environment in terms of vibrations and non inertial forces. With an interrogation time of 10 seconds for a circular orbit at an altitude of 700 km, we expect a long term measurement for a mission duration of 18 months with an accuracy of 10^{-17} [80].

The goal of the ICE project is to develop an experiment which makes the link between the standard techniques develop in laboratory ans the future Space mission. Our objective is to implement the main principles planned for the Space instrument including a double

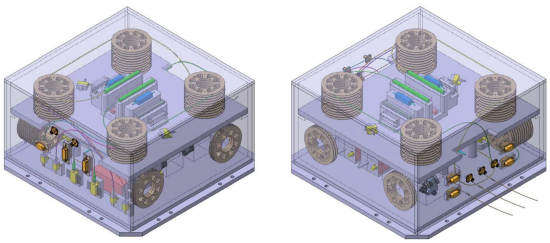

FIGURE 3.1 – Industrial Design (SODERN) of the reference laser for the Space mission STE-QUEST

species (^{87}Rb and ^{39}K) atom interferometer, a dipole trap to produce ultra cold sources, and tests in microgravity environment. Moreover, the achievement of an atom interferometer on board the Zero-g plane allows to tackle the issues of rotations and vibrations, which are also present on a satellite. In a word, our experiment aims to demonstrate the functionality of the instrument in microgravity and to reach an intermediate level of accuracy of 10^{-10} on the Eötvös parameter. On board the 0g plane, we expect to demonstrate a short term sensitivity of 10^{-9} g.Hz$^{-1/2}$. Long term measurements on our zero-g simulator will complete this test with an integration time of 2 days to reach the expected level of 10^{-10}.

Our experiment is also a versatile platform to qualify the key components for Space applications and our work during the past decade contributed strongly to increase the maturity of our devices (Technology Readiness Level or TRL). Based on our developments, I proposed a design of the laser source for the instrument of the STE-QUEST mission, which is based on telecom technogoly and frequency doubling. Sodern validated the architecture by studying an industrial version of this laser source (see figure 3.1). This laser is currently under development in muQuanS.

3.2 Test of the Weak Equivalence Principle in a standard laboratory

3.2.1 ICE experiment

The activities on this experiment is strongly linked to the technological developpement dedicated to the industrial applications that I led in parallel (see chapter 4). The key components and subsystems of an atom interferometer has been tested and validated in relevant conditions onboard the zero-g plane during parabolic flight campaigns. Particularly, we developed a fiber laser source using telecom components associated to a frequency doubling stage [81]. This technology is now in all our laser systems developed in the compact atom sensors (see chapter 4).

Our robust and transportable device is comprised of a bank of fiber-based lasers, an ultra-stable frequency source and a titanium science chamber pictured in Fig. 3.2. The experiment has been designed to operate in microgravity, in the extreme environment of the zero-g plane and is meant to tolerate strong temperature variations, vibration levels and congestion. It is thus a compact and robust experimental setup in addition to be transportable. The apparatus consists in eight racks independently removable with a weight between 100 and 180 kg each

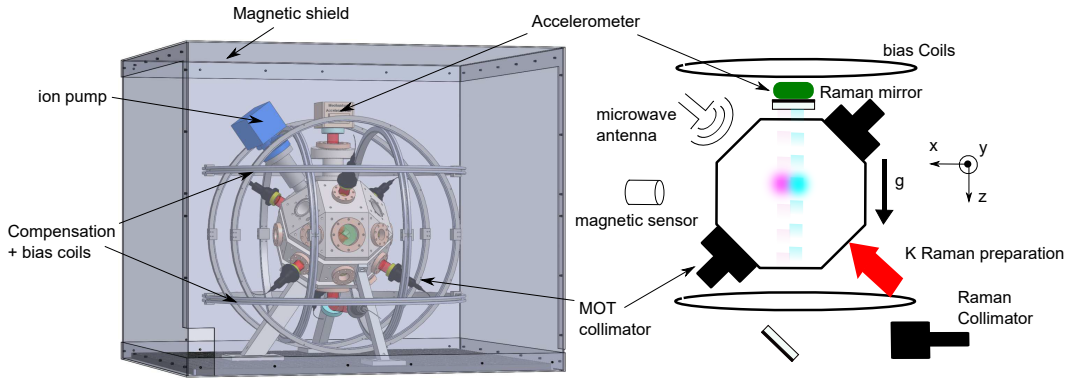

FIGURE 3.2 – Scheme of the Rb-K atom interferometer. Left : 3D view of the titanium vacuum chamber surrounded by the magnetic shield. Right : Lateral section of the chamber. Rubidium (pink) and Potassium (light blue) are cooled and trapped simultaneously at the center of the vacuum chamber. We release both atom clouds at the same time and measure their trajectories compared with the same reference mirror thanks to two overlapped retro-reflected beams (separated on the drawing for clarity). A corrected magnetic environment is assured thanks to a magnetic shield and a servo lock of the field with a magnetic sensor and a pair of Helmhotz coils. A mechanical accelerometer Titan from Nanometrics (green) is placed on the reference mirror mount.

(see Fig. 3.3 a)).

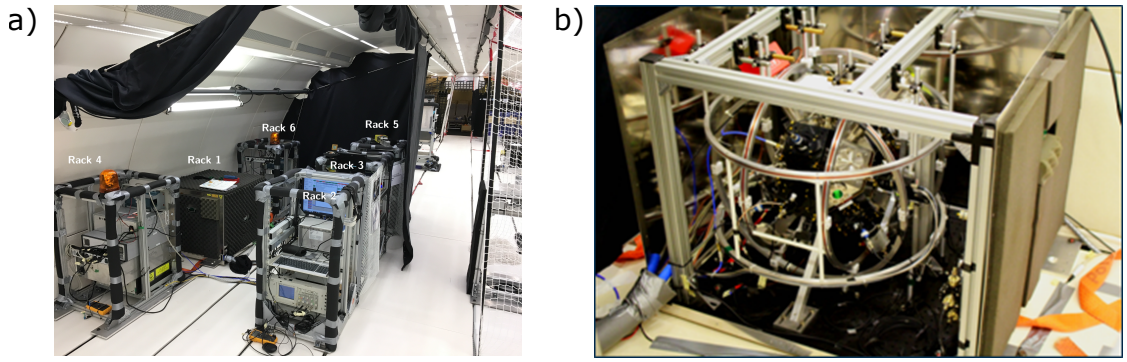

FIGURE 3.3 – a) ICE experiment onboard the zero-g plane. b) Science chamber inside the magnetic shield

The vacuum system is a small Rhombicuboctahedron with 26 faces made of Titanium. The science chamber is compliant with ultra high vacuum (below 10^{-11} mbar) (Fig. 3.3 b)). Viewports are sealed with indium which gives 19 optical axis for the laser cooling and trapping beams, the detection, the crossed far off resonance dipole trap and three axis for retro-reflected Raman beams for multi-axis inertial measurements. The complete system including the collimators and the detectors is surrounded by a magnetic shield to strongly reduce the external varying magnetic field in the plane or the simulator. Inside the shield, the homogeneity of the magnetic field is insured by Helmholtz coils pairs and lock-in electronics with a probe. The Raman beam is on the vertical axis, and the two frequencies are retro-reflected onto a reference mirror which allows to achieve counter-propagating transitions, thus induce spatial splitting of the wavepackets.

The laser architecture is based on the frequency-doubled telecom technology including external cavity diode lasers operating (ECDL) at 1560 nm (resp. 1534 nm for Potassium). The low power part consists in a master diode frequency-doubled and frequency-locked by

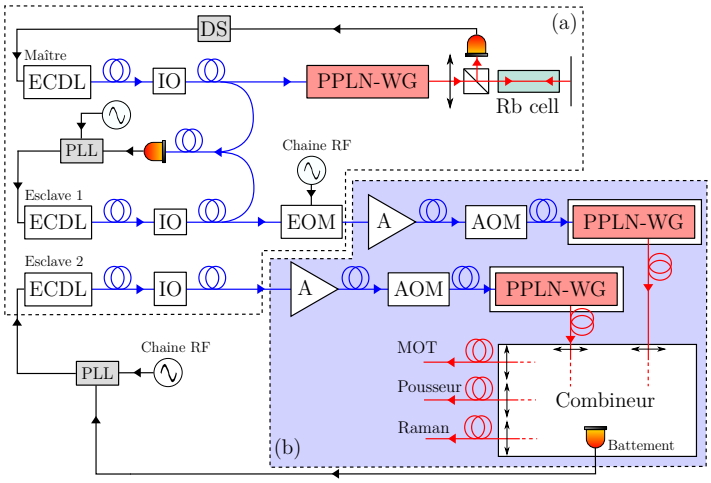

FIGURE 3.4 – ICE Experiment : the laser system architecture is based on telecom components and frequency doubling. ECDL : External Cavity Diode Laser. IO : Optical Isolator. EOM : Phase modulator. A : Erbium Doped Fiber Amplifier (EDFA). AOM : Acousto-Optic Modulator (AOM). PPLN-WG : frequency doubling stage. DS : Lock-in Amplifier. PLL : Phase Lock Loop. Chaine RF : RF/microwave source.

absorption spectroscopy on the ^{85}Rb $|5S_{1/2}, F = 3\rangle \rightarrow |5P_{3/2}, F' = 3, 4\rangle$ crossover. A first slave diode is phase locked on the master signal with an offset frequency of 1.4 GHz. A second slave diode is phase locked with the first slave diode and allows to create the second frequency which can be used both as a repumper for the laser cooling stage and the Raman second frequency for the interferometry stage. Two 2W Erbium-doped fiber amplifiers (EDFA) amplify the optical power of each slave and two acousto-optic modulators (AOM) are used to control the optical power on each path. The three frequency doubling stages (PPLN-WG) are composed of a waveguide implemented in a Periodically-Poled Lithum Niobate (PPLN) crystal. Finally, a micro-optics bench made of glass and developed by MuQuanS and Kylia combines the two slaves output beam then splits the combined signal in three paths for the magneto-optical trap, the Raman/detection beam and the pushing/imaging beam. Inside the splitter, mechanical shutters are placed on the three paths to provide a high attenuation during the interferometer sequences and an additionnal AOM is placed on the Raman/detection path for a good control of the Raman pulses. The total output power is 500 mW at 780 nm. The whole laser system is immune to misalignment and the power fluctuations are low (1% percent). Two similar systems are currently developed for Potassium (767 nm for the D2 transition and 770 nm for the D1 transition).

The K and Rb atomic sources are derived from overlapped 3D magneto-optical traps (MOTs) loaded from a hot background vapor provided by a dispenser. Lasers on the D2 transition for both species (respectively 780 nm and 767 nm) and on the D1 transition for K (770 nm) are all combined into the same 6 cooling beams. The Rb and K interferometer beams are combined in the same collimator and are retro-reflected by a mirror to induce velocity-sensitive two-photon Raman transitions. We measure the relative displacement of Rb and K with respect to this reference mirror in two overlapped retro-reflected beams. The two optical rulers have a slightly different periodicity because of the different wavelength for Rb (780.24 nm) and K (766.7 nm) but the ratio is controlled with an accuracy of 1 MHz (3 ppb) thanks to the frequency lock of the lasers. The preparation of states is done by a microwave antenna for Rb and via copropagating Raman transitions for K (see chapter 2). A servo-lock control of the magnetic field is applied to compensate the temporal variation due to Eddy currents. We

measure the field with an external magnetic sensor (Model MAG03MCTPB500 3-axis flux gate sensor" from Bartington Instruments) and apply a feedback field on the atoms using a pair of Helmholtz coil. A mu-metal magnetic shield is placed around the experiment to prevent external fields from interfering with our measurement.

During the full sequence the atoms stays in the center of the experiment. This implies some constraints, especially on the detection scheme. The science chamber is not designed to separate spatially the two output of the interferometer [1]. It means we need to detect the two population in $|F = 1\rangle$ and $|F = 2\rangle$ sequentially in time (see Fig. 3.5 (a)). For each specie, a first pulse of detection is applied with only the cooling frequency (no repumping light) in order to detect the population in $|F = 2\rangle$. Then we apply a second pulse with the two frequencies to detect the total atom number. Then we can extract the population ratio.

Especially this detection scheme is a problem for Potassium, which has a very short depumping time because of the narrow level structure. Fig. 3.5 (b) shows the fast decrease of the fluorescence signal during the detection of $|F = 2\rangle$ population. A fast and sensitive detector is required. Moreover, a strong brackground in our single chamber is also a limitation. The detector is an Avalanche Photodiode (APD), with the disadvantage of being small and thus highly sensitive to misalignment.

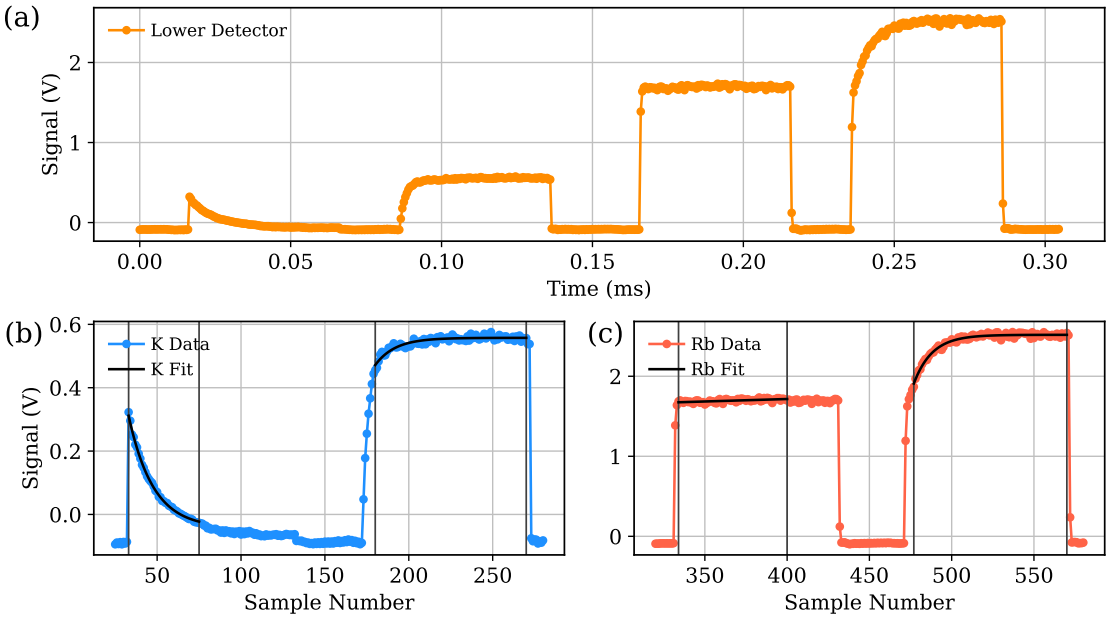

FIGURE 3.5 – Typical detection signals for ^{39}K and ^{87}Rb. (a) Full detection trace recorded by the acquisition system ($\sim$ 500 kHz bandwidth). An analysis of ^{39}K (b) and ^{87}Rb (c) signals is shown on the bottom row. For each species S, fluorescence signals representing N_S^2 (left peak) and N_S^{total} (right peak) are fit to a model consisting of an exponential plus a constant, and the maximum within each fit window (marked by vertical lines) is extracted. When combined with the background measurement, we obtain the normalized population P_S^2 with a typical statistical uncertainty of 0.62% and 1.9% for ^{87}Rb and ^{39}K, respectively.)

Finally we should notice the solid angle is not optimized because of the geometry of the experiment. To improve this aspect, we have an aperture to allow us to put a lens inside the structure. At this place we have a gain of a factor 2 on the distance between the atoms and the first lens to collect the fluorescence. The new design of the science chamber will include an optical access allowing a large solid angle to optimize the collection of the signal and increase

1. Of course ultracold atoms change the situation and allows accurate spatial imaging on a CCD camera

the resolution of future imaging systems.

3.2.2 WEP test with a double species atom interferometer

The atom specie ^{87}Rb is a usual choice for atom interferometry with conventional and well mastered methods (see discussion on the choice of the species in section 3.1.4). On the contrary, Potassium properties bring several difficulties. The atomic level structure is very narrow, which makes the laser cooling and fluorescence detection more complicated and the spectroscopy signal less clean and less accurate. Fortunately, grey molasses cooling and optical state preparation (chapter 2) make Potassium suitable for metrology applications. Thanks to these methods we get **the best contrast and signal to noise ratio** of Potassium interference fringes to our knowledge (see chapter 2).

In standard gravity the interrogation time is limited to 2T=50 ms due to the compactness of the science chamber. Despite this limitation system our study demonstrated a WEP test **with two species** close to the state of the art, which is a remarkable result which paves the way to a test with a different interest from those achieved with the two isotopes of Rb (see table 3.2).

As one goes to larger sensitivities, or when the vibration noise is large (such as onboard a moving vehicle), the motion of the reference mirror becomes a significant source of phase noise. In most cases, one must employ methods to either suppress or reject the phase noise resulting from mirror vibrations. The primary method to suppress ambient vibrations is to place the apparatus on an anti-vibration platform [82, 83], but this solution is not generally compatible with onboard applications. Hence, we use two methods to reject vibration noise. The first is to perform the interferometers simultaneously and with the same scale factor ($\mathcal{S}_{\mathrm{Rb}} = \mathcal{S}_{\mathrm{K}}$), this ensures a maximum amount of common mode rejection. It is then possible to measure the differential phase by fitting an ellipse to the interferometer output for each species plotted parametrically [84] [see Fig. 3.6(b)]. The second method involves monitoring the mirror vibrations with a mechanical accelerometer and correcting for the noise by computing the corresponding vibration phase[85, 84]. This method is presented chapter 4.

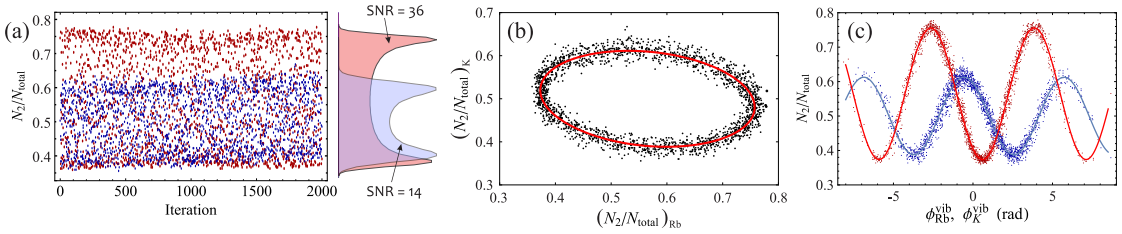

FIGURE 3.6 – (a) Raw transition probability for simultaneous ^{87}Rb (red points) and ^{39} (blue points) interferometers with a total interrogation time of $2T = 40$ ms. The probability density measured from these 2000 measurements is shown on the right, which enables one to extract of the fringe contrast and SNR for each species. (b) Parametric plot of the raw measurements from (a). The high degree of correlation between these data results in an ellipse. A fit to these data (solid line) yields this differential phase shift between interference fringes, which is primarily caused by systematic effects. (c) Reconstruction of the fringes using the FRAC method. Here, sinusoidal fits (solid lines) can be used to directly extract the sensitivity to the acceleration of each species.

Figure 3.6 shows simultaneous measurements from the laboratory using $2T = 40$ ms. Figure 3.6(a) displays the raw transition probability for both species for 2000 accelerations measurements (requiring $\sim$ 30 minutes of data acquisition). These points are integrated over

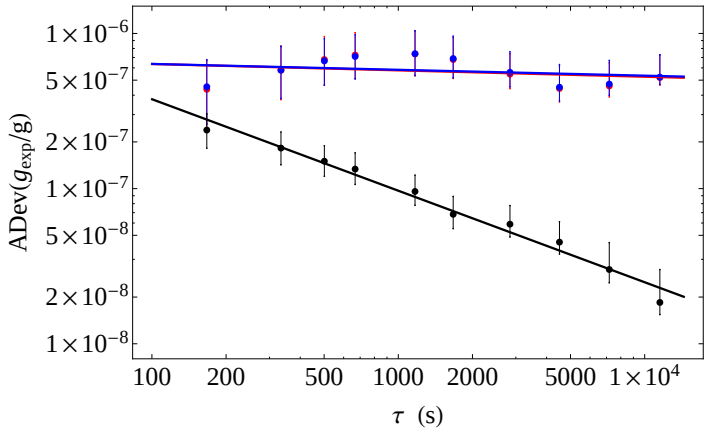

FIGURE 3.7 – Allan deviation of the accelerations measured using Rubidium (red) and Potassium (blue) alone, and differential measurement (black) corresponding to the η parameter quantifying the WEP test.

the horizontal axis to obtain the probability density distribution. By fitting a function that is the convolution of an inverse sine and of a Gaussian to the probability density, we extract the contrast and SNR of each interferometer [85]. Figure 3.6(b) displays a parametric plot of the potassium transition probability as a function of the rubidium one for the same data presented in Fig. 3.6(a). Since the vibration noise is common mode for both species, there is a high degree of correlation between these data—resulting in an ellipse with an eccentricity determined by the differential phase between the two interference fringes. Fitting an ellipse to these data yields an estimate of $\Delta\Phi_d$ with a statistical precision of ~ 10 mrad—corresponding to a WEP violation sensitivity of $\delta\eta \sim 1.5\times10^{-7}$. Figure 3.6(c) shows the reconstructed interference fringes using the FRAC method, from which we can directly measure the acceleration sensitivity of each species : $\delta a_{\mathrm{Rb}} \simeq 5.2\times10^{-8}\,g$ and $\delta a_{\mathrm{K}} \simeq 8.3\times10^{-8}\,g$.

The Allan deviation for each atomic interferometer Rubidium (red) and Potassium (blue) is limited by the residual bias drift of the classical accelerometer, while the Allan deviation of η is integrated as a white noise over 12 hours to reach a precision of 5×10^{-8} (figure 3.7).

3.2.3 Accuracy of the WEP test on ground

For the WEP test we achieved on ground, we led a complete study of the systematic errors. The measured Eötvös parameter can be decomposed into a sum of terms depending on different systematic error sources :

$$\eta = \frac{g_{Rb} - g_K}{g} + \eta_{\Delta k} + \eta_b + \eta_{sys}, \tag{3.14}$$

with

$$\begin{aligned} \eta_{\Delta k} &= \frac{\Delta k_{Rb}}{k_{Rb}}\frac{g_{Rb}}{g} - \frac{\Delta k_K}{k_K}\frac{g_K}{g} \\ \eta_b &= -\left(\frac{\Delta k_{Rb}}{k_{Rb}} - \frac{\Delta k_K}{k_K}\right)\frac{b}{g} \\ \eta_{sys} &= \left(\frac{\Phi_{Rb}^{\uparrow,sys} - \Phi_{Rb}^{\downarrow,sys}}{k_{Rb}F_{Rb}} - \frac{\Phi_K^{\uparrow,sys} - \Phi_K^{\downarrow,sys}}{k_K F_K}\right) \end{aligned} \tag{3.15}$$

The first term corresponds to the violation of the WEP. The second term corresponds to an error on the wave vector Δk_j, coming from the control on the laser frequencies at the level of 1 MHz and the angle between the Rb and K Raman beams. We measured the relative

Systematic Effect	$g^{\uparrow,Rb}_{sys}$ $(10^{-6} m.s^{-2})$	$g^{\downarrow,Rb}_{sys}$ $(10^{-6} m.s^{-2})$	$g^{\uparrow,K}_{sys}$ $(10^{-6} m.s^{-2})$	$g^{\downarrow,K}_{sys}$ $(10^{-6} m.s^{-2})$
Quadratic Zeeman effect	8.69 (0.62)	-11.02 (0.62)	70.8 (4.4)	-117.9 (4.4)
Magnetic gradient force	-0.04 (0.0002)	-0.04 (0.0002)	-1.52 (0.036)	-1.41 (0.036)
1 Photon LightShift	0.00 (0.54)	0.00 (0.54)	3.1 (0.3)	-3.1 (0.3)
2 Photon LightShift	-6.83 (0.16)	-7.61 (0.16)	-6.56 (0.31)	-8.08 (0.31)
Parasitic Lines	-34.1 (3.1)	-34.1 (3.1)	0 (0)	0 (0)
Wavefront curvature	$2 \times 10^{-3}(6 \times 10^{-4})$	$2 \times 10^{-3}(6 \times 10^{-4})$	$9 \times 10^{-2}(1.4 \times 10^{-2})$	$1 \times 10^{-2}(1.4 \times 10^{-2})$
Wavefront aberration	0.00 (0.37)	0.00 (0.37)	0.00 (0.81)	0.00 (0.81)
First order gravity gradient	$-1.7 \times 10^{-3}(3 \times 10^{-4})$	$-1.7 \times 10^{-3}(3 \times 10^{-4})$	$-2.1 \times 10^{-3}(3 \times 10^{-4})$	$-1.9 \times 10^{-3}(3 \times 10^{-4})$
Coriolis Effect	0.10 (0.01)	0.10 (0.01)	0.41 (0.02)	0.41 (0.02)

TABLE 3.3 – Systematic errors and uncertainties on their estimation (value in parenthesis) for each individual atom interferometer and for both sign of the wave vector k_j.

angle with an uncertainty of 10 μrad[2]. The third term is due to the bias of the classical accelerometer b. This term stays small compared to $\eta_{\Delta k}$ because this bias is much smaller than g and we remove this drift to first order. The forth term corresponds to the systematic errors of each atom interferometer.

Table 3.3 presents the estimation of the systematic errors for each individual atom interferometer depending of the sign of k_j. For Potassium, Quadratic Zeeman effect and the force due to the magnetic field gradient are the major contributions in terms of uncertainty. Quadratic Zeeman effect is not perfectly rejected with the differential measurement for the $+k_j$ and $-k_j$ configurations because of the different trajectories of the atoms in both cases. One Photon light shift is not compensated on Potassium but we expect to reject this term with the two measurements $-k_j$ and $+k_j$. Parasitic lines of the Rb laser create a significant shift which also contributes significantly to the error budget. Then the wavefront aberration is difficult to measure at the location of the atoms. We consider here a curvature of amplitude $\lambda/10$ on the full size of the optics (diameter of 1 inch).

Parasitic lines

This systematic error is present for the Rb interferometer due to the use of an EOM to generate the second Raman frequency. The phase shift due to the parasitic interferometers is the only effect depending on the relative position between the atoms and the reference mirror. To evaluate the phase shift, we compared two datasets, where the main difference is the mirror position with a variation of $\delta z = -5.5$mm for a reference position of the mirror $z_m = -304.1$mm. We calculate their contribution in function of T based on the model described in [86]. The phase variation versus the interrogation time T for two different positions of the reference mirror allows to validate our knowledge of the experiment parameters and the contribution of the parasitic lines in our error budget.

Quadratic Zeeman effect

The magnetic field in the vacuum chamber is first evaluated using co-propagating Raman spectroscopy with the atoms distributed in the three internal states $|F = 1, m_F = 0, \pm 1\rangle$. The frequency splitting between the 3 resonances is directly linked to the magnetic field $B(T_{FF})$, where T_{FF} is the free fall duration of the atoms. Since the atoms are in the ground state of the D2 transition ($5^2S_{1/2}$), we can use the Breit Rabi formula to extract $B(T_{FF})$:

$$E_{J=1/2,m_J,I,m_I} = \frac{-\Delta E_{hfs}}{2(2I+1)} + g_I \mu_B m B \pm \frac{\Delta E_{hfs}}{2}(1 + \frac{4mx}{2I+1} + x^2)^{1/2} \tag{3.16}$$

2. An error on the absolute angle of k_j relative to vertical is not a bias in our measurement because this angle is defined by the common reference mirror for both species, and since the correction to the magnitude of g is very small this does not significantly affect the scale of $\eta = \Delta g/g$ (we rely on local g to obtain the denominator since our single interferometer measurement is biased by the mechanical accelerometer).

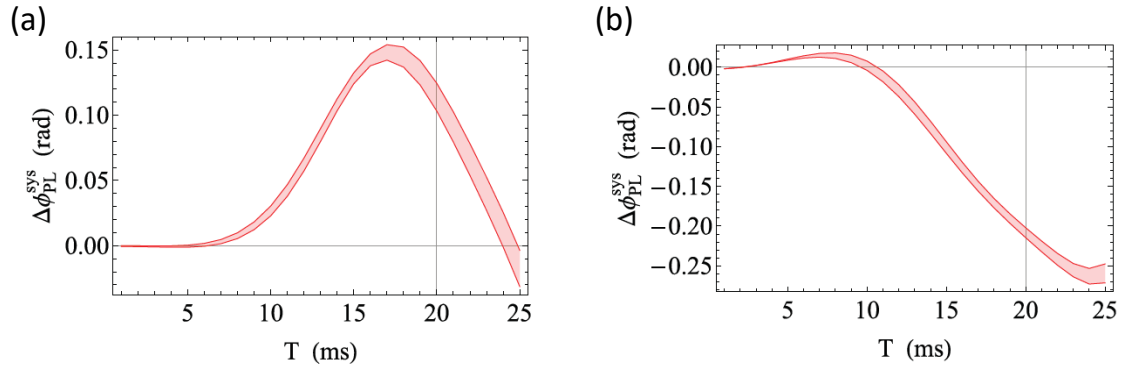

FIGURE 3.8 – Phase Shift due to the parasitic lines versus the interrogation time T for two different positions of the reference mirror z_m (a) and $z_m + \delta z$ (b). The theoretical model includes our estimated and measured parameters (distance between the atom and the reference mirror, initial velocity...).

where ΔE_{hfs} is the hyperfine splitting, $m = m_I \pm m_J$ with the same sign as the 3^{rd} term in Eq. 3.16 and :

$$x = \frac{(g_J - g_I)\mu_B B}{\Delta E_{hfs}} \tag{3.17}$$

We measure the frequency splitting between $|F = 1, m_F = +1\rangle$ and $|F = 1, m_F = 0\rangle$, then resolve the second order equation coming from Eq. 3.16.

The magnetic field B versus T_{FF} for Rb and K is determined with a sensitivity of about $5 \cdot 10^{-4}$ G (blue curve on Fig. 3.9). This measurement need to be corrected by the vector and tensor Light Shift (LS). The vector LS explains the difference between the measurements with Rb and K [87]. For our experimental parameters, the virtual magnetic field due to the vector LS is -6.7 mG for Rb and -9.5 mG for K.

This magnetic field profile includes a temporal part due to residual Eddy currents (after the correction of the real time compensation explained in section 3.2.1) and a spatial magnetic field gradient. The spatial magnetic field gradient has been evaluated by varying the magnetic field gradient compensation and removed the Eddy currents by let the coils on during the full sequence. The residual magnetic field gradient is 4 G/cm. We then take into account the different trajectories of the atoms for the $+k_j$ and $-k_j$ pulse (Fig.3.9 for K) for the gradient part, and add the purely temporal magnetic field profile which is the same for $+k_j$ and $-k_j$. We obtain two profiles $B_j(z_\uparrow(t))$ and $B_j(z_\downarrow(t))$ for each species (Fig.3.9 (green) and (red) for K). These curves are used to calculate the Quadratic Zeeman effect on the atomic transition $|F = 1, m_F = 0\rangle \rightarrow |F = 2, m_F = 0\rangle$ states coming from Equ. 3.16 for small fields :

$$\Delta\omega_j^{\uparrow,\downarrow}(z) = \frac{(g_J - g_I)^2 \mu_B^2 B_j^2(z_{\uparrow,\downarrow}(t))}{2\hbar\Delta E_{hfs}} = 2\pi * K * B_j^2(z_{\uparrow,\downarrow}(t)) \tag{3.18}$$

Then we can deduced the bias phase due to Zeeman effect :

$$\Phi_j^{\uparrow,\downarrow,Zeeman} = 2\pi K \int_{-\infty}^{+\infty} g_S^j(t) B_j^2(z_{\uparrow,\downarrow}(t)) dt \tag{3.19}$$

where $g_S^j(t)$ is the sensitivity function of the atom interferometer.

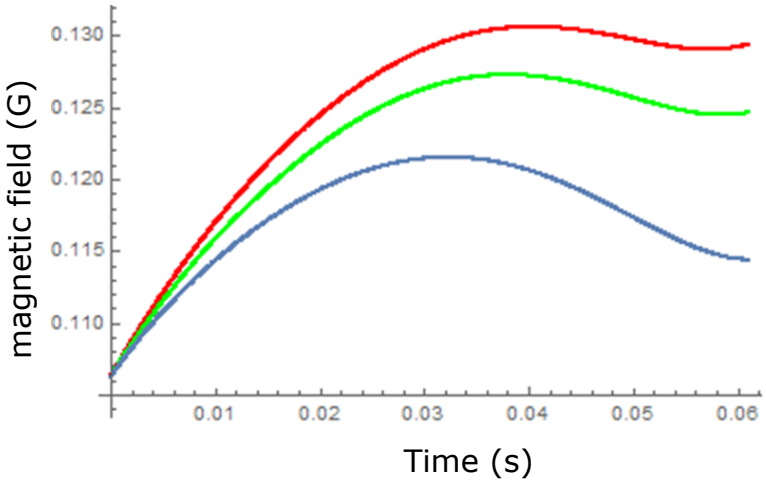

FIGURE 3.9 – Magnetic field seen by the K atoms in the $+k_j$ configuration (green) and the $-k_j$ atom interferometer (red). The field includes a temporal part common to the two trajectories and a spatial gradient which depends on the trajectory. The blue curve is the magnetic field measured with co-propagating Raman transitions, without any recoil modifying the trajectory.

Magnetic field gradient

In addition to the frequency shifts of the atomic level, magnetic field gradient implies a force, even if the atom is in the non magnetic state $|m_F = 0\rangle$:

$$F_S = -hKB \cdot \nabla B \tag{3.20}$$

where h is Planck's constant, K is a constant depending on the level structure of the atom and is defined in Eq. 3.19. This force has an opposite sign for an atom in state $|F = 2, m_F = 0\rangle$ compared to an atom in the state $|F = 1, m_F = 0\rangle$, so this effect is partially rejected in a Raman Mach-Zehnder interferometer. Because of the trajectories, the rejection is not perfect and a phase shift is expected [88] :

$$\Phi_{\nabla B} = \frac{2}{3}k\left(\frac{hK}{m}\nabla B\right)^2\left[\left(v_0 + \frac{v_R}{2}\right)T + gT^2\right]T^2 \tag{3.21}$$

where v_0 is the initial velocity and v_R is the recoil velocity.

One Photon Light Shift

The method to measure the One Photon Light Shift is based on Raman Spectroscopy. We scan the Raman frequency and measure the resonances of both $+k_j$ and $-k_j$ counter propagating and co propagating Raman transition for different laser intensities and different times of flight before the Raman pulse. The estimated phase shift is calculated using the following equation :

$$\delta\Phi_{LS1P} = \frac{\delta_{LS}^{(3)}}{\Omega_R^{(3)}} - \frac{\delta_{LS}^{(1)}}{\Omega_R^{(1)}} \tag{3.22}$$

where $\delta_{LS}^{(i)}$ is the 1 photon light shift and $\Omega_R^{(i)}$ the Rabi frequency for the i pulse. Fig 3.10 shows the phase shift versus the laser power. We observed an offset of the phase shift, especially for Potassium (the phase doesn't go to zero at zero optical power). In fact, for short time of flight, a shift of the Raman transition of about 13 kHz is due to a partial detection

of the atom cloud. The recoil on the diffracted atoms has a strong influence on the atom trajectories, especially for Potassium. Consequently the position of the diffracted atom cloud on the detector strongly depends on the time of the Raman pulse. This effect creates a bias on the Raman spectroscopy.

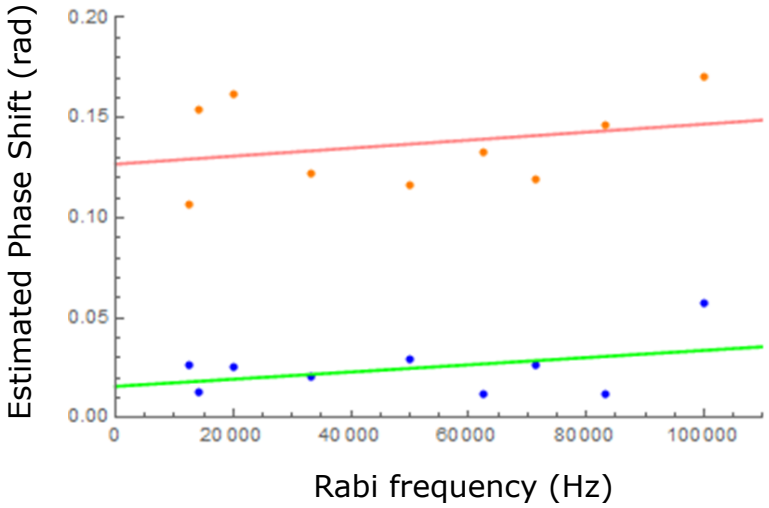

FIGURE 3.10 – Phase shift (orange for potassium and blue for Rubidium) versus Rabi frequency (π-pulse conditions) due to One Photon Light shift estimated by Raman spectroscopy of the co- and counter-propagating transitions. The slope of the fit curves (red for Potassium and green for Rubidium) corresponds to the Light Shift. The offset phase is due to a partial detection of the atom cloud which modify the shape of the Raman resonance spectroscopy.

Two photon Light Shifts

Two photon light shifts due to off resonance two photon transitions provides a bias which cannot be removed by the alternated $+k_j/-k_j$ measurements [89]. The first frequency shift is due to counter-propagating transitions :

$$\Delta\omega^{Contra} = \frac{\Omega_R^2}{\pm 8\omega_D} + \frac{\Omega_R^2}{4(\pm 2\omega_D + 4\omega_R)} \tag{3.23}$$

with $\omega_D = kv$ is the Doppler shift and $\omega_R = \frac{\hbar k^2}{2m}$ the recoil frequency. The second frequency shift is due to co-propagating transitions between $|m_F = 0\rangle$ to $|m_F = 0\rangle$ due to an imperfect polarization :

$$\Delta\omega^{Co} = \frac{\Omega_{co}^2}{\pm 4(\pm\omega_D + \omega_R)} \tag{3.24}$$

We measure experimentally the amplitude of the residual co-propagating transition for a Raman power and a pulse duration τ corresponding to $\Omega_R\tau = \pi$. The transition probability is $P^{Rb} = 0.098$ (resp. $P^K = 0.183$) and gives $\Omega_{Co}^{Rb} = 0.203\Omega_R^K$ which corresponds to a polarisation extinction ratio of 17dB, and $\Omega_{Co}^K = 0.281\Omega_R^K$ which corresponds to a polarization extinction ratio of 14dB. The different contributions of Two Photon Light Shifts are summarized in table 3.4.

Coriolis phase shift

The rotation of the Earth creates a Coriolis acceleration if the atoms don't perfectly fall perpendicularly to the reference mirror. The uncertainty of the Coriolis term comes from

Raman Transition	$+k_{Rb}$ $(10^{-6}m.s^{-2})$	$-k_{Rb}$ $(10^{-6}m.s^{-2})$	$+k_K$ $(10^{-6}m.s^{-2})$	$-k_K$ $(10^{-6}m.s^{-2})$
Counter-propagating	-6.52	-7.30	-6.10	-7.47
Co-propagating	-0.31	-0.31	-0.46	-0.61
Total	-6.83	-7.61	-6.56	-8.08

TABLE 3.4 – Light Shift due to each off resonance two photon transitions.

the uncertainty on the measurement of the transverse velocity of the atom clouds, which is measured with spatial imaging with an uncertainty of 10%. We measured an initial velocity of 1 mm.s^{-1} for Rb and 4 mm.s^{-1} for K.

Gravity gradient

The effect of the vertical gravity gradient Γ is calculated using [1] :

$$\Phi_{Grad} = \Gamma k_{eff} T^2 \left[\frac{7}{12} g T^2 + (v_0 + \frac{1}{2} v_R) T + z_0 \right] \tag{3.25}$$

The velocity v_0 is estimated to 0.16 m.s^{-1} for Rubidium and Potassium, the main contribution being the free fall of the atoms before the first pulse. This initial velocity can be evaluated with Raman spectroscopy with a precision of 1%. The last term of Eq 3.25 depends of the initial position of the two atom clouds. The overlap of two thermal clouds (temperature of a few μK) is very difficult to control and evaluate. We consider a very conservative uncertainty on the relative position between the two clouds of about the size of the atom cloud $\pm$0.5mm.

Total accuracy on the Eötvös parameter

A usual method for an atom gravimeter to find the fringe corresponding to the true value of g consists in varying the interrogation time T and scanning the frequency chirp α. The value of g corresponds to the value of alpha α_0 which cancels the phase shift for any T :

$$\delta\phi = (k_{eff} g - 2\pi\alpha) T^2 \tag{3.26}$$

To validate our estimation of the systematic errors, we measure the value of the central fringe α_0 while varying the interrogation time T and compare it to the evaluated phase calculated by the model including the main systematic errors (Quadratic Zeeman effect, one photon and two photon Light Shift, the parasitic lines). The results are shown on Fig. 3.12 for Rb and Fig. 3.11 for K.

For Potassium, the Quadratic Zeeman effect is very strong, and even if we evaluate very well the magnetic field with an accuracy of less than 1 mG, our measurement is very sensitive to the initial position and velocity of the atoms, which includes the recoil velocity, the initial velocity after the molasses and the velocity selected by the Raman pulse. Since we estimate the one photon and two photon light shifts better than the Quadratic Zeeman effect, our strategy is to use our measurement of the central fringe to calibrate the parameters used in our model of the Quadratic Zeeman effect. Considering our magnetic field profile, an error of $\pm 0.1 v_R$ gives an uncertainty of 80 mrad for an interrogation time 2T=40 ms. The strong difference between the $+k_j$ and $-k_j$ is not only due to the recoil velocity which has an opposite sign but also due to a different selected velocity class in each case. We emphasize that unlike usual consideration there is no rejection of the quadratic Zeeman effect with the alternative measurement with $+k_j$ and $-k_j$.

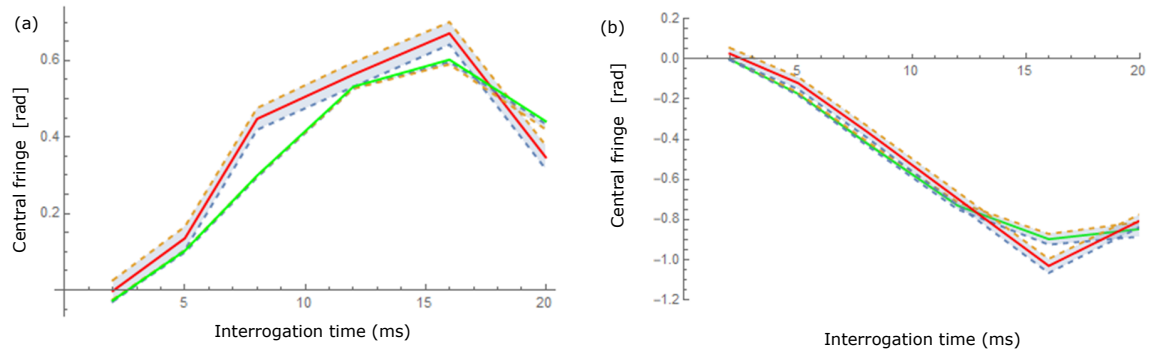

FIGURE 3.11 – Comparison of our model with the measurement of the central fringe for the Potassium interferometer. For each direction of the effective wave vector of the Raman beam ((a) $+k_j$ and (b) $-k_j$), estimated central fringe (green) based on the systematic errors study (Quadratic Zeeman effect, one photon and two photon light shift) and measured central fringe (red) versus the interrogation time. The margin for our model are defined by changing the initial velocity of the cloud by $\pm 0.1 v_R$. The uncertainty on the measured fringes comes from the residuals of the fit.

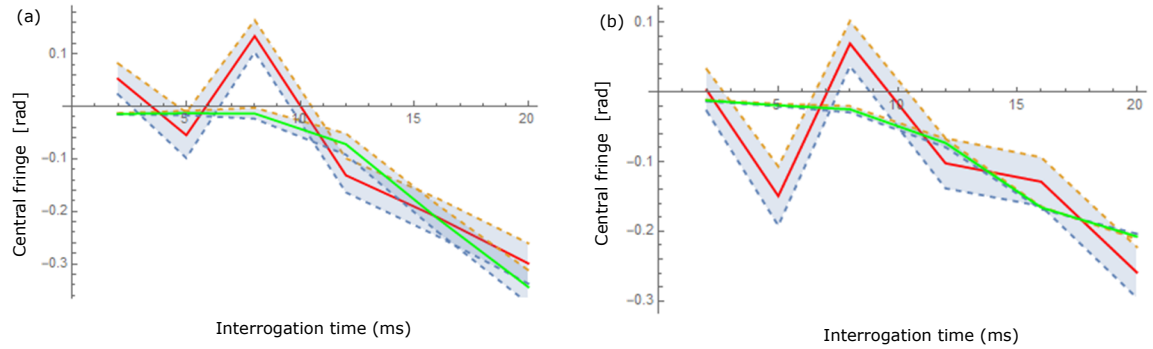

FIGURE 3.12 – Comparison of our model with the measurement of the central fringe for the Rubidium interferometer. For each direction of the effective wave vector of the Raman beam ((a) $+k_j$ and (b) $-k_j$), estimated central fringe (green) based on the systematic errors study (Parasitic Lines, Quadratic Zeeman effect, one photon and two photon light shift) and measured central fringe (red) versus the interrogation time. The margin for our model are defined by changing the initial velocity of the cloud by $\pm 0.1 v_R$. The uncertainty on the measured fringes comes from the residuals of the fit.

A similar study is done for Rubidium (Fig. 3.12). The main systematic error is the phase shift due to the parasitic lines, which also depends on the trajectory of the atoms.

Table 3.5 summarizes the different errors on the Eötvös parameter. The error budget is in agreement with the measurement of $\eta = -0.86 \cdot 10^{-6}$ within the error bars defined by the uncertainties $(1.07 - 0.86 \pm 0.57 \cdot 10^{-6})$.

3.3 Atom interferometry in microgravity

3.3.1 Double single diffraction and double diffraction

The classical configuration of a Raman atom interferometer is to send the two required frequencies in the same beam which is retroreflected by a reference mirror. This mirror is in practical essential to define physically a phase reference for the inertial effect we want to measure. Consequently, two Raman transitions are possible : k_1 incident and k_2 reflected, or k_2 incident and k_1 reflected, k_i being the wave vector for the i frequency. In the case of a gra-

Term in Eq 3.14	Systematic Error	$\eta_{sys}(10^{-6})$	$\delta\eta_{sys}(10^{-6})$
$\eta_{\Delta k} + \eta_b$	k ratio Uncertainty	0.00	0.001
$\eta_{\Delta k} + \eta_b$	k differential norm (angle between the beams)	0.015	0.001
η_{sys}	B gradient Force	0.15	$1.6 \cdot 10^{-3}$
η_{sys}	Quadratic Zeeman effect	2.28	0.46
η_{sys}	1 Photon LightShift	0.0	0.06
η_{sys}	2 Photon LightShift	0.01	0.04
η_{sys}	Parasitic Interferometer	-3.48	0.32
η_{sys}	Wavefront curvature	-0.009	0.002
η_{sys}	Wavefront aberration	0.0	0.09
η_{sys}	First order gravity gradient	$3.2 \cdot 10^{-5}$	$4 \cdot 10^{-5}$
η_{sys}	Coriolis Effect	-0.03	0.002
	Total	-1.07	0.57

TABLE 3.5 – List of systematic errors on the differential measurement (η_{sys}), and their uncertainties ($\delta\eta_{sys}$).

vimeter, the degeneracy of the two Raman transitions is broken thanks to the Doppler effect. Each Raman transition can be chosen by the sign of the frequency chirp which maintains the frequency matching condition during the fall of the atoms.

In microgravity, the Doppler effect is null and the two Raman transitions happens simultaneously. It is still possible to achieve a Mach Zehnder atom interferometer. According to the atom temperature and the Raman Rabi frequency, two regimes are possible : double single diffraction and double diffraction.

The principle of the double single diffraction (DSD) is to achieve a velocity selection with the Raman pulses to a non null value, "cutting" in the velocity distribution (see Fig 3.13). Two symmetric velocity classes $\pm v$ are selected and each velocity class achieves an independent atom interferometer with an area with opposite signs and a reverse wave vector k_{eff}. We assume we don't have spatial detection so that we detect the outputs of both atom interferometers simultaneously on a single photodiode. Since each atom participates to one of the two interferometers, we have to sum the probability transitions (and not the amplitude of the wave functions) corresponding to the outputs of each atom interferometer. The phase shift of the double single diffraction is then given by the following equation :

$$P = P_0 - 2A\cos\left(k_{eff}aT^2 + \delta\phi_{dep}\right)\cos(\delta\phi_{las} + \delta\phi_{ind}) \tag{3.27}$$

where a is the acceleration along the wave vector k_{eff}, A is related to the contrast of each independent interferometer, and $\delta\phi_{las}$ is the laser phase. The first remark is that we cannot scan the laser phase to determine the inertial measurement. Secondly, only the systematic errors which are k_{eff}-dependent $\delta\phi_{dep}$ contributes to the bias of the measurement. The k_{eff}-independent systematic errors $\delta\phi_{ind}$ contributes to the "contrast" term and need to be controlled to maintain the signal.

The double diffraction (DD) regime consists in achieving a four photon process involving atoms in the velocity class $v = 0$. This technique is similar to the simultaneous multi-axis interferometer presented in chapter 2. Here we achieve a single interferometer with a area twice larger than the single diffraction interferometer (Fig. 3.13). The phase shift becomes :

$$P = P_0 - A\cos\left(2k_{eff}aT^2 + \delta\phi_{dep}\right) \tag{3.28}$$

The main advantages of the double diffraction is the sensitivity which is doubled, and the

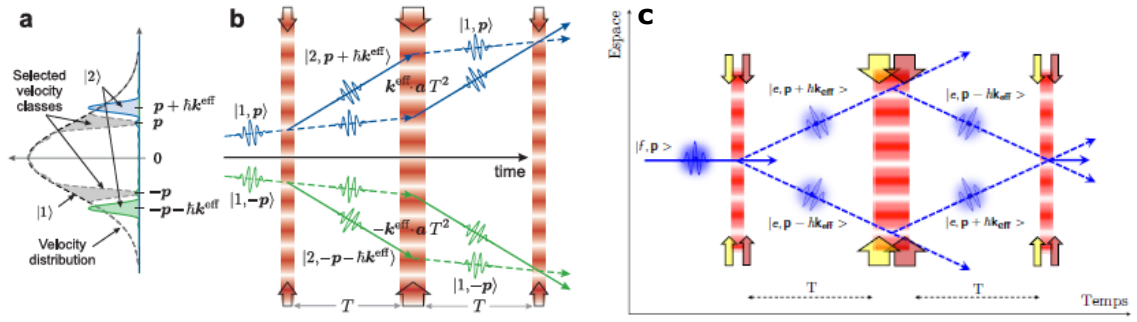

FIGURE 3.13 – Principles of the double single-diffraction interferometer. (a) Velocity distribution of the atoms in microgravity. The Raman frequency is tuned near the half-maximum– simultaneously selecting two symmetric velocity classes $\pm v = \pm p/M$. (b) Double single-diffraction interferometer trajectories. (c) Double Raman diffraction [10]

.

reduced systematic errors because of the symmetry of the interferometer [3]. The difficulty is the natural velocity selection of the double diffraction regime which reduces strongly the atom number participating to the atom interferometer. Using ultracold atoms can increase the efficiency of the double diffraction regime, the goal being to increase the atom number in this ultra cold atom source.

In both regimes DSD and DD, it is not possible to scan the laser phase which can be unpractical. To solve this issue, we can imagine a mechanical displacement of the mirror, if we are able to control the movement very accurately ($\lambda/100$ for a phase shift of 10 mrad) while maintaining the normal of the reference mirror. Another solution is to break the symmetry of the atom interferometer and thus creating a spatial separation of the wavepackets at the output of the interferometer in a well controlled way. For instance changing the norm of the effective wave vector k_{eff} can be precise since it is just an optical frequency to control. In the same way, we can modify the interrogation time T during the second part of the atom interferometer. We can also apply an accurate rotation of the reference mirror with a piezo-electric tip-tilt mount.

Finally, ONERA proposed a trick to avoid the double diffraction regime by creating an artificial Doppler shift. They apply a frequency chirp β on the Raman lasers [90]. As the reflected beams are delayed with respect to the incoming ones by $t_d = 2L/c$ (where L is the atom-mirror distance), the incoming laser frequencies will be shifted by $\delta\omega = 2\pi\beta t_d$ at the position of the atoms, allowing one transition to be detuned with respect to the other by $2\delta\omega$. This allows one to selectively address one of the Raman pairs only. This effect can be understood as mimicking an effective atomic velocity in the reference frame of the lasers, leading to an equivalent Doppler shift $\omega_D = 2\pi\beta t_d$.

3.3.2 Microgravity platforms

Several microgravity platforms exist worldwilde to test cold atom experiments in relevant conditions. These tests are used to prepare the future instruments which will be on board a satellite for future Space missions. Table 3.6 presents the most important platforms used in our community.

Our research group have access to two microgravity platforms which are complementary in terms of duration in weightlessness and repetition rate. The zero-g plane offers a long duration

3. The two wavepackets are always in the same state and consequently the sensitivity function is null

Platform	**Experiments**	**Free Fall duration**	**Repetition Rate**	**Microgravity level**
Zero-g simulator	ICE (WEP test Rb/K) [37]	0.5 s	1 parabola each 13 s	50 mg (Noise : 5 mg)
Zero-g plane	ICE (WEP test Rb/K) [88]	22 s	31 parabolas times three days for each campaign	50 mg
Bremen Drop Tower	QUANTUS (BEC Rb/K, Bragg interferometer) [91]	9 s (catapult)	two drop per day	1μg
Sounding Rocket	MAIUS (BEC Rb/K, Bragg interferometer) [92]	360 s	one flight per year	$< 10\mu$g
International Space Station	Cold Atom Laboratory (CAL, BEC Rb/K) [93]	Infinite	-	10-100 mg
HITec elevator (2020+) [94]	TBD	4 s	300 tests per day	10^{-6} g

TABLE 3.6 – Comparison of the microgravity platforms used to test cold atom experiments in weightlessness.

of microgravity but it is very difficult to accumulate data. On the contrary the 0g simulator has a small free fall duration but the high repetition rate allows us to accumulate data for statistics and increase our sensitivity. These two platforms are described in details later. In both cases, the strong advantage compared to the other platforms is the easy access, which allows to use standard experiments in terms of weight, power consumption, size and system control. The drawback is the high level of vibrations. On the contrary some platforms such as the Bremen drop tower and the sounding rocket have low vibration noise but requires more compact devices, and their access is very limited. An interesting trad-off is the future HITec elevator which will offer a high repetition rate and a long interrogation time. To be exhaustive, I mentioned here the International Space Station (ISS) and the NASA project Cold Atom Laboratory which constitutes not only a remarkable technology demonstration but it will also be able to achieve many cold atom experiments in microgravity (bubble shaped traps, ultra cold matter,...). Atom interferometry is also planned but the environment conditions (vibrations...) are not satisfying for metrology and constitutes only an intermediate step towards a scientific mission on board a satellite.

3.3.3 Parabolic flight campaigns on board the ZERO-G plane

On Earth, the force due to the ground naturally counterbalanced gravity, which gives the sensation of weight. In absence of any forces due to the ground (or air drag), the object is in free fall. To be in weightlessness on board the zero-g plane (Fig. 3.14 (a)), the pilot controls the plane to compensate the forces exerted on the plane except for gravity : the lift, the drag and the thrust. In practice, the compensation of these non gravitational forces is not perfect. This is what we call microgravity [4]. On board the zero-g plane, residual accelerations reach a peak to peak value 0.5 m.s^{-2} during a parabola. The vibrations noise spectrum is presented on Fig 3.14 (c). With the parameters of our atom interferometer ($\tau_\pi = 5\mu$s and

4. We emphasize that microgravity doesn't mean absence of gravity

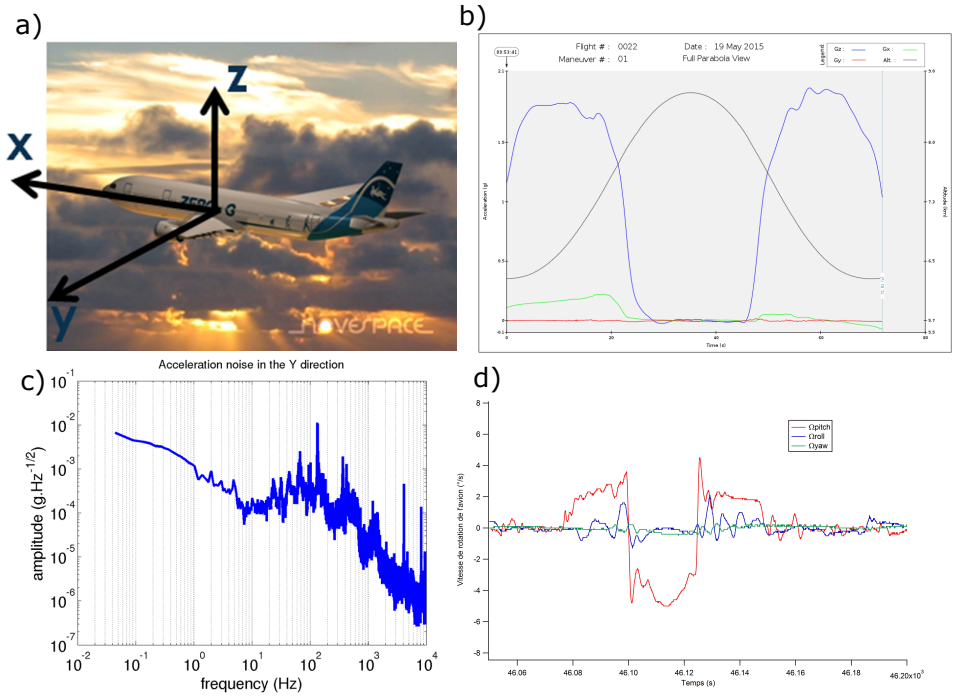

FIGURE 3.14 – a) Novespace Zero-g plane with the definition of the different axes X, Y, Z. b) Acceleration profile along the three axes X, Y, Z and the altitude of the plane during the trajectory (black). c) Noise spectrum of vibrations during the microgravity phase. d) Rotation rates during the trajectory of the plane.

$T = 1 - 100$ms) the frequency range in the bandwidth of interest is 10 Hz-100 kHz [5].

The plane is in steady flight at an altitude of 6500 m. The parabola (Fig 3.14 (b)) starts with an hypergravity phase (1.8 g) during which the tilt of the plane increase to reach an angle of about 45° in 20 seconds. When the plane reaches an altitude of 8000 m, it enters progressively in the microgravity phase while the pilots cancel the lift, the drag and the thrust. The microgravity phase lasts approximatively 20 seconds during which the plane trajectory is a parabola. The top of the trajectory is at the altitude of 9000 m. Once the plane is back at an altitude of 8000 m with an angle of -45°, the pilots turn the motors on and starts a second hypergravity phase during twenty seconds to be back in steady flight.

For this experiment, the technical solutions we implement need to be robust considering the demanding environment of the plane. The major difficulties are :

— Gravity change (1g-2g-0g-2g-1g) implies a strong mechanical robustness of the experiment. For instance using a honey comb for the laser bench is not suitable. That's why we focus our effort on fibered laser system.

— Vibrations and shocks coming from the motors, the transportation of the experiment in the plane.

— Temperature variations : The experiment stays in the plane during two weeks night and day. The temperature can go between -5° and 35°.

In 2015, we demonstrated the first double species atom interferometer in free fall. This result constitutes the first worlwide **WEP test using quantum particles in microgravity** [88].

On board the aircraft the dominant source of phase noise is caused by the vibrations of the reference mirror, which serves as the inertial phase reference for both ^{87}Rb and ^{39}K sensors.

5. The low frequency part (< 10 Hz) can be an issue to implement free floating solutions during a parabola. A free floating object will move "a lot" (more than one meter in one second) inside the plane.

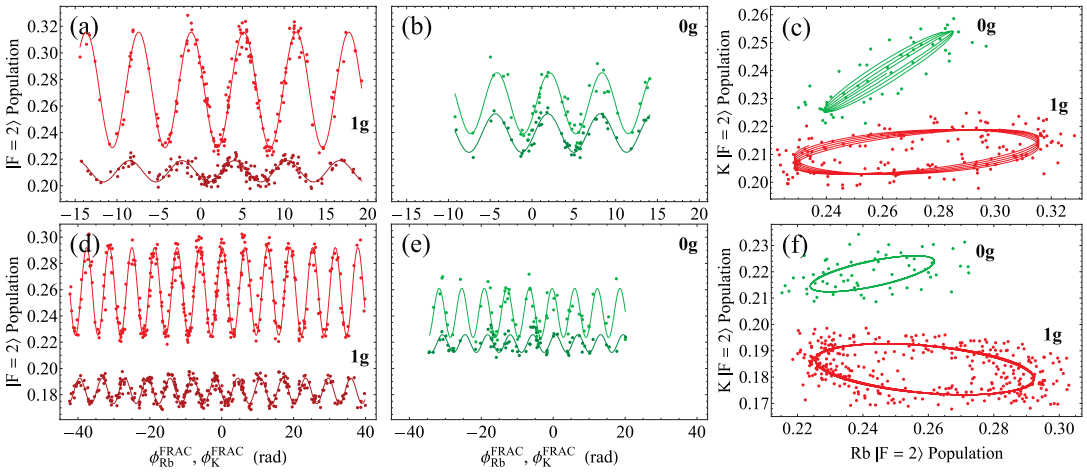

FIGURE 3.15 – Simultaneous K-Rb interferometer fringes during standard- and micro-gravity. The normalized population in the ground state $|F = 2>$ for each species is correlated with the vibration-induced phase ϕ^{vib} for an interrogation time $T \simeq 1$ (a-c) and $T \simeq 2$ (d-f). Fringes labeled 0g were recorded over three consecutive parabolas for plot (b), and five parabolas for plot (e), consisting of approximately 12 points per parabola. Fringes labeled 1g were recorded during periods of steady flight between parabolas, and consist of approximately 70 points per maneuver. In plots (a,b,d,e), solid lines indicate least-squares fits to sinusoidal functions, which yield a typical SNR of 7 for ^{87}Rb and 5 for ^{39}K data. Plots (c) and (f) show correlations between population measurements for each interferometer. The solid lines are parametric representations of the corresponding fit functions shown in (a,b,d,e).

Hence, the atomic signal caused by it's motion is indistinguishable from motion of the atoms. To make this distinction, we measured the mirror motion with a mechanical accelerometer from which we compute the vibration-induced phase ϕ_{vib} and correlate it with the normalized output population for each species. We refer to this process as the fringe reconstruction by accelerometer correlation (FRAC) method (see chapter 4). Furthermore, since the two pairs of Raman beams follow the same optical pathway and operate simultaneously, the vibration noise is common mode and can be highly suppressed from the differential phase between interference fringes.

Figure 3.15 displays interferometer fringes for both ^{87}Rb and ^{39}K, recorded during steady flight (1g) and in weightlessness (0g) during parabolic maneuvers, for interrogation times T = 1 and 2 ms. Correlation between the potassium and rubidium interferometers is clearly visible when the same data are presented in parametric form (Figs. 3.15 (c) and 3.15 (f)). We obtain general Lissajous figures when the acceleration sensitivity of the two species are not equal, as shown in Fig. 3.15(c). These shapes collapse into an ellipse (with an ellipticity determined by the differential phase) only when the interferometer scale factor ratio $\kappa \approx 1$ (Fig. 3.15 (f)).

3.3.4 ZERO-G Simulator

A 3 m high zero-g simulator is installed in our laboratory since 2018 and allow us to put the science chamber in weightlessness during 500 ms, and increase by one order of magnitude on the interrogation time (compared to standard gravity). We expect a gain of two orders of magnitude for the WEP test. The tests on this platform complete the parabolic flights campaigns. If the duration of microgravity is shorter, the high repetition rate is interesting for studies of accuracy and long term stability. Moreover the simulator is an ideal tool to prepare the experiment for the plane in relevant conditions.

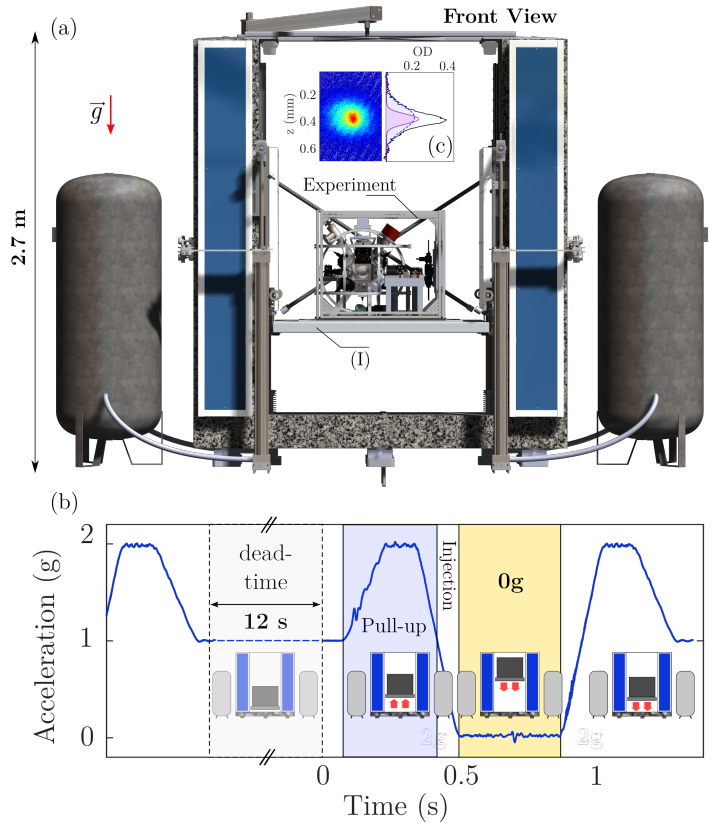

FIGURE 3.16 – (a) Schematic of the Einstein elevator. The payload (I), including the science chamber, cooling beam optics and imaging system, is driven vertically along two air-bearing translation stages. (b) Acceleration profile of the science chamber for sequential parabolas of 400 ms, separated by a dead time of 12 s required to let the motors cool down. (c) Absorption image of the BEC transition after a time-of-flight of 50 ms in 0g. The projection of the vertical axis shows the typical double structure of the cloud. The blue (violet) curve is a least-squares fit to the thermal distribution (condensed fraction).

The 0g-simulator (Fig. 3.16) has been designed by the French company Symétrie [6]. The principle of the 0g-simulator relies on mimicking the trajectory of an object in free fall (i.e. a parabola). A 250 kg experiment (450 kg including the whole moving part) is launched upwards to be in weightlessness for half a second during a perfect 1D parabola obtained by compensating air drag using linear motors. The trajectory is generated by measuring the position of the platform using a micrometric rule at each time-step and servo-lock electronics. The science chamber is fixed on a 120 × 120 cm-large plate. The platform moves vertically along the pair of granite columns thanks to two carriages. In order to allow an accurate guidance of the moving part and eliminate friction with the granite, four air bearings have been added the sides of each carriage. The air-cushion is created using a pressure/vacuum system which maintains the air bearings 10 μm far from the granite surface. Since the motors cannot generate the force needed to compensate for the weight of the moving part and to accelerate the mass upwards, a weight compensation system was implemented. The compensation is achieved through four air cylinders fuelled by two air tanks of 1000 L on the sides of the engine, which can deliver up to 2 bars of air pressure. The cycling rate of the simulator is limited by the required duration (12 s) to cool down the motors.

6. The company is specialized in hexapod systems and high-precision-positioning

Rubidium cold atom interferometer in microgravity

We demonstrate the potential of our apparatus by realizing an atom accelerometer which exhibits a state-of-the-art sensitivity in microgravity. The fringes of an atom accelerometer in the double single diffraction (DSD) regime are reconstructed by correlation with a classical accelerometer (Fig. 3.17 (a)). We show the contrast is maintained around 15% for longer interrogation times (Fig. 3.17 (b)). Despite the limited sensitivity of the classical accelerometer which prevents the fringe reconstruction, the histogram of the population ratio demonstrates the functioning of the atom accelerometer for an interrogation time $2T = 100$ ms which corresponds to an atomic sensitivity of $9.10^{-8}g$ per shot (Fig. 3.17 (c)). The temperature of the atoms is 4 μK. The cold atom source is prepared during the steady phase before the movement of the platform. At the beginning of the microgravity phase, we achieve a molasses phase and start the atom interferometer.

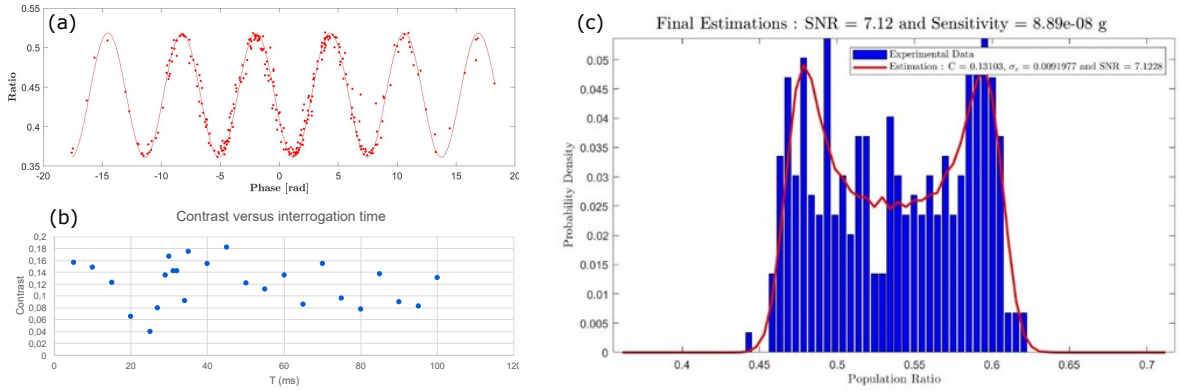

FIGURE 3.17 – (a) Fringes of a Mach-Zehnder atom interferometer achieved in microgravity on the zero-g simulator for an interrogation time 2T=20 ms.(b) Contrast of the atom fringes versus the interrogation time. (c) Histogram of the population ratio at the output of the interferometer for 2T=200 ms.

Bose Einstein Condensation in microgravity

Using the all optical method described in chapter 2, we report on the all-optical production of Bose-Einstein condensates in microgravity (see fig. 3.16(c)). Forced evaporative cooling in a 3-m high Einstein elevator results in 4×10^4 condensed atoms every 13.5 s, with a temperature as low as 35 nK. In this system, the atomic cloud can expand in weightlessness for up to 500 ms, paving the way for atom interferometry experiments with extended interrogation times and studies of ultra-cold matter physics at low energies on ground or in Space [37].

Ultra-low temperatures are ideal for atom interferometers with extended interrogation times in order to mitigate the influence of the beam imperfections that can result in contrast loss (e.g. due to intensity inhomogeneity) and systematic effects (e.g. wavefront aberrations). At the beginning of the 0g phase, the ODT power is decreased in 40 ms to decompress the trap. At this stage, our BEC contains 4×10^4 atoms for a spatial expansion corresponding to 35 nK. The ODT power is 10 mW ($\eta = 3.5$) for an average trap frequency of 39 Hz ($\omega_x = 2\pi \times 50$ Hz, $\omega_y = 2\pi \times 41$ Hz, $\omega_z = 2\pi \times 28$ Hz). The minimum trap frequency is currently limited by the optical power resulting from the maximum extinction ratio of the AOM. Simple solutions, including reducing the output power of the fiber laser and using the spatial modulation of the beams, will be investigated.

We recently get our first signal of double diffraction (DD) with ultracold atoms. Figure 3.18 (a) shows the absorption imaging during the atom interferometer. The central cloud on the second image is due to the absence of state preparation. These atoms are in the Zeeman states $|m_F = \pm 1\rangle$ which are not resonant with the double diffraction Raman transition of the first pulse. We compare the Rabi oscillations of the double diffraction regime in microgravity with the ones in single diffraction and standard gravity (see 3.18 (c)). For the same experimental parameters (laser power and frequency detuning), we measure the π pulse duration $\tau_{0g} = 25\mu$s in the DD case which corresponds to $\tau_{1g}/\sqrt{2}$.

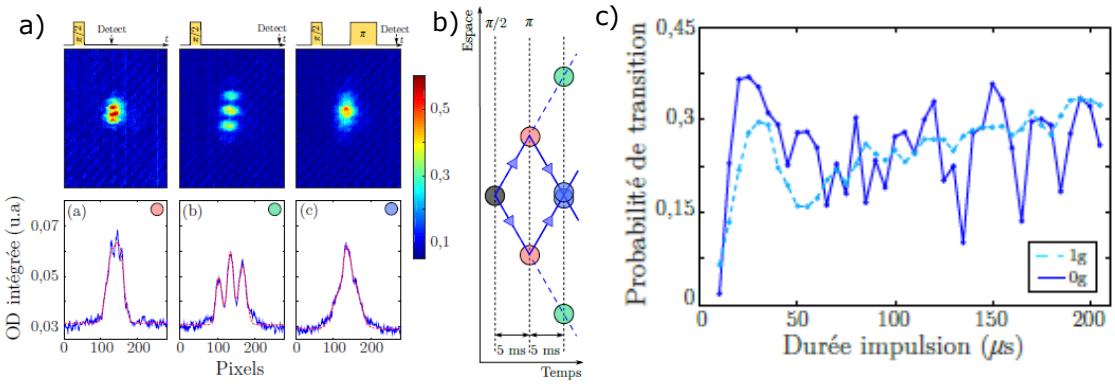

FIGURE 3.18 – Double diffraction interferometry. (a) Absorption imaging during the atom interferometer and profile of the optical density integrated along the horizontal direction for three cases : Time of flight of 5 ms after the first $\pi/2$ pulse ; Time of flight of 10 ms after the first $\pi/2$ pulse ; Time of flight of 5 ms after the π pulse. (b) Scheme of the double diffraction atom interferometer : the circles corresponds to the positions of the atom wavepackets during the sequence. (c) Rabi Oscillations in 1g for a temperature of 100 nK (dashed light blue) and in 0g for a temperature of 300 nK (dark blue). The π pulse duration is $\sqrt{2}$ shorter in the double diffraction case.

3.3.5 Expected sensitivity and accuracy with ultracold atoms in microgravity

Because of micro-gravity, the atom interferometer can operate in the double diffraction (DD) regime. Since Doppler effect is suppressed, the atoms are resonant with both $+k_j$ and $-k_j$ transition at the same time [10]. The first benefit is to double the sensitivity for a given interrogation time since the wave-packets are separated by twice the recoil momentum $\hbar k_j$. The second advantage is the rejection of some systematic errors, especially the output of the interferometer is insensitive to laser phase fluctuations. Nevertheless double diffraction requires long pulses with a velocity selection of the order of the recoil velocity. It implies a loss of atoms on an atom source at a temperature of a few μK since only the atoms in a well defined velocity class are diffracted. The recent implementation of a dipole trap and evaporative cooling allow us to produce the ultracold source which fits with the DD regime.

Expected sensitivity and long term stability

The expected sensitivity is calculated on the basis of the current performances of our apparatus producing an ultracold gas of 10^4 atoms at 30 nK. Vibrations on the plateform of the simulator during the trajectory can impact our measurement in terms of sensitivity. If

	Expected Performances	Remarks
Temperature Rb/K	30 nK	Rotation Ω=5 mrad.s^{-1}
Interrogation time T	100 ms	
Splitting	4$\hbar$k	Double diffraction
SNR	25	10^4 atoms, $C = 0.25$
One shot sensitivity	1.5×10^{-8}	set of fringe of 80 points
Sensitivity @ 2 days	1.3×10^{-9}	

TABLE 3.7 – Performances of an atom interferometer on the zero-g simulator with the current status of the experiment.

Term in Eq 3.14	Systematic errors	η_{sys}	$\delta\eta_{sys}$
	Unit	10^{-9}	10^{-9}
$\eta_{\Delta k}$	k ratio Uncertainty	0.0	2.6
$\eta_{\Delta k}$	k differential norm (angle between the beams)	15	1
η_{sys}	Quadratic Zeeman effect	0	0
η_{sys}	Magnetic gradient force	-1613	1.66
η_{sys}	1 Photon LightShift	0	0
η_{sys}	2 Photon LightShift	0	0
η_{sys}	Parasitic Interferometer	0	0
η_{sys}	Wavefront aberration	0	0.7
η_{sys}	First order gravity gradient	0	0.03
η_{sys}	Coriolis Force	-2.3	142
	Total	-1585	142

TABLE 3.8 – List of expected errors on the differential measurement ($\Delta\eta$), and their uncertainties ($\delta\eta$) on the 0g simulator. Here similar conditions as today are considered : relative angle of Rb and K beam (norm of the wave vector), laser frequency accuracy (ratio of the wave vectors), wavefront aberration of $\lambda/10$, no rotation compensation on rotation, magnetic field gradient.

we increase the sensitivity of the atom interferometer, the FRAC method will be limited by the noise of the classical accelerometer for an individual measurement. Fortunately, double species differential measurements allow to reach the limit of sensitivity of the atom sensors [95, 84].

The table 3.7 presents the expected parameters of the atom interferometer with the current status of the experiment. The interrogation time and the contrast is limited by the rotation rate of the platform. A one shot measurement corresponds to a set of 80 points for one fringe acquired in 1040 s (cycling time of 13.5s). We can do 166 fringes in two days to integrate the signal. We consider the experiment is stable and the signal is integrated as a white noise.

Error budget

The table 3.8 shows the expected error budget, with similar experimental conditions to we have today, except for the parasitic interferometers which will be soon suppressed using a double slave laser system. The four major limitations are Coriolis phase shifts, the magnetic field gradient, the accuracy of the laser frequencies and finally the wavefront aberration.

Coriolis is significant ($10^{-6}g$) because of the strong transverse velocity 1 mm.s^{-1} and the rotation rate 5 mrad.s^{-1} due to the platform movement. For the WEP test, the Coriolis term is the same for Rb and Potassium at first order so we can expect a rejection, that's why the value of η is smaller than the uncertainty. Uncertainty on the residual velocity is considered

to be at the level of 0.1 mm.s^{-1}.

If the quadratic Zeeman effect itself has no contribution to the phase shift, magnetic field gradient can still imply a force. The force created by the magnetic field gradient is significant in the double diffraction regime because the atoms stays in the same state during the interferometer. In case of a constant magnetic field (B,∇B), The phase shift is then :

$$\Phi_{\nabla B} = k\left(\frac{hK}{m}B\cdot\nabla B\right)T^2 \tag{3.29}$$

The uncertainty in Table 3.8 is calculated from the accuracy of the measurement of the magnetic field (see section 3.2.3).

The uncertainty on the norm of the respective wave vector k_{eff} due to the angle between the beams and the uncertainty on the ratio related to the laser frequencies corresponds to the current status of the experiment.

Wavefront aberrations are a usual major limitation in terms of uncertainty. The reduction of the temperature helps a lot. With a temperature of 30 nK for Rubidium and Potassium, aberration of $\lambda/10$ over a optics of diameter half inch gives an uncertainty of $0.7\cdot10^{-9}$ (Table 3.8). Here we don't take into account the curvature since the atoms don't fall in the beam. We consider this contribution is weaker than the phase shift due to wavefront aberration.

Light shifts

The first term of the two photon light shift due to contrapropagating transitions (see equation 3.23) is suppressed, since the two photon transition with opposite vector $-k_j$ is on resonance by definition (the dipole force is null on resonance [96]). The second term due to the transition $|e,p+\hbar k_{eff}\rangle \rightarrow |g,p+2\hbar k_{eff}\rangle$, with $\omega_D = 0$ becomes :

$$\Delta\omega_{0g}^{Contra} = \frac{\Omega_R^2}{16\omega_R} \tag{3.30}$$

The two photon light shift due to residual copropagating transitions becomes :

$$\Delta\omega_{0g}^{Co} = \frac{\Omega_{co}^2}{4\omega_R} \tag{3.31}$$

Note that these frequency shifts are a priori independent of the time of flight, if we suppose the Rabi pulsation is constant. Moreover, the sensitivity function to a phase shift as defined in the case of a single diffraction atom interferometer is null in the case of the DD regime. It implies there is no sensitivity to any frequency shift of the atomic levels. Consequently light shifts, as well as the quadratic zeeman effect, have no contribution to the interferometer phase shift.

Gravity gradient

Some terms in the gravity gradient phase shift canceled because of microgravity ($g_0 = 0$ in the frame of the experiment) and the double diffraction interferometer (the center of mass has no recoil). We get the following phase shift :

$$\Phi_{Grad} = \Gamma k_{eff} T^2 \left[v_0 T + z_0\right] \tag{3.32}$$

Finally this contribution depends only on the initial velocity v_0 and position x_0 of Rubidium and Potassium. In Table 3.8, we consider a conservative uncertainty of 1 mm.s^{-1} on

	Expected Performances	requirements
Temperature Rb/K	30 nK	Rotation compensation $\delta\Omega = 500\mu$rad.s^{-1}
Interrogation time T	250 ms	
Splitting	$4\hbar$k	Double diffraction
SNR	100	10^4 atoms, $C = 1$
One shot sensitivity	0.6×10^{-9}	set of fringe of 80 points
Sensitivity @ 2 days	0.5×10^{-10}	
Highest error contributions	B gradient ($\delta\eta = 0.9 \times 10^{-10}$) k_{eff} ratio ($\delta\eta = 1 \times 10^{-10}$) Wavefront ($\delta\eta = 0.7 \times 10^{-10}$) k_{eff} norm ($\delta\eta = 1 \times 10^{-10}$) Coriolis ($\delta\eta = 1 \times 10^{-10}$)	$dB/dz < 10^{-4}$ G.m^{-1} $\delta(f_{Rb} - f_K) < 50$ kHz $\lambda/100$ on a half inch optics $\theta_{Rb} - \theta_K < 15\mu$rad $\delta v_{Rb}^{\perp} - \delta v_K^{\perp} < 100\mu m.s^{-1}$ and rotation compensation of $\delta\Omega = 5\mu$rad.s^{-1}
Expected Accuracy ($\delta\eta$)	2×10^{-10}	

TABLE 3.9 – Roadmap towards a high accuracy WEP test with ultra cold atoms on the Zero-G simulator.

the velocity and an uncertainty of 0.1 mm on the position of each atom cloud.

Roadmap towards a WEP test at 10^{-10}

Table 3.9 presents the points to improve in order to reach a sensitivity and an accuracy of 10^{-10}. To increase the interrogation time, a compensation of the rotations is required to maintain the contrast. Considering the temperature of the atom cloud, a gain of one order of magnitude on the residual rotation rate is sufficient (500 μrad.s^{-1}). We consider a SNR= 100 for an interrogation time of $2T = 500$ ms in the double diffraction regime. We anticipate a sensitivity on η of $0.6 \cdot 10^{-9}$ for a set of 80 points for each atom interferometer. A long term sensitivity of $0.5 \cdot 10^{-10}$ is expected after 2 days of integration time for a cycling time of 13.5 s.

Table 3.9 summarizes the main experimental requirements and the expected performances. Improvement in accuracy first require to reduce drastically the residual rotation to a level of 5 μrad.s^{-1}. Then a compensation of the magnetic field gradient is required to a level below 10^{-4} G.m^{-1}. Improvement in accuracy will also require to work on the frequency lock of the lasers, the relative tilt between the two interrogation beams and the transverse velocity of the atoms. With a temperature of 30 nK for Rubidium and Potassium, aberration of $\lambda/100$ over a optics of diameter half inch gives an uncertainty of $0.7 \cdot 10^{-10}$.

3.3.6 Rubidium atomic clock in microgravity

Fig. 3.19 displays optical Ramsey fringes in microgravity measured as a function of the frequency difference between Raman lasers, centered on the clock transition ν_c of ^{87}Rb. 480 ms corresponds to the longest interrogation time for Ramsey spectroscopy in weightlessness ever achieved and is on the order of magnitude of the best atomic fountains. The Half-Width at Half-Maximum (HWHM) defined as $\Delta\nu = 1/2T$ is about 1 Hz. The ultimate short term sensitivity σ of the interferometer in weightlessness conditions is given by the following expression :

$$\sigma = \frac{1}{\pi}\frac{\Delta\nu}{\nu_c}\frac{1}{\mathrm{SNR}} \tag{3.33}$$

These data were acquired with a thermal cloud of 10^8 atoms at 4 μK. Due to the expanding size of the atomic cloud, the contrast drops when the interrogation time is increased since

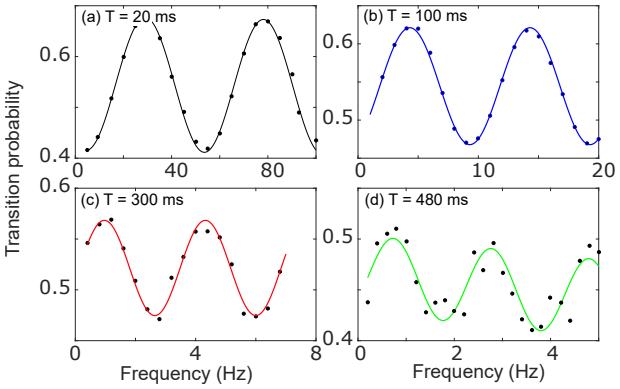

FIGURE 3.19 – Ramsey fringes obtained in microgravity for different interrogation time T.

the detection area is spatially finite (Fig. 3.20 (a)). As a consequence, the Signal to Noise Ratio (Fig. 3.20 (b)) also decreases which strongly limits the short term sensitivity of the measurement ($\sigma = 10^{-11}$ for $T = 480$ ms). The best sensitivity is reached for $T = 200$ ms which corresponds to a trade-off between the contrast loss and the resolution $\delta\nu$ (Fig. 3.20 (c)).

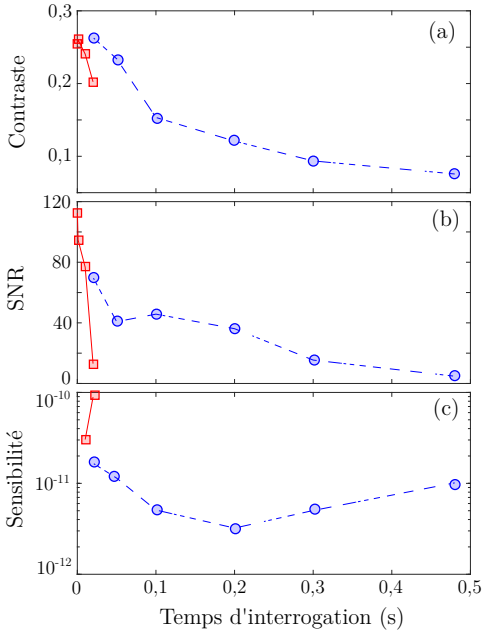

FIGURE 3.20 – Contrast (a), Signal to Noise Ratio (b) and short term sensitivity (c) of the Rb Ramsey fringes in microgravity (blue) versus the interrogation time.

3.3.7 Light-Pulse Potassium Atomic clock

Figure 3.21 displays optical Ramsey fringes measured as a function of the frequency difference between Raman lasers. Using $T = 40$ ms, we obtain a statistical uncertainty in the fractional frequency of $\Delta f/f = 4.1 \times 10^{-11}$ with a single fringe measurement–more than a 30-fold improvement over the previous best measurements at 1.3×10^{-9} [97]. Our measurement is sensitive to light shifts from the Raman beams. In addition, we apply a bias field of ≈ 100

mG in order to increase the efficiency of the state preparation scheme, but this too shifts the clock transition frequency due to the quadratic Zeeman effect. A preliminary study of the dominant systematic effects indicates our accuracy is limited at the level of a few 10^{-9} due to Zeeman shifts, AC Stark shifts, and the calibration of our frequency source. We estimate frequency shifts due to cold collisions to be less than 100 mHz at our densities of $\approx 5 \times 10^9$ atoms/cm^3.

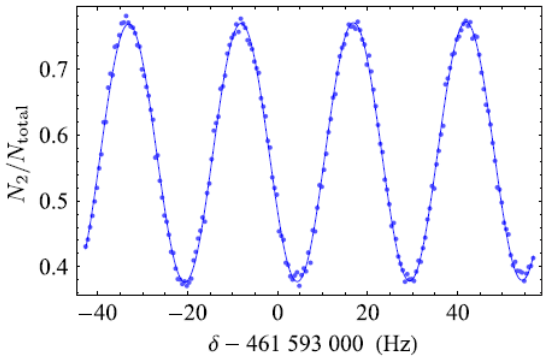

FIGURE 3.21 – Optical Ramsey fringes using $T_R = 40$ms and $\tau_R = 3\mu$s. The corresponding sinusoidal fit (solid line) gives a relative statistical error of $\delta f/f = 4.1 \times 10^{-11}$. Measurements were carried out near the peak of the Ramsey pattern where the SNR was largest. This peak is shifted by −126.8(2) kHz from the central fringe corresponding to the hyperfine frequency splitting at 461.719720 MHz [97] due to the AC Stark effect from the Raman beams. The corresponding shift of the central fringe is 11.2(1) Hz. Similarly, we estimate a shift due to the quadratic Zeeman effect of -114.3(4) Hz.

Based on the data obtained with Rubidium atoms in microgravity (Fig 3.20), we can reasonably expect a gain of one order of magnitude on the 0g simulator and reach $\delta f/f = 3 \times 10^{-12}$.

3.4 Large Scale Factor Interferometer using ultracold atoms

The guiding principle to push the performances of the CAI at best is the increase of the scale factor, which is proportional to the area of the atom interferometer. We present here a short review of the current experiments on this topic.

3.4.1 Increase of the interrogation time

The first solution is to increase the interrogation time T. Microgravity tackles the limitation related to the fall of the atoms. The second main limitation on T is the velocity dispersion of the atom cloud due to the temperature. The challenge of our community is to use ultracold atom source to improve the performances of the CAI. Up to now the state of the art atom interferometers are based on atom source cooled by laser ($> 1\mu$K), because the atom number and the SNR is higher for the current interrogation time ($T \approx 200$ms). Increase the atom number in the ultracold atom source is thus necessary. Phase diffusion due to the collisions can also limit the performances but can be mitigated by decompressing the trap to reduce the atom density.

At Syrte ultracold atoms with a temperature down to 50 nK are used to characterize the wavefront aberration of their apparatus and thus reduce the main uncertainty in the full error budget of their gravimeter down to 10^{-9}g [98]).

In Kasevich's group, the 10 m high fountain interferometer requires ultracold temperature to benefit from the large interrogation time. They demonstrate temperature as low as 50 pK using atom lensing [44]. At this stage one major challenge at long T is the control of the phase (vibrations, laser phase noise...) but differential measurements were achieved to measure the gravity gradient [99] or for a WEP test [65].

In Close's group they studied the question whether the coherence of the BEC improves the performances of the atom interferometer. They made a comparison of a interferometer using BEC versus thermal clouds with the same velocity dispersion [100]. They optimized the detection scheme for the readout phase on a Bragg interferometer [101]. They also achieved a ^{85}Rb/^{87}Rb BEC atom interferometer, including the study of the miscibility of the two sources and the phase shift on the atom interferometer due to the collisions with the other specie [102].

The group of Ernst Rasel demonstrated a Mach Zhender interferometer in microgravity using Bragg transitions and BECs of Rubidium. They image space fringes at the output of an open interferometer (similar to Young's slit) [103]. They also demonstrated a gravimeter on ground using the same technology of atom chips with a sensitivity of 3.7×10^{-6} g [104].

3.4.2 Large Momentum Transfer

The second solution to enlarge the area of the atom interferometer is to increase the spatial separation of the wave packets using Large Momentum Transfer (LMT). The reduced velocity dispersion of the ultracold atom sources increases the efficiency of LMT techniques which are highly selective in velocity. The double diffraction regime [10] mentioned above is the natural regime in microgravity and increase the sensitivity by a factor 2 compared to the standard two photon Raman interferometer. A similar technique can be achieved with Bragg transition [103, 105]. Bragg pulses can be generalized to multiphotonic transition to achieve LMT. Using multiple pulses of multi-photonic Bragg transitions [4], or using Bloch oscillations [106, 107, 108], it is possible to provide N times the two photon recoil, and then increase the sensitivity of the interferometer by a factor N :

$$\phi = N\hbar k a T^2 \tag{3.34}$$

Coherent splitting of the wave packets for $N > 400\hbar k$ has been demonstrated [109]. In Kasevich's group, large separation of the wavepackets above 50 cm was demonstrated using ultracold atoms and LMT [4].

3.5 Publications

— B. Battelier, et al., *Exploring the Foundations of the Universe with Space Tests of the Equivalence Principle* (2019) https ://arxiv.org/abs/1908.11785

— A. Trimeche, et al., *Concept study and preliminary design of a cold atom interferometer for space gravity gradiometry*, Classical and Quantum Gravity, 36, 21 (2019) https ://arxiv.org/abs/1903.09828

— G. Lefevre, et al., *Studies of general relativity with quantum sensors*, Proceedings of the 52nd Rencontres de Moriond on Gravitation (2017) https ://arxiv.org/abs/1705.10475

— B. Barrett, L. Antoni-Micollier, L. Chichet, B. Battelier, T. Lévèque, A. Landragin, P. Bouyer, *Dual Matter-Wave Inertial Sensors in Weightlessness*, Nature Communications, **7**, 13786 (2016)

— B. Barrett, L. Antoni-Micollier, L. Chichet, B. Battelier, P.-A. Gominet, A. Bertoldi, P. Bouyer, *Correlative methods for dual-species quantum tests of the weak equivalence principle*, New. J. Phys., **17**, 085010 (2015).
— B. Altshul, et al., *Quantum tests of the Einstein Equivalence Principle with the STE-QUEST space mission*, Advances in Space Research, **55**, 501-524 (2015)
— T. Schuldt, et. al, *Design of a dual species atom interferometer for space*, Experimental Astronomy, **39**, 167–206 (2015)
— G. Stern, B. Battelier, R. Geiger, G. Varoquaux, A. Villing, F ; Moron, O. Carraz, N. Zahzam, Y. Bidel, O. Chaibi, R. Pereira Dos Santos, A. Bresson, A. Landragin, P. Bouyer, *Light-pulse atom interferometry in microgravity*, Eur. Phys. J. D. **53**, 353-357 (2009)

Chapitre 4

Miniaturized cold atoms inertial sensors for onboard applications

An important part of my research activities is based on the innovative concepts and on the development of key technological components for compact and transportable cold atoms inertial sensors. During the first years, we focused on the development of a compact gravimeter, including a strong integration of the laser system. This activity led to the creation of the start-up muQuanS which develops commercial quantum gravimeters for different applications such as geophysical research, exploration of underground resources and civil engineering. Since 2016, we have been working on on-board devices dedicated to inertial navigation. Only a gyro-stabilized atom gravimeter has been demonstrated so far onboard a boat and a plane [110]. Our goal is to develop a new generation of strap-down inertial sensors. This implies to tackle strong issues of contrast loss and systematic errors due to the movement of the mobile as well as to improve the robustness of the system in the difficult environment conditions such as temperature variations and vibrations. Moreover it is necessary to push the integration further by going towards a complete miniaturization of the cold atom inertial sensor.

The problem of positioning and navigation is easily stated : how does one determine the trajectory of an object as a function of time ? Nowadays, the global positioning system (GPS) is the primary system used for many positioning and guidance applications. However, when a GPS signal is not available (for example, when the satellite does not have a direct line-of-sight with the receiver, or in specific environment where electromagnetic waves cannot propagate), the determination of the position becomes impossible. In this case, one relies on inertial navigation systems (INS) — autonomous "black boxes", consisting of a combination of gyroscopes and accelerometers, where changes in position and velocity are determined by integrating the output of these sensors.

Because the principle of inertial navigation is to integrate data from inertial sensors, their performances degrade with the duration of the mission and inertial system cannot generally be used on their own but need to be combined with other systems. Laboratory research that has been carried out over the past 20 years has demonstrated the tremendous potential of matter-wave interferometry for making ultra-sensitive measurement systems for inertial effects. The availability of ultra-sensitive inertial sensors based on matter-wave interferometry would drastically change the landscape of inertial navigation as it would allow to have almost error free inertial navigation systems.

The goal of the Joint Laboratory **iXAtom**- a collaboration between our group and the French company iXblue -is to develop cold atoms sensors dedicated to inertial navigation. We developed an absolute three axis hybridized quantum accelerometer which is about to

be tested in relevant environments. To reach this goal, several measurement campaigns are planned. In parallel we plan to miniaturize the atomic sensor by reducing the dimensions of the sensor head thanks to new concepts. In the future our projects will focus on atom gyroscopes which are today less mature, but their development has a strong interest for navigation since they constitute the limiting factor on the long term drift of the position measurement. The final goal is to produce all the components of a full quantum inertial navigation system (INS).

Last but not least, cold atoms technology is envisioned for future Space applications, for instance to measure gravity gradients and reconstruct the Earth gravitational potential. These Space instruments require compact ultracold atoms sources and face the same issues as Earth-based on-board applications such as the effect of the rotation of the satellite or the robustness of the apparatus in a demanding environment.

4.1 Integration and miniaturization of the laser system

One of the most important and complex parts of cold-atom-based systems is the laser source. Typically, these systems demand the control of the optical frequency with an accuracy of the order of 100 kHz, and a tuning range of 1GHz around the atomic transition. Fast tunability over this range in less than 1 ms is also desired to independently optimize the different phases of a measurement sequence (e.g. cooling, preparation, interrogation and detection).

4.1.1 Fibered laser using telecom components and frequency doubling

Since the begining of my activities on compacts atom sensors, we focused on laser systems based on telecom technology associated to frequency doubling [111]. The advantages of the telecom technology are numerous for the onboard applications considering there are Telcordia qualified : they are fibered and robust, reliable in terms of temperature fluctuations and vibrations and have a long lifetime. More specifically I developed fibered laser systems for the experiment on board the ZERO-G plane (ICE), a compact atom gravimeter (MINIATOM/μQuanS) and an atomic clock (Rubiclock). This work led to a technology transfer towards industrial partners, such as Quantel and μQuanS which supply now cold atoms laboratories with commercial robust fibered lasers.

4.1.2 Agile dual-frequency laser source with reduced parasitic sidebands for atom interferometry

The architecture of the laser system developed for MINIATOM includes several key ideas for robust solutions in general. It is based on phase modulation using electro-optical modulator [112, 113]. Our approach, which has evolved from similar techniques used in the microwave frequency domain, [114] consists of using a single diode laser locked on an atomic resonance, generating the desired optical frequencies by creating multiple sidebands with phase modulators, and then filtering out the undesired ones. Unlike most laser systems for cold-atom experiments, which are typically based on a master/slave architecture, our frequency agility is achieved by adjusting the microwave frequency signal sent to the optical phase modulators.

The laser source is a tunable distributed feedback (DFB) laser diode (40 mW, ITU channel 21, Emcore 1772 DWDM) which has a typical linewidth of 500 kHz [1], and with a frequency

1. The linewidth of the DFB diode can be a limitation on the phase noise of an atom interferometer [82].

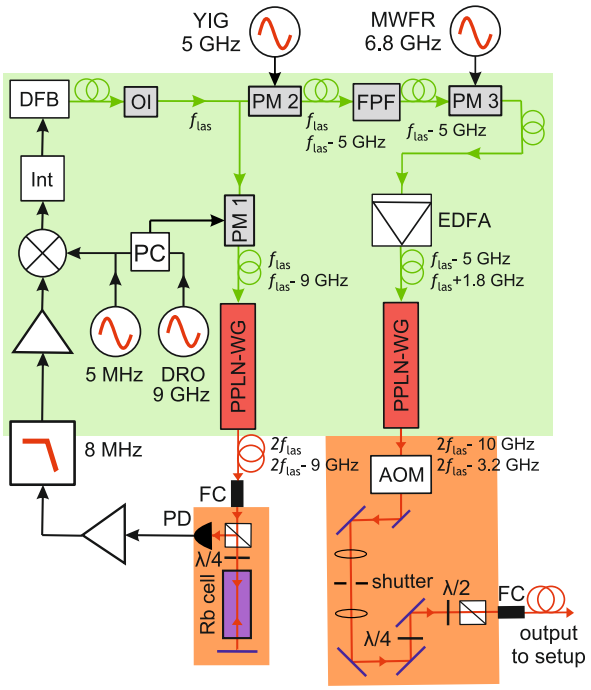

FIGURE 4.1 – Architecture of the laser source. We use telecom components (green area) to develop a compact fiber-based laser system. A small free-space optical bench (orange area) was implemented with 780 nm optical components to control the frequency of the laser (f_{las}) via saturated absorption spectroscopy, to control the power of the laser output via an AOM, and to filter the polarization. OI : optical isolator ; PM : phase modulator ; FPF : Fabry-Perot filter ; EDFA : erbium-doped fiber amplifier ; PPLN-WG : periodically-poled lithium-niobate waveguide ; MWFR : microwave frequency reference ; YIG : yttrium-iron garnet oscillator ; DRO : dielectric resonator oscillator ; AOM : acousto-optic modulator ; Int : integrator ; PC : power combiner ; FC : fiber coupler ; PD : photodiode.

controlled via temperature feedback over a range of 300 GHz. After an optical isolator, a small part of the optical power is diverted, frequency-doubled via SHG and then sent to a saturated absorption spectroscopy module. A dielectric resonator oscillator (DRO) generates a microwave signal of 9.18 GHz, which is amplified to 20 dBm, and sent to the phase modulator PM1 to shift the laser frequency at the input of the spectroscopy module [115]. We also apply a 5 MHz signal on the same phase modulator to generate sidebands on the input light. The measured absorption signal is later demodulated at the same frequency to obtain an error signal. The laser frequency after SHG, $2f_{\text{las}}$, is then servo-locked using the sideband at $2f_{\text{las}} - 9.18$ GHz, which is set on resonance with the crossover transition $F = 3 \rightarrow F' = 3(4)$ of ^{85}Rb—corresponding to a detuning of ~ 1 GHz to the blue of the $F = 2 \rightarrow F' = 3$ cycling transition of ^{87}Rb.

Phase modulator PM3 (10 GHz, 1550 nm, PHOTLINE MPZ-LN-10), located after the Fabry-Perot filter in Fig. 4.1, creates the repumping frequency that is used for cooling, detection, and as the second Raman frequency for the interferometer. To generate the modulation at 6.8 GHz, a compact microwave source was developed [116]. This beam is then amplified by an erbium-doped fiber amplifier (EDFA, 27 dBm, Manlight HWT-EDFA-PM-SC-HPC27) yielding 560 mW at 1560 nm. Frequency doubling from 1560 nm to 780 nm is accomplished via SHG in a periodically-poled lithium niobate waveguide (PPLN-WG), where the confine-

An alternative solution is the Telcordia-qualified external cavity diode from Redfern Integrated Optics, which exhibits a linewidth of < 10 kHz.

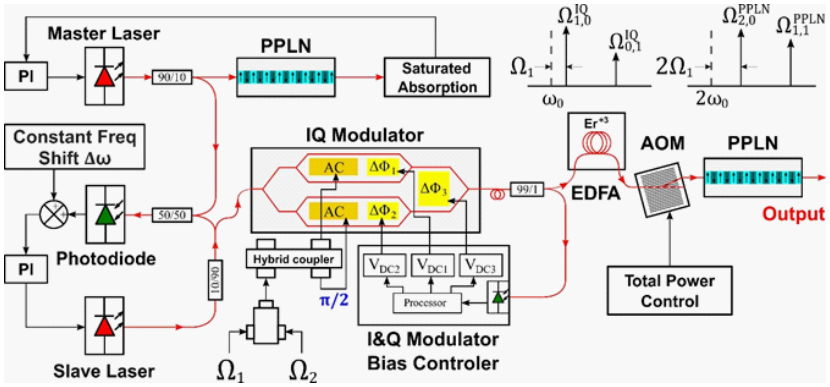

FIGURE 4.2 – Architecture of the laser source based on telecom components and frequency doubling, and including am IQ modulator developed by iXblue. To generate the two optical frequencies required for a complete sequence of atom interferometry, we suppress the carrier and generate two single sidebands (CS-DSSB).

ment of the optical mode leads to high intensities and thus high efficiencies [2]. We typically obtain 280 mW at the output of this module. Since fibered components at 780 nm are not fully reliable from the polarization point of view, to avoid a significant loss of power, we implemented a conservative free-space platform that contains an acousto-optic modulator (AOM) and a mechanical shutter to switch on and off the output light.

4.1.3 Laser source using an IQ modulator

Pushing further the technique of light modulation, a new step of integration has been reached with a new architecture (figure 4.2) including an electro-optical component combining phase and amplitude modulation (IQ modulator). The issue of the phase modulator is the generation of parasitic lines due to the different harmonic frequencies. Here the IQ modulator allows to suppress the carrier and generate a single sideband (CS-SSB). One originality of our architecture is to create two "single" sidebands (CS-DSSB) locking together in phase. The laser system has been tested successfully and allow to achieve an atomic interferometer with a reduced influence of the parasitic lines. We estimate the bias due to the residual lines to be below 100 ng (further investigation will be pushed further).

With an agility of 200 MHz/μs, this architecture can be employed for many applications like atom launching, chirp to compensate high accelerations, compensation of zero-velocity atom for interferometry [90].

4.1.4 Development of key components for miniaturized laser systems

At Institut d'Optique in Palaiseau I started an activity to develop key components dedicated to laser source for cold atoms. The idea is to be able to use these key components for a complete hybridization, on a **single chip**, of all the functions required for laser cooling and atom interferometry and then reach the ultimate level of compactness for on-board applications.

In this context, we led several studies in collaboration with μQuanS and CNES to develop a fast optical switch based on integrated optics and a frequency doubling stage integrating a cavity to increase the efficiency of the second harmonic generation.

2. This is a key element and we found reliable PPLN-WG components from the Japanese manufacturer NTT.

We also worked with the french company KLOE to develop a Photonic Integrated Circuit (PIC) playing the role of a beam splitter. It consists in a Multimode Interference waveguide (MMI). The principle is to design the waveguide with a good control of its dimensions, and to use the interference between the different modes such as Talbot effect to couple the light nodes in monomode output waveguides. The production of the component is based on laser photolithography and direct laser writing of an organic polymer. The process is compliant with the accuracy required for the MMI component. In the frame of this cooperation KLOE developed a 1x2 splitter but the advantage of the technology is that it can be easily generalized to 1xN, N being arbitrary without increase of the size and complexity of the component.

I also led studies of specific fiber optics dedicated to our applications. Polarization maintaining fibers are sensitive to curves and temperature fluctuations, especially if the input polarization is not perfectly aligned with the slow axis. IXFiber (iXBlue Photonics) developed new polarizing fibers which have more stable properties in terms of polarization and allows to simplify the optical system (no cube and waveplate are required anymore), and increase the quality of the polarization (PER above 40 dB can be reached easily). The principle of the polarizing fiber is to guide a single linear polarization along a proper axis of the birefringent fiber. Polarization fluctuations are not propagated and implies only small fluctuations of the optical power. During the tests, the measured PER was 39 dB. The drawback of this technology is that any curvature of the fiber shifts the range of wavelength acceptance. This problem was solved thanks to a new design of the optical fiber and a robust packaging avoiding strong curvatures. Following this study, I coordinated the COFIPOL project (ANR/DGA Astrid Maturation) which aimed to develop fibered optical components using polarizing fibers. Our consortium supplied micro-optics beamsplitters with high performances in terms of power losses and polarization stability.

4.1.5 Miniaturization of the laser source

During the past years, strong efforts have been done to integrate robust and compact systems. At this stage, some integration improvements are still to be done but require only engineering development and no strong gap in compactness is expected. The next technology breakthrough in terms of miniaturization will require to hybridize the laser functionalities to minimize the number of components.

Hybridization of an optical amplifier and a beamsplitter

I led a collaboration with III-V Lab and KLOE to hybridize and integrate on a single substrate a Semiconductor Optical Amplifier (SOA) and an integrated beamsplitter (MMI). The main idea is to "mode-match" the large spatial mode at the output of the tapered amplifier and the input of the MMI which is already a large (multi-mode) waveguide by design.

The work focused on the definition of the geometrical parameters of the atom chip including the MMI and the SOA, in order to achieve the integration of the two functionalities on the same platform and optimize the optical interfaces. Optical simulations were done to improve the injection of the optical power in the output waveguides of the MMI. Optical tapers were inserted for this purpose. 780 nm 1x2 MMI components were achieved with a good equilibrium between the two outputs and insertion losses of 6.5 dB.

III-V Lab developed a series of SOA combing an optical output of 500 mW and a good quality of the spatial mode of the output beam. Three types of structures of tapered amplifiers were achieved and characterized. The amplifiers were first tested without input power in a

superluminescent mode (power-current characteristic, optical spectrum, beam spatial mode profile), and then with input power in a amplification mode.

We confronted several technical issues during the integration of the two components. More specifically, the chips from KLOE and III V Lab were not compliant together. Nevertheless no fundamental impossibility were demonstrated during this study and this solution stays promising for future ultra-compact laser sources in full integrated optics.

We propose in the two following subsections two architectures of a full integrated laser system for cold atoms, following two different strategies with different materials.

SiO_2 Telecom laser source

We propose an architecture based on telecom components and frequency doubling, where Photonic Integrated Circuits (PIC) replace the fibers. The main material for this laser source is glass (SiO_2) which has interesting properties :

1. High transparency (VIS to NIR)
2. Low index material (1.5)
3. No electro-optic or non-linear properties
4. No limitation in wafer size dimension

For instance Teem photonics developed ion exchanged protocols to produce very well controlled waveguides in glass. The technology is simple, scalable and flexible and offer some advantages compared to fibers :

1. Graded-index profile waveguides
2. High fiber coupling efficiency
3. Polarization maintaining
4. Low birefringence

Moreover, active components based on Erbium Doped waveguides was developed 20 years ago. Laser sources [117] and Amplifiers are available and have the strong advantage of a perfect mode-matching with the waveguide circuit. A DFB laser with a linewidth of a few 10 kHz has been demonstrated. A Erbium Doped Waveguide Amplifier (EDWA) from Teem Photonics delivers a maximum power around 160 mW for a pump power of 600 mW.

The architecture is presented on Fig. 4.3. The light emitted by the DFB laser seeder is splitted into two. The first path is used to stabilize the laser frequency with a servo-lock on a frequency comb produced by a ring micro-resonator. This solution is for instance envisioned for compact atomic clocks [118]. The second part of the seeder light is going through a IQ modulator which allows to generate the two frequencies required for cooling and atom interferometry. The signal is then amplified by an EDWA and then frequency doubled in a PPLN waveguide. Pump light (for instance at 980 nm) is needed to pump all the active components of the system (DFB, Comb micro-resonator, EDWA).

GaAs 780 nm laser source

We propose a new architecture based on Gallium arsenide (GaAs) constituted of one single diode and a 780 nm IQ modulator amplified by a tapered Amplifier (TA) (see Fig. 4.4). The interest is that all these components can be done of the same material.

GaAs is environmentally stable, radiation-hard and lacking undesired pyroelectric effects. Originally developed for Aerospace and Defense applications, these useful properties make

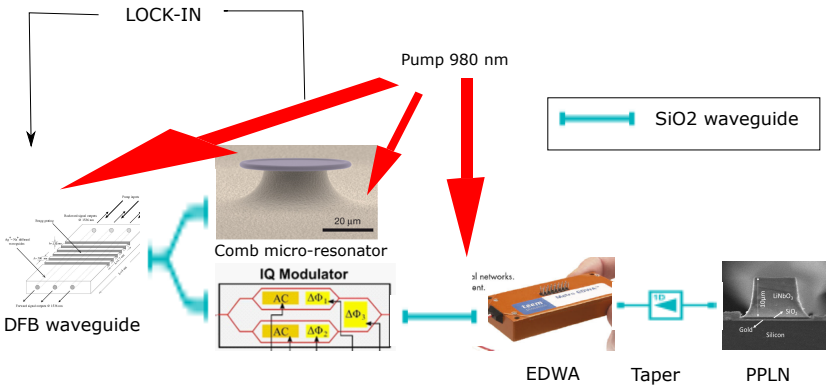

FIGURE 4.3 – Architecture of a miniaturized laser source based on telecom components and frequency doubling, integrated on a chip using SiO_2 PIC. The DFB laser is frequency lock using the reference coming from the comb generated by the ring micro-resonator. The IQ modulator developed by iXblue will generate all the required frequencies. The Erbium Doped Waveguide Amplifier will amplify the signal which is then frequency doubled in the PPLN waveguide. A common signal at 980 nm is used for the DFB, EDWA and the micro-resonator.

GaAs high-speed modulator technology desirable for all system applications. Essentially field-operated, low-current devices they do not require temperature control and are stable, robust and long-lived.

GaAs has remained the material of choice for mm-wave electronic devices and integrated circuits for several decades. It has many desirable properties for RF devices which must survive and operate in harsh environments :

1. Semi-insulating (SI) GaAs substrates are low-cost and have high-resistivity so they can provide low-loss coplanar transmission-lines.
2. The electron mobility is high - six times higher than in silicon and almost 60% higher than InP. This enables low optical loss and high RF bandwidth in opto-electronic and electronic devices.
3. The related ternary $Al_xGa_{1-x}As$ is closely lattice-matched to GaAs throughout the range of aluminium fraction x. Increasing x further increases the band-gap and reduces the refractive-index. This enables considerable freedom in designing AlGaAs/GaAs hetero-structures for the confinement of electrons (in quantum wells) and photons (in optical waveguides).

$Al_xGa_{1-x}As$ has similar properties to GaAs up to $x \approx 0.4$ where the fundamental energy gap becomes indirect, higher aluminum fractions than this are rarely used. In addition to the basic properties listed above, the AlGaAs material system is a direct-gap semiconductor which can be used as a light emitter (LED or Laser) for wavelengths shorter than the fundamental band-edge ($\approx$ 870nm).

As a non-elemental III-V compound, the crystal is non-centrosymmetric. This provides a linear electro-optic (LEO) effect, which is a small change in refractive-index in response to an applied electric field. Electro-optic Modulators exist commercially for telecom wavelength (Axenic UK). GaAs phase modulator are developed in Humboldt-Universität zu Berlin (HUB) [119]. The IQ modulator at 780 nm currently under development with iXblue is made of Lithium niobate and need to be adapted in GaAs.

Today, this approach has been chosen by HUB [120] for the experiments in microgravity on the sounding rocket. The integration is done in micro-optics. A master-oscillator-power-amplifier (MOPA) concept is chosen to combine the spectrum quality and the relatively high

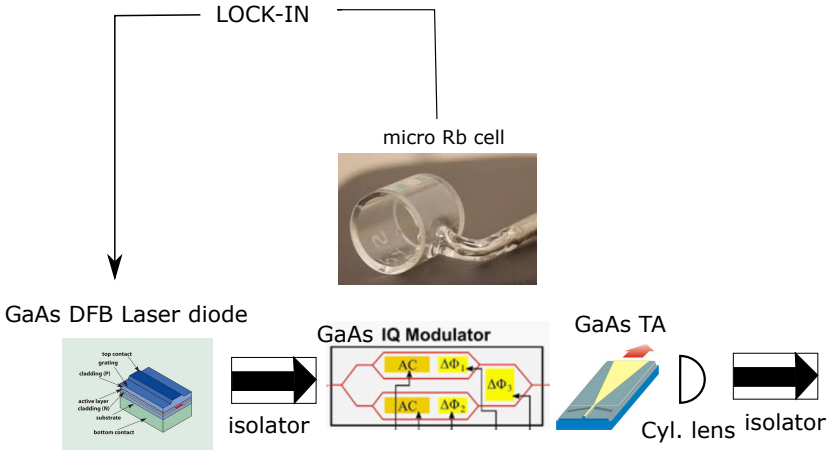

FIGURE 4.4 – Architecture of a miniaturized laser source based on GaAs. The DFB laser is frequency locked using the reference signal coming from a micro Rb cell. The IQ modulator developed by iXblue can be implemented on a GaAs chip. A Tapered Amplifier (TA) will amplify the signal. Optical isolators are necessary to avoid feedbacks. Micro-optics are used to shape the beams.

power required for our applications. The difficulties for this source is the requirement of an optical isolator and the poor quality of the beam profile which requires beam engineering with optics (cylindrical lens) and implies loss of coupling in a fiber.

4.2 Compact cold atom gravimeter

The use of atom interferometers to measure gravity was demontrated in laboratories at the beginning of the 90's [121]. Nowadays, they are at the state of the art in terms of accuracy (10^{-9}g), with a outstanding long term stability (a few 10^{-10} g) [122]. These performances make them good candidates for a technology breakthrough in all fields related to gravity measurements (underground exploration, geophysics, inertial navigation). Ten years ago, these high-level measurements were achieved by complex and bulky experiments, and it was hardly conceivable to transport these devices outside the research laboratories. In this context I have started an activity of technological transfer to make up for the gap between proof-of-principle experiments and an industrial product.

The MINIATOM project aimed to achieve a compact gravimeter based on cold atoms technology (figure 4.5). The main simplification of the sensor head comes from an architecture allowing to use a single laser beam to achieve a complete atom interferometer (instead of 6 independant beams of the usual experiment), using a pyramidal reflector [123]. This concept were put into practice in order to build a sensor with a volume as small as 0.1 m^3. The second simplification focuses on the laser source based on telecom technology and frequency doubling (paragraph 4.1). Each key subsystem of the prototype was validated separately in order to get a full mobile instrument for field measurements. The dimensions of the sensor head are fixed by the size of the pyramidal reflector (2 cm) and the duration of the interferometer (2T = 100 ms). The science chamber includes all the required functions to manipulate and detect the atoms : various optical accesses, coils to control of the magnetic field, laser beam shaping, and polarization control (LC retarder).

Following the MINIATOM project, a start-up company, μQuanS, was founded in April 2011 to develop and commercialize cold atom gravimeters. This new generation of measuring tools will find its applications in inertial navigation, geophysics, or metrology more generally

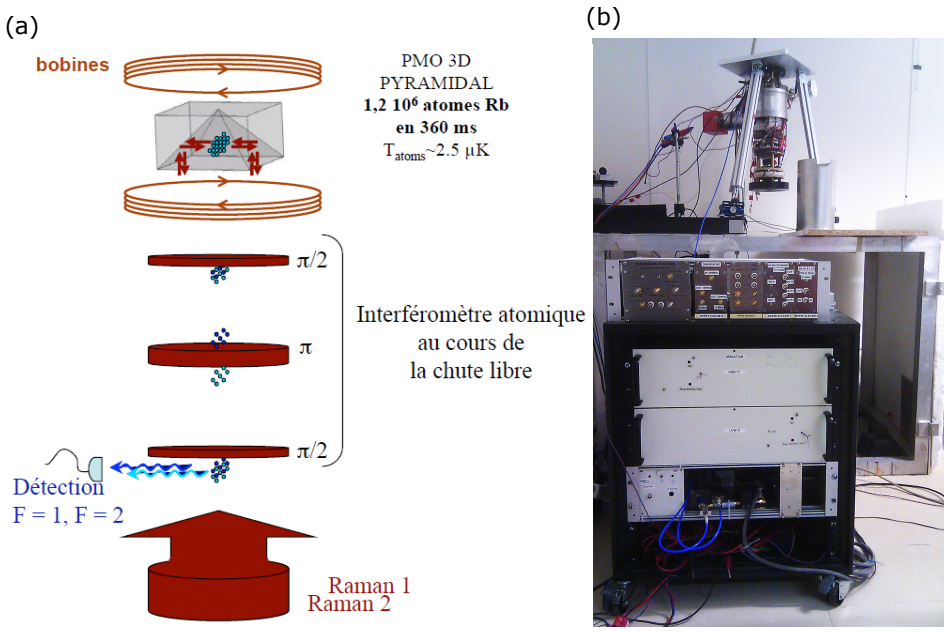

FIGURE 4.5 – (a) The use of the pyramidal reflector allows to achieve an atom interferometer with a single laser beam. (b) Picture of the prototype of a compact cold atom gravimeter (MINIATOM). Up in the back : the sensor head and the magnetic shield. In the front : The laser source based on telecom components and frequency doubling.

(www.muquans.com).

4.3 Operation of an on-board atom interferometer

Operating a very sensitive atom interferometer in an environment with a high level of vibrations such as a plane is a mandatory challenge for our tests during the parabolic flights and inertial navigation. If the mirror moves more than half the optical wavelength $\lambda/2$, the phase shift of the atom interferometer is larger than π. In these conditions, even when the atom interferometer is operational, the rough atomic signal looks like a random distribution of points and the fringes are blurred.

To tackle the problem of vibrations, we developed an hybridization method with a classical accelerometer fixed on the reference mirror and which allows to measure the vibrations of this mirror during the measurement. Using these signals, we finalize a method to reconstruct the atomic fringes (FRAC) based on the correlation between the atom signal and the signal of the classical accelerometer a_{AM}. We can calculate the expected phase shift thanks to the response function of the atom interferometer $f(t)$:

$$\phi^{vib} = k_{\text{eff}} \int_{t_i}^{t_i+2T} f(t-t_i) a_{AM}(t) dt \tag{4.1}$$

By plotting the output of the interferometer (population ratio of the internal states in our case) versus the expected phase shift, the interference fringes are reconstructed (figure 4.6).

As a pioneer experiment of an onboard atom interferometer, we confronted experimentally for the first time to the loss of contrast due to two effects. First, the vibrations not only scan the atomic phase, but also can make the laser frequency out of resonance of the Raman transition randomly because of the Doppler effect. The second issue is the non overlap of

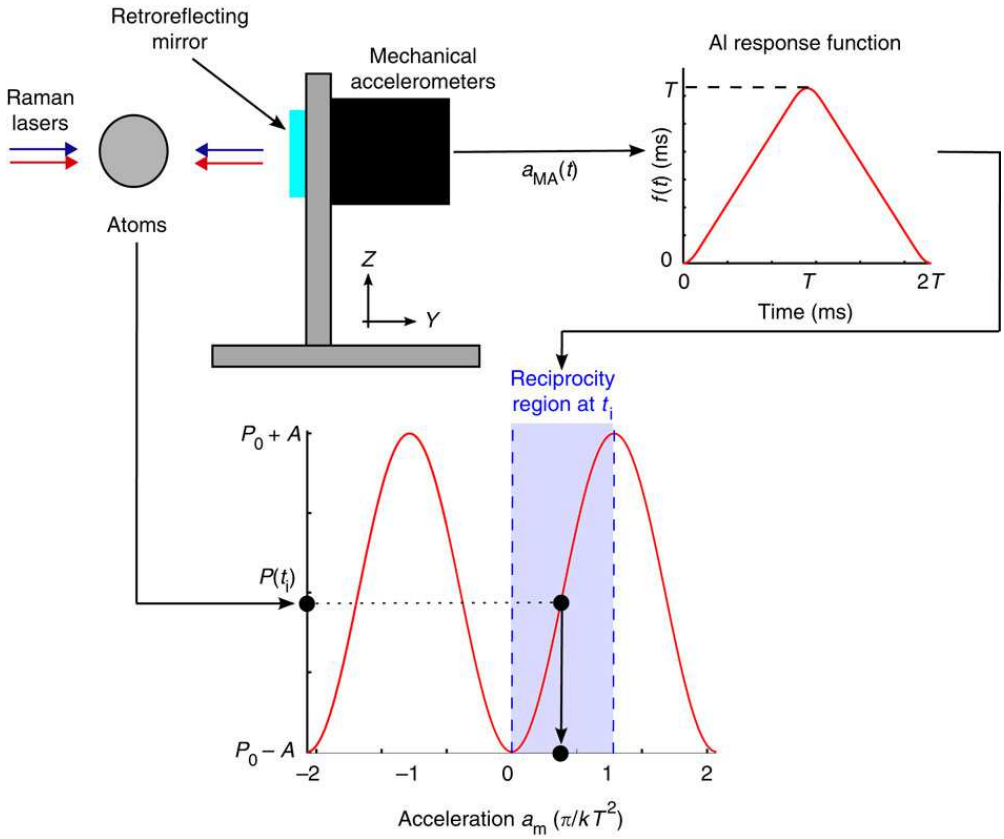

FIGURE 4.6 – The signal of the mechanical accelerometer is filtered by the response function $f(t)$ of the CAA [85, 84], and gives the reciprocity region where the interferometer operates at the measurement time $t_i = iT_{\text{cyc}}$, where T_{cyc} is the cycle time of the experiment. In this example, the reciprocity region corresponds to the $0 - \pi/k_{\text{eff}}T^2$ interval. The value provided by the CAA, $P(t_i)$, is then used to refine the acceleration measurement within the reciprocity region. The acceleration is obtained by inverting the response $P(t_i)$ within this region (red curve).

the wavepackets at the output of the atom interferometer when the interrogation time T is increased. The contrast is lost if the separation of the wave packets is larger than the coherence length (ie the De Broglie wavelength). Our model is compliant with the experimental results onboard the ZERO-G plane [88]. These aspects are specifically studied below.

4.3.1 Measurement of the vibrations of the ZERO-G plane

The measurement of the vibrations of the plane achieved by our team in 2010 within the ICE project can be considered as the preliminary and pioneer experiment paving the way towards inertial navigation with cold atoms [124, 85]. Most other atom interferometer experiments are designed to measure the acceleration along the vertical axis, such as gravimeters where the goal is to make precise measurements of g for various applications. In these cases, mirror vibrations are highly damped by passive or active isolation stages. On the contrary, for inertial navigation, the small accelerations caused by vibrations can be an important part of the signal needed to determine the position of an object, and therefore should not be rejected. They also constitute a strongly varying signal, and make it challenging for CAAs to operate in a precise manner. Additional difficulties arise in the specific regime of low velocity and low acceleration, for which the usual techniques used in atomic gravimeters cannot be applied (the counter-propagating transition frequencies are degenerate for both $\pm\mathbf{k}_{\text{eff}}$ directions).

During parabolic flight campaigns in 2010, we measured the horizontal acceleration of the aircraft with a mobile CAA utilizing a laser-cooled sources of ^{87}Rb atoms [85]. Our best performance in this configuration was obtained with an interrogation time of $T = 3$ ms, a signal-to-noise ratio of $SNR = 3.1$ and a cycling time of $T_{cyc} = 500$ ms, which gives a one-shot sensitivity of $\delta a = \frac{1}{SNRk_{eff}T^2} = 2.3 \times 10^{-4}$g. To achieve this, we recorded the acceleration of the reference mirror using a mechanical accelerometer, and convolved it with the response function of the CAA to obtain an estimate of the inertial phase, $\Delta\Phi$. The accuracy of this estimate was sufficient to locate the half-fringe number. Then we inverted the output of the CAA, $P(t_i)$, within this half fringe to obtain a more precise value of the acceleration, as shown in Fig. 4.6. Using the same principle as a Vernier scale, we summed the coarse output of the mechanical accelerometer with the precise value estimated from the CAA. This process is illustrated in Fig. 4.7. In this way, we were able to measure the horizontal acceleration of the plane during a full flight, with alternating $1g$ and $0g$ maneuvers, as shown in Fig. 4.7(d). The discontinuity in the measurement is due to the $2g$ phase on either side of the $0g$ phases, where the CAA is not designed to operate. More details can be found in [85].

In principle, this technique can be extended to higher precision with larger T until the point where the resolution of the mechanical accelerometer limits the determination of the interferometer half-fringe number. This limit occurs when the phase shift induced by the self-noise of mechanical accelerometer, S_{self} given in $g/\sqrt{\text{Hz}}$, reaches $\sim \pi/2$. A more precise calculation based on the frequency response of the interferometer [84] yields $\phi_{\text{self}} = \frac{1}{\sqrt{3}} k_{\text{eff}} S_{\text{self}} T^{3/2} < \pi/2$. State-of-the-art mechanical accelerometers exhibit self-noise levels of $S_{\text{self}} < 10^{-7}\, g/\sqrt{\text{Hz}}$, meaning T could potentially be extended beyond 300 ms before reaching this limit. However, onboard the aircraft we found that the interrogation time was limited by a loss of contrast due to vibrations. This is caused by the random accelerations of the reference mirror which induce a significant shift in the laser frequency seen by the atoms δ_{vib} due to the Doppler effect :

$$\delta_{\text{vib}}(t) = \mathbf{k}_{\text{eff}} \cdot \int_{t_i}^{t} \mathbf{a}_{\text{vib}}(t')dt'. \tag{4.2}$$

Obviously, this time-dependent shift depends on the nature of the vibration spectrum and the particular time interval chosen. We characterize this effect by the maximum shift over the interval $\{t_i, t_i + 2T\}$, given by $\delta_{\text{vib}}^{\max} = 2k_{\text{eff}} a_{\text{vib}}^{\max} T$, where $a_{\text{vib}}^{\max} \simeq 0.5$ m/s^2 is the maximum vibration amplitude measured on the Zero-G plane. Thus, at $T = 10$ ms we find $\delta_{\text{vib}}^{\max} \simeq 160$ kHz, which is large when compared with the Rabi frequency $\Omega_{\text{eff}} \simeq 25$ kHz, which determines the "bandwidth" of the Raman pulse. If the laser is off-resonant during one of the Raman pulses, the atoms are not efficiently excited and consequently the interferometer contrast decreases. We studied and solved the problem elsewhere (see paragraph 4.3.3).

4.3.2 Hybridization of quantum and classical sensors

Our goal is to go towards a complete hybridization of classical sensors (accelerometer, gyroscopes) and atom interferometers. In this context, we aim to do develop a new type of inertial sensor hybridizing a matter wave interferometer and a inertial navigation system (INS) using fiber optical gyroscopes (FOG) and quartz accelerometers. More precisely, our goal is to achieve an INS where each axis of the classical accelerometer is replaced by an hybrid axis combining quantum and classical measurements. For this purpose our study focuses on the measurement continuity and the increase of the dynamic range which are the main limitation of a CAA but essential for inertial navigation. More generally the apparatus

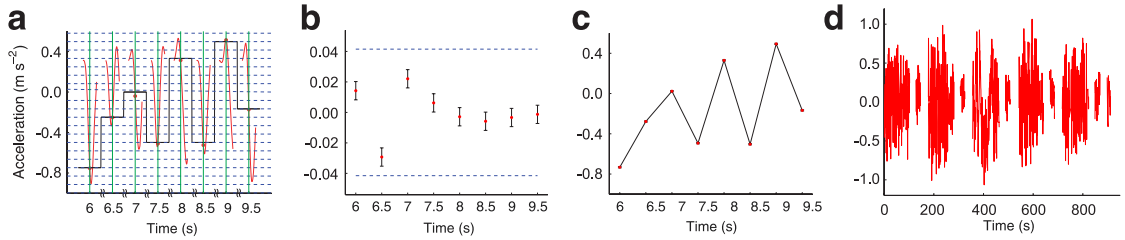

FIGURE 4.7 – (a) In red, the signal recorded by the mechanical accelerometer in the time window $\{t_i - 2T, t_i + 2T\}$ around the measurement times $t_i = iT_{\mathrm{cyc}}$ (vertical green lines), with $T_{\mathrm{cyc}} = 500$ ms and $T = 1.5$ ms. The accelerometer signal has been filtered by the response function $f(t)$ of the interferometer [85, 84], and the red points represent the value of the signal at t_i. This value determines the reciprocity region where the interferometer operates, delimited by two horizontal dashed lines. In this way, the accelerometer provides a coarse measurement (black step-like signal). (b) The CAA is then used for the high-resolution measurement within its reciprocity region, bounded by the two blue dashed lines at $\pm\pi/2k_{\mathrm{eff}}T^2 \simeq \pm 0.087$ m/s^2. The error bars represent the noise of the CAA, which is 0.0065 m/s^2 per shot in this example (SNR = 4.3). (c) The total acceleration is the sum of the black step-like signal in (a) and the CAA measurements in (b). (d) Full signal measured by the hybrid sensor onboard the Novespace A300 Zero-G aircraft during successive $1g$ and $0g$ phases of flight. For this data set, the resolution of the sensor in 1 s is more than 100 times below the acceleration fluctuations of the aircraft.

will be compliant with onboard applications, especially considering vibrations and rotations.

In collaboration with iXblue, we developped an optimal method to hybridize a classical and a quantum accelerometer using Kalman filtering [125]. Here the objective is to correct the bias of the classical accelerometer with the absolute measurement of the atom interferometer. More specifically we demonstrate a strong robustness in severe experimental conditions (Fig. 4.8). To simulate real conditions outside the lab, we apply temperature variations of the critical components (including the classical accelerometer) and we modulate the loss of contrast of the atom interferometer by applying fluctuations of the laser power. We show we are able to track and correct the bias of the classical accelerometer using the atomic measurement and despite the non perfect conditions. The noise spectrum and the Allan variance of the acceleration measured by the hybrid sensor are presented Fig. 4.8 (c) and (d).

Preliminary tests of hybridization with an INS during a flight campaign

Preliminary tests of hybridization of an atom accelerometer and an Inertial Navigation System (INS) were achieved during a flight campaign. The goal of this hybridization is to correct the bias drift of the classical accelerometer with the absolute measurement of the atom interferometer. The physical fusion of the two systems requires to put the INS on the same mechanical mount as the reference mirror of the atom interferometer (Fig. 4.9 (b)). The correlation between the classical and the quantum sensor has been done on the vertical axis. We evaluated the bias drift of the classical accelerometer using a Kalman filter. Fig. 4.9) shows the result for three different interrogation times. The graph on 4.9) (c) shows how fast the uncertainty on the prediction of the bias is reduced by integrating in time. This data set proves our method applies on a relevant signal (the plane acceleration) which varies very fast.

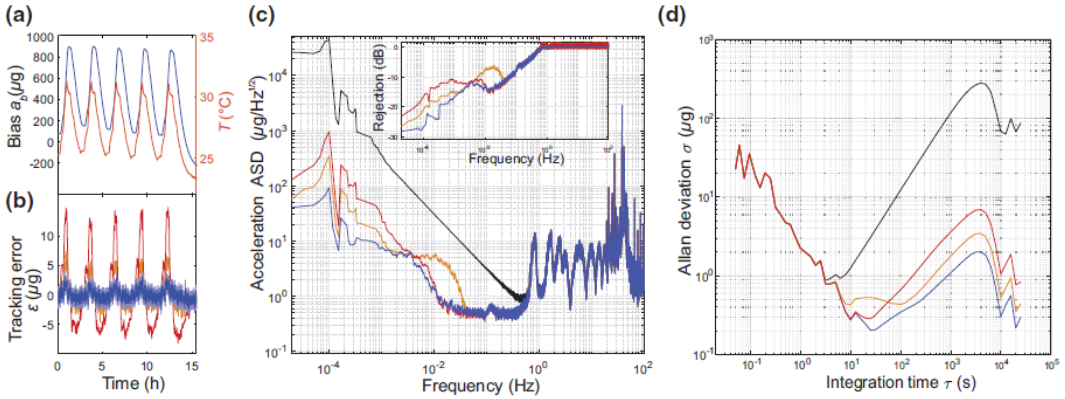

FIGURE 4.8 – (a) Accelerometer bias determined by the KF algorithm (blue) and temperature (red) as a function of time. The temperature modulation produces large bias variations of approximately 1 mg. The standard deviation of the estimate is smaller than the line thickness. (b) Bias tracking error using the KF (blue) and by sine-fitting with 8 (brown) or 25 (red) points. The rms value of the true bias tracking error is 0.89μg for the KF—in good agreement with the estimated standard deviation displayed as a shaded area. For the sine-fitting method, the true rms errors are 2.3μg and 5.9μg for 8- and 25-point stacks. (c),(d) Amplitude spectral density and Allan deviation of the standalone (black) and the hybrid accelerometers using the KF (blue) and sine-fitting with 8-point (brown) and 25-point (red) stacks. The ASD shows that, at low frequencies, the error rejection (inset) corresponds to a first-order high-pass filter. The error rejection is also visible in the Allan deviation, where the long-term drift of the hybrid accelerometer is reduced by more than 2 orders of magnitude compared to the standalone one.

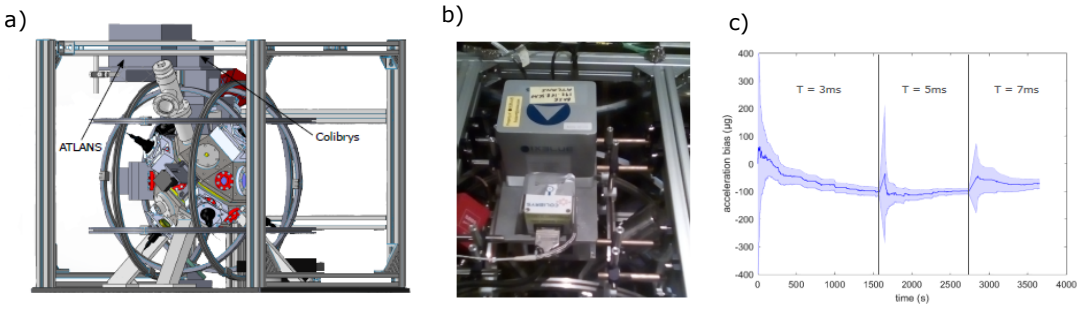

FIGURE 4.9 – a) and b) Integration of the INS (iXblue ATLANS) on the experiment ICE. c) Measurement of the bias of the classical accelerometer using a Kalman filter and the output of the atom interferometer.

.

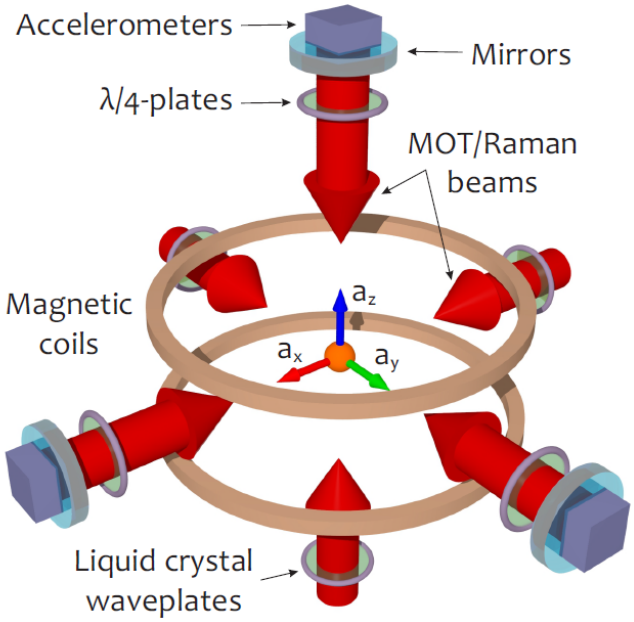

FIGURE 4.10 – Architecture of the 3 axis cold atom accelerometer. The same 3 retroreflected beams are used for both cooling and trapping and Raman interferometry. The input polarization of the beam is switched using Liquid Crystal Waveplates (LCW) between the two steps of the sequence.

4.3.3 3D atom accelerometer

Previously we hybridized a 3 axis mechanical accelerometer with a one axis atom interferometer. We present here a 3 axis hybridized atom accelerometer. In the past, atom interferometers were designed to be sensitive to inertial effects along a single axis, defined by the interrogation beam. Nevertheless there is no fundamental limitation to extend this technique to two or three axes [126, 2, 127].

Our short term strategy is to measure *alternatively* the acceleration along each axis by switching the direction of the Raman beam. We demonstrated theoretically that simultaneous measurement of the different acceleration component is not impossible (see chapter 2) and the experimental achievement of these principles constitutes our middle term objective.

A prototype of compact and transportable 3D atom accelerometer has been developed within the joint laboratory iXAtom (figures 4.10 and 4.11 (a)). To set up the 3 axis cold atom sensor, three pairs of Raman beam are aligned along the axes x, y et z and retroreflected by independent mirrors. We use this very same beams to trap and cool the atom cloud which are centered at the crossing of the 3 beams by design. These beams can be pulsed simultaneously or sequentially to proceed the sequence $\pi/2-\pi-\pi/2$ splitting, reflecting and recombining the atoms. A mechanical accelerometer is rigidly fixed to the back of each retro-reflection mirror to measure vibrations. These vibration measurements will be converted to phase shifts of the interferometer along each axis, and correlated with the atomic populations measured by fluorescence imaging in the same spirit as described in the previous sections.

We demonstrated for the first time the measurement of the three components of the vector acceleration with a 3D cold atom interferometer in a tilted configuration with a random angle (Fig. 4.11 (b)). Moreover, we developed a real time compensation of the Doppler effect produced by the random accelerations of the vehicle and which implies a loss of contrast of our onboard CAA. We showed this method allows our atom interferometer to operate in any orientation, which is worldwide premiere. Fig. 4.11 (b) shows the Allan deviation of the

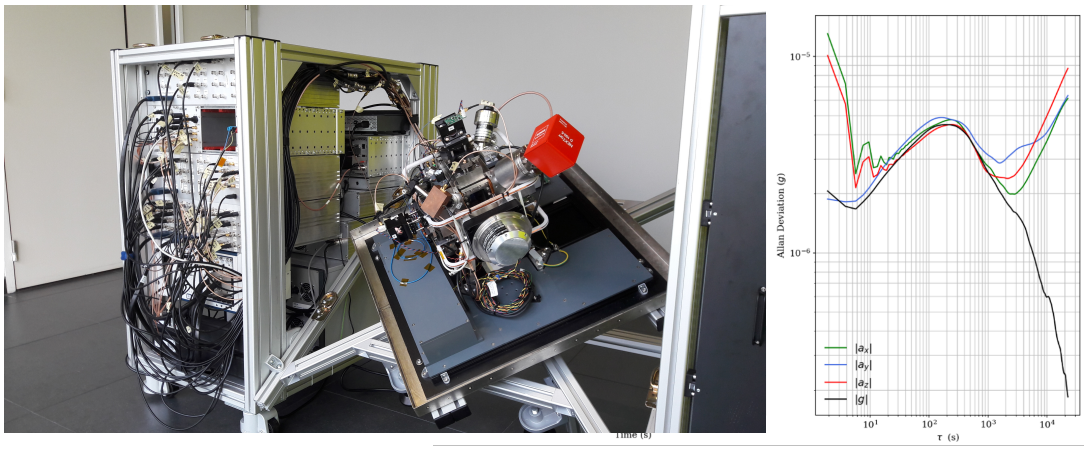

FIGURE 4.11 – (a) Mobile 3D cold atom accelerometer. On the left, the laser system and the electronics. On the right, the sensor head is tilted with angle of approx. 35deg. (b) 3D measurements a_x (green), a_y (blue), and a_z (red), of the vector acceleration. The three independent components drift after 1000 s because of the tilt of the experiment but the norm of the vector $|g|$ (black) is stable.

.

acceleration measured by the hybrid accelerometer along the three axes a_x, a_y, a_z. After an integration time of 100 s, we show a drift of the three values because the tilt of the complete experiment is drifting. On the contrary the norm of the vector acceleration $|g|$ is stable and continues to be integrated as a white noise after 100 s.

Systematic errors

A study of the systematic errors in the vertical direction has been done. We focus here on the particularities of our device. The first specificity is the laser system which is presented above. The parasitic lines influence is strongly reduced with the IQ modulator compared to a phase modulator. The systematic error is estimated to be below 100 ng by a theoretical model and is confirmed by the measurement of the phase shift for different experimental parameters (different interrogation times T and time of flight before the first pulse). A second specificity is the use of a LCW (see Fig. 4.10) to switch the polarization between the cooling phase and the atom interferometer. Defects of polarization give raise to non negligible two photon light shift which drifts because of temperature fluctuations. This effect can be mitigated by a good control of the LCW temperature.

Additional difficulties arise when we tilt the experiment and consider a non vertical axis. The position of the atom cloud in the Raman beam depends on the angle. This displacement leads to several angle dependent systematic errors : two photon light shifts, wavefront aberration,.... Moreover the knowledge of the relative angle between different axes is a priori unknown and need to be calibrated.

4.3.4 Error on the π pulse condition of the atomic beam splitters

Because of the movement of the atoms inside the laser beam, it is in practice difficult to achieve a perfect interferometer on a board mobile vehicle. When the atoms move in the laser beam, the intensity seen by the atoms is not the same and the π pulse conditions is not satisfied anymore. First the condition $\Omega_R\tau \neq \pi/2$ implies a loss of signal due to the atom escaping from the interferometer on the mirror pulse. These atoms don't contribute to the interferometer if the de Broglie wavelength (typically 1 μm) is larger than the spatial

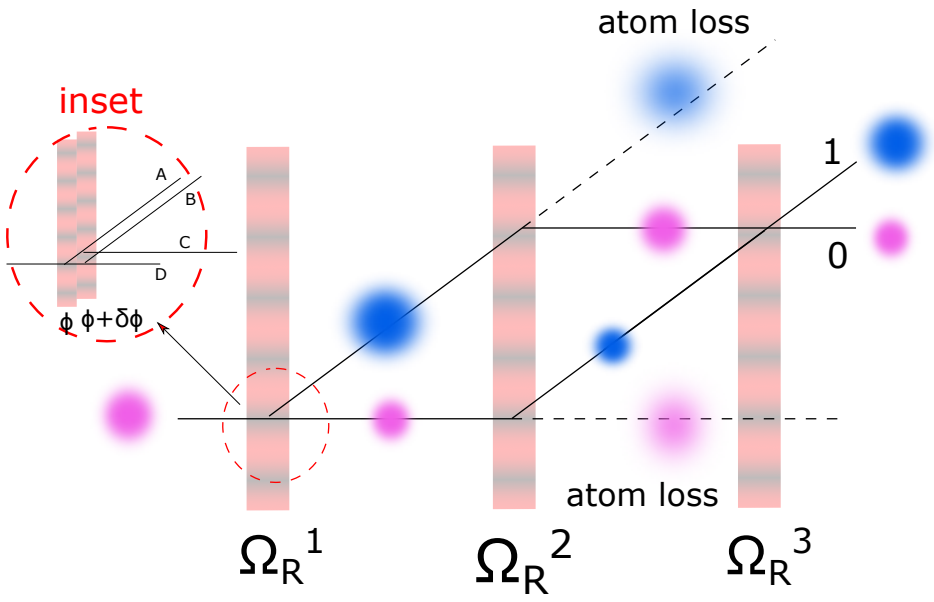

FIGURE 4.12 – The condition $\Omega_R^i \tau \neq \pi/2$ for each pulse i implies loss of signals on the mirror pulse and population imbalance along the two paths of the atom interferometer. Inset : Our model to calculate the effect of a phase shift $\delta\phi$ during a pulse consists in decomposing the pulse into two subpulses of phase ϕ and $\phi + \delta\phi$. The spatial separation of the output A and B (resp. C and D) is considered very small compared to the de Broglie wavelength so that we can sum the amplitudes.

splitting the different path (typically 250 μm for Rb and $T = 10ms$). The attenuation term is $\sin(\Omega_R \tau)$ (in amplitude).

Secondly, the sensitivity and response function are modified. The sensitivity function is calculated using the evolution matrices and by decomposing the pulse into two subpulses when the phase jump $\delta\phi$ happens during this pulse. When $\Omega_R \tau$ is constant, the sensitivity function stays odd and becomes [128] :

$$g_\Omega(t) = \begin{cases} \frac{\sin(\Omega_R t)}{\sin(\Omega_R \tau)} & 0 < t < \tau \\ 1 & \tau < t < T + \tau \\ -\frac{\sin(\Omega_R (t - T - 2\tau))}{\sin(\Omega_R \tau)} & T + \tau < t < T + 2\tau \end{cases} \tag{4.3}$$

We can then calculate the response function used to calculate phase due to accelerations. The function is even :

$$f_\Omega(t) = \begin{cases} \frac{\cos(\Omega_R t)}{\Omega_R \sin(\Omega_R \tau)} + T + \frac{-2\cos(\Omega_R \tau)+1}{\Omega_R \sin(\Omega_R \tau)} & 0 < t < \tau \\ (T + \tau - t) + \frac{\cos(\Omega \tau)-1}{\Omega_R \sin(\Omega_R \tau)} & \tau < t < T + \tau \\ \frac{\cos(\Omega_R (T+2\tau) - \Omega_R t)-1}{\Omega_R \sin(\Omega_R \tau)} & T + \tau < t < T + 2\tau \end{cases} \tag{4.4}$$

We get the following phase shift with the modified scale factor for a constant acceleration g :

$$\delta\Phi = \int_{-\infty}^{+\infty} g_s(t) k g t dt = k g (T + 2\tau_R) \left[T + \frac{2}{\Omega_R} \tan\left(\frac{\Omega_R \tau}{2} \right) \right] \tag{4.5}$$

In the case of different $\Omega_R^{1,2,3}$ for the three pulses of the atom interferometer, the sensitivity

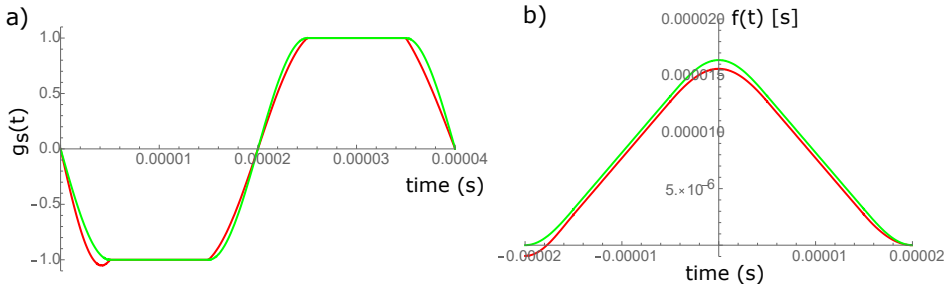

FIGURE 4.13 – Sensitivity function (a) and Response function (b) for an interrogation time $T = 10\mu$s, $\tau = 5\mu$s, $\Omega_R^1\tau = \Omega_R^2\tau = \Omega_R^3\tau = \pi/2$ (green) and $\Omega_R^1\tau = 1.2\pi/2$,$\Omega_R^2\tau = 0.8\pi/2$ and $\Omega_R^3\tau = 0.6\pi/2$ (red).the small value of T is arbitrarily chosen for a good readability of the curve but have no connection with the reality of the experiments.

.

function becomes (Fig. 4.13 (a)) [128] :

$$\tilde{g}_\Omega(t) = \begin{cases} 0 & t \leq -T - 2\tau \\ -\frac{\sin[\Omega_R^1(t+T+2\tau)]}{\sin(\Omega_R^1\tau)} & -T - 2\tau < t < -T - \tau \\ -1 & -T - \tau < t < -\tau \\ \frac{\sin[\Omega_R^2 t]}{\sin(\Omega_R^2\tau)} & -\tau < t < \tau \\ 1 & \tau < t < T + \tau \\ -\frac{\sin[\Omega_R^3(t-T-2\tau)]}{\sin(\Omega_R^3\tau)} & T + \tau < t < T + 2\tau \\ 0 & t \geq T + 2\tau \end{cases} \tag{4.6}$$

And the response function becomes (Fig. 4.13 (b)) :

$$\tilde{f}_\Omega(t) = \begin{cases} \frac{1}{\Omega_R^3}\tan\left(\frac{\Omega_R^3\tau}{2}\right) - \frac{1}{\Omega_R^1}\tan\left(\frac{\Omega_R^1\tau}{2}\right) & t \leq -T - 2\tau \\ \frac{1}{\Omega_R^1\sin(\Omega_R^1\tau)}(\cos(\Omega_R^1\tau) - \cos[\Omega_R^1(t+T+2*\tau)]) + \frac{1}{\Omega_R^3}\tan\left(\frac{\Omega_R^3\tau}{2}\right) & -T - 2\tau < t < -T - \tau \\ t + T + \tau + \frac{1}{\Omega_R^3}\tan\left(\frac{\Omega_R^3\tau}{2}\right) & -T - \tau < t < -\tau \\ \frac{1}{\Omega_R^2\sin(\Omega_R^2\tau)}(\cos(\Omega_R^2 t) - \cos[\Omega_R^2\tau]) + T + \frac{1}{\Omega_R^3}\tan\left(\frac{\Omega_R^3\tau}{2}\right) & -\tau < t < \tau \\ -t + T + \tau + \frac{1}{\Omega_R^3}\tan\left(\frac{\Omega_R^3\tau}{2}\right) & \tau < t < T + \tau \\ \frac{1}{\Omega_R^3\sin(\Omega_R^3\tau)}(1 - \cos[\Omega_R^3(t-T-2\tau)]) & T + \tau < t < T + 2\tau \\ 0 & t \geq T + 2\tau \end{cases} \tag{4.7}$$

The parity break of the interferometer symmetry between the first and the third Raman pulse makes it sensitive to the atom velocity. That is why f(t) is not perfectly zero for $t \leq -T - 2\tau$.

This assymetry of the interferometer creates another velocity dependence. If the Raman condition is not perfectly fullfilled (because of Doppler effect or light shifts for instance), it implies a phase shift which creates a displacement of the wavepacket during the pulse. if Ω_R is not constant, this effect is not rejected by the symetry of the interferometer and creates a velocity dependent phase shift [129, 130].

4.3.5 Additional phase shifts due to gravity gradient and rotations

The movement of the vehicle has a strong influence on the phase shift of the atom interferometer and can be modeled. The trajectories of the atomic wavepackets along the arms of the interferometer can be determined analytically by solving the Euler-Lagrange equations using a power series expansion in time t, see for example [131]. Subsequently, the phase shift is calculated by the formula [132] :

$$\phi = k_1 \cdot r_A - 2k_2 \frac{r_B + r_{B2}}{2} + k_3 \frac{r_C + r_{C2}}{2} \tag{4.8}$$

for a $\pi/2 - \pi - \pi/2$ single diffraction interferometer with effective wave numbers $k_{1,2,3}$ corresponding to two photon transitions.

We can for instance calculate the first term in T for a constant gravity gradient T_{zz}. The equation of movement is :

$$\ddot{z} = -g - T_{zz}\left(z_A + v_A t - \frac{1}{2}gt^2\right) \tag{4.9}$$

which gives :

$$\phi_{zz} = k_{eff}T^2\left[-g - T_{zz}\left(z_A + v_A T + \frac{7}{12}gT^2\right)\right] \tag{4.10}$$

where $v_A = v_0 + v_R/2$ is the sum of the initial velocity and the half recoil velocity, corresponding to the trajectory of the center of mass of the wave packets.

Calculations has been done at higher terms in presence of rotations of axis y (Ω_y, $\Omega_x = \Omega_z$=0) and gravity gradients (T_{xx},T_{yy},T_{zz}), see for instance [133]. Here are the principle terms for a single diffraction Mach Zhender atom interferometer in the lowest orders in T :

$$\begin{gathered}
\phi_x = k_{eff}x_A\left(T_{xx}\Omega_y + 2\Omega_y^3 - T_{zz}\Omega_y\right)T^3 \\
\phi_z = k_{eff}z_A\left(T_{zz} + \Omega_y^2\right)T^2 \\
\phi_{vx} = 2k_{eff}v_{x,A}\Omega_y T^2 \\
\phi_{vz} = k_{eff}v_{z,A}\left(T_{zz} - 3\Omega_y^2\right)T^3 \\
\phi_g = -T_{zz}\tfrac{7}{12}gT^4
\end{gathered} \tag{4.11}$$

These phase shifts depends on the initial position (x_A, z_A) and the initial velocity ($v_{x,A}$,$v_{z,A}$) of the atom cloud compared to the reference mirror in the mobile frame.

4.3.6 Loss of contrast due to gravity gradient

Gravity gradients can create a loss of contrast for long interrogation times [134]. This effect is due to the generation of open interferometers (see Fig.4.14 (a)), where the classical trajectories characterizing the motion of the wave packets do not close in phase space and the resulting relative displacements in position and momentum, $\delta\mathcal{R}$ and $\delta\mathcal{P}$, cause a reduction of the quantum overlap between the interfering states in each exit port. In the position representation this reduction is due to two effects : first, a decreasing spatial overlap of the two envelopes ; second, spatial oscillations in the product of one wave function and the other complex conjugate, whose integral over space gives the quantum overlap of the two states. The contrast for an open interferometer of duration $2T$ can be written :

$$C \approx \left| \int d^3x \exp\left[\frac{i}{\hbar}\left(\delta\mathcal{P} - \frac{m}{2T}\delta\mathcal{R}\right)^T \mathbf{x}\right] |\psi_c(\mathbf{x}, 2T)|^2 \right| \tag{4.12}$$

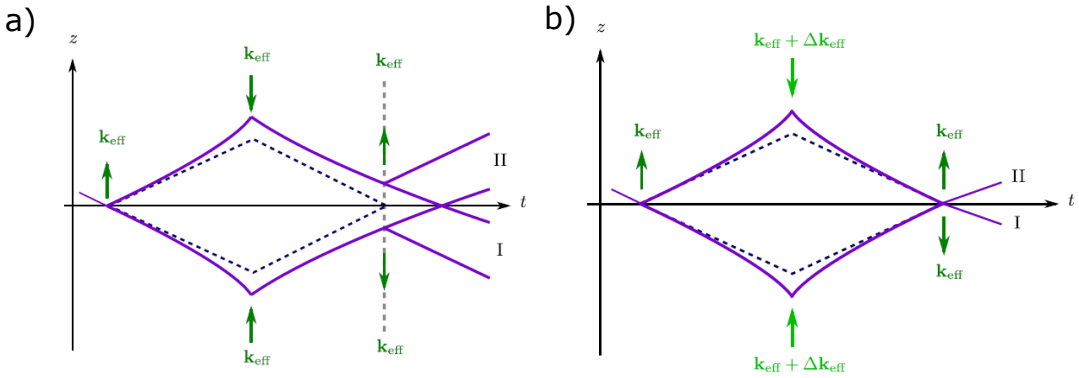

FIGURE 4.14 – a) Central trajectories for a Mach-Zehnder interferometer in the presence of gravity gradients as seen in a suitable freely falling frame. The tidal forces tend to open up the trajectories compared to the case without gravity gradients (dashed lines). The momentum transfer from the laser pulses is also indicated for the different branches. The picture on the left shows the tidal forces experienced by objects in a freely falling frame (the Einstein elevator) as a consequence of the gravity gradient. b) Central trajectories for the same situation depicted in a) but with a suitable adjustment of the momentum transfer from the second laser pulse so that a closed interferometer, with vanishing relative displacement between the interfering wave packets in each port, is recovered[134].

.

In the case of a constant gradient T_{zz}, we find the following displacement in phase space :

$$\begin{aligned} \delta\mathcal{R} &= \left(T_{zz}T^2\right)\mathbf{v_R}T \\ \delta\mathcal{P} &= \left(T_{zz}T^2\right)m\mathbf{v_R} \end{aligned} \tag{4.13}$$

To mitigate this effect, it is interesting to point out that a vanishing final displacement in phase space, $\delta\mathcal{P} - \frac{m}{2T}\delta\mathcal{R} = 0$, could be achieved by suitably adjusting the momentum transfer of the mirror pulse (this would lead for instance to trajectories symmetric under time inversion around the time of the mirror pulse in the case depicted in figure 4.14 (b)). The value of the momentum transfer of the second pulse is then :

$$\mathbf{\Delta k_{eff}} = (T_{zz}T^2/2)\mathbf{k_{eff}} \tag{4.14}$$

4.3.7 Phase shift and Loss of Contrast due to Rotations

The rotation is currently the major issue for any on-board applications, not only for navigation but also Space missions.

First it creates a phase shift due to the Coriolis acceleration in a rotating frame :

$$\Phi_{Cor} = 2\mathbf{k_{eff}} \cdot (\mathbf{v} \times \mathbf{\Omega})T^2 \tag{4.15}$$

If we measure the rotation rate $\mathbf{\Omega}$ with a gyroscope, and calculate the relative transverse velocity $\mathbf{v}$ of the reference mirror compared to the atom cloud using the gyroscope and the accelerometers. In any case, even in a steady mode, we expect a strong effect due to the angle of the experiment θ which gives $v = g\sin(\theta)t_{Tof}$, where t_{Tof} is the time of flight of the atom cloud before the first pulse of the atom interferometer.

In a mobile, the rotation of the reference mirror implies a non overlap of the two atomic wave packets in phase space at the output of the atom interferometer, especially because the Coriolis acceleration on the two paths traveled by the wave packets is not the same. A similar

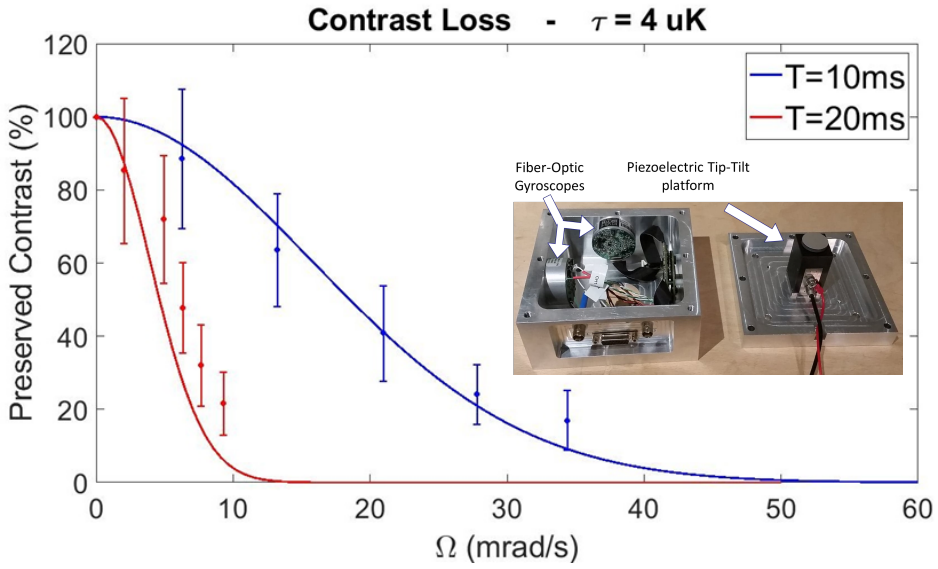

FIGURE 4.15 – Loss of contrast for two interrogation time (T=10 ms in blue and T=20 ms in red) due to a rotation rate of the reference mirror applied by the tiptilt mount. The temperature of the atom cloud is 4 μK. Inset : Mechanical structure including a two axis fiber-optic gyroscope (FOG) on the left and the piezoelectric tiptilt mount on the right. The left part is screwed on top of the right part.

.

calculation to the one developed for the gravity gradient can be done. To obtain the displacement momentum vector, we have evaluated the classical trajectories of the interferometers by solving the Euler-Lagrange equations using the Lagrangian :

$$\mathcal{L}(\mathbf{r},\mathbf{v}) = \frac{1}{2}m(\mathbf{v}+\Omega\times\mathbf{r})^2 \tag{4.16}$$

which describes the motion of non-interacting particles with mass m, undergoing a constant rotation $\mathbf{\Omega} = (\Omega_x, \Omega_y, \Omega_z)$, where the vectors $\mathbf{r}$ and $\mathbf{v} = \dot{\mathbf{r}}$ are defined in the rotating frame.

The displacement vector is :

$$\delta\chi = \delta\mathcal{P} - \frac{m}{2T}\delta\mathcal{R} = \frac{\hbar k_{eff}}{2}\begin{pmatrix} 2\Omega_y T + 3\Omega_x\Omega_z T^2 \\ -2\Omega_x T + 3\Omega_y\Omega_z T^2 \\ -3(\Omega_x^2+\Omega_y^2)T^2 \end{pmatrix} \tag{4.17}$$

This effect leads to a contrast loss of the interferometer :

$$C \approx e^{-(k_{eff}\sigma_v T)^2(\Omega T)^2} \tag{4.18}$$

where Ω is the norm of the rotation rate vector, T is the interrogation time, k_{eff} is the effective wave vector, and σ_v the velocity distribution of the atom cloud.

Figure 4.15 presents the contrast loss of the atom interferometer versus the rotation rate. The contrasts are measured using a sinusoidal fit of the atom fringes. The error bars corresponds to the fit residuals. We find a good agreement with the theory of a temperature of the atom cloud of 4 μK.

In practice, the rotation of the mobile (the zero-g plane or a boat for instance) can reach 6°/s. For this rotation rate and the temperature of the atom cloud (4 μK), the contrast is lost completely for a interrogation time of 10 ms. A first solution is to compensate the rotation

of the mobile by making the reference mirror turn in the reverse direction to maintain a fix direction of the Raman beam in a referential frame defined by the first pulse of the atom interferometer. The technical solution is based on a piezo-electric tiptilt mirror mount. Since the rotation rate of the mobile is a priori unknown, a real-time compensation of the rotation is required (inset of Fig 4.15). Fiber-optic gyroscopes (FOG) measure the rotation rates $\Omega_X(t)$, $\Omega_Y(t)$, which allows to calculate the angle $\theta_{X,Y}(t)$ we need to apply to the mirror mount. The angle of the tiptilt mount itself is servo locked. To have an efficient rotation compensation, FOGs and the reference mirror have to be mechanically linked.

A second solution (compatible of the first one) is the production of ultracold atoms. By reducing the temperature of the atoms, we increase the maximum rotation rate which is tolerated. According to equation 4.18 this effect varies as the square root of the temperature.

The loss of contrast presented here is linked to the fact that due to the method of detection by fluorescence, we average spatial fringes coming from the splitting between the wave packets on the third pulse of the atom interferometer. Similarly to the point source interferometry, spatial imaging can allow to resolve the fringes and extract the signal.

4.4 Full hybridization of a quantum/classical INS

The next step will be the extension of the hybridization including fiber optical gyroscopes (FOG) to measure the three axes of acceleration **and** rotation such as a complete Inertial Navigation System (INS) based on cold atom technology.

Navigation required to know the three components of the vector acceleration and the three components of the vector rotation. Moreover, Gyroscopes is required to correct the Coriolis phase shift (Eq. 4.15) due to the transverse displacement of the atoms and the real time compensation of the rotation to avoid the loss of contrast (see section 4.3.7).

Remark : The control and the knowledge of the alignment of the different axes of all the sensors is critical and a special care is required for the the integration of the FOG on our 3D atom accelerometer.

4.4.1 Navigation strapdown algorithm

First the gyroscope signals Ω_x,Ω_y,Ω_z is integrated to obtain the rotation matrix R (see Fig. 4.16 (a)) :

$$R(t) = R_0 \exp\left[\int_{t_0}^{t} \left(\begin{bmatrix} 0 & -\Omega_z & \Omega_y \\ \Omega_z & 0 & -\Omega_x \\ -\Omega_y & \Omega_x & 0 \end{bmatrix} \right) dt' \right] \tag{4.19}$$

Then the accelerations measured in the body frame $\mathbf{a}_b$ are projected onto the navigation frame :

$$\mathbf{a}_n(t) = R(t)\mathbf{a}_b(t) \tag{4.20}$$

Finally we apply a correction for local gravity vector $\mathbf{g}(\mathbf{r})$ and Coriolis acceleration and integrate :

$$\mathbf{v}_n(t) = \mathbf{v}_n(0) + \int_{t_0}^{t} \left[\mathbf{a}_n - \mathbf{g}(\mathbf{r}_n) - 2\mathbf{v}_n(0) \times \mathbf{\Omega}\right] dt' \tag{4.21}$$

and

$$\mathbf{r}_n(t) = \mathbf{r}_n(0) + \int_{t_0}^{t} \mathbf{v}_n dt' \tag{4.22}$$

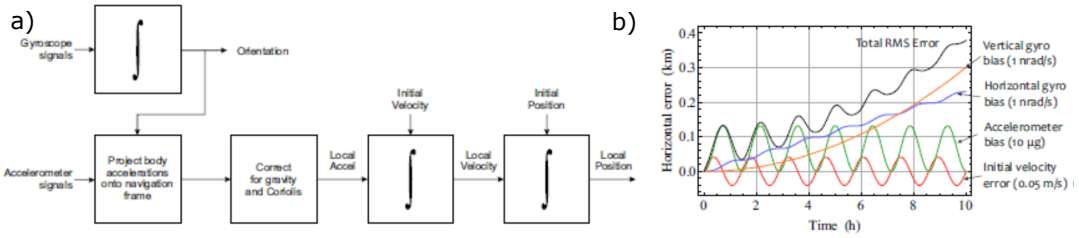

FIGURE 4.16 – a) Strapdown algorithm using a Kalman filter and the inertial measurement of rotations and accelerations. b) Navigation errors in horizontal position including the different contribution of the sensor biases.

The errors in horizontal position are coming from the following biases. First the horizontal acceleration bias δa_x implies an error which oscillates in time :

$$\left(\frac{1-\cos\omega_S t}{\omega_S^2}\right)\delta a_x \tag{4.23}$$

where $\omega_S = \sqrt{g/R_E}$ is the Schuler frequency and R_E is the Earth's radius.

Then the horizontal gyroscope bias $\delta\Omega_x$ implies an error which increases linearly in time :

$$R_E\left(t-\frac{\sin\omega_S t}{\omega_S}\right)\delta\Omega_x \tag{4.24}$$

Finally the vertical gyroscope bias $\delta\Omega_z$ gives the following error :

$$R_E\Omega_E\cos L\left(\frac{t^2}{2}-\frac{1-\cos\omega_S t}{\omega_S^2}\right)\delta\Omega_z \tag{4.25}$$

where L is the latitude.

With a correction at a level of 100 ng on the acceleration vector (we are limited by the knowledge of gravity at this level), we expect to improve the navigation error by a factor 100 on short term (after one hour of navigation). At long term, the navigation is limited by the gyroscope bias in the vertical direction which varies as the square of the time. The different error terms are plotted on Fig. 4.16 (b).

In the future, we can imagine to hybridize cold atom gyroscopes of high sensitivity with FOG to reduce the noise of the measurement and integrate faster to an high level of precision. Moreover an absolute gyroscope with a bias lower than $10^{-6}\,\mathrm{deg.hr}^{-1}$ will allow to improve the long term performances.

4.4.2 Interleaved atomic measurements in an inertial frame

The atom interferometer can be considered as a phase ruler measuring the trajectory of the atoms compared to the reference mirror (or the reverse). The atoms follows a reference parabola and the mirror moves around this reference trajectory (see Fig. 4.17 (a)). Is it possible to extract directly the position signal ? We discuss here about the conditions required to extract such a signal using a sequence of atomic phase measurement Φ_j.

For onboard applications, the movement of the atoms in the system is an intrinsic limitation and we are necessarily in the regime of low interrogation time T. Moreover the usual conditions in our model of an atom interferometer correspond to the perturbative regime described for instance in [1]. For the case of rotation the condition is $\Omega t \ll 1$. Consequently

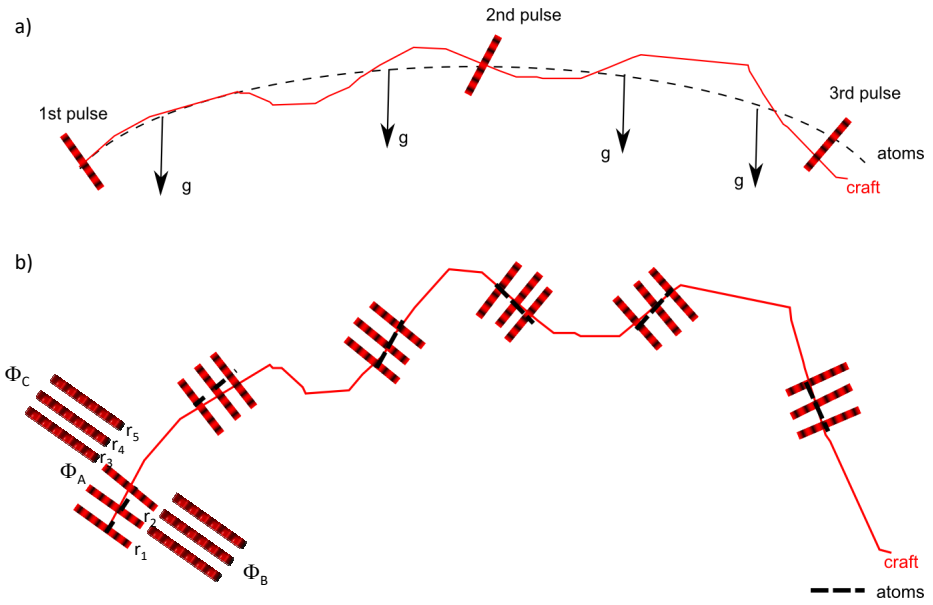

FIGURE 4.17 – a) Our atom interferometer measures the position of the center of mass at each laser pulse. b) Interleaved measurements allow to extract the position variation between two successive points $r_{i+1} - r_i$ by combining several atomic phases Φ_j. The interleaved interferometers are plotted only for a few measurement for the clarity of the figure.

the direction of the vector k_{eff} needs to be maintained constant in an inertial frame during the atom interferometer.

The mid point theorem [2] claims the laser phase at the position r_i of the center of mass of the wavepackets is printed on the wavefunction for each pulse i. We have the following relation between the phase Φ_A of the interferometer $j = A$ and the relative positions during the three pulses r_1, r_2 and r_3 :

$$r_3 - r_2 = \frac{\Phi_A}{k_{eff}^A} + r_2 - r_1 \tag{4.26}$$

The idea here is to achieve interleaved measurements to acquire redundant measurements of the difference of position between two pulses $r_{i+1} - r_i$. Moreover, this method has the advantage to suppress the deadtimes, which is essential for navigation. The two first pulses of the interferometer B corresponds to the two last pulses of the interferometer A (see Fig. 4.17 (b)). The next measurement Φ_B gives us :

$$r_4 - r_3 = \frac{\Phi_B}{k_{eff}^B} + r_3 - r_2 = \frac{\Phi_B}{k_{eff}^B} + \frac{\Phi_A}{k_{eff}^A} + r_2 - r_1 \tag{4.27}$$

This measurement principle can be reiterated.

Evaluating the orientation of the wave vector k_{eff}^j is necessary for each measurement j, which requires a gyroscope (classical or quantum). Moreover a real-time compensation of the rotation, including a gyroscope, is required to stays in the perturbative regime $\Omega T \ll 1$. The idea is to keep the wave vector along a constant direction during the atom interferometer thanks to the real-time compensation.

4.5 Future developments of on-board inertial cold atom sensors

4.5.1 Gravity Gradiometer

Gravity gradiometry is seriously considered for many applications. For instance techniques such as gravity mapping and matching are envisioned for navigation. A gravity gradient has also the advantage to reject the vibrations which often constitute a limitation for onboard applications. Classical technologies (for instance a set of accelerometers attached to a rotating platform allowing to extract the full tensor of the gravity gradient [135]) already exists but only relative instruments which requires calibration are available on the market. The absolute character of atom interferometers is thus promising to bring a technology breakthrough in this field. Another advantage of cold atoms technology is that we have also access to the gravity measurement with the same apparatus [136].

Another field of applications is the study of the Earth gravity field. Several scientific communities (oceanography, geophysics, solid-earth...) are permanently demanding of instruments measuring the gravity gradient. Several Space missions have been launched (GOCE, GRACE, GRACE-FO) using electrostatic accelerometers. Considering the importance of such data which cannot be available with any other kind of instruments, the future missions are already studied and a new technology which could combine both better spatial and temporal resolution will be considered with high interest by these communities.

Nowadays atom gravity gradiometers only exist as lab experiments (TRL 3) [136]. One of our future goal is to develop a compact onboard gravity gradiometer to increase the maturity of the technology. In this context, access to the 0g plane and the 0g simulator will allow us to work in a relevant experiment by developing new experimental protocols compliant with microgravity for future Space missions.

A simple architecture of a cold atom gradiometer is to have two atom sources separated by a distance d and achieve two simultaneous atom interferometers to measure the local gravity by the two atom clouds. The differential phase between the two interferometers is directly related to the gravity gradient :

$$\Phi_{gradio} = \Phi_2 - \Phi_1 = k(a_2 - a_1)T^2 = kT_{zz}dT^2 \tag{4.28}$$

where T_{zz} is the gravity gradient along the z direction.

We plan to tackle several challenges on the ICE experiment.

Precise control of the spatial separation between the two atom clouds

The distance d between the two atom clouds contributes to the scale factor of the atom gradiometer and need to be controlled with the same accuracy as the expected level of performances of the instrument. Bloch oscillations in an accelerated optical lattice constitute a promising solution since it can allow to give a well controlled number N of recoil $N\hbar k$, N being arbitrarily large (see also chapter 3). Bloch oscillations is a velocity dependent process which requires ultracold atoms to be efficient. Our experimental configuration based on our all-optical method in a dipole trap make the implementation of the Bloch techniques easily achievable.

The accelerated optical lattice is applied along the measurement axis in a retro-reflected configuration. It is then possible to transfer a large momentum to the atoms in two opposite directions. Moreover, the momentum is well controlled since it is a integer of photonic recoil

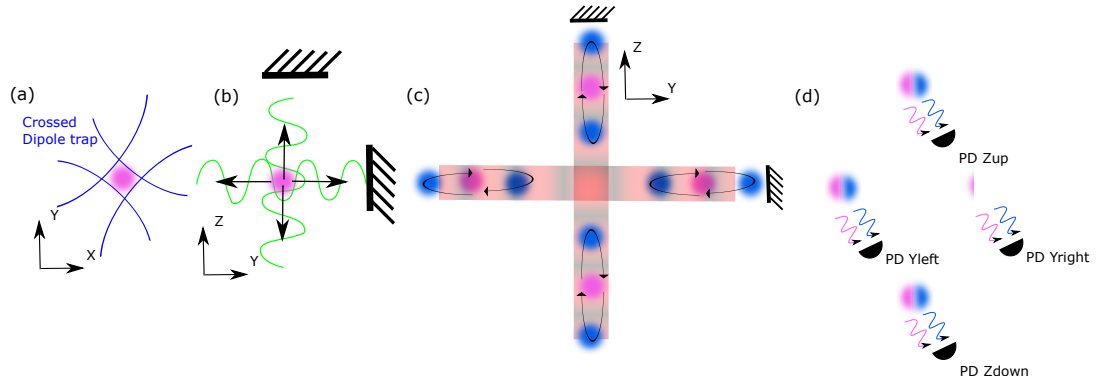

FIGURE 4.18 – 2D atomic gravity gradiometer (a) An ultra-cold atom cloud is produced by evaporative cooling in an optical trap at the center of the vacuum system. (b) For each axis of measurement, a two-frequencies retro-reflected laser beam creates two accelerated optical lattices in the two opposite directions. The initial atom cloud is split in four parts (4 black arrows). The four secondary atom clouds are slow down and stopped with the same Bloch oscillations technique. In the 2D case, we obtain two pairs of atomic clouds. (c) Each pair of atomic clouds is interrogated using three successive laser pulses to measure their differential acceleration regarding to a reference mirror. The atoms are initially prepared in state $|1\rangle$ (pink) and the first 2D pulse diffracts each atom into two wavepackets which are now in state $|2\rangle$ (blue). The second pulse reflect the two (eight in total) wavepackets. The third 3D pulse recombines each pair of wavepackets. d) The atom populations in $|1\rangle$ et $|2\rangle$ for the four spatially separated atom clouds are detected by fluorescence with a set of photodiodes or a CCD camera.

$N\hbar k$, N can be arbitrary large (experiments demonstrated $N > 400$ [109]).

The same protocol is used to stop the atoms. To control perfectly the distance between the two atom clouds, it is also necessary to control perfectly the duration between the accelerating and the decelerating pulses.

Differential measurement and common mode rejection

A key point of an atomic gradiometer is the differential acceleration measurement using a single retro-reflected beam and a single reference mirror common to the two separated atom clouds. In a 1D configuration (measurement along one axis), this Raman beam is superposed to the accelerated lattice. This way it is possible to reject several common modes, for instance the frequency and power fluctuations of the laser, and the vibrations of the reference mirror. One of the challenge is to demonstrate experimentally strong rejection of the residual accelerations. As for the WEP test with two different atom species, our methods to extract the differential phase [84] can apply here.

3D measurements of the gravity gradient

Scientific communities request the 3D measurement of the gravity gradient. Multi-axis measurements of acceleration is studied for inertial navigation in our team (see section 4.3.3). We propose here an alternative method adapted to the use of ultra-cold atoms and the measurement of the gravity gradient. As mentioned before, the spatial separation of the atoms clouds is achieved using Bloch oscillations. The idea is to extend this separation in 2 then 3 dimensions. Figure 4.18 illustrates the 2D case. This method requires a high sensitivity and complex imaging system to measure the six outputs simultaneously.

Expected performances on our compact experiment

On our compact system (ICE experiment), The sensitivity of our experiment will be limited by the short distance between the two atom clouds, due to the dimension of the vacuum chamber which limits this distance to 10 cm. In microgravity, each atom interferometer of duration 2T=500 ms and a signal-to-noise ratio (SNR) of 100 will have a sensitivity of $10^{-8} m.s^{-2}$ per shot. Then we get a sensitivity to gravity gradient of $10^{-7} s^{-2}$ ($100E$) per shot. In the future, the sensitivity of the atomic gravity gradiometer will be improved by using large momentum transfer in the atom interferometer or improving the signal-to-noise ratio by increasing the atom number or using squeezed states. In terms of accuracy, there is no comparison with classical technologies which achieve only relative measurements, limited by the technical limitation of accurate positioning of macroscopic instruments. On the contrary, the atom position can be controlled within the ultimate limit of Heisenberg uncertainty principle and offer the possibility to measure absolute gravity gradients.

Design of an atom gravity gradiometer for Space

In collaboration with SYRTE and LUH, we led a study of an architecture proposed by Carraz and al. [137, 133]. The objective was to design a atomic gradiometer of high performance with a sensitivity of 5 mE.Hz$^{-1/2}$. Contraints on the size of the payload limits the distance between the two clouds at 50 cm. As previously mentioned, this is a strong limitation in terms of sensitivity. From this study we focused on some difficulties we need to tackle in the future.

The main principles of the design are :

— Baseline with **one** atom source split into two clouds separated by a distance of 50 cm
— **3D** cold atom gradiometer : **3 independent vacuum chambers**
— One reference mirror inside the vacuum chamber for T_{YY}, **three independent tilted mirrors inside the vacuum chamber for T_{ZZ} and T_{XX}**
— Interrogation time of 5 s
— Launching and splitting velocity : 204 $\hbar$k
— longitudinal atom cloud velocity during the interferometer and the detection : 4 $\hbar$k

The main dimensions of the vacuum chamber are based on the displacement of the atoms clouds. The atoms are first launched from the chip thanks to Raman transition and Bloch lattices. Then they are slowdown and split into two clouds corresponding to the two arms of the gradiometer. They are then stopped vertically and continue to move horizontally to complete the atom interferometer. In the detection zone, the three outputs expand freely during one second and are recombined thanks to a π pulse.

Figure 4.19 shows the design of the vacuum system for T_{ZZ} and T_{XX}. The main dimensions of the vacuum chamber are adapted to the displacement of the atoms clouds. The architecture of the BEC chamber where the ultra-cold atom source is produced is inspired by the solution designed for STE-QUEST-AI [138] but without the dipole trap. In the 2D-MOT chamber a beam of pre-cooled atoms is created by a two dimensional magneto-optical trap [139]. This pre-cooled beam of atoms is formed out of the background gas pressure created by a dispenser. In the BEC chamber this atom beam is caught by a three dimensional magneto-optical trap and the atoms are then transferred in a purely magnetic trap. The magnetic fields for the traps are created by a combination of a three-layer atom chip and comparably small magnetic coils. In the magnetic trap the atomic cloud is compressed and then cooled via RF-evaporation. The ship is parallel with the plane of the atoms clouds displacements. The transport beams launch the atoms into the cold atom interferometer (CAI) chamber. Once inside this science

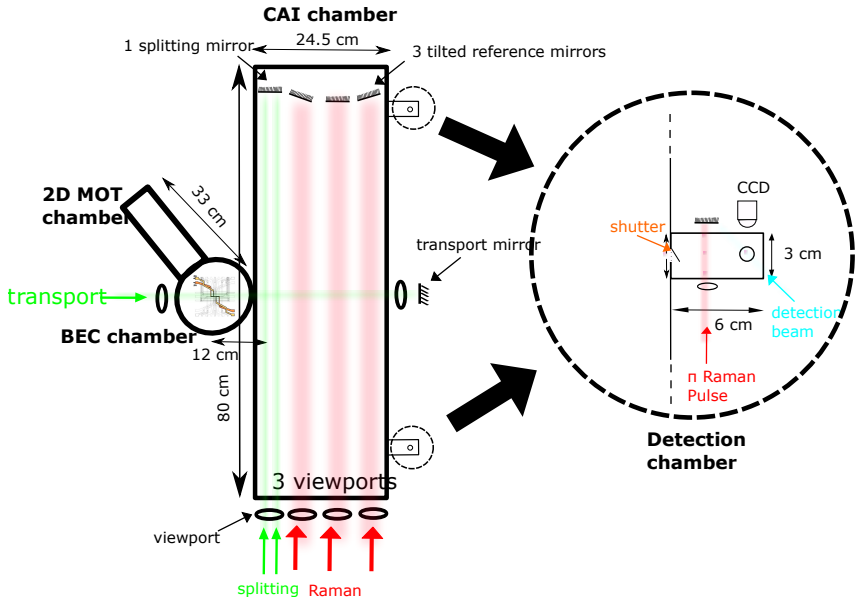

FIGURE 4.19 – Design of the vacuum system for T_{ZZ} and T_{XX}. An atom beam is produced in the 2D MOT chamber. Then the atoms are trapped in a mirror 3D MOT on a chip in the BEC chamber, where the ultra-cold atom source is achieved. Then the atom cloud is launched thanks to a Raman pulse and horizontal Bloch lattices towards the CAI chamber where the differential interferometer is produced. The atom source is slowed down thanks to horizontal Bloch lattices,then split and stopped at the entrance by applying vertical Bloch lattices. The detection is achieved in a separated small chamber in order to avoid parasitic lines. A π Raman pulse is applied to bring back the diffracted states back at the center. The detection of the 3 clouds is done by fluorescence collected on a CCD camera.

chamber, the cloud is split into two and they are stopped vertically with Bloch lattices. Then both upper and lower interferometers are done simultaneously to reject common noise such as vibrations and laser power fluctuations. 4 mirrors are fixed inside the vacuum system : one for the two vertical Bloch lattices and three tilted reference mirrors for the interferometer to compensate the rotation of the satellite which can create bias terms in the output phases and a loss of contrast. In terms of accuracy, the quality of the beam phase profile implies state of the art quality optics. The relative angle between two consecutive reference mirrors is 7 mrad corresponding to the mean rotation rate of the satellite. The two mirrors for the $\pi/2$ pulses are fixed on piezoelectric tip-tilt mounts to allow the fine control of the relative angle between the three reference mirrors. A dynamic range of $\pm 30\mu$rad and an accuracy of 10 nrad is needed, which is slightly beyond the state of the art of this technology and require custom development. The impact of these actuators on the power budget is not negligible and their power consumption needs to be optimized. For the T_{YY} cold atom interferometer (CAI), a single reference mirror is used for the splitting and the 3 interferometer pulses instead of 3 independent reference mirrors and no tiptilt mount is needed.

As previously mentioned, the rotation of the reference mirror (with the satellite) is a major issue. During this study the issue to control accurately the angles between the beams of the atom interferometer arises. Indeed, the CAI is highly sensitive to the rotations of the satellite in terms of contrast and phase shift. This control needs to be done inherently during the assembly, and/or dynamically with an active "real-time" control to correct the variation of rotations of the satellite or compensate a misalignment of the optical components. The solution of tilting the Raman beams implies a different position of the upper and the lower atom cloud in the laser profile. We studied the feasibility of a micro optical bench allowing

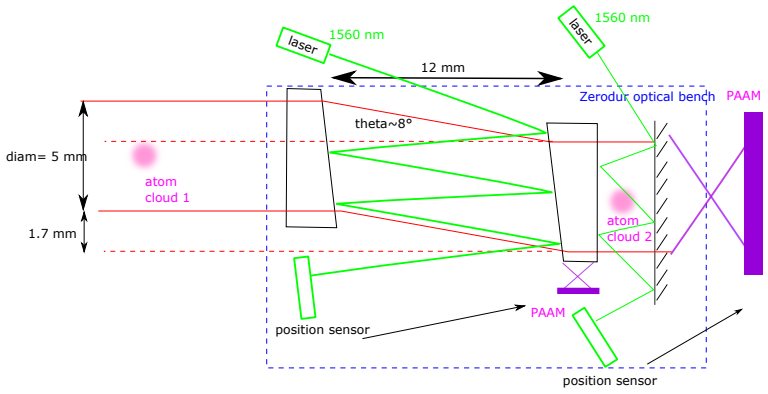

FIGURE 4.20 – System with two prisms to translate transversally the beam between the two atom clouds. a PAAM system allows to control the angle of the common reference mirror. A laser beam is reflected on the two tilted faces of the prisms and is sent on a position detector to control the relative angle between the two prims.

the beam to be translated in the transverse direction.

Our solution was based on a system of two identical prims (provided by the same piece of glass to make sure they are identical). The translation depends of the angle between the two faces of the prims and the distance between them (see Fig. 4.20). The microbench would be assembled on a ZeroDur mount, which is very stable with temperature variations, and vacuum compliant.

The alignment of the components on the micro optical bench is a strong challenge. The state of the art gives a precision around $10\mu rad$, that is to say three orders of magnitude above the specifications (10 nrad). There are basically two issues : the angle is difficult to measure during the mounting, and there is no known method to maintain the precision during the "gluing" of the components.

Piezoelectric technology is promising for the active "real-time" control of the Raman beam and allows to reach very high resolution. We identified the model S-330 2SL (Physik Instrument) corresponding to a tip-tilt mount with the following specifications :

- dynamic range : 10 μrad. This parameter has to be extended to 150 μrad (trade-off dynamic range/resolution)
- The resolution in rotation rate (1 μrad/s) satisfies the specifications.
- The repeatability (60 nrad) needs to be improved
- The angle resolution (20 nrad) is only a factor 2 above the specifications. A dedicated development seems feasible.

As an alternative, a solution developed for Lisa (PAAM : Point Ahead Angle Mechanism) can be adapted to our application [140]. It allows to rotate the mirror around an axis in the mirror plane.

Thanks to an active control of the orientation of the optics, we can imagine a solution which satisfies the contraints on the angles of the Raman beams. For instance a PAAM is used for the reference mirror to control the general angle of the Raman beam (see Fig. 4.20). A second PAAM supporting one of the prism allows to control the parallelism of the beams. To servo lock the angles, a laser beam at another wavelength (1560 nm for instance so that a dichroic coating can be put on the optic surfaces) is reflected on the two tilted faces of the prisms (respectively the prism and the reference mirror) and is sent on a position detector to control the relative angle between the two prims (respectively the prism and the reference mirror).

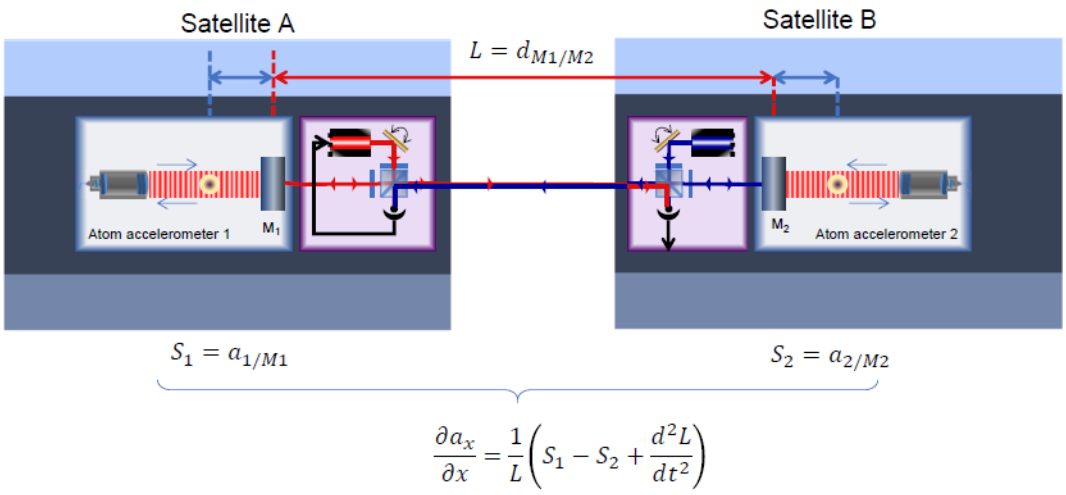

FIGURE 4.21 – Mission scenario involving twin satellites each equipped with a cold atom accelerometer. A laser telemeter is used to monitor the distance between the two satellites and couples the measurements of the two atom interferometers.

GRACE type scenario using cold atom accelerometers

An alternative scenario is to use two satellites, as for GRACE-FO, with a laser link measuring the distance between the two reference mirrors. The idea is to increase, by a large amount (100km versus 50 cm), the distance between the two acceleration measurements in order to increase the sensitivity to the gravity gradient. A study to evaluate this solution has been led at CNES (see Fig. 4.21). The major difference with GRACE-FO is the presence absolute accelerometers allows us to use the acceleration signal of these devices. In the case of GRACE-FO, the measurement is done by the laser link which is derivated twice and the relative accelerometers are used to remove the non inertial force from the signal. This implies an improvement in the data process, and no filtering (which can imply signal losses) is thus necessary.

4.5.2 Miniaturized atomic beam gyroscope

The development of a compact cold atom gyroscope adapted to inertial navigation will constitutes an important step to build a full cold atom inertial navigation system.

The project consists in building a miniaturized atomic beam gyroscope suitable for inertial navigation. The idea is to benefit from advantages of atom interferometry in terms of sensitivity and stability and make such a device compact enough to be compliant with onboard applications, with a volume typically 100 times smaller than the state of the art of cold atoms gyroscopes. Our efforts will focus on the design of a miniaturized vacuum chamber with an optical access adapted to atom interferometry, and an oven providing a collimated atomic beam with a strong flux and working in any orientation. During a first phase, we will aim at demonstrating the first measurement of a rotating rate with an atomic beam with a compact device contained in a volume of 10 dm^3.

The strategic position of our project is original in the cold atoms' community. Only a few experiments exist in France (mainly Observatoire de Paris) and worldwide (USA, Germany), and all of them are large (1 m long typically). To go towards miniaturization, most research groups opt for the use of Bose-Einstein condensates produced on atom chips [141], but the technological challenge is strong, the weak atom flux limits theoretically the signal to noise

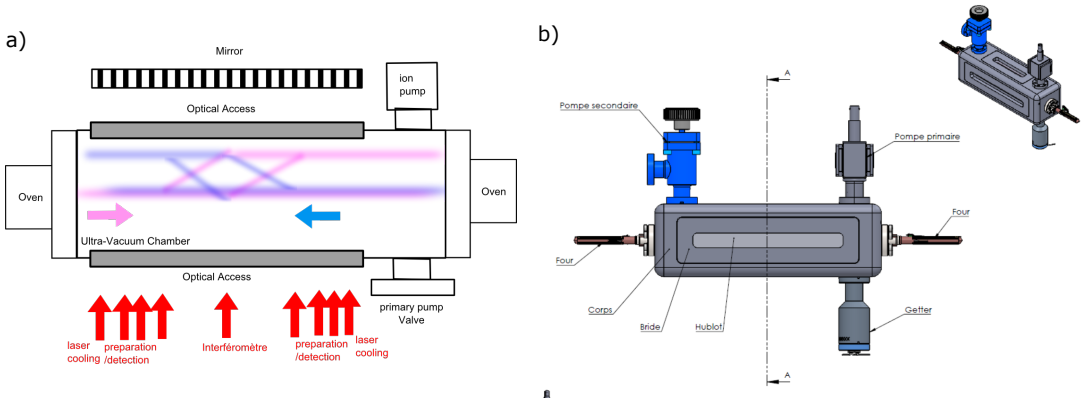

FIGURE 4.22 – (a) Drawing of the compact atomic beam gyroscope. The pink (respect. blue) atomic beam propagating from left to right (respect. from right to left) is represented following the different trajectories during the atom interferometer. Several laser beams (Red) are needed to control the trajectory of the atoms and to detect them. (b) CAO drawings of a miniature atomic beam gyroscope

ratio, and first interferometry signals have just been demonstrated with such systems [142]. Our approach is orthogonal to the atom chip development and focus on the optimization of the atom flux, and the method like the one used for existing cold atoms gyroscopes reassures us to achieve at short term rotation measurements with a miniaturized system.

An atomic beam gyroscope is composed of several parts. The first essential component is the oven producing the atomic beam. A Rubidium stock is set down in the oven and is heated at a temperature about 100° C. Porous material absorbing the gas and small geometrical aperture are necessary to collimate the atomic beam [143]. The design of the oven must be dedicated to onboard applications and will require a special care about the orientation of the system which can be random. To avoid liquid Rubidium contamination of the vacuum system, previous technics developed for optically pumped atomic clocks [144] will be considered. Finally, the lifetime of the oven (time to consume the Rubidium) is another important parameter.

The second key component is the ultra-vacuum cell. The pressure needs to be low enough ($< 10^{-9}$ mbar) to avoid collisions between the molecules of the residual gas and the atoms in the beam contributing to the signal. A pumping system (ion pump, getter) is required. The optical accesses of the vacuum cell need to include all the functions : 2D laser cooling of the atom beam, preparation of the quantum states with optical pumping, 3 interferometer beams and detection.

Our atom interferometer is also sensitive to accelerations, and more particularly gravity. This phase term can be rejected by achieving a measure of the rotation rate with two contra-propagating beams, which requires a second oven oriented in the opposite direction.

4.5.3 Hybrid magneto-grating chip for ultra-cold atoms

The common thread of future developments is the hybridization of the laser functions and the atom trapping on a single magneto-optical chip. It includes several aspects : hybridization of the optical functions laser source integrated on a chip using micro-optics and Photonic Integrated Circuits (PIC), magnetic and dipole traps, periodic potentials...

One of our future project consists in integrating optical functions on a atom chip . The idea is to create all the beams required for a 3D atom accelerometer from a single one using

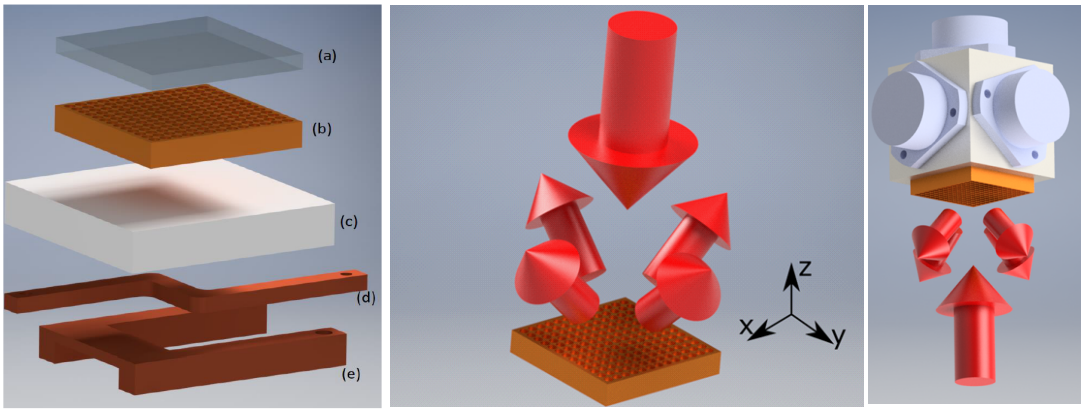

FIGURE 4.23 – (left) We envision to combine several techniques and configurations to create the ideal chip for multi-axis atom interferometry. This chip would include wires on an printed circuit board to generate the magnetic field(d)-(e), the optical grating (b) and a dichroic coating (a). (middle) The incoming and diffracted beams overlap above the grating where the MOT and optical molasses are realized. The same beams will be used as pairs of Raman beams. (right) The atom interferometers will be subsequently hybridized with classical accelerometers to form a low-bias, high-dynamic range, high-bandwidth inertial sensor.

a diffractive component. We propose to use an approach based on a grating magneto-optical trap (G-MOT) [145], which requires only a single laser beam for cooling, preparation and interrogation of the atoms. We envision a G-MOT where an incoming beam is diffracted in the ± 1 orders with equal proportions along two orthogonal directions, as shown in Fig. 4.23 (middle). This permits efficient loading and cooling of the atoms and provides beams in different spatial directions that can be used for a sequential multidimensional CAI, with acceleration-sensitive axes determined by the different combinations of wavevector directions. Utilizing velocity-sensitive Raman transitions, along with a controlled magnetic-launch of the atoms, we can select a specific sensitivity axis. The relative angles between the sensitive axes are determined solely by the grating geometry and are thus expected to exhibit an excellent long-term stability. Additionally, by utilizing a centimeter-scale glass vacuum cell, we will reduce the required volume, power consumption and overall complexity of the full sensor head.

In the Mach-Zehnder accelerometer configuration, the interferometer is sensitive to the acceleration along an axis defined by the difference of wavevectors between the beams from which photons are absorbed and emitted. We plan to use the four diffracted beams from the grating to create different wavevector combination allowing to design interferometers sensitive to the acceleration along different axes (see Fig. 4.24 (a)). This method will be used to measure the acceleration sequentially along at least three non-colinear directions, from which we can reconstruct the full acceleration vector. To develop the techniques which will be required on the grating, we will use the sensitivity to the atomic velocity of the Raman transitions, in combination with a careful choice of the incoming polarizations and quantization magnetic fields that suppress many parasitic interferometers, to choose a specific pair of beams that optimize the atom interferometers along each axis.

Figure 4.24 (b) shows the calculated Raman transition probability as a function of the frequency difference between the two Raman lasers. Each resonance is associated with a momentum transfer along a different direction, which involve specific pairs of incident and diffracted beams. Since the separation between peaks is proportional to the atomic velocity, it is possible to use this velocity to discriminate between resonances. In order to achieve sufficient

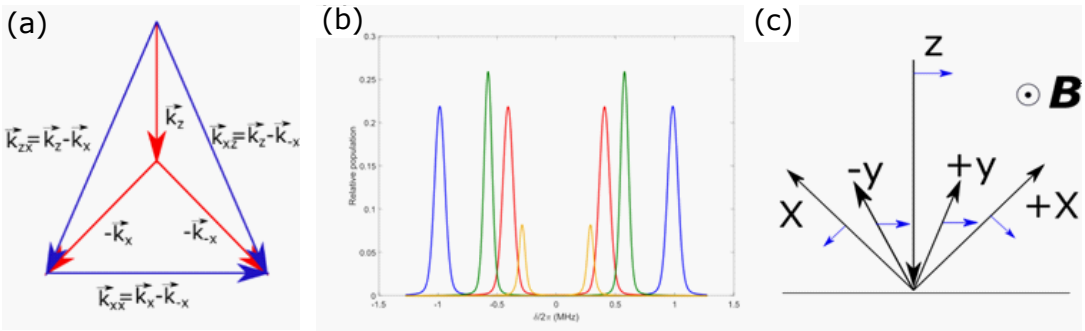

FIGURE 4.24 – (a) Wavevectors associated with incident and diffracted beams in the XZ-plane (acceleration-sensitive axes are shown in blue). A similar Delta-configuration is present in the YZ-plane. (b) Population transferred with a momentum kick along k_{xx} (green), k_{zx} (blue), k_{xz} (red) and k_{xy} (yellow) by a light pulse with length π/Ω_{xz}. The intensity of the incident beam is 60 W/m^2, and the sample temperature is 3 μK. The initial speed is diagonal to the X and Z axes : (0.32, 0, 0.32) m/s^2. (c) Incoming and diffracted light direction (black arrows), polarization (blue arrows) and magnetic field geometry. The light is linearly polarized along the X-axis, perpendicular to the magnetic field. This configuration suppresses all interferometers involving the incident beam and diffracted beams along the Y-axis.

frequency separation between resonances, the velocity must be oriented in a direction non-parallel to the incident and diffracted beams.

A specific development will be done to integrate an ultra-cold atomic source and the diffraction grating on a single chip (fig. 4.23 (left)). This new step aims to increase the performance of the miniaturized multi-axis sensor. This chip will be integrated on the miniaturized device to validate the performance of the multi-axis interferometer with ultra-cold atoms. We emphasize that implementing an ultra-cold source will allow us to overcome the limitations set by thermal atomic sources, including the ability to implement spatially resolved detection techniques, and increase the interference fringe contrast due to an improvement of the efficiency of the multi-axis Raman transitions.

Our main expertise concerns all optical methods to produce ultracold atoms. In parallel, atom chips are promising especially in terms of compactness, and hybridization of the methods can be interesting, especially to combine the large capture volume of magnetic traps and strong stiffness of dipole traps [146]. The idea to integrate the optical dipole trap (laser+focusing optics) on the magnetic atom chip was patented with iXblue. For instance, we can imagine to integrate dichroic coating offering the possibility to use beam at other wavelength for the dipole trap or Bloch oscillations (see Fig. 4.23 (left)).We can also imagine ring geometries for ultracold atom gyroscope. First signals have just been demonstrated on this system [142]. Miniaturized ultracold atom sources are also seriously considered for space applications. In this context, we have a collaboration with LCAR and CNES to optimize such atom sources.

4.6 Publications

— D. O. Sabulsky, J. Junca, G. Lefèvre, X. Zou, A. Bertoldi, B. Battelier, M. Prevedelli, G. Stern, J. Santoire, Q. Beaufils, R. Geiger, A. Landragin, B. Desruelle, P. Bouyer, B. Canuel, *A fibered laser system for the MIGA large scale atom interferometer*, Scientific Reports, **10**, 3268 (2020)

— P. Cheiney et al., *Navigation-compatible hybrid quantum accelerometer using a Kalman*

Filter, Phys. Rev. Applied. **10**, 034030 (2018)

— B. Battelier, B. Barrett, L. Fouché, L. Chichet, L. Antoni-Micollier, H. Porte, F. Napolitano, J. Lautier, A. Landragin, P. Bouyer, *Development of compact cold-atom sensors for inertial navigation*, Proceedings of SPIE, Quantum Optics, **9900**, 990004 (2016)

— B. Barrett, P.-A. Gominet, E. Cantin, L. Antoni-Micollier, A. Bertoldi, B. Battelier, P. Bouyer, J. Lautier, A. Landragin, *Mobile and remote inertial sensing with atom interferometers*, Proceedings of the International School of Physics "Enrico Fermi", **188**, 493-555 (2014)

— V. Ménoret, R. Geiger, G. Stern, N. Zahzam, B. Battelier, A. Bresson, A. Landragin, P. Bouyer, *Dual-wavelength laser source for onboard atom interferometry*, Optics Letters, **36**, 21, 4128–4130 (2011)

— R. Geiger, V. Ménoret, G. Stern, N. Zahzam, P. Cheinet, B. Battelier, A. Villing, F. Moron, M. Lours, Y. Bidel, A. Bresson, A. Landragin, P. Bouyer, *Detecting inertial effects with airborne matter-wave interferometry*, Nature Communications, **2**, 474 (2011)

— G. Stern, B. Allard, M. Robert-De-Saint-Vincent, J-P Brantut, B. Battelier, T. Bourdel, P. Bouyer, *A frequency doubled 1534 nm laser system for potassium laser cooling*, Applied Optics **49**, 16 (2010)

Chapitre 5

Outlook : ultra-cold quantum gases in microgravity

Our ability to produce ultra-cold atoms in microgravity paves the way to create quantum objects with new properties. The unique topological configuration of ultra-cold atoms confined in 2D bubble-shaped traps is worth being studied. Interactions and the shell trap curvature play essential roles in vortices dynamics and phase transitions involving both Bose Einstein condensation and superfluidity. Our experiment installed on the ZERO-G simulator is a perfect tool adapted to this research activity. I want to emphasize the easy access of microgravity with this apparatus making such experiments available in all laboratories. Moreover our optical methods based on laser cooling (grey molasses), a telecom dipole trap and painting potentials are powerful tools to develop a new generation of experiments, exploring a large panel of physical phenomena going from condensed matter physics (BKT transition, Anderson localization) to the heart of quantum mechanics (cold atoms at extreme low temperature, Bell's inequalities).

5.1 Quantum Bubbles in microgravity

5.1.1 Bose Einstein Condensation in cold gases

We start with a short reminder about the main features of Bose Einstein Condensation.

Saturation of the excited levels

Let's consider a ideal gas of N bosons at temperature T in cubic box of size L^3. In the approximation of the continuous spectrum, the total atom number can be expressed as a function of the density of states $\mathcal{D}(\epsilon)$ and $n(\epsilon)$ the statistical distribution of the population for each energy state ϵ :

$$N = \int_0^\infty \mathcal{D}(\epsilon) n(\epsilon) d\epsilon = \int_0^\infty \frac{\mathcal{D}(\epsilon)}{e^{\beta(\epsilon-\mu)-1}} d\epsilon = \frac{L^3}{\lambda_{th}^3} \frac{2}{\sqrt{\pi}} \int_0^\infty dx \sqrt{x} \frac{1}{e^{x-\beta\mu}-1} \tag{5.1}$$

where $\beta = 1/k_B T$ and μ the chemical potential. The condition $n(\epsilon) \geq 0$ for all ϵ implies the chemical potential μ is negative so the term $e^{\beta\mu}$ is between 0 and 1. We can thus write the phase space density :

$$\rho^{3D} \lambda_{th}^3 = g_{3/2}\left(e^{\beta\mu}\right) \tag{5.2}$$

The relation between $\rho^{3D}\lambda_{th}^3$ and μ stop to have a solution above the critical value $\rho^{3D}\lambda_{th}^3 = 2.612$, which is the signature of the Bose Einstein condensation. In an harmonic trap, the density is resplaced by the central density $\rho^{3D}(\mathbf{0})\lambda_{th}^3 = 2.612$.

Coherence and macroscopic wave function

A Bose-Einstein condensation is often considered as an atom laser, with a full coherence. Without interactions, all the atoms fall in the fundamental level of the harmonic trap. In this case, the wave function describing the system is a Gaussian function.

In the case of an interacting Bose gas, we can write the atom field operator as in optics with the Glauber transformation, which is used to describe a system where photons occupy macroscopically a mode of the electromagnetic field :

$$\hat{\Psi}(\mathbf{r}) = \sqrt{N}\psi(\mathbf{r}) + \delta\hat{\Psi}(\mathbf{r}) \tag{5.3}$$

where ψ is a classical field and $\delta\hat{\Psi}$ represents the quantum fluctuations of the Bosonic field. The hypothesis of condensation amounts to neglect these fluctuations. We call about symmetry breaking because the phase of the quantum field, previously unknown, takes the value imposed by the macroscopic wave function ψ. This field follows the Gross-Pitaievskii (GP) equation :

$$i\hbar\frac{\partial}{\partial t}\psi(\mathbf{r},t) = -\frac{\hbar^2}{2m}\nabla^2\psi + U(\mathbf{r})\psi + Ng|\psi(\mathbf{r}|^2\psi(\mathbf{r}) \tag{5.4}$$

We find a Schrödinger equation as in Optics, with an additional non linear term due to the interactions.

Superfluidity

The definition of superfluidity is related to fluid transport and is defined as the characteristic property of a fluid with zero viscosity. For example the existence of minimum critical velocity to put the fluid in movement is a signature of superfluidity. The superfluid velocity field is irrotational and the velocity can be expressed as the gradient of a phase S :

$$v_S = \frac{\hbar}{m}\nabla S \tag{5.5}$$

Irrotationality of flow is a fundamental feature of superfluids which leads for instance to the quantization of circulation and quantized vortices.

Superfluidity has been observed for the first time in Liquid Helium cooled below 2.2 K [147], and then explained by London [148]. Bose-Einstein condensation (BEC) is considered as a key phenomena hidden beyond superfluidity. A natural link between BEC and superfluidity [149] is given by the order parameter :

$$\Psi = |\Psi|e^{iS} \tag{5.6}$$

$|\Psi|$ is the square root of the condensate density, and the gradient of the phase S is directly related to the superfluid velocity (see Eq. 5.5).

Interactions and quantum fluctuations of the Bosonic field play a crucial role in the case of Liquid He and BEC is difficult to study in such systems. For instance, Liquid He is 100% superfluid but only 10% is condensed. The situation is different in the case of dilute systems such as ultracold Bose gases, which then constitute nice objects to study the relationship between BEC and superfluidity..

Hydrodynamic (HD) equations of superfluid at $T = 0$ can be retrieved from the GP equation if quantum pressure is negligible (this is the case if the cold gas is dilute).

$$\frac{\partial}{\partial t}n + \nabla(v_S n) = 0 \tag{5.7}$$

$$m\frac{\partial}{\partial t}v_S + \nabla\left(\frac{1}{2}mv_S^2 + \mu(n) + V_{ext}\right) = 0 \tag{5.8}$$

n is the total density and can differ from the density of the BEC. These equations are useful to study the collective modes and the free expansion of cold atom gases.

Reciprocally, the hydrodynamic behavior cannot be used as a proof of superfluidity. For irrotational velocity flow the two HD equations of superfluid and collisional regime [149] coincide. For instance, collective oscillations of irrotational nature are identical (provided the equation of state is the same). On the contrary, rotational effects provide a more stringent test of superfluidity. The signature will be the appearance of vortices above a critical rotation rate.

A quantum fluid having no viscosity, he cannot developed vorticity at its heart. The only way to put it in rotation is to create singularities lines where the cloud density is zero and where the whirl vector is localized. We can show that, as the consequence of the existence of the macroscopic wave function, the circulation of the velocity field around the vortices is quantified, the circulation quanta being $\hbar/m$.

5.1.2 Two-dimensional ultra-cold Bose gas

Low dimensional systems, particularly in 2D, have been arousing many studies for a long time. Indeed, the density of states, which differs from the tridimensional case (3D), modifies strongly the expected physical effects [1].

To illustrate this effect in a simple way, let's consider a ideal gas at temperature T, confined in a square box of size L^2. The density of states $\mathcal{D}(\epsilon)$ is constant for a uniform 2D gas. Using the Bose-Einstein statistic law and supposing a progressive variation of the population in the the different energy level :

$$N = \left(\frac{L}{\lambda_{th}}\right)^2 \int_0^{+\infty} \frac{dx}{e^{x-\beta\mu} - 1} \tag{5.9}$$

In the thermodynamic limit $N, L \to \infty$ with the spatial density $\rho = N/L^2$ constant, we get the following equation :

$$\rho\lambda_{th}^2 = -\ln\left(1 - e^{\beta\mu}\right) \tag{5.10}$$

For any value of $\rho\lambda_{th}^2$, it is possible to find a chemical potential μ. it means there is no condensation in 2D (absence of saturation of the excited levels).

Let's consider now the case with interactions. As soon as the 30's, Peierls showed the long range order cannot be established in a solid in reduced dimensionality [150]. In the same way, Bose-Einstein condensation in a homogeneous 2D system is impossible at non zero temperature.

To understand this statement a proof by contradiction can be given. Suppose the temperature is low but not zero, and the condensate is present in the mode $\mathbf{k} = 0$, with a spatial density ρ_0. We can prove the particle number $\tilde{n}_\mathbf{k}$ in the state $\mathbf{k} \neq 0$ satisfies :

$$\tilde{n}_\mathbf{k} \geq -\frac{1}{2} + \frac{k_B T}{\hbar^2 k^2/m}\frac{\rho_0}{\rho} \tag{5.11}$$

1. The regime considered in this chapter is not purely 2D but "quasi-2D" : interactions are 3D (often the case in the existing experiments where the scattering length is much smaller than the size of the wave function in the fundamental level), even if the "physical" behavior of the system is 2D.

In the thermodynamic limit the particles number N' in the excited states is :

$$N' = \sum_{\mathbf{k}} \tilde{n}_{\mathbf{k}} = \frac{L^2}{4\pi^2} \int \tilde{n}(\mathbf{k}) d^2k \tag{5.12}$$

When $k \to 0$, the principal term in the inequality 5.11 varies as $1/k^2$. This lead to a diverging logarithmic contribution when the inferior bound of the integral goes to 0. It means the initial statement of the existence of a BEC is wrong.

Nevertheless, in presence of interactions, a phase transition between a normal phase and a superfluid phase, discovered by Berezinskii [151], Kosterlitz et Thouless [152] (BKT transition which were the subject of the Physics Nobel Prize in 2016) is expected and differs from the Bose-Einstein condensation in 3D. The loss of superfluidity at the transition is related to the break of vortex/antivortex pairs present in the superfluid phase. In view of its difference, the 2D physics is very rich and gave birth to a large panel of experiment, such as the measurement of the superfluid density in Liquid Helium films [153] and the study of collisions in hydrogen 2D gases [154]. New phenomena can appear such as Quantum Hall effect when a 2D electron gas is immersed in a magnetic field. Materials with surprising properties were discovered like High Tc supraconductors constituted of a superposition of CuO planes. Finally, we can cite quantum wells in laser diodes which are honorable representatives of the 2D systems.

For a 2D Bose gas with interactions, the superfluid phase can be described as a quasi BEC which can be decomposed by blocks where the phase is quasi constant [155]. In other word it corresponds to a BEC with a fluctuating phase $S(\mathbf{r})$, which corresponds to a quasi Long Range Order (LRO).

$$\Psi(\mathbf{r}) = |\Psi(\mathbf{r})| e^{iS(\mathbf{r})} \tag{5.13}$$

For any non null T, S(r) is "spontaneously" non constant (no external excitation of the system).

The expected phase transitions in the different cases are presented on Fig. 5.1 and are based on the discussions in [156]. The relation between BKT and BEC transition is subtle. In a general way, the parameters of the experiment such as the interactions or the size of the system play a role.

Box trap

For large systems, the first relevant mechanism that occurs when increasing the phase space density is a BKT transition (see Fig. 5.1 (b)). However, the approach of the BKT threshold always results in the appearance of a significant condensed fraction. We can qualify this "BKT-driven" condensation as "interaction-enhanced", since it would not take place in an ideal gas with the same density and temperature. According to the Penrose-Onsager criterion, no condensate is expected in an infinite system since $g_1(r)$ vanishes at infinity for any non-zero temperature.

In the regime of a small system the first phenomenon that is encountered when the phase space density is increased is "conventional" Bose-Einstein condensation as for an ideal Bose Gas (see Fig. 5.1 (c)). As in the 3D case, in the presence of weak repulsive interactions the formation of a condensate is accompanied by the apparition of a superfluid fraction with a comparable value.

Harmonic trap

In an harmonic trap, the density of states is $\mathcal{D}(\epsilon) \propto \epsilon$. Let's consider N bosons confined in a potential $V(r) = m\omega^2 r^2/2$ in a plane. The Bose Einstein condensation appends below

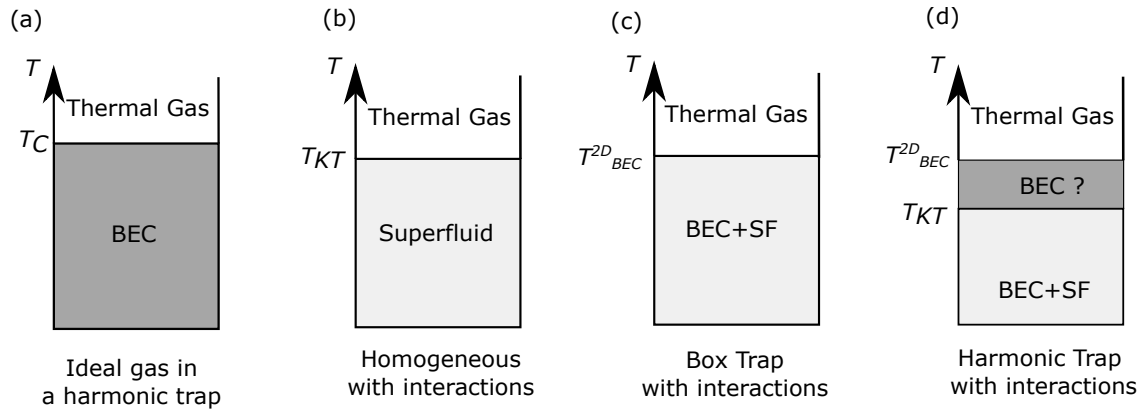

FIGURE 5.1 – Different existing phases in a 2D Bose gas. (a) In the case of a ideal gas localized in an harmonic trap, there is a non-zero critical temperature T_c under which there is a Bose Einstein condensate (BEC). (b) In the case of an homogeneous gas with interactions, there is no true condensate at non-zero temperature but there is a superfluid phase corresponding to a quasi-condensate with a fluctuating phase below a critical temperature T_{KT}. In the case of a gas with interactions localized in a box trap, the situation is complex and two different regimes are possible depending on the size of the system. For large systems, the situation tend towards the case (b) of the infinite homogeneous gas, and the BEC transition is BKT-driven (or in other words interactions-enhanced). (c) For small systems, There is a standard BEC transition first as in the case of the ideal gas. (d) In the case of the harmonic trap, the situation depends of the experimental parameters.

the critical temperature T_c [157] (see Fig. 5.1 (a)) :

$$N_{c,id} = \frac{\pi^2}{6}\left(\frac{k_B T_c}{\hbar\omega}\right)^2 \tag{5.14}$$

With interactions, the question "what comes first" is even more subtle in the case of a harmonically trapped gas because of the inhomogeneous density profile. We can think of the BEC transition as a special non-interacting limit of the more general BKT theory. In [158], they tune the interactions and measure the critical point for the emergence of the coherence from the BEC regime (no interactions) to BKT regime (interactions) and the evolution of the critical atom number is consistent with the predicted value of N_c^{BKT}. Experimentally, in the regime of low g, the BKT and the BEC transition are no longer distinct.

In the regime of the existing experiment, BEC occurs before BKT transition only for extremely weakly interacting gas. In this case, BEC occurs at a finite phase space density D_{BEC} in the trap center, which can be in principle lower than than D_C. In Bill Philips' group [159], an increase of the coherence length larger than the thermal cloud and a reduction of the density fluctuations happens above T_{KT} and is presented as a signature of Bose Einstein Condensation. This happens "before" the appearance of a superfluidity phase (see Fig. 5.1 (d)). They also image a three component spatial profile confirming this fact. Their experiment is very peculiar in the sense it demonstrates a separation between BEC and superfluidity. This effect is not observed yet on experiments with larger interactions.

5.1.3 2D cold gases in a shell shaped trap

New kind of traps are invented and produced to highlight the influence of the density of states, especially in 2D systems. We can cite the production of cold atoms inside a box shaped trap [160], similar to an homogeneous gas except for the edge effects. Proposals to

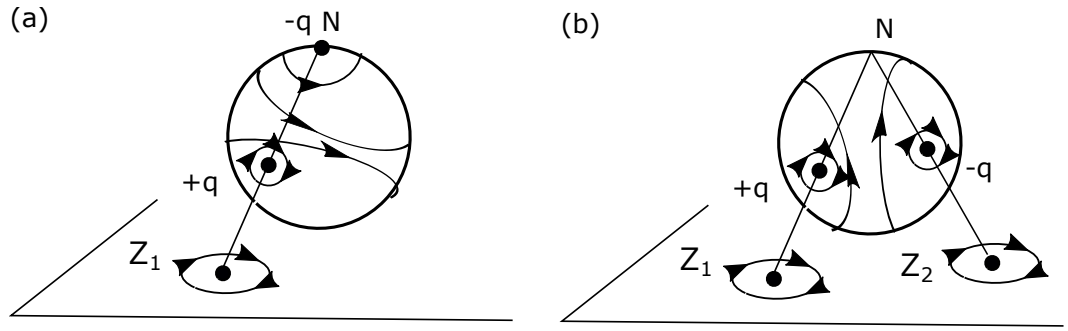

FIGURE 5.2 – (a) Function projected onto the sphere representating a vortex of charge q at the point associated with z_1 and an antivortex at the north pole N. (b) Function projected onto the sphere representing a vortex at the point associated with z_1, and an antivortex at the point associated with z_2.

create bubble-shaped traps are based on the use of a magnetic trap and atoms dressed by RF or microwave fields [161]. Unattainable in standard gravity because the atoms fall at the bottom of the trap, these experiments are proposed today for the NASA Cold Atom Laboratory (CAL) which produces ultracold atoms onboard the International Space Station (ISS) [162].

A spherical surface is topologically inequivalent to the 2D flat plane. In particular, the presence of a point at infinity allows only for couples of topological defects to exist, being vortex-antivortex dipoles, or free vortices (see Fig. 5.2). Despite this fact, the BKT theory is expected identical on a sphere. Indeed, the spherical surface is locally isomorphic to the Euclidean plane [163].

BEC transition on a sphere exists at non zero temperature T_{BEC}. In reference [164] Bose Einstein Condensation is present before BKT ($T_{BKT} < T_{BEC}$), especially when nR^2 is not too big (small sphere radius R or low atom density n). The BEC temperature range without superfluidity is reducing when the size of the sphere or the atom number increases. This region was experimentally observed in a quasi-2D finite-size Bose gas [159] (Fig. 5.1(d)). At low density, the curvature of the sphere may play the same role of their 2D weak external potential.

Static, dynamic, and topological properties of hollow systems differ from those that are fully filled as a result of the presence of a boundary associated with an inner surface. For instance, a different response of the collective modes for a filled BEC and a hollow ultracold gas is expected [165, 166]. Shell-shaped BECs would be a test bed for quantum fluids in this topology, which naturally occurs in several diverse situations from laboratory-based micron scales to astronomical scales. In cold atomic systems, condensate shells are expected in Bose-Fermi mixtures [167, 168, 169] and optical-lattice "wedding-cake" structures [170, 171, 172] where Mott-insulating regions effectively trap superfluid layers [173].

Concrete and robust signatures are expected due to the emergence of an inner boundary, inclusive of a dip in breathing-mode-type collective mode frequencies and a restructuring of surface mode structure across the transition [165]. It is expected that the frequency spectrum of the breathing modes shows a pronounced depression as it evolves from the filled sphere limit to the hollowing transition [166]. Surface modes bring also a strong signature of the hollowness of the trap but are more difficult to excite.

We want to study several features expected for quantum bubbles :

— **Define the phase diagram expected in 2D shell traps**. Ideally we need to modify the interaction strength using Fesbach resonances, since interactions play a key role for

the relationship between BEC and BKT transitions. An interesting feature would be to change the radius of the sphere going from an harmonic trap type regime (as curvature may play the role of the harmonic potential) to an homogeneous trap ($R \to \infty$). In some way, the sphere topology hollows to control the harmoniticity of the trap.

— **Study of the dynamics of the vortices**. Defects such as vortices on a curved surface experience a force due to the local curvature [174, 175]. A vortex-antivortex pair annahiles itself because of the long range interaction between the two vortices [176]. A way to stabilize the pair is to put the bubble in rotation above a critical rotation rate. The pair is stabilized by being at the opposite diameter of the sphere and in the direction of the rotation axis. It has also been demonstrated in the context of magnetic excitations that two vortices of same charge will expel each other [177].

— **Study of the transition between a thin shell and a full sphere**. A study of the excited modes [166] allows to highlight the hollowness of a BEC. Morever, the critical rotation rate to stabilize the vortex on the surface of the quantum bubble is increasing with the thickness of the shell [176]. The measurement of this critical rotation rate is a way to estimate the hollowness of the system.

5.1.4 All optical method to create an atom bubble trap

We propose here an all optical alternative method to RF-dressed states in magnetic traps, which is clearly better for 3D detection and offers the possibility to use Feschbach resonances to change the interaction strength. Our method to produce quantum bubbles is inspired by double dressed states which have been studied in our group to trap Rubidium atoms close to a surface [178] combining the telecom wavelength of the dipole trap and a laser emitting at 780 nm. Let's first explain this principle in 1D. If the optical frequency of the dipole trap laser is blue detuned compared to $5p_{3/2} \to 4d_{5/2}$ ($\lambda < 1529$ nm), the excited state $5p_{3/2}$ sees a repulsive potential while the atoms in the ground state $5s_{1/2}$ are trapped (which corresponds to the usual dipole trap). The $5s - 5p$ transition frequency $w_0(z)$ therefore depends on the distance z. Double dressing is achieved by using a second laser at frequency w_L ($\lambda = 780$ nm) tuned close to the free space $5s - 5p$ transition $w_{0,vac}$. The resulting AC Stark shift on the $5s$ state, is governed by the spatially-dependent detuning $\Delta(z) = w_L - w_0(z)$ (see Fig 5.3(b)), which cancels at position z_B. This position directly depends on the laser frequency 780 nm w_L. For positions $|z| < |z_B|$, the detuning $\Delta(z)$ is positive (blue) and the doubly-dressed potential expels the atoms away from the center of the telecom laser beam. As depicted in Fig 5.3(c) a trap is then formed by the doubly-dressed state potentials.

The dipole force depends on the relative state populations ρ_{ee} ($5P$) and ρ_{gg} ($5S$) [96]. In the quasi-static regime :

$$\mathbf{F}_{dip}(\mathbf{z}) = -\frac{dU_{5P}}{dz}\rho_{ee}(z)\mathbf{z} - \frac{dU_{5S}}{dz}\rho_{gg}(z)\mathbf{z} \tag{5.15}$$

where U_{5P} and U_{5S} are the respective potentials created by the telecom laser on the two states $5P$ and $5S$. The populations are given by the optical Bloch equations. In the quasi-static mode :

$$\rho_{ee}(z) = \frac{\Omega_R^2}{\Gamma^2 + 4\Delta(z)^2 + 2\Omega_R^2} \tag{5.16}$$

and

$$\rho_{gg}(z) = 1 - \rho_{ee}(z) \tag{5.17}$$

Ω_R is the Rabi frequency related to the 780 nm light and Γ the lifetime of the excited

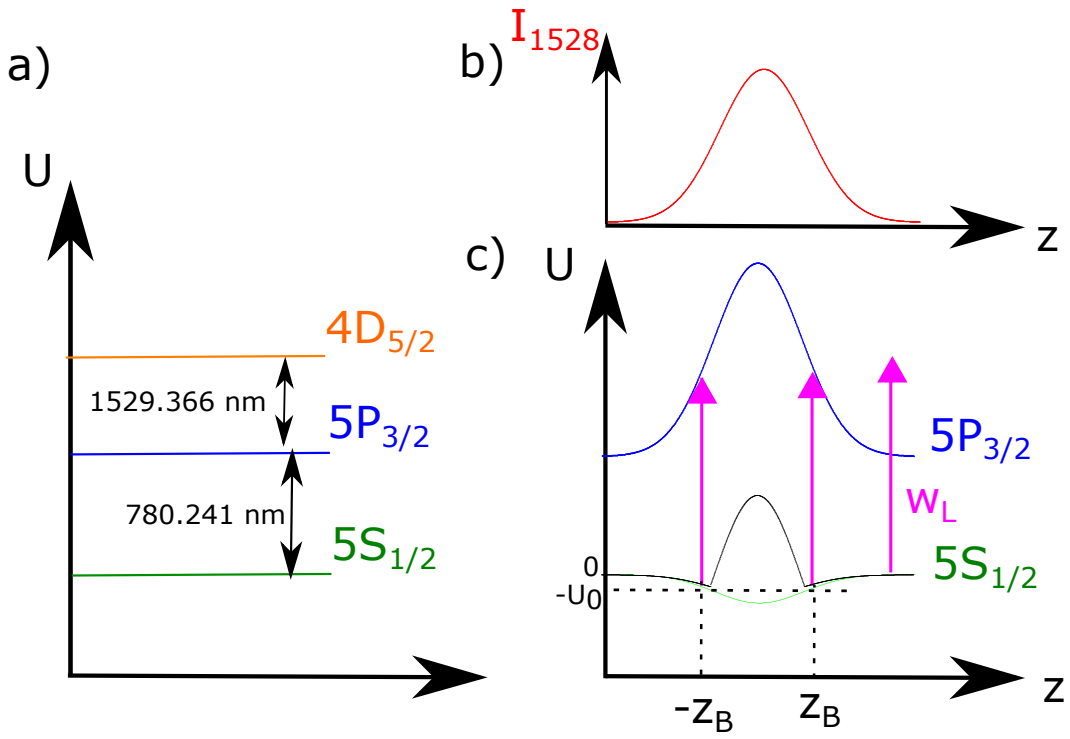

FIGURE 5.3 – a) Rubidium level structure b) Intensity profile of the dipole/double dressed state laser blue detuned compared to the $5p_{3/2} \rightarrow 4d_{5/2}$ transition. c) Modulated $5p$ (blue) and $5d$ (green)states. By adding a light beam at 780 nm (w_L), we obtain a double dressed state (black) with two minima at $-z_B$ and z_B.

state $5p_{3/2}$. The spatial dependence of the detuning $\Delta(z)$ "modulates" the populations and consequently "shapes" the total force by counterbalancing the forces applied on each state.

If we consider an atom coming from the outside of the trap, the total dipole potential is :

$$U_{tot}(z) = -\int_{\infty}^{z} \left(\frac{dU_{5P}}{dz'} \rho_{ee}(z') + \frac{dU_{5S}}{dz'} \rho_{gg}(z') \right) dz' \tag{5.18}$$

The potential $U_{tot}(z)$ (Fig. 5.4 (a)) is calculated for the following parameters. The telecom laser has a beam waist of 10 μm, a wavelength $\lambda = 1529.26$nm and the power is $P = 0.925$ W in a single beam configuration. Concerning the 780 nm laser light, $\Omega_R = 2\pi \times 10$ MHz and the detuning on the transition $5s - 5p$ is $\Delta(z = \infty) = 0$ Hz . Fig. 5.4 (b) shows the evolution of the population in the two states 5S and 5P when the atoms enter the double dressed trap.

For this parameters, we found a trap frequency of 11 kHz, a trap depth of $U_0/h = -5.1$ MHz and a radius of the bubble $|z_B| = 17.7$ μm.

We now estimate the lifetime due to heating in the trap located at z_B. The required time for a trapped atom to emit spontaneously a photon is related to the population in the excited state :

$$\tau_d = \frac{1}{\Gamma \rho_{ee}(z_B)} \tag{5.19}$$

We can deduce the escaping time required for the atoms to accumulate enough energy (above the trap depth U_0) to escape the trap :

$$\tau_\Gamma = \frac{2mU_0}{p_{eff}^2 \Gamma \rho_{ee}(z_B)} \tag{5.20}$$

where $p_{eff} = \hbar k$ is the momentum recoil due to the emission of one photon. With the trap

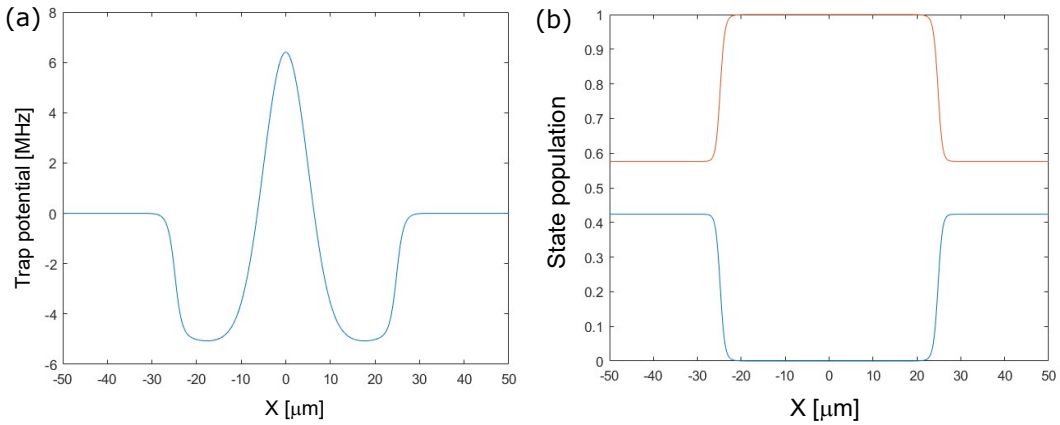

FIGURE 5.4 – (a) Calculation of the double dressed potential $U_{tot}(x)$ in 1 dimension. (b) Population in the state $5p_{3/2}$ (blue) and in the state $5s_{1/2}$ (orange) versus the position of the atoms.

parameters presented just above, we get a diffusion time $\tau_d = 1.1$ms and an escaping time $\tau_\Gamma = 1.4$ s. Other limitations for the lifetime need to be investigated : the tunnelling effect accross the bubble trap, the anti-damping effect due to non adiabatic terms in the dipole force, and a transitory heating due to the fact the atom is not trapped anymore just after a spontaneous emission. It has been done in another context for another double dressed traps which inspired this proposal (see the thesis of Maxime Bellouvet [180]).

In 3D, the trap corresponds to an equipotential surface of the initial dipole trap and has a shape of an ellipsoid or a sphere. The atoms are trapped in this shell. Moreover, a technique of spatial modulation, thanks to an acousto-optical modulator (already implemented on our experiment), allows to control the geometry of the initial dipole trap and thus the sphericity of the shell trap. We should emphasize here that using the same laser beam for the dipole trap ($5S$ state) and the repulsive potential of the $5P$ state ensures a perfect alignment of the two effects, which makes the experiment robust for our modulation method.

Unlike the RF dressed states method which requires large coils or an atom chip, the all optical method allows a good optical access. Moreover, the strong tunability of the trap is guaranteed by the control of the laser parameters. More specifically, tuning between the filled sphere and thin shell limit offers a means of achieving dimensional cross-over from three-dimensional (3D) to two-dimensional (2D) behavior. We expect thermodynamics and collective mode properties to be acutely sensitive to dimensionality.

We can imagine to generalize our concept of time-modulated potential in 2D. Indeed in our configuration, our trap is an ellipse with the strongest confinement in the vertical direction. The idea is to implement a second AOM perpendicular to the first one and to modulate in the vertical Z direction.

3D detection

To study these quantum bubbles, we envision to set up a 3D detection scheme. The classical method to detect ultracold atoms is to project the shadow of the atom cloud on a CCD camera through the absorption of a resonant beam. The disadvantage is the information loss in the direction of the absorption beam which integrates the signal in the propagation direction. This is particularly problematic in our case, since we want to explore the full sphere.

A 3D detection scheme has been proposed in [181]. The principle is to let the atom cloud

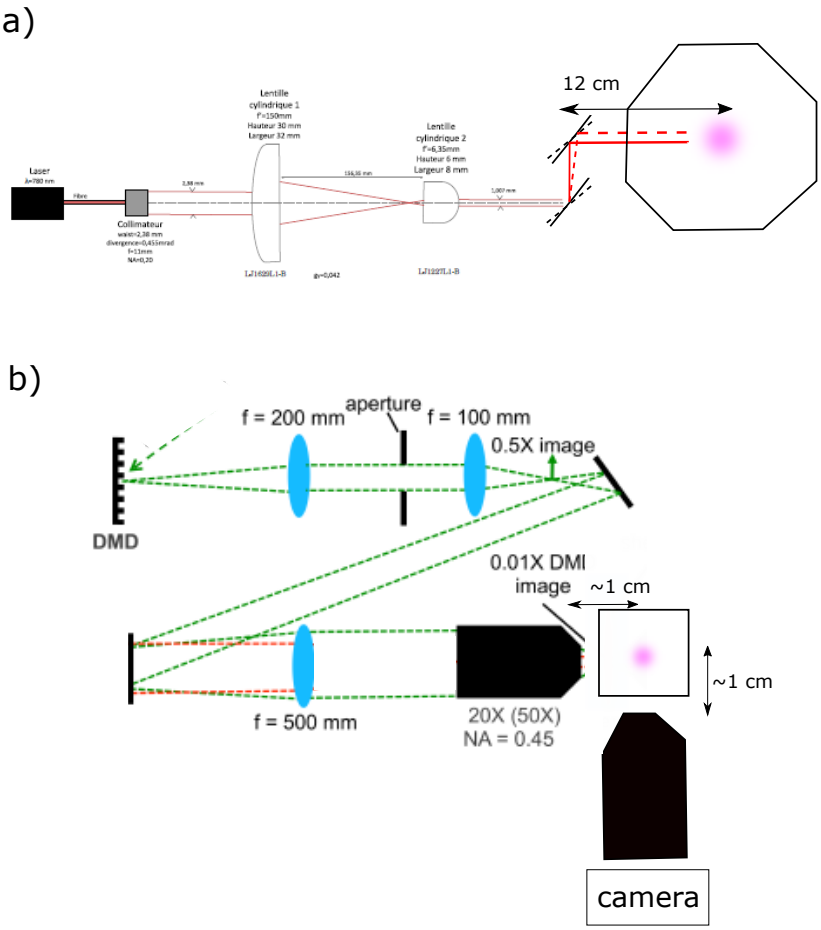

FIGURE 5.5 – a) "Macroscopic" scheme of the 3D detection on the current experiment. The light sheet is created by a telescope composed of two cylindrical lenses. The sheet is displaced by two synchronised rotating mirrors. b) "Microscopic" scheme of the 3D detection on a future experiment. A Digital Micromirror Device (DMD) creates a profile which is imaged on the atoms through a system composed of a set of lenses and an objective.

fall in a light sheet situated in the imaging plane of an optical system of large numerical aperture. The problem for experiments in microgravity is that the atom cloud doesn't "fall" (more exactly the experiment falls with the atoms as well). We'd like to adapt this method by moving spatially the light sheet, scanning the atom clouds, while keeping the spatial resolution of the detection system.

A "macroscopic" solution will be installed on our current setup (see Fig.5.5 (a)). The atom cloud after free expansion has a diameter of 1 mm, and is imaged by 10 light sheet pulses with a thickness of 100 microns. A "microscopic" solution (see Fig.5.5 (b)) will be installed on the next generation of our experiment. The atom cloud of 100 microns of diameter will be imaged in situ, using 10 light sheet pulses with a thickness of 10 microns.

For the 2D case, it has been shown theoretically that the two-point density correlation function after TOF can provide information on the in situ g_1 function, at least in the superfluid regime [156]. This method is also specific to 3D time of flight, where the phase noise evolves into density noise in interaction-free ballistic expansion. The 3D detection we want to develop can be used to study the density correlation.

Is a quantum bubble still a bubble after time of flight ?

The answer to this question is probably dependent of the experimental parameters (radius R and thickness δr of the bubble, interaction strength,...). Let's consider a 2D bubble ($\mu, k_B T < \hbar\omega$). δr is the width of the wave function of the fundamental energy level in the radial direction. If we neglect the curvature ($R >> \delta r$) so we can apply Local Density Approximation, it is still a sphere after free expansion. We turn the full double dressed state trap off and the bubble expand. The first phase of the expansion is due to interactions and mainly happen in the most confined radial direction, so the sphere will become thick. Then we reach the stage of velocity/position correspondence, and then the sphere just scales proportionally with time of flight.

When the curvature is not negligible, the dynamics of the spherical shell upon release of the trapping potential has noteworthy features absent in the case of the filled sphere. Upon release, the initial confinement of the condensate causes the outer edge to expand outwards and the inner edge to collapse inwards. As a result, the system can potentially exhibit accumulation of mass at the center, and the condensate can interfere with itself when diametrically opposite regions come together. Upon trap release and subsequent expansion, the system displays self-interference fringes [182].

5.1.5 Rotation of the quantum bubble

The presence of vortices in rotating BECs constitutes a direct proof of the superfluidity of the ultracold gas. In the same way, we can envision to put the sphere in rotation to reveal the superfluidity of the system. The existence of a critical rotation rate to insure the stability of a vortex-antivortex pair has been studied theoretically [176]. Further theoretical background is currently under investigation for faster rotations and the study of a system containing multi-vortices.

Our setup of optical time averaged potential can be used to generate this rotation. A second AOM orthogonal to the first one is necessery to modulate in 2D. The idea is to produce a rotating ellongated trap in a vertical plane perpendicular to the rotation axis (see for instance [183] for a rotating 3D BEC). The elliptical trap is created by a fast modulation along the diagonal direction which is time averaged for the atoms. The time averaged potential $\xi(t)$ (see paragraph 2.6 in chapter 2) is now applied in a diagonal direction θ. Then the idea is to rotate "slowly" (compared to the modulation of the time averaged potential) the ellipsoid trap. The modulation functions on the two AOMs X and Y are :

$$\xi_x(t) = \xi(t)\cos(\theta(t))u_x \tag{5.21}$$

$$\xi_y(t) = \xi(t)\sin(\theta(t))u_y \tag{5.22}$$

Fig. 5.6 presents the principles to make the bubble rotate. We need to adapt the configuration of our dipole trap to have two independent crossed beams.

5.1.6 Analogy with other bubble-shaped objects

Bubbles of smectic Liquid Crystals

In the field of complex fluids, the properties of auto-organisation of matter are studied by a new approach consisting in taking advantage of topological defects in crystal liquid

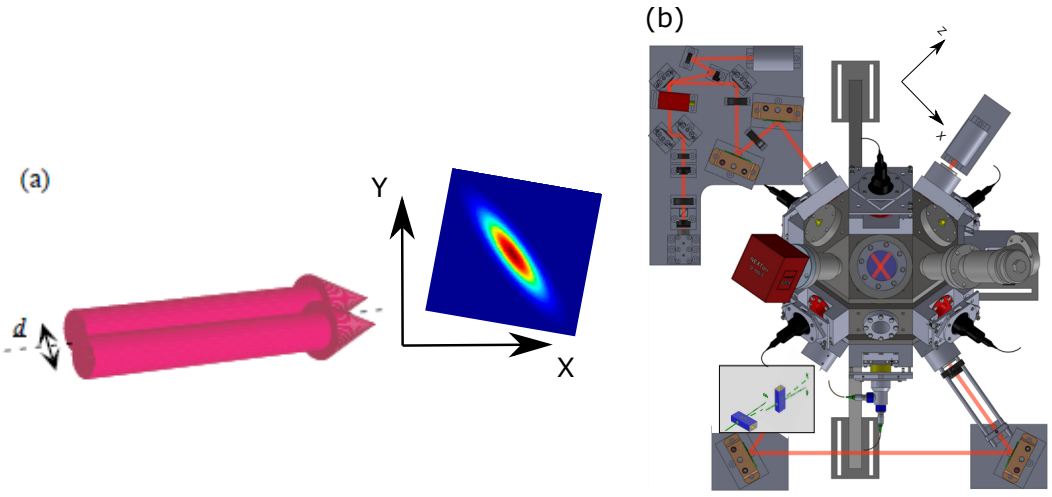

FIGURE 5.6 – (a) Time averaged anisotropic trap in the vertical plane $X-Y$ created by applying our modulation function in the diagonal direction. (b) Set up of the experiment including two orthogonal AOMs in the second pass (Inset) which modulate spatially the position of the laser beam in the 2D plane $X-Y$.

films. These defects control numerous properties of the condensed matter. Smectic [2] Liquid Crystals (LC) are layered phases of rod-shaped organic molecules, in which each layer is a two-dimensional fluid on the order of a molecular length in thickness. Because of their layering, smectics can readily be made to form films that are freely suspended in air or vacuum. These fluid structures are quantized in thickness, everywhere corresponding to some integral number N of smectic layers, which can be as small as a single molecular monolayer ($\approx$ 3 nm thick) for some materials. Smectic films are structures of fundamental interest in condensed matter physics for many reasons and especially because they allow to study systems in low dimentionality [184]. X-ray scattering studies of in-plane molecular ordering in smectic films have provided the most convincing evidence to date for the hexatic phase and its melting behavior [185], a scenario emerging from the theoretical work by Kosterlitz and Thouless [152].

By inserting nanoparticles in these liquid crystals, we induce a trapping of this nanoparticles in the topological defects whose evolution can then be observed. These defects, by their size and nature, guide the displacement of the nanoparticles and the nanoparticle assembles can be controlled. In the case of ultracold gases, our detection techniques allows more direct observation of the topological defects. Nevertheless, an analogous experiment including Potassium atoms trapped in Rubidium vortices can be envisioned.

Such LC bubbles have been tested in microgravity. Indeed, the absence of gravity avoids sedimentation of inclusions and air movement due to convection masking intrinsic thermo-mechanical effects in the films. A parabolic flight and sounding rocket experiments were conducted in preparation for the ISS flight [184]. OASIS project is a NASA/DLR collaboration and in this frame the assembling of nanoparticles on a LC film is the subject of a CNES program research for parabolic flight campaigns [186].

2. The orientation of the molecules are ordred and the system exhibits an order in position

Normal fluids

In a space shuttle experiments [187] on normal fluid shells, sloshing modes show marked signatures of inner and outer boundaries, akin to those predicted in preliminary theoretical work on BEC shells [166].

Vortices are also present in classical fluids such as soap bubbles (rotating or not) where the dynamics of the vortices is studied to understand the behavior of hurricanes in the atmosphere of the Earth [188]. Despite obvious differences between the classical and the quantum world, it can be interesting to compare the two fields and maybe extract some unexpected similarities.

The system used in [188] is a half bubble heated from below in a specially designed cell capable of rotating the bubble at different rates. Once formed, the bubble is subject to strong convection due to the heating at the base of the bubble. The most intriguing aspect is that after a short period, a large vortex may emerge. The emergence of vortices occurs both for bubbles not subjected to rotation and in bubbles subjected to rotation. By studying the effects of rotation of the bubble on the vortex properties, they found that rotation favors vortices near the pole, similarly as in the case of vortex-antivortex pair in BEC [176].

5.2 Anderson Localization

Ultracold atoms constitute very promising systems to study Anderson localization due to the exquisite control of the disorder parameters. Pioneering experiments have been realized, first in 1D [189, 190], then in 3D [191, 192, 193, 194] and very recently in 2D. However, the first attempts to study the critical regime in 3D, the "holy grail" for Anderson localization, have suffered from limitations and remain controversial. Previously these experiments have been faced to two main difficulties, (i) due to the limited stability of the magnetic levitation, and (ii) to a fundamental problem : the important spreading of the atomic energy distribution that appears while ramping up the disorder amplitude to reach the Anderson transition (see Fig. 2c). These two difficulties constitute real experimental "bottlenecks" for the study of the Anderson transition and have prevented so far the study of the critical regime. They are also most likely at the origin of the significant deviations that have been reported between recent numerical calculations [195] and the experimental estimations of the mobility edge (see Fig. 2d).

Using the unique possibilities offered by the microgravity platform, combined with a new spectroscopic scheme based on state dependent disorder potentials developed at LCF [196], we aim to overcome these limitations and provide the first precise study of the Anderson transition with ultracold atoms.

The first issue is directly linked to the fact the Anderson transition is a continuous quantum phase transition : there is no sudden annulation of the transport at the transition but a continuous annulation of the diffusion constant as we approach the transition. More precisely the diffusion constant is expected to behave as $D \sim (E - E_c)^\nu$, where ν is the critical exponent. Since the diffusion constant is almost null just above the mobility edge, very long expansion time is required in practice to differentiate between a true localization or very slow diffusion. More precisely, an order of magnitude of the diffusion constant in the critical regime is given by

$$D \sim \frac{\hbar}{3m} \sim 250\mu m^2/s \tag{5.23}$$

meaning that the typical expansion of the atomic could $\Delta x = \sqrt{2Dt}$ is only on the order of a few tens of micrometers (i.e. the typical size of the initial cloud) after 1 second of expansion !

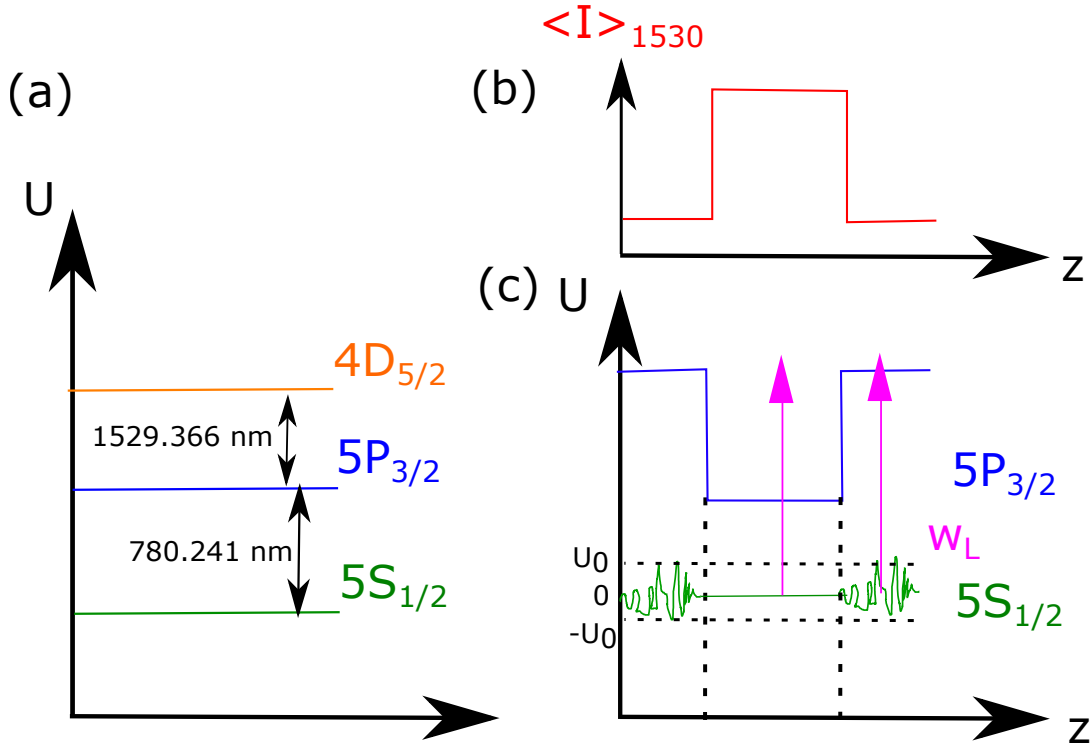

FIGURE 5.7 – (a) Rubidium level structure. (b) Averaged intensity profile of the dipole laser red detuned compared to the $5p_{3/2} \rightarrow 4d_{5/2}$ transition. This square shaped profile can be produced with our technique of painted potential. (c) Light Shifted $5p$ (blue) and $5s$ (green) states. The light beam at 780 nm (w_L) with a detuning $\sim +1$GHz produce a 3D speckle pattern. The disorder potential is "seen" by the atoms only if the dipole laser is off.

Reaching high enough stability on the magnetic levitation to enable such a long expansion time is difficult on ground. Much longer expansion time is then expected is presence of the much better controlled microgravity offered on-board the zero g plane which provides 20 s of microgravity.

A second and fully independent issue is the important broadening of the energy distribution that was reported in the first experimental attempts (see e.g. [192]) when the disorder amplitude was ramped up to reach the transition. In order to understand the origin of this effect, it is worth to recall that it is widely accepted that the 3D Anderson transition appears around the so-called Ioffe-Regel criterion $kl^* \sim 1$, where l^* is the transport mean free path. This criterion is also known to coincide with the onset of the very strong scattering regime [197], since the wave barely has time to oscillate between two scattering events. This means that when one aims to reach the Anderson transition, one reach at the same time the regime where the disorder perturbates dramatically the system, such that the switch on of the disorder is associated with an important energy broadening. It is then necessary to use a new scheme in order to "bypass" the energy broadening associated with the disorder switch on. Our idea for the loading of the disorder potential is based on using a telecom laser creating a strong light shift ($\Delta \sim 60$ GHz for $\lambda_{1530} = 1529.8$ nm and a total power of 2×15 W), making the atoms "disappear" regarding the 780 nm laser close to resonance ($\delta \sim +1$ GHz) producing the 3D disorder potential. A 3D box potential can be creating if we generalize our scheme by adding a second AOM perpendicular to the first one, as for the rotation of the bubble. This scheme offer a perfect control of the turn off of the disorder potential with an extinction ratio less than 2%.

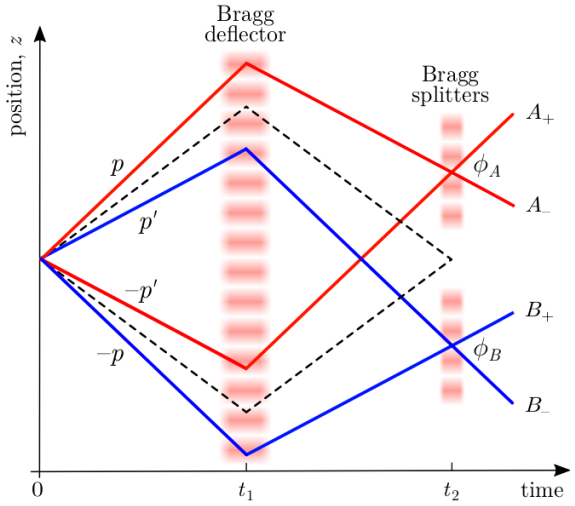

FIGURE 5.8 – Schematic diagram of the protocol used to observe two particle interference (LCF). An atomic four wave mixing effect creates a pair in a superposition : $|p,-p\rangle+|p',-p'\rangle$. Laser standing waves then act as deflectors and beam splitters to mix the different momentum modes. Interference is detected in the correlations between detectors at the A and B outputs. High enough fringe contrast can lead to the violation of a Bell inequality.

5.3 Bell's inequalities

We can also envision a new generation of atom interferometry experiments with large spatial separations achievable in microgravity.

The Palaiseau group has recently demonstrated multiple particle interference with entangled states of metastable helium atoms [198]. In this experiment atoms were entangled using only their motional degrees of freedom. This technique can be used to test Bell inequalities with these states. A pair of atoms is created in an entangled momentum state : $|p,-p\rangle + |p',-p'\rangle$. By mixing these momentum states (an example is shown Fig 5.8), it is possible create a state whose correlations can satisfy a CHSH inequality [199]. An optical equivalent was realized in 1990 [200]. The challenge is to mix these states on Bragg beam splitters and perform correlation measurements to test Bell's inequalities over large distances while controlling the phases (Φ_A,Φ_B) of the two interleaved interferometers.

The methods developed using He* can be adapted to an alkali atom, for instance Rubidium. The Palaiseau atomic pair production protocol is quite general, and depends only on the presence of atom-atom interactions and a far detuned optical lattice [201]. The goal is to push the Bell tests with times of flight up to 600 ms, giving a separation of about one cm if we assume that the momentum p or p' in the superposition are equivalent to a two-photon recoil.

The 3D detection scheme described in paragraph 5.1.4 based on a moving light sheet is particularly adapted to such experiments. Atoms in free flight cross a sheet of resonant light and the fluorescence emitted is imaged with a wide numerical aperture [181, 202]. Single atom detection efficiencies above 99 % have been reported in conjunction with in-plane spatial resolution of a few microns. This technique could also offer the third spatial dimension if the light sheet is pulsed. It will allow us first order correlation function g_2 of the intensity profile. Since in the Bell test only very dilute clouds have to be detected, the high quantum efficiency of the light sheet detector is very appealing for two reasons : the coincidence yield needed to be measured scales quadratically with it and it allows also efficient post-selection.

Chapitre 6

Conclusion

I presented how light manipulation of cold matter waves is a rich field, going from fundamental physics to direct applications such as gravity surveys or inertial navigation. In the first chapter, I reviewed all optical methods to cool and trap the atoms, and interrogate them to perform an atom interferometer. Laser cooling via grey molasses, involving the production of dark states, offers a solution to atom species such as Potassium where standard techniques are inefficient. These delta enhanced grey molasses combined with a painted optical potential at the telecom wavelength play a key role to an efficient new method optimizing the loading trap efficiency. Multi-dimensional atom optics are promising tools for future multi-axis cold atom sensors and a 2D/3D control of the wave packets more generally (topological fields).

In a second chapter I focused on the use of cold atom interferometers to probe the frontier of General Relativity and Quantum mechanics. Indeed it is particularly relevant to test the weak equivalence principle with quantum particles such as two atom species (Rb and K) of different masses and following the same trajectory, within the fundamental limit of Heisenberg's uncertainty principle. For this purpose, it is necessary to produce ultra-cold atom sources in microgravity to prepare future Space missions where the inertial environment will be clean enough to perform an unperturbed measurement of the acceleration due to gravity. An important step on the roadmap is to tackle the systematic errors and will require to control the relative position of the two clouds and limit strongly the spatial expansion of the two cold gases inside the laser beams and the residual magnetic field environment.

The third chapter described previous and current developments of the technology in the field of the quantum inertial sensors. Bulky and unstable experiments built 15 years ago have moved on to products on the market (gravimeters and atomic clocks from muQuanS) and reliable experiments achieving parabolic flights on board a plane. Strong efforts have been done on fibered laser systems, including development of key components such as a new generation of electro-optical modulators and polarizing fibers. The next steps will consist in miniaturizing these quantum sensors and solving the problems related to high levels of vibrations and rotations.

Last but not least, light manipulation of ultra-cold atoms in microgravity, which now at hand in our laboratory, pave the way to new catalogue of cold atoms experiments in the field of condensed matter and quantum optics. We show that the light techniques described in this manuscript offer new all optical solutions providing a favorable optical access and gives the opportunity to implement 3D detection schemes. Theses techniques will simplify the study of phase transition in bubble traps as well as the study of the vortices formation and dynamics. More specifically the topology of the quantum bubble implies a subtle relationship between BEC and superfluidity and our capability to manipulate the quantum bubble, putting it in

rotation for instance, is crucial in this context.

The current and future improvements of the technology in all aspects will be rewarded in the next years by new astonishing achievements for both fundamental physics and real life applications. A dedicated laser development is for instance required for the all optical bubble trap proposed here, but our connection with industrials make it feasible in our facilities. Moreover, the improvement of the CMOS sensors (sensitivity, time-frame...) will have a direct impact on our 3D detection scheme for which successive images in a short time are required.

Microgravity test platforms enlarge the potential of future experiments, even in standard laboratories. In parallel, the permanent increase of the Technology Readiness Level (TRL) of cold atom systems make Space a reachable playground at short term. Cold atoms set ups have already been sent in Space with the NASA CAL laboratory on the International Space Station [203] and the Chinese cold atom clock [204]. Such pathfinder missions need to be pursued, especially in the field of atom interferometry, and a scientific mission can be reasonably expected in the next ten or fifteen years. Among the scientific objectives, the WEP test is a most fascinating but difficult goal. Gravity differs from all other forces because the corresponding universal coupling implies that gravitation is a geometrical attribute of space-time itself rather than a field over space-time like all other known interactions. Finally the WEP test plays a central role for our understanding of the universe, including the frontier of Quantum mechanics and Relativity, Cosmology and Particles physics as well. Following the recent success such as the Microscope mission [57], it is very important to pursue because all tests put strong constraints on the theoretical models, which all predicts a violation of this principle. At what level a violation will be measured ? It is a mystery.

In absence of gravity, it is possible to reach extreme low temperature. A simple process consists in decompressing adiabatically the dipole trap, which is practically limited when we have to compensate gravity. In principle, it is possible to reach temperature below 1 pK, and it can allow to test principles of quantum mechanics in a regime difficult to explore. For example antiferromagnetism states predicted in lattices [205] possess low energy and long observing time to study such physical phenomena is required which become available in Space.

For a longer term view, technology development of "integrated" atomtronic devices is promising with hybrid magneto-optical atom chip or atoms trapped in hollow core fibers for instance.

The dream of a fully autonomous Inertial Navigation System can be reachable in the future using cold atom technology. A strong miniaturisation of the atom accelerometer is the first challenge. Then the measurement of the rotation rate is the next limitation for long term navigation. Atomic gyroscopes have a strong potential (highly favorable scale factor of the Sagnac phase) which is not exploited yet. The sensitivity area and the atom flux which are limited compared to the optical counterpart are the practical limitations at this stage.

Guided atom interferometry is often considered to increase the interrogation time in compact devices. Unfortunately adding a force (the atomic waveguide) is expected to strongly perturb the inertial measurement and constitutes an illogical challenge especially to study gravity which is a weak interaction. Rotation measurements are maybe more naturally adapted to guided atoms, since this is the formation of a loop of matter waves which matter to get a Sagnac phase (of course the atomic waveguide still pertub the measurement, expecially inhomogeneities). Guided gyroscopes are studied with a production of a ring potential, using dressed states for instance [206]. Sackett *et al.* [142] recently demonstrated the first measurement of rotation rate with guided atoms. At this stage, the sensitivity need to be increased which is quite challenging considering the reduced atom flux.

These first experiments are based on Rubidium. Strontium can be an interesting alterna-

tive for the future. First continuous sources with high phase space densities are available [46] and are promising solutions to increase the atom flux. Then, based on development led for clocks, guided Strontium in an optical trap at a magical wavelength to mitigate light shifts has been demonstrated [207]. In the future guiding Strontium in hollow fibers [208] to increase significantly the area can also contribute to build a next generation of atomic gyroscopes.

Bibliographie

[1] P. Storey and C. Cohen-Tannoudji. The Feynman path integral approach to atomic interferometry. *J. Phys. II France*, 4 :1999–2027, 1994.

[2] C. Antoine and Ch. J. Bordé. Exact phase shifts for atom interferometry. *Physics Letters A*, 306 :277–284, 2003.

[3] P. Gillot, O. Francis, A. Landragin, F. Pereira Dos Santos, and S. Merlet. Stability comparison of two absolute gravimeters : optical versus atomic interferometers. *Metrologia*, 51 :L15, 2014.

[4] T. Kovachy, P. Asenbaum, C. Overstreet, C. A. Donnelly, S. M. Dickerson, A. Sugarbaker, J. M. Hogan, and M. A. Kasevich. Quantum superposition at the half-metre scale. *Nature*, 528(7583) :530–533, 2015.

[5] J Hartwig, S Abend, C Schubert, D Schlippert, H Ahlers, K Posso-Trujillo, N Gaaloul, W Ertmer, and E M Rasel. Testing the universality of free fall with rubidium and ytterbium in a very large baseline atom interferometer. *New Journal of Physics*, 17(3) :035011, mar 2015.

[6] B. Battelier, B. Barrett, L. Fouché, L. Chichet, L. Antoni-Micollier, H. Porte, F. Napolitano, J. Lautier, A. Landragin, and P. Bouyer. Development of compact cold-atom sensors for inertial navigation. *Proceedings of SPIE, Quantum Optics*, 9900 :990004, 2016. (arXiv :1605.02454 [physics.atom-ph]).

[7] T. L. Gustavson, P. Bouyer, and M. A. Kasevich. Precision rotation measurements with an atom interferometer gyroscope. *Physical review letters*, 78(11) :2046, 1997.

[8] P. Cheinet, B. Canuel, F. Pereira Dos Santos, A. Gauguet, F. Yver-Leduc, and A. Landragin. Measurement of the sensitivity function in a time-domain atomic interferometer. *IEEE Transactions on Instrumentation and Measurement*, 57(6) :1141–1148, 2008.

[9] B. Barrett, P. Cheiney, B. Battelier, F. Napolitano, and P. Bouyer. Multidimensional atom optics and interferometry. *Phys. Rev. Lett.*, 122 :043604, Feb 2019.

[10] T. Lévèque, A. Gauguet, F. Michaud, F. Pereira Dos Santos, and A. Landragin. Enhancing the area of a Raman atom interferometer using a versatile double-diffraction technique. *Physical Review Letters*, 103 :080405, 2009.

[11] Alex Sugarbaker, Susannah M. Dickerson, Jason M. Hogan, David M. S. Johnson, and M. A. Kasevich. Enhanced Atom Interferometer Readout through the Application of Phase Shear. *Phys. Rev. Lett.*, 111 :113002, 2013.

[12] B. Gouraud. Private discussion. 2019.

[13] M. V. Berry. Quantal phase factors accompanying adiabatic changes. *Proceedings of the Royal Society of London. Series A, Mathematical and Physical Sciences*, 392(1802) :45–57, 1984.

[14] D Jaksch and P Zoller. Creation of effective magnetic fields in optical lattices : the hofstadter butterfly for cold neutral atoms. *New Journal of Physics*, 5 :56–56, may 2003.

[15] Alban Urvoy, Zachary Vendeiro, Joshua Ramette, Albert Adiyatullin, and Vladan Vuletić. Direct laser cooling to bose-einstein condensation in a dipole trap. *Phys. Rev. Lett.*, 122 :203202, May 2019.

[16] D. Boiron, C. Triché, D. R. Meacher, P. Verkerk, and G. Grynberg. Three-dimensional cooling of cesium atoms in four-beam gray optical molasses. *Physical Review A*, 52, 1995.

[17] A. Burchianti, G. Valtolina, J. A. Seman, E. Pace, M. De Pas, M. Inguscio, M. Zaccanti, and G. Roati. Efficient all-optical production of large ^{6}Li quantum gases using D_1 gray-molasses cooling. *Physical Review A*, 90 :043408, 2014.

[18] F. Sievers, S. Wu, N. Kretzschmar, D. Rio Fernandes, D. Suchet, M. Rabinovic, Colin V. Parker, L. Khaykovich, C. Salomon, and F. Chevy. Simultaneous sub-Doppler laser cooling of fermionic ^{6}Li and ^{40}K on the D_1 line : theory and experiment. *Physical Review A*, 91(2) :023426, 2015.

[19] Andrew T. Grier, Igor Ferrier-Barbut, Benno S. Rem, Marion Delehaye, Lev Khaykovich, Frédéric Chevy, and Christophe Salomon. Λ-enhanced sub-doppler cooling of lithium atoms in D_1 gray molasses. *Physical Review A*, 87 :063411, 2013.

[20] D. Rio Fernandes, F. Sievers, N. Kretzschmar, S. Wu, C. Salomon, and F. Chevy. Sub-Doppler laser cooling of fermionic ^{40}K atoms in three-dimensional gray optical molasses. *Euro. Phys. Lett.*, 100 :63001, 2012.

[21] Dipankar Nath, R. Kollengode Easwaran, G. Rajalakshmi, and C.S. Unnikrishnan. Quantum interference-enhanced deep sub-Doppler cooling of ^{39}K atoms in gray molasses. *Physical Review A*, 88 :053407, 2013.

[22] G. Salomon, L. Fouché, P. Wang, A. Aspect, P. Bouyer, and T. Bourdel. Gray-molasses cooling of 39K to a high phase-space density. *Euro. Phys. Lett.*, 104(6) :63002, 2013.

[23] F. Papoff, F. Mauri, and E. Arimondo. Transient velocity-selective coherent population trapping in one dimension. *J. Opt. Soc. Am. B*, 9(3) :321–331, Mar 1992.

[24] Yong-qing Li and Min Xiao. Electromagnetically induced transparency in a three-level Λ-type system in rubidium atoms. *Phys. Rev. A*, 51 :R2703–R2706, Apr 1995.

[25] Hong Yuan Ling, Yong-Qing Li, and Min Xiao. Coherent population trapping and electromagnetically induced transparency in multi-zeeman-sublevel atoms. *Phys. Rev. A*, 53 :1014–1026, Feb 1996.

[26] Daniel Finkelstein-Shapiro, Simone Felicetti, Thorsten Hansen, Tõnu Pullerits, and Arne Keller. Classification of dark states in multilevel dissipative systems. *Phys. Rev. A*, 99 :053829, May 2019.

[27] F. T. Hioe and J. H. Eberly. n-level coherence vector and higher conservation laws in quantum optics and quantum mechanics. *Phys. Rev. Lett.*, 47 :838–841, Sep 1981.

[28] James R. Morris and Bruce W. Shore. Reduction of degenerate two-level excitation to independent two-state systems. *Phys. Rev. A*, 27 :906–912, Feb 1983.

[29] D V Kosachiov, B G Matisov, and Y V Rozhdestvensky. Coherent phenomena in multilevel systems with closed interaction contour. *Journal of Physics B : Atomic, Molecular and Optical Physics*, 25(11) :2473–2488, jun 1992.

[30] T. S. Tiecke. Properties of potassium, May 2011. www.tobiastiecke.nl.

[31] L. Antoni-Micollier, B. Barrett, L. Chichet, G. Condon, B. Battelier, A. Landragin, and P. Bouyer. Generation of high-purity low-temperature samples of ^{39}K for applications in metrology. *Phys. Rev. A*, 96 :023608, Aug 2017.

[32] M. Landini, S. Roy, L. Carcagní, D. Trypogeorgos, M. Fattori, M. Inguscio, and G. Modugno. Sub-Doppler laser cooling of potassium atoms. *Physical review A*, 84 :043432, 2011.

[33] V. Gokhroo, G. Rajalakshmi, R. K. Easwaran, and C. S. Unnikrishnan. Sub-Doppler deep-cooled bosonic and fermionic isotopes of potassium in a compact 2D$^+$-3D MOT set-up. *Journal of Physics B*, 44 :115307, 2011.

[34] Nir Davidson, Heun Jin Lee, Mark Kasevich, and Steven Chu. Raman cooling of atoms in two and three dimensions. *Phys. Rev. Lett.*, 72 :3158–3161, May 1994.

[35] J. Reichel, F. Bardou, M. Ben Dahan, E. Peik, S. Rand, C. Salomon, and C. Cohen-Tannoudji. Raman cooling of cesium below 3 nk : New approach inspired by lévy flight statistics. *Phys. Rev. Lett.*, 75 :4575–4578, Dec 1995.

[36] A. Aspect, E. Arimondo, R. Kaiser, N. Vansteenkiste, and C. Cohen-Tannoudji. Laser cooling below the one-photon recoil energy by velocity-selective coherent population trapping. *Phys. Rev. Lett.*, 61 :826–829, Aug 1988.

[37] G. Condon, M. Rabault, B. Barrett, L. Chichet, R. Arguel, H. Eneriz-Imaz, D. Naik, A. Bertoldi, B. Battelier, P. Bouyer, and A. Landragin. All-optical bose-einstein condensates in microgravity. *Phys. Rev. Lett.*, 123 :240402, Dec 2019.

[38] J.-F. Clément, J.-P. Brantut, M. Robert-de Saint-Vincent, R. A. Nyman, A. Aspect, T. Bourdel, and P. Bouyer. All-optical runaway evaporation to bose-einstein condensation. *Phys. Rev. A*, 79 :061406, Jun 2009.

[39] Simon Stellmer, Benjamin Pasquiou, Rudolf Grimm, and Florian Schreck. Laser cooling to quantum degeneracy. *Phys. Rev. Lett.*, 110 :263003, Jun 2013.

[40] Richard Roy, Alaina Green, Ryan Bowler, and Subhadeep Gupta. Rapid cooling to quantum degeneracy in dynamically shaped atom traps. *Phys. Rev. A*, 93 :043403, Apr 2016.

[41] G. Rosi, A. Burchianti, S. Conclave, D. S. Naik, G. Roati, C. Fort, and F. Minardi. Λ-enhanced grey molasses on the D2 transition of Rubidium-87 atoms. *Sci. Rep.*, 8 :1301, 2018.

[42] D. S. Naik, H. Eneriz-Imaz, M. Carey, T. Freegarde, F. Minardi, B. Battelier, P. Bouyer, and A. Bertoldi. Loading and cooling in an optical trap via hyperfine dark states. *Phys. Rev. Research*, 2 :013212, Feb 2020.

[43] Y. Castin and R. Dum. Bose-einstein condensates in time dependent traps. *Phys. Rev. Lett.*, 77 :5315–5319, Dec 1996.

[44] Tim Kovachy, Jason M. Hogan, Alex Sugarbaker, Susannah M. Dickerson, Christine A. Donnelly, Chris Overstreet, and Mark A. Kasevich. Matter wave lensing to picokelvin temperatures. *Phys. Rev. Lett.*, 114 :143004, Apr 2015.

[45] J. P. Brantut, J. F. Clément, M. Robert de Saint Vincent, G. Varoquaux, R. A. Nyman, A. Aspect, T. Bourdel, and P. Bouyer. Light-shift tomography in an optical-dipole trap for neutral atoms. *Phys. Rev. A*, 78 :031401, Sep 2008.

[46] Chun-Chia Chen, Shayne Bennetts, Rodrigo González Escudero, Benjamin Pasquiou, and Florian Schreck. Continuous guided strontium beam with high phase-space density. *Phys. Rev. Applied*, 12 :044014, Oct 2019.

[47] M. Landini, S. Roy, G. Roati, A. Simoni, M. Inguscio, G. Modugno, and M. Fattori. Direct evaporative cooling of ^{39}k atoms to bose-einstein condensation. *Phys. Rev. A*, 86 :033421, Sep 2012.

[48] Bindiya Arora, M. S. Safronova, and Charles W. Clark. Magic wavelengths for the $np-ns$ transitions in alkali-metal atoms. *Phys. Rev. A*, 76 :052509, Nov 2007.

[49] T. Damour, F. Piazza, and G. Veneziano. Violations of the equivalence principle in a dilaton-runaway scenario. *Phys. Rev. D*, 66 :046007, 2002.

[50] C. M. Will. The Confrontation between General Relativity and Experiment. *Living Rev. Relativity*, 9 :3, 2006.

[51] T. Damour. Theoretical aspects of the equivalence principle. *Class. and Quant. Grav.*, 29(18) :184001, 2012.

[52] M. A. Hohensee, H. Müller, and R. B. Wiringa. Equivalence Principle and Bound Kinetic Energy. *Phys. Rev. Lett.*, 111(15) :151102, 2013.

[53] Clifford M. Will. *Theory and Experiment in Gravitational Physics*. Cambridge University Press, 2 edition, 2018.

[54] J. G. Williams, S. G. Turyshev, and D. H. Boggs. Lunar laser ranging tests of the equivalence principle. *Classical and Quantum Gravity*, 29(18) :184004, 2012.

[55] Guillaume Voisin, Ismaël Cognard, Paulo Freire, Norbert Wex, Lucas Guillemot, Grégory Desvignes, Michael Kramer, and Gilles Theureau. An improved test of the strong equivalence principle with the pulsar in a triple star system, 2020.

[56] S. Schlamminger, K.-Y. Choi, T. A. Wagner, J. H. Gundlach, and E. G. Adelberger. Test of the equivalence principle usinga rotating torsion balance. *Physical Review letters*, 100 :041101, 2008.

[57] Pierre Touboul, Gilles Métris, Manuel Rodrigues, Yves André, Quentin Baghi, Joël Bergé, Damien Boulanger, Stefanie Bremer, Patrice Carle, Ratana Chhun, Bruno Christophe, Valerio Cipolla, Thibault Damour, Pascale Danto, Hansjoerg Dittus, Pierre Fayet, Bernard Foulon, Claude Gageant, Pierre-Yves Guidotti, Daniel Hagedorn, Emilie Hardy, Phuong-Anh Huynh, Henri Inchauspe, Patrick Kayser, Stéphanie Lala, Claus Lämmerzahl, Vincent Lebat, Pierre Leseur, Fran çoise Liorzou, Meike List, Frank Löffler, Isabelle Panet, Benjamin Pouilloux, Pascal Prieur, Alexandre Rebray, Serge Reynaud, Benny Rievers, Alain Robert, Hanns Selig, Laura Serron, Timothy Sumner, Nicolas Tanguy, and Pieter Visser. Microscope mission : First results of a space test of the equivalence principle. *Phys. Rev. Lett.*, 119 :231101, Dec 2017.

[58] A. Peters, K. Y. Chung, and S. Chu. High-precision gravity measurements using atom interferometry. *metrologia*, 38 :25–61, 2001.

[59] S Merlet, Q Bodart, N Malossi, A Landragin, F Pereira Dos Santos, O Gitlein, and L Timmen. Comparison between two mobile absolute gravimeters : optical versus atomic interferometers. *Metrologia*, 47(4) :L9–L11, jun 2010.

[60] D. Schlippert, J. Hartwig, H. Albers, L. L. Richardson, C. Schubert, A. Roura, W. P. Schleich, W. Ertmer, and E. M. Rasel. Quantum test of the universality of free fall. *Physical Review letters*, 112 :203002, 2014.

[61] M. G. Tarallo, T. Mazzoni, N. Poli, D. V. Sutyrin, X. Zhang, and G. M. Tino. Test of the Einstein Equivalence Principle for 0-Spin and half-integer-spin atoms : search for spin-gravity coupling effects. *Physical Review Letters*, 113 :023005, 2014.

[62] L. Zhou, S. Long, B. Tang, X. Chen, F. Gao, W. Peng, W. Duan, J. Zhong, Z. Xiong, J. Wang, Y. Zhang, and M. Zhan. Test of the equivalence principle at 10^{-8} level by a dual-species double-diffraction Raman atom interferometer. *Physical Review Letters*, 115 :013004, 2015.

[63] Lin Zhou, Chuan He, Si-Tong Yan, Xi Chen, Wei-Tao Duan, Run-Dong Xu, Chao Zhou, Yu-Hang Ji, Sachin Barthwal, Qi Wang, Zhuo Hou, Zong-Yuan Xiong, Dong-Feng Gao, Yuan-Zhong Zhang, Wei-Tou Ni, Jin Wang, and Ming-Sheng Zhan. United test of the equivalence principle at 10^{-10} level using mass and internal energy specified atoms, 2019.

[64] Yuan Cheng Le-Le Chen Qin Luo Wen-Jie Xu Lu-Shuai Cao Xiao-Chun Duan Zhong-Kun Hu Ke Zhang, Min-Kang Zhou. Testing the universality of free fall by comparing the atoms in different hyperfine states with bragg diffraction. *Chinese Physics Letters*, 37(4) :043701, 2020.

[65] Peter Asenbaum, Chris Overstreet, Minjeong Kim, Joseph Curti, and Mark A. Kasevich. Atom-interferometric test of the equivalence principle at the 10^{-12} level, 2020.

[66] Chris Overstreet, Peter Asenbaum, Tim Kovachy, Remy Notermans, Jason M. Hogan, and Mark A. Kasevich. Effective inertial frame in an atom interferometric test of the equivalence principle. *Phys. Rev. Lett.*, 120 :183604, May 2018.

[67] P Perez and Y Sacquin. The GBAR experiment : gravitational behaviour of antihydrogen at rest. *Classical and Quantum Gravity*, 29(18) :184008, aug 2012.

[68] Brett Altschul, Quentin G. Bailey, Luc Blanchet, Kai Bongs, Philippe Bouyer, Luigi Cacciapuoti, Salvatore Capozziello, Naceur Gaaloul, Domenico Giulini, Jonas Hartwig, Luciano Iess, Philippe Jetzer, Arnaud Landragin, Ernst Rasel, Serge Reynaud, Stephan Schiller, Christian Schubert, Fiodor Sorrentino, Uwe Sterr, Jay D. Tasson, Guglielmo M. Tino, Philip Tuckey, and Peter Wolf. Quantum tests of the einstein equivalence principle with the ste–quest space mission. *Advances in Space Research*, 55(1) :501 – 524, 2015.

[69] C. Lämmerzahl. On the equivalence principle in quantum theory. *General Relativity and Gravitation*, 28 :1043–1070, 1996.

[70] Lorenza Viola and Roberto Onofrio. Testing the equivalence principle through freely falling quantum objects. *Phys. Rev. D*, 55 :455–462, Jan 1997.

[71] P C W Davies. Quantum mechanics and the equivalence principle. *Classical and Quantum Gravity*, 21(11) :2761–2772, may 2004.

[72] Magdalena Zych and Caslav Brukner. Quantum formulation of the einstein equivalence principle, 2015.

[73] G Rosi, G. D'Amico, F. Sorrentino, M. Prevedelli, M. Zych, C. Brukner, and G. M. Tino. Quantum test of the equivalence principle for atoms in coherent superposition of internal energy states. *Nature Commmunications*, 8(15529), 2017.

[74] Remi Geiger and Michael Trupke. Proposal for a quantum test of the weak equivalence principle with entangled atomic species. *Phys. Rev. Lett.*, 120 :043602, Jan 2018.

[75] T. M. Niebauer, M. P. McHugh, and J. E. Faller. Galilean test for the fifth force. *Phys. Rev. Lett.*, 59 :609–612, Aug 1987.

[76] Michael A. Hohensee and Holger Müller. Precision tests of general relativity with matter waves. *Journal of Modern Optics*, 58(21) :2021–2027, 2011.

[77] S. Fray, C. A. Diez, T. W. Hänsch, and M. Weitz. Atomic interferometer with amplitude gratings of light and its applications to atom based tests of the equivalence principle. *Physical Review Letters*, 93 :2400404, 2004.

[78] Jan Rudolph, Thomas Wilkason, Megan Nantel, Hunter Swan, Connor M. Holland, Yijun Jiang, Benjamin E. Garber, Samuel P. Carman, and Jason M. Hogan. Large momentum transfer clock atom interferometry on the 689 nm intercombination line of strontium. *Phys. Rev. Lett.*, 124 :083604, Feb 2020.

[79] M. Armano, H. Audley, G. Auger, J. T. Baird, M. Bassan, P. Binetruy, M. Born, D. Bortoluzzi, N. Brandt, M. Caleno, L. Carbone, A. Cavalleri, A. Cesarini, G. Ciani, G. Congedo, A. M. Cruise, K. Danzmann, M. de Deus Silva, R. De Rosa, M. Diaz-Aguiló, L. Di Fiore, I. Diepholz, G. Dixon, R. Dolesi, N. Dunbar, L. Ferraioli, V. Ferroni, W. Fichter, E. D. Fitzsimons, R. Flatscher, M. Freschi, A. F. García Marín, C. García Marirrodriga, R. Gerndt, L. Gesa, F. Gibert, D. Giardini, R. Giusteri, F. Guzmán, A. Grado, C. Grimani, A. Grynagier, J. Grzymisch, I. Harrison, G. Heinzel, M. Hewitson, D. Hollington, D. Hoyland, M. Hueller, H. Inchauspé, O. Jennrich, P. Jetzer, U. Johann, B. Johlander, N. Karnesis, B. Kaune, N. Korsakova, C. J. Killow, J. A. Lobo, I. Lloro, L. Liu, J. P. López-Zaragoza, R. Maarschalkerweerd, D. Mance, V. Martín, L. Martin-Polo, J. Martino, F. Martin-Porqueras, S. Madden, I. Mateos, P. W. McNamara, J. Mendes, L. Mendes, A. Monsky, D. Nicolodi, M. Nofrarias, S. Paczkowski, M. Perreur-Lloyd, A. Petiteau, P. Pivato, E. Plagnol, P. Prat, U. Ragnit, B. Raïs, J. Ramos-Castro, J. Reiche, D. I. Robertson, H. Rozemeijer, F. Rivas, G. Russano, J. Sanjuán, P. Sarra, A. Schleicher, D. Shaul, J. Slutsky, C. F. Sopuerta, R. Stanga, F. Steier, T. Sumner, D. Texier, J. I. Thorpe, C. Trenkel, M. Tröbs, H. B. Tu, D. Vetrugno, S. Vitale, V. Wand, G. Wanner, H. Ward, C. Warren, P. J. Wass, D. Wealthy, W. J. Weber, L. Wissel, A. Wittchen, A. Zambotti, C. Zanoni, T. Ziegler, and P. Zweifel. Sub-femto-g free fall for space-based gravitational wave observatories : Lisa pathfinder results. *Phys. Rev. Lett.*, 116 :231101, Jun 2016.

[80] Baptiste Battelier, Joël Bergé, Andrea Bertoldi, Luc Blanchet, Kai Bongs, Philippe Bouyer, Claus Braxmaier, Davide Calonico, Pierre Fayet, Naceur Gaaloul, Christine Guerlin, Aurélien Hees, Philippe Jetzer, Claus Lämmerzahl, Steve Lecomte, Christophe Le Poncin-Lafitte, Sina Loriani, Gilles Métris, Miguel Nofrarias, Ernst Rasel, Serge Reynaud, Manuel Rodrigues, Markus Rothacher, Albert Roura, Christophe Salomon, Stephan Schiller, Wolfgang P. Schleich, Christian Schubert, Carlos Sopuerta, Fiodor Sorrentino, Tim J. Sumner, Guglielmo M. Tino, Philip Tuckey, Wolf von Klitzing, Lisa Wörner, Peter Wolf, and Martin Zelan. Exploring the foundations of the universe with space tests of the equivalence principle, 2019.

[81] V. Ménoret, R. Geiger, G. Stern, N. Zahzam, B. Battelier, A. Bresson, A. Landragin, and P. Bouyer. Dual-wavelength laser source for onboard atom interferometry. *Opt. Lett.*, 36(21) :4128, 2011.

[82] J. Le Gouët, T. E. Mehlstäubler, J. Kim, S. Merlet, A. Clairon, A. Landragin, and F. Pereira Dos Santos. Limits to the sensitivity of a low noise compact atomic gravimeter. *Applied Physics B*, 92 :133–144, 2008.

[83] Min-Kang Zhou, Zhong-Kun Hu, Xiao-Chun Duan, Bu-Liang Sun, Le-Le Chen, Qiao-Zhen Zhang, and Jun Luo. Performance of a cold-atom gravimeter with an active vibration isolator. *Phys. Rev. A*, 86 :043630, Oct 2012.

[84] B. Barrett, L. Antoni-Micollier, L. Chichet, B. Battelier, P.-A. Gominet, A. Bertoldi, P. Bouyer, and A. Landragin. Correlative methods for dual-species quantum tests of the weak equivalence principle. *New. J. Phys.*, 17(08) :085010, 2015.

[85] R. Geiger, V. Ménoret, G. Stern, N. Zahzam, P. Cheinet, B. Battelier, A. Villing, F. Moron, M. Lours, Y. Bidel, A. Bresson, A. Landragin, and P. Bouyer. Detecting inertial effects with airborne matter-wave interferometry. *Nature Communications*, 2 :474, 2011.

[86] O. Carraz, R. Charrière, M. Cadoret, N. Zahzam, Y. Bidel, and A. Bresson. Phase shift in an atom interferometer induced by the additional laser lines of a Raman laser generated by modulation. *Physical Review A*, 86 :033605, 2012.

[87] Qing-Qing Hu, Christian Freier, Yuan Sun, Bastian Leykauf, Vladimir Schkolnik, Jun Yang, Markus Krutzik, and Achim Peters. Observation of vector and tensor light shifts in ^{87}Rb using near-resonant, stimulated raman spectroscopy. *Phys. Rev. A*, 97 :013424, Jan 2018.

[88] B. Barrett, L. Antoni-Micollier, L. Chichet, B. Battelier, T. Lévèque, A. Landragin, and P. Bouyer. Dual Matter-Wave Inertial Sensors in Weightlessness. *Nature Communications*, 7 :2041–1723, 2016.

[89] A. Gauguet, T. E. Mehlstäubler, T. Lévèque, J. Le Gouët, W. Chaibi, B. Canuel, A. Clairon, F. Peirera Dos Santos, and A. Landragin. Off-resonant Raman transition impact in an atom interferometer. *Physical Review A*, 78 :043615, 2008.

[90] I. Perrin, J. Bernard, Y. Bidel, A. Bonnin, N. Zahzam, C. Blanchard, A. Bresson, and M. Cadoret. Zero-velocity atom interferometry using a retroreflected frequency-chirped laser. *Phys. Rev. A*, 100 :053618, Nov 2019.

[91] van T. Zoest, N. Gaaloul, Y. Singh, H. Ahlers, W. Herr, S.T. Seidel, W. Ertmer, E. Rasel, M. Eckart, E. Kajari, S. Arnold, G. Nandi, W. P. Schleich, R. Walser, A. Vogel, K. Sengstock, K. Bongs, W. Lewoczko-Adamczyk, M. Schiemangk, T. Schuldt, A. Peters, T. Könemann, H. Müntiga, C. Lämmerzahl, H. Dittus, T. Steinmetz, T. W. Hänsch, and J. Reichel. Bose-Einstein condensation in microgravity. *Science*, 328 :1540, 2008.

[92] D. Becker, M. D. Lachmann, S. T. Seidel, H. Ahlers, A. N. Dinkelaker, J. Grosse, O. Hellmig, H. Müntinga, V. Schkolnik, T. Wendrich, A. Wenzlawski, B. Weps, R. Corgier, T. Franz, N. Gaaloul, W. Herr, D. Lüdtke, M. Popp, S. Amri, H. Duncker, M. Erbe, A. Kohfeldt, A. Kubelka-Lange, C. Braxmaier, E. Charron, W. Ertmer, M. Krutzik, C. Lämmerzahl, A. Peters, W. P. Schleich, K. Sengstock, R. Walser, A. Wicht, P. Windpassinger, and E. M. Rasel. Space-borne bose–einstein condensation for precision interferometry. *Nature*, 562 :1476–4687, 2018.

[93] Ethan R. Elliott, Markus C. Krutzik, Jason R. Williams, Robert J. Thompson, and David C. Aveline. Nasa's cold atom lab (cal) : system development and ground test status. *npj Microgravity*, 4 :2373–8065, 2018.

[94] Christoph Lotz, Yvonne Wessarges, Jörg Hermsdorf, Wolfgang Ertmer, and Ludger Overmeyer. Novel active driven drop tower facility for microgravity experiments investigating production technologies on the example of substrate-free additive manufacturing. *Advances in Space Research*, 61(8) :1967 – 1974, 2018.

[95] F. Pereira Dos Santos. Differential phase extraction in an atom gradiometer. *Phys. Rev. A*, 91 :063615, Jun 2015.

[96] J. Dalibard and C. Cohen-Tannoudji. Dressed-atom approach to atomic motion in laser light : the dipole force revisited. *J. Opt. Soc. Am. B*, 2(11) :1707–1720, Nov 1985.

[97] E. Arimondo, M. Inguscio, and P. Violino. Experimental determinations of the hyperfine structure in the alkali atoms. *Rev. Mod. Phys.*, 49 :31–75, Jan 1977.

[98] R Karcher, A Imanaliev, S Merlet, and F Pereira Dos Santos. Improving the accuracy of atom interferometers with ultracold sources. *New Journal of Physics*, 20(11) :113041, nov 2018.

[99] Peter Asenbaum, Chris Overstreet, Tim Kovachy, Daniel D. Brown, Jason M. Hogan, and Mark A. Kasevich. Phase shift in an atom interferometer due to spacetime curvature across its wave function. *Phys. Rev. Lett.*, 118 :183602, May 2017.

[100] Kyle S. Hardman, Carlos C. N. Kuhn, Gordon D. McDonald, John E. Debs, Shayne Bennetts, John D. Close, and Nicholas P. Robins. Role of source coherence in atom interferometry. *Phys. Rev. A*, 89 :023626, Feb 2014.

[101] P. B. Wigley, K. S. Hardman, C. Freier, P. J. Everitt, S. Legge, P. Manju, J. D. Close, and N. P. Robins. Readout-delay-free bragg atom interferometry using overlapped spatial fringes. *Phys. Rev. A*, 99 :023615, Feb 2019.

[102] C C N Kuhn, G D McDonald, K S Hardman, S Bennetts, P J Everitt, P A Altin, J E Debs, J D Close, and N P Robins. A bose-condensed, simultaneous dual-species mach–zehnder atom interferometer. *New Journal of Physics*, 16(7) :073035, jul 2014.

[103] H. Müntinga, H. Ahlers, M. Krutzik, a. Wenzlawski, S. Arnold, D. Becker, K. Bongs, H. Dittus, H. Duncker, N. Gaaloul, C. Gherasim, E. Giese, C. Grzeschik, T. W. Hänsch, O. Hellmig, W. Herr, S. Herrmann, E. Kajari, S. Kleinert, C. Lämmerzahl, W. Lewoczko-Adamczyk, J. Malcolm, N. Meyer, R. Nolte, a. Peters, M. Popp, J. Reichel, a. Roura, J. Rudolph, M. Schiemangk, M. Schneider, S. T. Seidel, K. Sengstock, V. Tamma, T. Valenzuela, a. Vogel, R. Walser, T. Wendrich, P. Windpassinger, W. Zeller, T. van Zoest, W. Ertmer, W. P. Schleich, and E. M. Rasel. Interferometry with Bose-Einstein Condensates in Microgravity. *Physical Review Letters*, 110(9) :093602, 2013.

[104] S. Abend, M. Gebbe, M. Gersemann, H. Ahlers, H. Müntinga, E. Giese, N. Gaaloul, C. Schubert, C. Lämmerzahl, W. Ertmer, W. P. Schleich, and E. M. Rasel. Atom-chip fountain gravimeter. *Phys. Rev. Lett.*, 117 :203003, Nov 2016.

[105] K. S. Hardman, P. J. Everitt, G. D. McDonald, P. Manju, P. B. Wigley, M. A. Sooriyabandara, C. C. N. Kuhn, J. E. Debs, J. D. Close, and N. P. Robins. Simultaneous precision gravimetry and magnetic gradiometry with a bose-einstein condensate : A high precision, quantum sensor. *Phys. Rev. Lett.*, 117 :138501, Sep 2016.

[106] G. D. McDonald, C. C. N. Kuhn, S. Bennetts, J. E. Debs, K. S. Hardman, M. Johnsson, J. D. Close, and N. P. Robins. $80\hbar k$ momentum separation with bloch oscillations in an optically guided atom interferometer. *Phys. Rev. A*, 88 :053620, Nov 2013.

[107] Rym Bouchendira, Pierre Cladé, Saïda Guellati-Khélifa, Fran çois Nez, and Fran çois Biraben. New determination of the fine structure constant and test of the quantum electrodynamics. *Phys. Rev. Lett.*, 106 :080801, Feb 2011.

[108] Victoria Xu, Matt Jaffe, Cristian D. Panda, Sofus L. Kristensen, Logan W. Clark, and Holger Müller. Probing gravity by holding atoms for 20 seconds. *Science*, 366(6466) :745–749, 2019.

[109] Martina Gebbe, Sven Abend, Jan-Niclas Siemß, Matthias Gersemann, Holger Ahlers, Hauke Müntinga, Sven Herrmann, Naceur Gaaloul, Christian Schubert, Klemens Hammerer, Claus Lämmerzahl, Wolfgang Ertmer, and Ernst M. Rasel. Twin-lattice atom interferometry, 2019.

[110] Y. Bidel, N. Zahzam, C. Blanchard, A. Bonnin, M. Cadoret, A. Bresson, D. Rouxel, and M. F. Lequentrec-Lalancette. Absolute marine gravimetry with matter-wave interferometry. *Nature Communications*, 9 :2041–1723, 2018.

[111] R. Thompson, M. Tu, D. Aveline, N. Lundblad, and L. Maleki. High power single frequency 780 nm laser source generated from frequency doubling of a seeded fiber amplifier in a cascade of PPLN crystals. *Opt. Express*, 11(14) :1709–1713, Jul 2003.

[112] Olivier Carraz, Renée Charrière, Malo Cadoret, Nassim Zahzam, Yannick Bidel, and Alexandre Bresson. Phase shift in an atom interferometer induced by the additional laser lines of a raman laser generated by modulation. *Phys. Rev. A*, 86 :033605, Sep 2012.

[113] Fabien Theron, Olivier Carraz, Geoffrey Renon, Nassim Zahzam, Yannick Bidel, Malo Cadoret, and Alexandre Bresson. Narrow linewidth single laser source system for onboard atom interferometry. *Appl. Phys. B*, 118(1) :1–5, 2014.

[114] J. Popiel-Gorski. *Frequency Synthesis : Techniques and Applications*. IEEE Computer Society Press, 1975.

[115] Wencui Peng, Lin Zhou, Shitong Long, Jin Wang, and Mingsheng Zhan. Locking laser frequency of up to 40 ghz offset to a reference with a 10 ghz electro-optic modulator. *Opt. Lett.*, 39(10) :2998–3001, May 2014.

[116] J. Lautier, M. Lours, and A. Landragin. A compact micro-wave synthesizer for transportable cold-atom interferometers. *Review of Scientific Instruments*, 85(6) :063114, 2014.

[117] Sylvain Blaize, Lionel Bastard, Cedric Cassagnetes, Guy Vitrant, and Jean-Emmanuel Broquin. Ion-exchanged glass dfb lasers for dwdm. In *SPIE OPTO*, 2002.

[118] Zachary L. Newman, Vincent Maurice, Tara Drake, Jordan R. Stone, Travis C. Briles, Daryl T. Spencer, Connor Fredrick, Qing Li, Daron Westly, B. R. Ilic, Boqiang Shen, Myoung-Gyun Suh, Ki Youl Yang, Cort Johnson, David M. S. Johnson, Leo Hollberg, Kerry J. Vahala, Kartik Srinivasan, Scott A. Diddams, John Kitching, Scott B. Papp, and Matthew T. Hummon. Architecture for the photonic integration of an optical atomic clock. *Optica*, 6(5) :680–685, May 2019.

[119] B. Arar, H. Wenzel, R. Güther, O. Brox, A. Maaßdorf, A. Wicht, G. Erbert, M. Weyers, G. Tränkle, H. N. J. Fernando, and A. Peters. Double-heterostructure ridge-waveguide gaas/algaas phase modulator for 780 nm lasers. *Applied Physics B*, 116 :1432–0649, 2014.

[120] Max Schiemangk, Kai Lampmann, Aline Dinkelaker, Anja Kohfeldt, Markus Krutzik, Christian Kürbis, Alexander Sahm, Stefan Spießberger, Andreas Wicht, Götz Erbert, Günther Tränkle, and Achim Peters. High-power, micro-integrated diode laser modules at 767 and 780 nm for portable quantum gas experiments. *Appl. Opt.*, 54(17) :5332–5338, Jun 2015.

[121] M. Kasevich and S. Chu. Measurement of the gravitational acceleration of an atom with a light-pulse atom interferometer. *Applied Physics B*, 332(5) :321–332, 1992.

[122] P. Gillot, O. Francis, A. Landragin, F. Pereira Dos Santos, and S. Merlet. Stability comparison of two absolute gravimeters : optical versus atomic interferometers. *Metrologia*, 51 :L15, 2014.

[123] Q. Bodart, S. Merlet, N. Malossi, F. Pereira Dos Santos, P. Bouyer, and A. Landragin. A cold atom pyramidal gravimeter with a single laser beam. *Applied Physics Letters*, 96(13) :134101, 2010.

[124] G. Stern, B. Battelier, R. Geiger, G. Varoquaux, A. Villing, F. Moron, O. Carraz, N. Zahzam, Y. Bidel, W. Chaibi, F. Pereira Dos Santos, A. Bresson, A. Landragin, and P. Bouyer. Light-pulse atom interferometry in microgravity. *Euro. Phys. J. D*, 53 :353, 2009.

[125] P. Cheiney, L. Fouché, S. Templier, F. Napolitano, B. Battelier, P. Bouyer, and B. Barrett. Navigation-Compatible Hybrid Quantum Accelerometer Using a Kalman Filter. *Phys. Rev. Applied*, 10 :034030, Sep 2018.

[126] B. Canuel, F. Leduc, D. Holleville, A. Gauguet, J. Fils, A. Virdis, A. Clairon, N. Dimarcq, Ch. J. Bordé, and A. Landragin. Six-axis inertial sensor using cold-atom interferometry. *Physical review letters*, 97 :010402, 2006.

[127] Ch. J. Bordé. Theoretical tools for atom optics and interferometry. *C. R. Acad. Sci. Paris*, 2 :509, 2001.

[128] A. Bonnin, N. Zahzam, Y. Bidel, and A. Bresson. Characterization of a simultaneous dual-species atom interferometer for a quantum test of the weak equivalence principle. *Physical Review A*, 92 :023626, 2015.

[129] Léo Morel, Zhibin Yao, Pierre Cladé, and Saïda Guellati-Khélifa. Velocity-dependent phase shift in a light-pulse atom interferometer, 2020.

[130] P. Gillot, B. Cheng, S. Merlet, and F. Pereira Dos Santos. Limits to the symmetry of a mach-zehnder-type atom interferometer. *Phys. Rev. A*, 93 :013609, Jan 2016.

[131] E. Arimondo, W. Ertmer, W. P. Schleich, E. M. Rasel, and editors. Atom optics and space physics. In *Proceedings of the International School of Physics Enrico Fermi*, 2009.

[132] C. J. Bordé. Quantum theory of atom-wave beam splitters and application to multidimensional atomic gravito-inertial sensors. *Opt. Lett.*, 36 :1572–9532, 2004.

[133] A Trimeche, B Battelier, D Becker, A Bertoldi, P Bouyer, C Braxmaier, E Charron, R Corgier, M Cornelius, K Douch, N Gaaloul, S Herrmann, J Müller, E Rasel, C Schubert, H Wu, and F Pereira dos Santos. Concept study and preliminary design of a cold atom interferometer for space gravity gradiometry. *Classical and Quantum Gravity*, 36(21) :215004, oct 2019.

[134] A. Roura, W. Zeller, and W. P. Schleich. Overcoming loss of contrast in atom interferometry due to gravity gradients. *New Journal of Physics*, 16 :12312, 2014.

[135] Alexey V Veryaskin. *Gravity, Magnetic and Electromagnetic Gradiometry*. 2053-2571. Morgan and Claypool Publishers, 2018.

[136] R. Caldani, K. X. Weng, S. Merlet, and F. Pereira Dos Santos. Simultaneous accurate determination of both gravity and its vertical gradient. *Phys. Rev. A*, 99 :033601, Mar 2019.

[137] O. Carraz, C. Siemes, L. Massotti, R. Haagmans, and P. Silvestrin. A spaceborne gravity gradiometer concept based on cold atom interferometers for measuring earth's gravity field. *Microgravity Science and Technology*, 26 :139, 2014.

[138] D. Aguilera, H. Ahlers, B. Battelier, A. Bawamia, A. Bertoldi, R. Bondarescu, K. Bongs, P. Bouyer, C. Braxmaier, L. Cacciapuoti, C. Chaloner, M. Chwalla, W. Ertmer, M. Franz, N. Gaaloul, M. Gehler, D. Gerardi, L. Gesa, N. Gürlebeck, J. Hartwig, M. Hauth, O. Hellmig, W. Herr, S. Herrmann, A. Heske, A. Hinton, P. Ireland, P. Jetzer, U. Johann, M. Krutzik, A. Kubelka, C. Lämmerzahl, A. Landragin, I. Lloro, D. Massonnet, I. Mateos, A. Milke, M. Nofrarias, M. Oswald, K. Peters, A. Posso-Trujillo, E. Rasel, E. Rocco, A. Roura, J. Rudolph, W. Schleich, C. Schubert, T. Schuldt, S. Seidel, K. Sengstock, C. F. Sopuerta, F. Sorrentino, D. Summers, G. M. Tino, C. Trenkel, N. Uzunoglu, W. von Klitzing, R. Walser, T. Wendrich, A. Wenzlawski, P. Weßels, A. Wicht, E. Wille, M. Williams, P. Windpassinger, and N. Zahzam. STE-QUEST - Test of the universality of free fall using cold atom interferometry. *Classical and Quantum Gravity*, 31 :159502, 2014.

[139] Patrick Cheinet. *Conception et Réalisation d'un Gravimètre à Atomes Froids.* PhD thesis, Université de Paris VI, 2006.

[140] Lisa Consortium. *LISA : Assessment Study Report.* 2011.

[141] Xiao-Jun Jiang, Xiao-Lin Li, Xin-Ping Xu, Hai-Chao Zhang, and Yu-Zhu Wang. Archimedean-spiral-based microchip ring waveguide for cold atoms. *Chinese Physics Letters*, 32(2) :020301, feb 2015.

[142] E. R. Moan, R. A. Horne, T. Arpornthip, Z. Luo, A. J. Fallon, S. J. Berl, and C. A. Sackett. Quantum rotation sensing with dual sagnac interferometers in an atom-optical waveguide. *Phys. Rev. Lett.*, 124 :120403, Mar 2020.

[143] Jun seok Yang, Dixin Zhang, Jiang Chen, Jinduo Wang, Hongwei Zhu, Yinguang Ma, and Liangyu Huang. Investigation on porous materials for cesium beam frequency standard in space environment. 2016.

[144] R.E. Drullinger, D.J. Glaze, and D.B. Sullivan. A recirculating oven for atomic beam frequency standards. pages 13–17, 02 1985.

[145] C. C. Nshii, M. Vangeleyn, J. P. Cotter, P. F. Griffin, E. A. Hinds, C. N. Ironside, P. See, A. G. Sinclair, E. Riis, and A. S. Arnold. A surface-patterned chip as a strong source of ultracold atoms for quantum technologies. *Nature Nanotechnology*, 8(2) :321–324, 2013.

[146] Y.-J. Lin, A. R. Perry, R. L. Compton, I. B. Spielman, and J. V. Porto. Rapid production of ^{87}Rb bose-einstein condensates in a combined magnetic and optical potential. *Phys. Rev. A*, 79 :063631, Jun 2009.

[147] J. F. ALLEN and A. D. MISENER. Flow of liquid helium ii. *Nature*, 141 :1476–4687, 1938.

[148] J. F. ALLEN and A. D. MISENER. The lambda-phenomenon of liquid helium and the bose-einstein degeneracy. *Nature*, 141 :643, 1938.

[149] S. Stringari. Cours du college de frane, chaire européenne : Condensation de bose einstein et superfluidité, 2005.

[150] R. E. Peierls. *Ann. Inst. Henri Poincaré*, 5 :177, 1935.

[151] V. L. Berezinskii. Destruction of long-range order in one-dimensional and two-dimensional systems possessing a continuous symmetry group. *Sov. Phys. JETP*, 34 :610–616, 1972.

[152] J. M. Kosterlitz and D. J. Thouless. Ordering, metastability and phase transitions in two dimensional systems. *J. Phys. C : Solid State Physics*, 6 :1181–1203, 1973.

[153] D. J. Bishop and J. D. Reppy. Study of the superfluid transition in two-dimensional 4he films. *Phys. Rev. Lett.*, 40 :1727, 1978.

[154] A. I. Safonov, S. A. Vasilyev, I. S. Yasnikov, I. I. Lukashevich, and S. Jaakkola. Observation of quasicondensate in two-dimensional atomic hydrogen. *Phys. Rev. Lett.*, 81 :4545, 1998.

[155] D. S. Petrov, M. Holzmann, and G. V. Shlyapnikov. Bose-einstein condensation in quasi-2d trapped gases. *Phys. Rev. Lett.*, 84 :2551–2555, Mar 2000.

[156] Zoran Hadzibabic and Jean Dalibard. *BKT Physics with Two-Dimensional Atomic Gases*, pages 297–323.

[157] Vanderlei Bagnato and Daniel Kleppner. Bose-einstein condensation in low-dimensional traps. *Phys. Rev. A*, 44 :7439–7441, Dec 1991.

[158] Richard J. Fletcher, Martin Robert-de Saint-Vincent, Jay Man, Nir Navon, Robert P. Smith, Konrad G. H. Viebahn, and Zoran Hadzibabic. Connecting berezinskii-kosterlitz-thouless and bec phase transitions by tuning interactions in a trapped gas. *Phys. Rev. Lett.*, 114 :255302, Jun 2015.

[159] P. Cladé, C. Ryu, A. Ramanathan, K. Helmerson, and W. D. Phillips. Observation of a 2d bose gas : From thermal to quasicondensate to superfluid. *Phys. Rev. Lett.*, 102 :170401, Apr 2009.

[160] Alexander L. Gaunt, Tobias F. Schmidutz, Igor Gotlibovych, Robert P. Smith, and Zoran Hadzibabic. Bose-einstein condensation of atoms in a uniform potential. *Phys. Rev. Lett.*, 110 :200406, May 2013.

[161] O. Zobay and B. M. Garraway. Atom trapping and two-dimensional bose-einstein condensates in field-induced adiabatic potentials. *Phys. Rev. A*, 69 :023605, Feb 2004.

[162] N. Lundblad, R. A. Carollo, C. Lannert, M. J. Gold, X. Jiang, D. Paseltiner, N. Sergay, and D. C. Aveline. Shell potentials for microgravity Bose-Einstein condensates. *npj Microgravity*, 5 :2373–8065, 2020.

[163] Burt A. Ovrut and Steven Thomas. Theory of vortices and monopoles on a sphere. *Phys. Rev. D*, 43 :1314–1322, Feb 1991.

[164] A. Tononi and L. Salasnich. Bose-einstein condensation on the surface of a sphere. *Phys. Rev. Lett.*, 123 :160403, Oct 2019.

[165] Kuei Sun, Karmela Padavić, Frances Yang, Smitha Vishveshwara, and Courtney Lannert. Static and dynamic properties of shell-shaped condensates. *Phys. Rev. A*, 98 :013609, Jul 2018.

[166] Karmela Padavić, Kuei Sun, Courtney Lannert, and Smitha Vishveshwara. Physics of hollow bose-einstein condensates. *EPL (Europhysics Letters)*, 120(2) :20004, oct 2017.

[167] Klaus Mølmer. Bose condensates and fermi gases at zero temperature. *Phys. Rev. Lett.*, 80 :1804–1807, Mar 1998.

[168] S. Ospelkaus, C. Ospelkaus, L. Humbert, K. Sengstock, and K. Bongs. Tuning of heteronuclear interactions in a degenerate fermi-bose mixture. *Phys. Rev. Lett.*, 97 :120403, Sep 2006.

[169] Bert Van Schaeybroeck and Achilleas Lazarides. Trapped phase-segregated bose-fermi mixtures and their collective excitations. *Phys. Rev. A*, 79 :033618, Mar 2009.

[170] G. G. Batrouni, V. Rousseau, R. T. Scalettar, M. Rigol, A. Muramatsu, P. J. H. Denteneer, and M. Troyer. Mott domains of bosons confined on optical lattices. *Phys. Rev. Lett.*, 89 :117203, Aug 2002.

[171] B. DeMarco, C. Lannert, S. Vishveshwara, and T.-C. Wei. Structure and stability of mott-insulator shells of bosons trapped in an optical lattice. *Phys. Rev. A*, 71 :063601, Jun 2005.

[172] Gretchen K. Campbell, Jongchul Mun, Micah Boyd, Patrick Medley, Aaron E. Leanhardt, Luis G. Marcassa, David E. Pritchard, and Wolfgang Ketterle. Imaging the mott insulator shells by using atomic clock shifts. *Science*, 313(5787) :649–652, 2006.

[173] R. A. Barankov, C. Lannert, and S. Vishveshwara. Coexistence of superfluid and mott phases of lattice bosons. *Phys. Rev. A*, 75 :063622, Jun 2007.

[174] Ari M. Turner, Vincenzo Vitelli, and David R. Nelson. Vortices on curved surfaces. *Rev. Mod. Phys.*, 82 :1301–1348, Apr 2010.

[175] Vincenzo Vitelli and Ari M. Turner. Anomalous coupling between topological defects and curvature. *Phys. Rev. Lett.*, 93 :215301, Nov 2004.

[176] Karmela Padavić, Kuei Sun, Courtney Lannert, and Smitha Vishveshwara. Vortex-antivortex physics in shell-shaped bose-einstein condensates, 2020.

[177] G.S. Milagre and Winder A. Moura-Melo. Magnetic vortex-like excitations on a sphere. *Physics Letters A*, 368(1) :155 – 163, 2007.

[178] Maxime Bellouvet, Caroline Busquet, Jinyi Zhang, Philippe Lalanne, Philippe Bouyer, and Simon Bernon. Doubly dressed states for near-field trapping and subwavelength lattice structuring. *Phys. Rev. A*, 98 :023429, Aug 2018.

[179] D. E. Chang, K. Sinha, J. M. Taylor, and H. J. Kimble. Trapping atoms using nanoscale quantum vacuum forces. *Nature Communications*, 5 :4343, 2014.

[180] Maxime Bellouvet. Condensation de bose-einstein et simulation d'une méthode de piégeage d'atomes froids dans des potentiels sublongueur d'onde en champ proche d'une surface nanostructurée, 2018.

[181] R Bücker, A Perrin, S Manz, T Betz, Ch Koller, T Plisson, J Rottmann, T Schumm, and J Schmiedmayer. Single-particle-sensitive imaging of freely propagating ultracold atoms. *New Journal of Physics*, 11(10) :103039, oct 2009.

[182] C. Lannert, T.-C. Wei, and S. Vishveshwara. Dynamics of condensate shells : Collective modes and expansion. *Phys. Rev. A*, 75 :013611, Jan 2007.

[183] K. W. Madison, F. Chevy, W. Wohlleben, and J. Dalibard. Vortex formation in a stirred bose-einstein condensate. *Phys. Rev. Lett.*, 84 :806–809, Jan 2000.

[184] Noel A. Clark, Alexey Eremin, Matthew A. Glaser, Nancy Hall, Kirsten Harth, Christoph Klopp, Joseph E. Maclennan, Cheol S. Park, Ralf Stannarius, Padetha Tin, and et al. Realization of hydrodynamic experiments on quasi-2d liquid crystal films in microgravity. *Advances in Space Research*, 60(3) :737–751, Aug 2017.

[185] R. Pindak, D. E. Moncton, S. C. Davey, and J. W. Goodby. X-ray observation of a stacked hexatic liquid-crystal *b* phase. *Phys. Rev. Lett.*, 46 :1135–1138, Apr 1981.

[186] Groupe de travail Thematique Sciences de la matière. Seminaire de prospective scientifique du cnes, 2019.

[187] T.G. Wang, A.V. Anilkumar, C.P. Lee, and K.C. Lin. Core-centering of compound drops in capillary oscillations : Observations on usml-1 experiments in space. *Journal of Colloid and Interface Science*, 165(1) :19 – 30, 1994.

[188] T. Meuel, Y. L. Xiong, P. Fischer, C. Bruneau, M. Bessafi, and H. Kellay. Intensity of vortices : from soap bubbles to hurricanes. *Scientific Reports*, 3 :3455, 2013.

[189] J. Billy, Z. Josse, V.and Zuo, A. Bernard, B. Hambrecht, P. Lugan, D. Clément, L. Sanchez-Palencia, P. Bouyer, and A. Aspect. Direct observation of anderson localization of matter waves in a controlled disorder. *Nature*, 453 :891–894, 2008.

[190] G. Roati, C. D'Errico, L. Fallani, M. Fattori, C. Fort, M. Zaccanti, G. Modugno, M. Modugno, and M. Inguscio. Anderson localization of a non-interacting bose–einstein condensate. *Nature*, 453 :895–898, 2008.

[191] SS Kondov, WR McGehee, JJ Zirbel, and B DeMarco. Three-dimensional anderson localization of ultracold matter. *Science (New York, N.Y.)*, 334(6052) :66—68, October 2011.

[192] F. Jendrzejewski, A. Bernard, K. Müller, P. Cheinet, V. Josse, M. Piraud, L. Pezzé, L. Sanchez-Palencia, A. Aspect, and P. Bouyer. Three-dimensional localization of ultracold atoms in an optical disordered potential. *Nature Physics*, 453 :398–403, 2008.

[193] G. Semeghini, M. Landini, P. Castilho, S. Roy, G. Spagnolli, A. Trenkwalder, M. Fattori, M. Inguscio, and G. Modugno. Measurement of the mobility edge for 3d anderson localization. *Nature Physics*, 11 :554–559, 2015.

[194] Donald H. White, Thomas A. Haase, Dylan J. Brown, Maarten D. Hoogerland, Mojdeh S. Najafabadi, John L. Helm, Christopher Gies, Daniel Schumayer, and David A. W. Hutchinson. Observation of two-dimensional anderson localisation of ultracold atoms, 2019.

[195] Michael Pasek, Giuliano Orso, and Dominique Delande. Anderson localization of ultracold atoms : Where is the mobility edge ? *Phys. Rev. Lett.*, 118 :170403, Apr 2017.

[196] V. Josse. Private discussion, 2020.

[197] Jérémie Richard, Lih-King Lim, Vincent Denechaud, Valentin V. Volchkov, Baptiste Lecoutre, Musawwadah Mukhtar, Fred Jendrzejewski, Alain Aspect, Adrien Signoles, Laurent Sanchez-Palencia, and Vincent Josse. Elastic scattering time of matter waves in disordered potentials. *Phys. Rev. Lett.*, 122 :100403, Mar 2019.

[198] Pierre Dussarrat, Maxime Perrier, Almazbek Imanaliev, Raphael Lopes, Alain Aspect, Marc Cheneau, Denis Boiron, and Christoph I. Westbrook. Two-particle four-mode interferometer for atoms. *Phys. Rev. Lett.*, 119 :173202, Oct 2017.

[199] John F. Clauser, Michael A. Horne, Abner Shimony, and Richard A. Holt. Proposed experiment to test local hidden-variable theories. *Phys. Rev. Lett.*, 23 :880–884, Oct 1969.

[200] J. G. Rarity and P. R. Tapster. Experimental violation of bell's inequality based on phase and momentum. *Phys. Rev. Lett.*, 64 :2495–2498, May 1990.

[201] M. Bonneau, J. Ruaudel, R. Lopes, J.-C. Jaskula, A. Aspect, D. Boiron, and C. I. Westbrook. Tunable source of correlated atom beams. *Phys. Rev. A*, 87 :061603, Jun 2013.

[202] Andrea Bergschneider, Vincent M. Klinkhamer, Jan Hendrik Becher, Ralf Klemt, Gerhard Zürn, Philipp M. Preiss, and Selim Jochim. Spin-resolved single-atom imaging of ^{6}Li in free space. *Phys. Rev. A*, 97 :063613, Jun 2018.

[203] David C. Aveline, Jason R. Williams, Ethan R. Elliott, Chelsea Dutenhoffer, James R. Kellogg, James M. Kohel, Norman E. Lay, Kamal Oudrhiri, Robert F. Shotwell, Nan Yu, and Robert J. Thompson. Observation of bose–einstein condensates in an earth-orbiting research lab. *Nature*, 582 :193, 2020.

[204] Liang Liu, De-Shen Lü, Wei-Biao Chen, Tang Li, Qiu-Zhi Qu, Bin Wang, Lin Li, Wei Ren, Zuo-Ren Dong, Jian-Bo Zhao, Wen-Bing Xia, Xin Zhao, Jing-Wei Ji, Mei-Feng Ye, Yan-Guang Sun, Yuan-Yuan Yao, Dan Song, Zhao-Gang Liang, Shan-Jiang Hu, Dun-He Yu, Xia Hou, Wei Shi, Hua-Guo Zang, Jing-Feng Xiang, Xiang-Kai Peng, and Yu-Zhu Wang. In-orbit operation of an atomic clock based on laser-cooled 87rb atoms. *Nature Communications*, 9 :2760, 2018.

[205] Anton Mazurenko, Christie S. Chiu, Geoffrey Ji, Maxwell F. Parsons, Márton Kanász-Nagy, Richard Schmidt, Fabian Grusdt, Eugene Demler, Daniel Greif, and Markus Greiner. A cold-atom fermi–hubbard antiferromagnet. *Nature*, 545 :462, 2017.

[206] Saurabh Pandey, Hector Mas, Giannis Drougakis, Premjith Thekkeppatt, Vasiliki Bolpasi, Georgios Vasilakis, Konstantinos Poulios, and Wolf von Klitzing. Hypersonic bose–einstein condensates in accelerator rings. *Nature*, 570 :205, 2019.

[207] Tomoya Akatsuka, Tadahiro Takahashi, and Hidetoshi Katori. Optically guided atom interferometer tuned to magic wavelength. *Applied Physics Express*, 10(11) :112501, oct 2017.

[208] Shoichi Okaba, Deshui Yu, Luca Vincetti, Fetah Benabid, and Hidetoshi Katori. Superradiance from lattice-confined atoms inside hollow core fibre. *Communications Physics*, 2 :136, oct 2019.